Development of Polymer Based Composite and Organic-Inorganic Hybrid Materials for Application as Single Ion Conducting Solid-State Electrolytes

by

Guangyu Wang

A dissertation submitted in partial fulfillment
of the requirement for the degree of
Doctor of Philosophy
(Materials Science and Engineering)
in the University of Michigan
2024

Doctoral Committee:

Professor John Kieffer, Chair
Professor Jinsang Kim
Assistant Professor Yiyang Li
Professor Wei Lu

Guangyu Wang

guangyuw@umich.edu

ORCID iD: 0000-0002-6245-9453

DEDICATION

To my wife, Mengge.

To my parents, Aiping and Zhiren.

I extend my sincere gratitude to each one of you for your unwavering love, invaluable support, and uplifting encouragement that have played an indispensable role throughout this truly extraordinary and once-in-a-lifetime journey. Your contributions have been the bedrock of my experience, making it all the more meaningful and memorable.

ACKNOWLEDGMENTS

First, I would extend my profound gratitude to my advisor, Dr. John Kieffer, whose unwavering support and mentorship have been the guiding lights on this challenging yet fulfilling academic journey. Dr. Kieffer not only provided direction but also instilled in me the confidence to navigate numerous obstacles that seemed insurmountable. My heartfelt thanks also go to the esteemed members of my committee, Dr. Jinsang Kim, Dr. Wei Lu, and Dr. Yiyang Li, for their valuable insights and meticulous evaluation of my research, shaping it into a more robust contribution to the field.

The camaraderie and intellectual exchange in the Kieffer Lab have been a source of inspiration and joy. I want to express my appreciation to Dr. M. Cameran Beg, Dr. Vazrik Keshishian, Jialong Ke, Jiun-Yeu Chang, Jindong Huang, and Dr. Wenkun Wu for their collaborative spirit and insightful discussions, which have significantly enriched the research process.

Lastly, I owe a special thanks to my family—my parents and my wife, Mengge—for being my unwavering support system. Without their encouragement, none of what I've accomplished would have been remotely possible. To all of you, I acknowledge a profound gratitude that I can never fully repay. Your influence on my journey is permanently etched in my heart, and I am eternally thankful for your profound impact.

TABLE OF CONTENTS

LIST OF FIGURES

LIST OF TABLES

LIST OF APPENDICES

APPENDIX

ABSTRACT

The transition from liquid to solid-state electrolytes (SSEs) for battery applications offers advantages such as higher energy density, enhanced safety, improved stability, and a solution to the dendrite growth issue during charging. Single-ion conduction is pursued to enhance charge carrier mobility and mitigate electrode degradation. In this thesis, we explore two material systems: polymer-matrix composites and organic-inorganic silica hybrid materials, with the aim of understanding ion transport mechanisms and optimizing material design for improved performance.

In the poly(ethylene) oxide (PEO)-based composite, an interfacial region develops surrounding amorphous $Li_{1.3}Al_{0.3}Ti_{1.7}(PO_4)_3$ (LATP) nanoparticles, exhibiting 30 times higher Li^+ mobility compared to the polymer matrix. We achieve uniform nanoparticle dispersion through a water-based in-situ precipitation method, leading to a 20°C conductivity of 3.8×10^{-4} S·cm^{-1} at a particle loading of 12.5 vol% and a Li^+ concentration of 1.65 nm^{-1}. Comparative infrared spectroscopy reveals increased disorder in the interphase polymer, offering low activation barrier cation migration pathways. Analysis using a transition state theory-based approach to examine the temperature dependence of ionic conductivity reveals that thermally activated processes within the interphase benefit more from higher activation entropy than from a decrease in activation enthalpy. Although lithium infusion from LATP particles is modest, charge carriers tend to concentrate in a space-charge configuration near the particle/polymer interface.

To improve Li^+ transference numbers, electrochemical stability, and mechanical strength, a hybrid design is pursued, consisting of a nano-porous silica backbone bi-functionalized with the cation donor 2-[(Trifluoromethanesulfonylimido)-N-4-sulfonylphenyl] ethyl (TFSISPE) anion and the molecular brush 2-[Methoxy(polyethyleneoxy)$_{6-9}$propyl] trimethoxysilane (oligo-PEG). A low-density nano-porous structure is created using sol-gel synthesis. The backbone functionalization is achieved through a carefully timed and phased introduction of pre-hydrolyzed TFSISPE anion and oligo-PEG to the partially gelled silica. As a result, cation donor groups are covalently bonded to the backbone. Subsequently, low-molecular-weight polyethylene oxide replaces the solvent in the nanopores. Oligo-PEG grafting increases the pore fill factor and significantly boosts ionic conductivity (5.2×10^{-4} S cm^{-1} at 20°C for a one-molar Li^+ concentration) by reducing conductivity osmotic drag resulting from entanglement between oligo-PEG and PEO. Anchoring the TFSISPE anion to the backbone yields a Li^+ transference number $t_{Li^+}\sim0.91$.

Incorporating liquid carbonates into the porous silica backbone, e.g., propylene carbonate (PC) and ethylene carbonate (EC), further enhances the conductivity of the hybrid material to 2.9×10^{-3} S·cm^{-1} at 20°C, with a Li^+ transference number of 0.9 for electrolytes with oligo-PEG grafting. However, liquid carbonates have poor thermal stability, even when confined to nanopores. The ionic liquid 1-Ethyl-3-methylimidazolium bis(trifluoromethylsulfonyl)imide (EMIM TFSI) proves to be the best pore medium for these hybrids. It has superior thermal stability, up to 275°C, thus potentially suitable for practical applications. It reaches ionic conductivities of nearly 10^{-2} S·cm^{-1}, but at the cost of a lower transference number (0.435) due to the binary salt nature of the ionic liquid. Cation mobility in these systems exhibits a maximum as a function of the average pore size, which is controlled by varying the water-to-TEOS ratio (R_w ratio) during the backbone synthesis. Here we provide a cumulative account of systematic materials design efforts. The sequential implementation

of these elements allows us to discern their individual importance of the various materials design elements and assess their collective influence on the performance characteristics of the materials.

CHAPTER I Introduction

1.1 Background and Motivation

The role of electrolytes in the realm of lithium-ion batteries is undeniably pivotal. In today's landscape, with an increasing demand for applications necessitating rapid charge-discharge rates, the quest for high-performance electrolytes has gained paramount significance. These high-performance electrolytes must exhibit attributes such as elevated ionic conductivity, robust thermal stability, and sufficient mechanical integrity.[1–3] Current carbonate liquid electrolytes, including propylene carbonate (PC), ethylene carbonate (EC), and their combinations, do not fully meet the safety requirements due to their flammability. Various efforts have been undertaken to address the safety concerns associated with carbonate solvents. These efforts have included mixing them with substances such as ethyl methyl carbonate (EMC), tris(2,2,2-trifluoroethyl)phosphate (TFEP), or ionic liquids, although these attempts have achieved only moderate success.[4–8] Arbizzani et al. found that mixtures of carbonates with high proportions of ionic liquids are more challenging to ignite; however, once ignited, they burn for an extended duration. Other reports have indicated that while these modified carbonate solvents show improved non-flammability, they still exhibit decomposition at relatively low temperatures, which could have a detrimental impact on their performance.[9,10]

Numerous endeavors have been undertaken to replace carbonate liquids, exploring both solid-state electrolytes (SSEs) and gel-type systems based on polymers, ceramics, glasses, and their resulting composites or hybrids.[11] In general, SSEs have the potential to enhance the durability, energy density, and operational safety of lithium-ion batteries.[12–16] Among various system designs, solid polymer electrolytes have garnered substantial attention. However, despite the relatively low glass transition temperatures (T_g) of polymers, their ionic conductivities significantly lag behind those of liquid electrolytes.[14,17–19] This shortfall can be partly attributed to the propensity of polymer chains to form crystalline domains, which hinder cation mobility. Various strategies have been employed to reduce the degree of crystallinity in solid polymer electrolytes. While some methods, such as plasticizing and blending with oligomers, have proven effective, they often come at the cost of increased reactivity with electrodes and compromised mechanical strength. However, some of these drawbacks can be mitigated by implementing special microstructure design approaches. One such approach is reported by Wang et al., who developed a flexible solid polymer electrolyte by incorporating a three-dimensional polyvinylidene fluoride (PVDF) network with in-situ thermocured Polyethylene glycol (PEO). This design resulted in a significant reduction of crystallinity in both phases of the material. Importantly, this solid polymer electrolyte exhibited a long cycling life of more than 1000 cycles, demonstrating its durability and stability.[20] Copolymerization is another widely adopted strategy; comb-like copolymers grafted with PEO side chains do not crystallize and exhibit excellent ionic conductivity.[21] Adding ceramic nanoparticles to the polymer matrix has also proven effective. The widely accepted explanation for this enhancement is that the nanoparticles act as plasticizers, inhibiting crystallization and preserving the segmental mobility of polymer chains.[22–25] Various types of particles have been tested, including passive fillers such as TiO_2, Al_2O_3 and SiO_2, as well as active fillers like $Li_{1.3}Al_{0.3}Ti_{1.7}(PO_4)_3$ (LATP) and $Li_{0.33}La_{0.557}TiO_3$ (LLTO).[26] Some of these active fillers themselves exhibit ionic conductivities of nearly 10^{-4} $S \cdot cm^{-1}$.[27] Consequently, it has

been suggested that active fillers directly contribute to charge transport by establishing their own conduction pathways, especially in electrolytes with high particle volume fractions.[28–31] However, the precise mechanism underlying the improvement in conductivity upon the addition of ceramic nanoparticles to the polymer composite electrolyte remains unclear.

While solid polymer electrolytes offer advantages such as safety, flexibility, and good contact with the electrode, their ionic conductivities typically fall within the range of 10^{-7} – 10^{-4} S·cm^{-1}. Additionally, the use of low T_g polymer matrices can compromise mechanical strength. Moreover, when the source of Li^+ is in the form of a binary salt, which is typical in solid polymer electrolytes, both Li^+ and its counterion move to the opposite electrodes during the charging and discharging of these batteries. Research conducted by Villaluenga et al. has shed light on dual-ion conducting electrolytes, revealing that only around one-third of the conductivity can be attributed to Li^+.[32] This attribution is quantified by the cation transference number (t^+), defined as $t^+ = \sigma_{cation}/(\sigma_{cation}+\sigma_{anion})$, where σ represents ionic conductivity. In such systems, only the cation participates in electrochemical reactions at the battery's electrodes. As a result, over time, the anion tends to accumulate at the anode while depleting at the cathode. This phenomenon can lead to electrode degradation, capacity deterioration, and a reduction in the batteries' output voltage.[32–34]

The goals of this thesis are twofold. Firstly, in solid polymer electrolytes, the aim is to clarify and substantiate the concept that the most highly conductive region is the interphase that develops between particles and the polymer matrix. Secondly, to further enhance ionic conductivity, mechanical strength, and meet the requirement of a single-ion conductor, hybrid systems based on silica gel are introduced and comprehensively evaluated.

1.2 Solid polymer electrolytes – conducting through interphase

In previous research, we uncovered evidence suggesting that the advantages of incorporating active nanoparticles into a polymer matrix go beyond just suppressing crystallization and/or offering potential Li^+ conduits. Specifically, in the study of a LATP/ PEO composite, we observed the development of high-mobility cation migration pathways within the interfacial region that forms around the nanoparticles.[26,30,35] The ionic conductivity in this material rises sharply upon adding LATP nanoparticles, and already at relatively small volume fractions, significantly exceeds the ionic conductivity of pure LATP as well as pure PEO. This observed behavior could not be explained by conventional rules of mixture for binary systems. To quantitatively evaluate our results, we developed an analytical model that assumed the presence of a third phase, corresponding to the interphase. Our three-phase model not only allowed us to estimate the magnitude of Li^+ conductivity within the interphase but also predicted the maximum conductivity achievable in the LATP/PEO composite, provided that the nanoparticles were uniformly distributed throughout the material.[35] This latter condition is essential because when the nanoparticles cluster or aggregate, the direct contact with one another overlaps with, and therefore eliminates, potential highly conductive interphase volume.

With conventional mechanical mixing, which has been widely used for fabricating composite SSEs, we were not able to achieve effective nanoparticle dispersion. Consequently, the ionic conductivity began to decrease when particle loadings exceeded approximately 15 wt%. This phenomenon has also been reported by other researchers.[27] Surface functionalization is a popular strategy aimed at enhancing nanoparticle dispersion in polymer matrix composites. This approach focuses on directly influencing the physical and chemical interactions at the interface between nanoparticles and their surroundings.[36] While it may indeed lead to improved particle dispersion, it is likely that surface

functionalization also alters the chemical factors that determine the constitution of the polymer in the vicinity of the particles. This alteration could potentially lead to a decrease in the inherent interphase ionic conductivity. Consequently, the interpretation of changes in the measured quantities would be ambiguous. Instead, we pursue the concept of *in-situ* precipitation, which involves liquid phase mixing resulting in spatially random nucleation sites while avoiding alteration of interfacial chemistries.[37]

1.3 Single ion conductor design concepts

Diverse strategies aimed at limiting the mobility of the counterion, thereby establishing what is commonly referred to as single-ion conductors (SICs), are currently under exploration.[38] These strategies include using bulky anions with reduced mobility, integrating anions into polymer chains through copolymerization, employing Lewis acid interactions between anions and immobile components like particle fillers, and anchoring anions to particles or matrix backbones.

1.3.1 Bulky anions

In pursuit of single-ion behavior, one approach involves the use of binary lithium salts containing low-mobility bulky anions. For instance, Dai et al. examined the Li^+ transference numbers in various lithium salts featuring anions of different sizes, such as $CF_3SO_3^-$ (Tf), $N(CF_3SO_2)_2^-$ (TFSI), $N(C_2F_5SO_2)_2^-$ (BETI), and $C(CF_3SO_2)_3^-$ (TFSM), when incorporated into a poly(vinylidene fluoride)–hexafluoropropylene copolymer. Their research revealed that larger anions corresponded to higher Li^+ transference numbers.[39] Similarly, Shah et al. conducted a study using perfluoropolyether electrolytes mixed with various binary lithium salts and observed an increasing trend in the transference number with larger anions.[40] Specifically, research by Zhang et al. compared PEO-based composite systems doped with $LiClO_4$ or LiTFSI. LiTFSI, with the bulky $TFSI^-$ anion, achieved a transference number of 0.39, whereas the $LiClO_4$-doped sample only

reached 0.27.[41] It's worth noting that transference numbers resulting from the use of bulky anions typically fall in the range of 0.2 – 0.5, providing single-ion conducting behavior, though not strictly a SIC.

1.3.2 Polymerization

The most prevalent path to achieving single-ion conductivity involves binding anions to the polymer chain through copolymerization, rendering them immobile and thus categorized as true single-ion conducting polymers.[42] The first such single-ion conducting polymers were reported in 1985, featuring a methacrylate backbone with ethylene oxide and lithiated carboxylate side chains.[43] Copolymeric SICs often incorporate a soft block for ion conduction, a structural block for stability, and a polymeric anion for cation attachment.[42] For example, ionomers were developed by Dou et al. through melt polycondensation of poly(ethylene glycol) (PEG) and dimethyl 5-sulfoisophthalate sodium salt, where the PEG spacer facilitates cation solvation and conduction.[44] Hoffmann et al. created a linear PEO-based ionomer with appended lithium 1,2,3-triazolate end groups, resulting in a conductivity of approximately 10^{-6} S·cm^{-1}.[45] Bouchet et al. designed a B-A-B triblock copolymer, consisting of B blocks based on poly(styrene trifluoromethanesulphonylimide of lithium) P(STFSILi) associated with a central A block based on a linear PEO.[38] Although copolymerization allows for tailored properties, copolymeric SICs generally exhibit a low ambient temperature ionic conductivity ranging from 10^{-8} to 10^{-5} S·cm^{-1},[38,43,46,47] primarily due to the reliance of ionic conduction on the segmental motion of soft blocks and poor ion dissociation from polymeric anions, which reduces the concentration of active cations. Thus, a desirable chain structure characterized by highly delocalized anions, low glass transition temperature flexible soft blocks, and flexible spacers between anions and the main chain is favored for improved conductivity.[14]

1.3.3 Lewis acid interaction

Numerous studies have reported promising results in enhancing transference numbers through the incorporation of inorganic additives, such as glass or ceramics, in the form of fibers or particles into polymer electrolytes.[48] The Lewis acid interaction between these fillers and anions increases the concentration of free cations near the interface, as anions temporarily adhere to the particle surface.[23–25,27] Significant improvements are typically observed when ceramics occupy a substantial portion of the electrolyte. For instance, Wang et al. achieved a Li^+ transference number of about 0.7 in a PEO-based composite mixed with over 50 wt% $La_{0.55}Li_{0.35}TiO_3$ (LLTO) nanofibers.[49] In comparison, Zhang et al. reached a modest transference number of 0.39 in a similar composite with 30 wt% LATP particles,[41] which is a small improvement, with respect to the control group transference number of 0.35 that did not contain fillers.[42] However, Croce et al. achieved a transference number of 0.6 in a PEO mixture with only 10 wt% TiO_2 powder, attributed to the large specific surface area of the nanosized particles, resulting in stronger Lewis acid interactions between the particle surface, anions, and PEO segments.[50]

1.3.4 Anchoring anion to particles or backbones

As illustrated in the **Figure 1-1**, Zhang et al. successfully performed surface modification on silica particles through a silanation reaction, followed by a free-radical polymerization of 2-acrylamido-2-methyl-propanesulfonic acid (AMPS). The final single-ion conductors were obtained by exchanging the H^+ with Li^+.[51] Zhao et al. attempted to attach a trifluoromethanesulfonimide (TFSI) analogue structure to silica particles. Since the TFSI analogue offers a high degree of charge delocalization, it can more readily dissociate with Li^+ and thus provide a greater number of free cations to participate in ion transportation, as depicted in the **Figure 1-2**.[52]

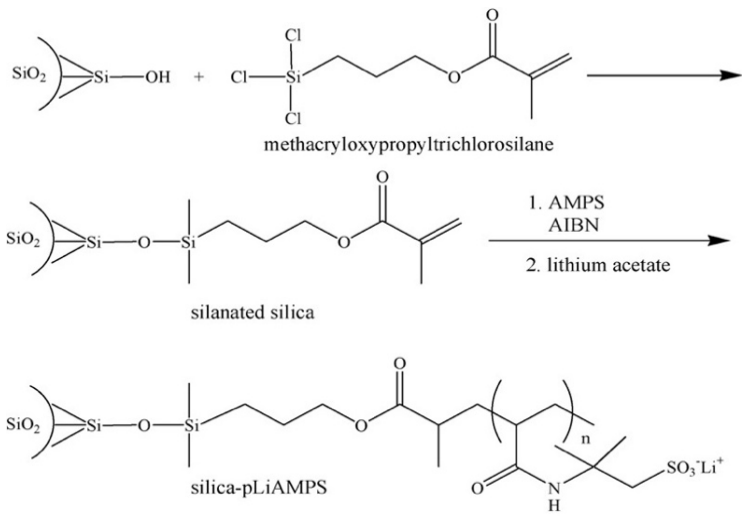

Figure 1-1 Scheme of the procedure of silica particle surface modification and free-radical polymerization.[51]

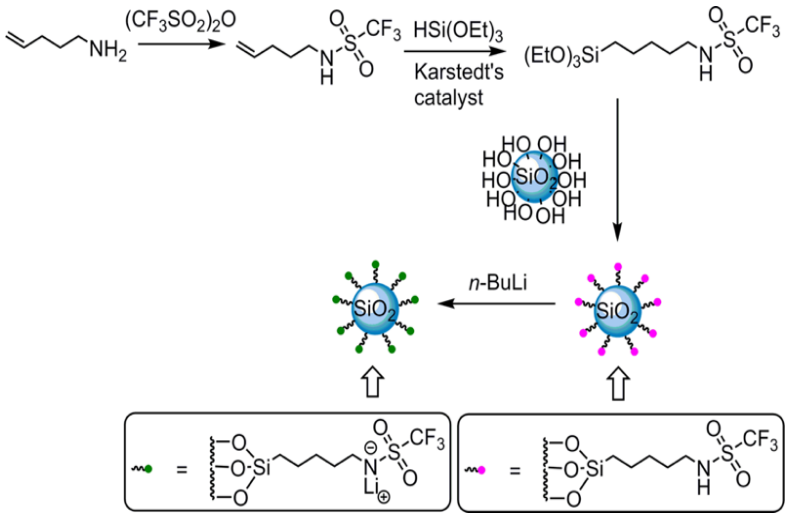

Figure 1-2 Synthesis route for Si-C_5NHTf and lithiation to Si-C_5NTFLi, by Zhao et al.[52]

1.4 Hybrid electrolyte systems based on silica gel

Hybrid materials have been increasingly researched in recent years. These materials are characterized by unique conjugates of organic and inorganic materials.[53] Early endeavors in this field include the work of Zhang et al., who covalently linked silica particles with 2-acrylamido-2-methyl-1-propanesulfonic acid (AMPS), resulting in a material exhibiting room a temperature conductivity of 10^{-6} S·cm^{-1}.[51] Schaefer[54] introduced a hybrid electrolyte by covalently bonding oligo-polyethylene

glycol (PEG) to silica particles and doping them with Lithium bis(trifluoromethanesulfonimide) (LiTFSI). This electrolyte displayed an ambient ionic conductivity of 10^{-4} S·cm^{-1} and a significantly higher modulus compared to the material without the attached polymer. Kim et al.[55] grafted 2-[(Trifluoromethanesulfonylimido)-N-4-sulfonylphenyl] ethyl (TFSISPE) anions onto silica particles. The functionalized hybrid particles were then blended with polyethylene oxide (PEO), achieving conductivities approaching 10^{-3} S·cm^{-1} at 30ºC.

In the majority of hybrid electrolytes documented in the literature, low T_g polymers are employed as matrix materials. This selection arises from the intrinsic trade-off between ionic mobility and mechanical rigidity within these materials, with the matrix playing a pivotal role in facilitating ion conduction. Consequently, a notable discrepancy arises between mechanical strength and conductivity. For the reconciliation of this discrepancy, a specific hybrid design featuring a porous, rigid backbone material stands out. Backbone materials, characterized by a high modulus network structure, offer significant potential in mitigating dendrite growth and enhancing the overall thermal stability of the electrolytic system.[11] The pursuit of such backbone materials has led to extensive exploration of various substances, encompassing inorganics like porous ceramic networks and silica-based gels, as well as organics like cross-linked polymers and high-stiffness linear polymers.[1,2,55–63] Among these, silica gel emerges as an exemplary choice due to its high specific surface area, high porosity, high rigidity, ease of synthesis, and functionalization. These properties have been substantiated by previous research efforts.[64]

However, the backbone alone cannot function as an electrolyte without its pores being filled by additional materials, which typically serve as conduits for ion conduction. The choices for fillers include liquid materials, such as carbonates, low molecular weight polymers, and ionic liquids.[11] For solid fillers, high molecular weight polymers like poly(ethylene oxide) (PEO), polyvinylidene fluoride (PVDF), or copolymers featuring polar groups are common choices.[11,27,61–63,65,66] The methods for

introducing fillers into the pores can include vacuum-assisted impregnation, hot-pressing, or in-situ polymerization depending on the filler, backbone properties, and fabrication methods.[11,61,65] While polymer fillers, regardless of molecular weight, often exhibit high viscosity at room temperature due to chain entanglement and intermolecular attractions. Consequently, the resulting hybrid electrolytes typically have conductivities ranging from 10^{-7} to 10^{-4} S·cm^{-1}, which is several orders of magnitude lower than the practical usage threshold of 10^{-3} S·cm^{-1}.[62,65,67,68] On the other hand, carbonate liquid fillers like EC or PC, while exhibiting a conductivity of 10^{-3} S·cm^{-1}, can present potential safety concerns due to their volatility under elevated temperatures (i.e. > 70°C), even when confined in a nano porous matrix.[69,70] In this context, ionic liquids (ILs) present a promising alternative to polymer and carbonate fillers. ILs are a class of organic salts that remain in a liquid state at or near room temperature. They are comprised of large organic cations and various anions, with common IL cations including imidazolium, pyridinium, alkylammonium, alkyl phosphonium, pyrrolidinium, guanidinium, and alkyl pyrrolidinium. IL anions can be chosen from a wide array of inorganic anions, including halides (Cl^-, Br^-, I^-), polyatomic inorganics (PF_6^-, BF_4^-), or organic anions such as NO_3^-, $TFSI^-$, and Tf^-.[71] ILs are known for their unique properties, including high thermal stability, non-flammability, and high ionic conductivity.[72–77] Moreover, ILs often possess a wide electrochemical window, enabling them to operate over a broad range of voltages without undesirable side reactions. These characteristics are especially advantageous for high-energy-density batteries.[74]

1.5 Sol-Gel synthesis and functionalization of the backbone material

1.5.1 Sol-Gel Synthesis

A sol is a colloidal suspension of solid particles in a liquid, and a gel is a continuous three-dimensional network that encompasses a liquid phase. The sol-gel process can be described as the

creation of an oxide network through polycondensation reactions of a precursor in a liquid. One commonly used precursor in the synthesis of silica gel is Tetraethyl orthosilicate (TEOS). The reaction initiates with hydrolysis, where the oxygen in water nucleophilically attacks the silicon atom, leading to the replacement of alkoxide groups (-OR) with hydroxyl groups (-OH), as depicted in the **Figure 1-3**. Subsequently, either water or alcohol condensation takes place, resulting in the formation of a siloxane network.[64,78]

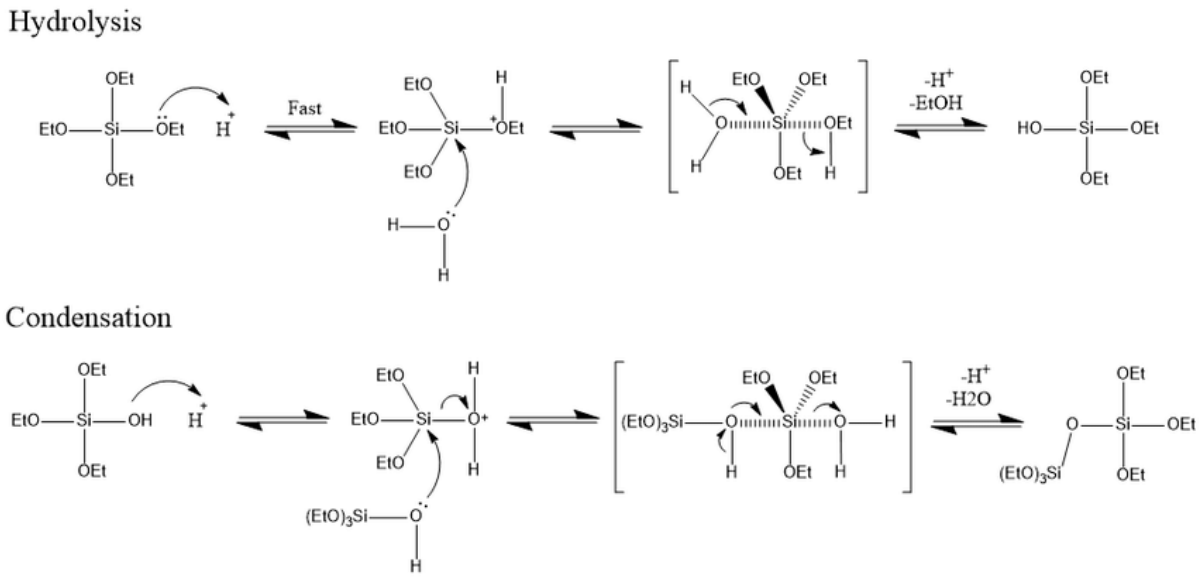

Figure 1-3 Hydrolysis and condensation reactions of TEOS.[79]

1.5.2 One pot functionalization/grafting of anions

The sol-gel process is well-known for producing a siloxane network. By altering the initial precursor used during synthesis, it's possible to modify and design the network to have unique properties. The concept behind one-pot synthesis of an anion-anchored silica backbone involves the polycondensation of TEOS and an anion-bearing silane. Bronstein et al.[80] used 3-trihydroxysilylpropyl-methylphosphonate (SPMP) in this process. They also employed 3-(glycidoxypropyl)trimethoxysilane (GLYMO) to enhance the compatibility of silica particles with a PEO matrix. The resulting SIC features single-layer anion-grafted silica particles dispersed in a PEO

matrix.[80] Meyer et al. conducted a similar one-pot synthesis of an organic-inorganic hybrid SIC, using 2-(4-chlorosulfonylphenyl)ethyl trimethoxysilane as the anion-bearing silane.[81] This one-pot approach is straightforward and reliable, although it has the drawback that the anionic precursor cannot be macromolecular, as the bulky anion might hinder the condensation reaction.

1.5.3 Two-step functionalization/grafting of anions

The two-step grafting approach typically involves the surface modification of silica using a coupling agent or functional group. Commonly used coupling agents possess hydrolysable groups that can react with the Si-OH end groups on the silica surface. The advantage of the two-step method lies in its ability to attach anions with complex structures or even polymeric anions. Kim et al. demonstrated a single-ion conducting solid polymer electrolyte (SPE) that contained mesoporous organosilica. The inner surface of the silica was functionalized using 2-[(Trifluoromethanesulfonylimido)-N-4-sulfonylphenyl]ethyl}trimethoxysilane (TMS-TFSISPE), as shown in the **Figure 1-4**.[55]

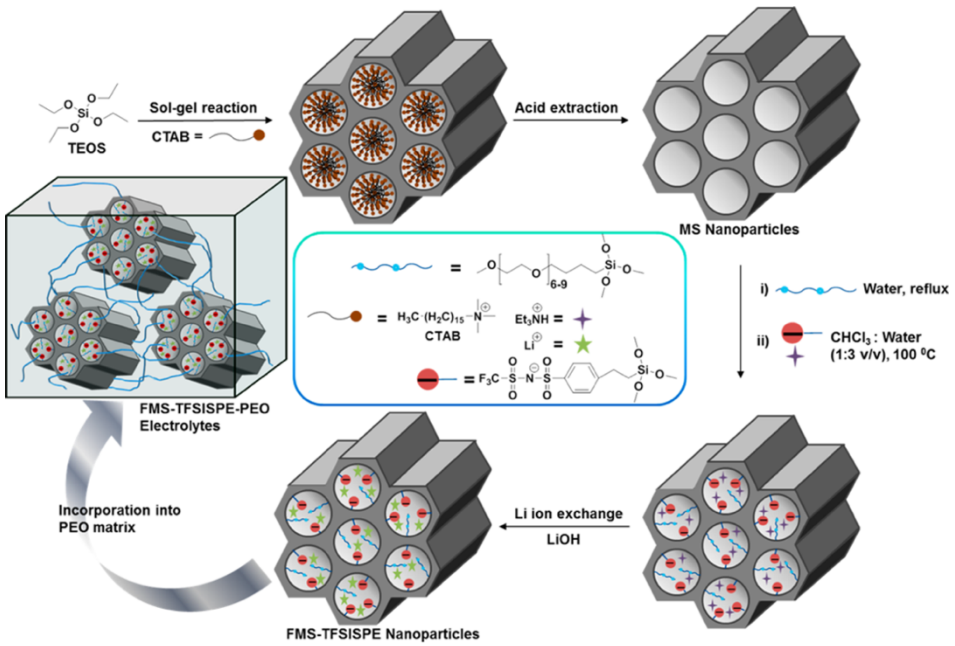

Figure 1-4 Two-step functionalization of a single ion conducting nanohybrid solid polymer electrolyte.[55]

1.6 Characterization techniques

1.6.1 Dielectric impedance spectroscopy

Dielectric Impedance Spectroscopy (DIS) is a technique employed for the measurement of resistance (R), capacitance (C), and inductance (L) by applying an alternating voltage, V(t), to a sample and subsequently measuring the current response, I(t), as illustrated in the **Figure 1-5**(a).[82,83]

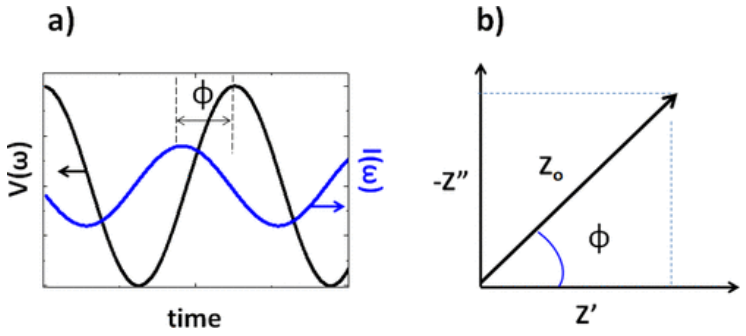

Figure 1-5 (a) Time-domain representation of V(t) and I(t). The phase angle **φ** depicts the time delay between the voltage input and the current response. (b) Frequency-domain representation of Z [83]

In the time domain, both $V(t)$ and $I(t)$ are represented as sinusoidal functions, characterized by a phase angle difference, φ:

$$V(t) = V_0\, e^{i\omega t}$$

$$I(t) = I_0\, e^{i(\omega t+\varphi)}$$

Here, V_0 and I_0 represent the amplitude of the voltage and resulting current signal, respectively, ω is the angular frequency of the applied AC voltage, and φ signifies the phase difference between $V(t)$ and $I(t)$.[83,84] The impedance, $Z(t)$, is determined as:

$$Z(t) = \frac{V(t)}{I(t)} = Z_0 e^{-i\varphi}$$

Where $Z_0 = V_0/I_0$. In the complex plane, impedance can be expressed in terms of two components: the magnitude Z_0 and the phase angle φ, as depicted in the **Figure 1-5**(b). The x-axis Z' represents

the real part, corresponding to resistance, while the y-axis Z" denotes the imaginary part.[83,84] Various methods exist for plotting DIS data. The Nyquist plot, for instance, represents -Z" on the y-axis against Z' on the x-axis in the complex plane, although it does not directly convey the frequency response. An alternative approach is to plot Z' or -Z" against $\log f$, where f represents frequency.[84]

The impedance of an ideal electrochemical cell can be represented through a combination of ideal electrical circuit elements, including the ideal resistor ($\varphi = 0$), ideal capacitor ($\varphi = 90°$), and inductor ($\varphi = -90°$). However, in the case of a real lithium-ion battery, additional elements are introduced to account for non-ideal behavior, namely the constant phase element (CPE) and Warburg impedance (W). The non-ideal characteristics of the electrical double layer, which exists between the electrode and the electrolyte, are attributed to factors such as surface roughness, leakage capacitance, and nonuniform distribution.[62,82] The CPE is utilized to model and compensate for this non-ideal behavior of the electrical double layer.[85] Warburg impedance is employed to describe the impedance generated by the lithium diffusion process. Given that a real cell exhibits behavior akin to "semi-infinite" Warburg impedance, where diffusion occurs in one dimension bounded by the planar electrode, the impedance manifests as a 45° angle in the low-frequency region.[82] Notably, the CPE can be considered a generalization of the Warburg element.[83]

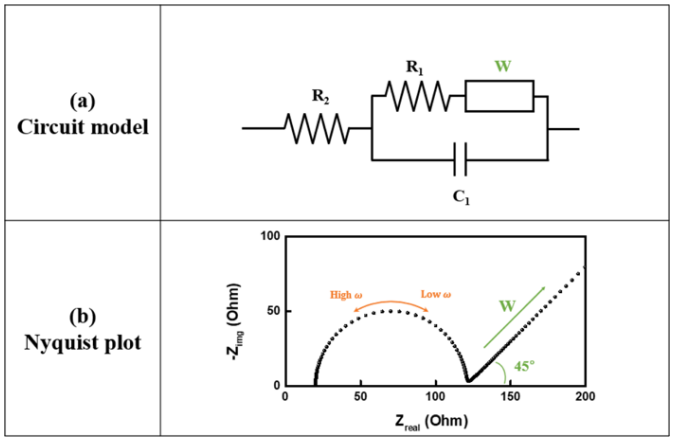

Figure 1-6 (a) Equivalent circuit and (b) Nyquist plot of a Randles cell model. [82]

The Randles model serves as a simplified representation of interfacial electrochemical reactions in the presence of the semi-infinite linear diffusion of electroactive species to flat electrodes. Many realistic models are adaptations or modifications of this basic Randles model.[86] As depicted in **Figure 1-6**(a), the equivalent circuit includes the series resistance R_2 and the charge transfer resistance R_1, which is essentially the resistance associated with the electrochemical reaction that occurs at the electrode-electrolyte interface. C_1 is the double layer capacitance, and it is connected in parallel with R_1, due to simultaneous charge transfer and charging of the double layer.[87] The W represents the Warburg element, and it is connected in series with the R_1, due to the key assumption that the rate of the charge transfer is controlled by diffusion of the electroactive species. In practice, the Warburg element is often approximated using several RC (resistor-capacitor) elements.[88] The Nyquist plot generated by this model typically features a semicircle in the high-frequency region, which represents the charge transfer process, and a tilted spike at lower frequencies, indicative of the Warburg element.

It's worth noting that the specific equivalent circuit model for a lithium-ion battery can vary depending on factors like electrode characteristics, cell type, and storage and cycling conditions, and there is no single standard circuit that fits all cells.[88–90]

1.6.2 Fourier transform infrared spectroscopy

Fourier transform infrared (FTIR) spectroscopy serves as a powerful tool for investigating molecular vibrations. For a nonlinear molecule comprising N atoms, there exist 3N-6 vibrational modes of motion (3N-5 for linear molecules). A key criterion for the observation of infrared absorption is a net change in the molecule's dipole moment as it undergoes vibrational or rotational movements.[91,92] Consequently, symmetric vibrations, as found in molecules such as O_2 and N_2, typically remain undetected in the infrared spectrum.[93] In contrast, asymmetric vibrations in the majority of

molecules are readily detected. In the mid-infrared region (1000–4000 cm^{-1}), two primary categories of vibrations are observed: stretching vibrations (ν), involving changes in bond lengths and bending vibrations (δ, in-plane, π, out-of-plane), involving adjustments in bond angles.[91]

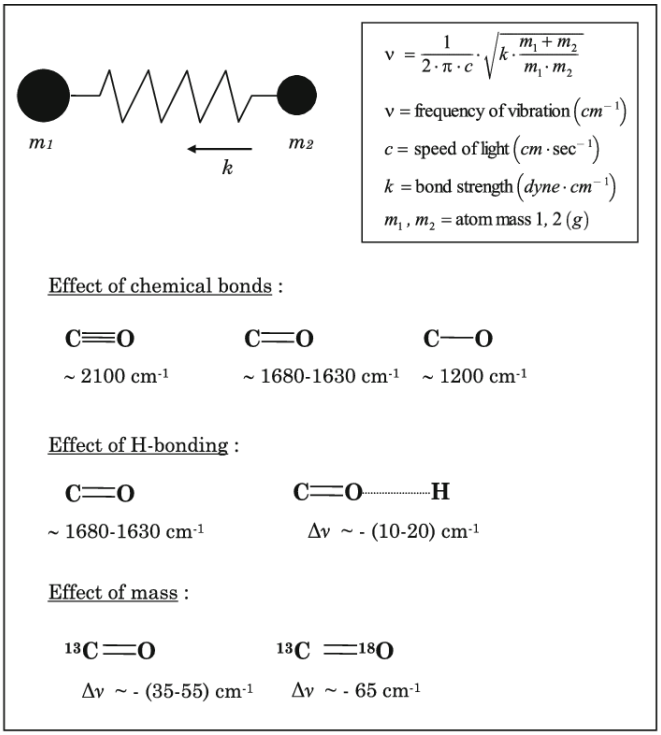

Figure 1-7 harmonic oscillator model for FTIR. The IR absorption frequencies depends on the nature of the chemical bonds, mass of the atoms, and atomic interactions (the environment).[91]

The stretching vibrations are often described using the harmonic oscillator model, which conceptualizes a chemical bond as a connection between two point masses (m_1 and m_2) linked by a spring characterized by stiffness (k), as depicted in the **Figure 1-7**. The oscillation frequency (ν) depends on the bond's strength, with higher frequencies associated with triple or double bonds in comparison to single bonds. It also varies according to the masses of the atoms participating in the vibration. In essence, vibrational frequencies are contingent on the intrinsic physicochemical properties of the corresponding molecule and can be likened to unique fingerprints for specific functional groups.[91,93] FTIR spectrum analysis can serve both qualitative and quantitative purposes,

primarily enabling the identification of functional groups or facilitating the determination of substance concentration 7based on Beer's law.[94,95] However, the quantitative aspects are sometimes less precise than those achievable through other analytical methods, such as gas chromatography.

Two commonly used FTIR techniques for bulk sample analysis are transmission FTIR and attenuated total reflection (ATR-FTIR).[96] In transmission FTIR, powdered potassium bromide (KBr) is blended with the sample to create a sample pellet by subjecting the mixture to high pressure.[97,98] This pellet is subsequently positioned in the path of the IR beam, with the resulting transmitted IR signal recorded by a detector. It is crucial to carefully assess the sample's concentration in the pellet to optimize the signal strength. On the other hand, ATR-FTIR involves bringing the sample into contact with an internal reflection element (IRE) characterized by a high refractive index. The IR radiation is focused onto the IRE's edge, reflected through the IRE, and then directed to a suitable detector.[99] While complete internal reflection occurs at the sample/IRE interface, the radiation (known as the evanescent wave) penetrates a short distance into the sample, where it can be absorbed.[99] This technique is advantageous as the sampling path length is independent of the sample's thickness, often eliminating the need for extensive sample preparation.[96]

1.6.3 Differential Scanning Calorimetry and glass transition

Differential Scanning Calorimetry (DSC) serves as a thermal analysis instrument, tasked with the determination of temperature-induced material transitions and the corresponding heat flow, as functions of both time and temperature.[100–102] The fundamental principle of DSC revolves around capturing the disparity in the heat flow rate (measured in mW = mJ s^{-1}) between a sample and an inert reference.[101,102] DSC instruments can be categorized into two primary types based on their operational mechanisms: heat-flux DSCs and power-compensated DSCs.[103] In a heat-flux DSC, as showed in **Figure 1-8**, a sample pan and an empty reference pan are positioned adjacent to each

other within the same furnace. The temperature difference between these two pans, caused by the heat capacity of the sample, is monitored, enabling the calculation of the sample's heat flow.[103] Conversely, in power-compensated DSC, the sample and reference pans are housed in separate furnaces where the thermal power delivered to these two pans is carefully controlled to maintain equivalent pan temperatures. The difference in heat flow is then recorded and plotted against the reference temperature.[101]

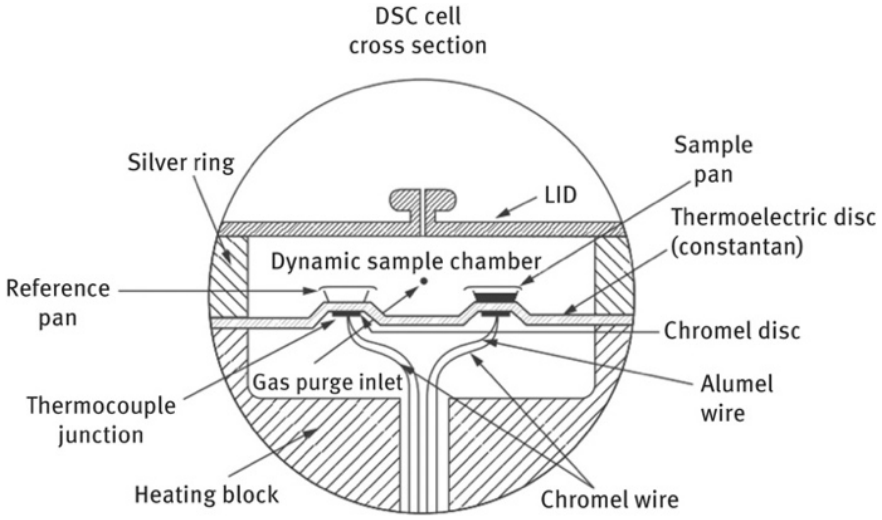

Figure 1-8 Schematic of a heat-flux DSC. [102]

DSC has found significant applications in diverse fields, including polymer and pharmaceutical sciences, as well as organic and inorganic chemistry. Some notable applications encompass the determination of purity levels, the glass transition temperature, melting and crystallization temperatures, heat of fusion, heat of reactions, and the kinetic assessment of chemical processes like curing, thermal degradation, and the kinetics of polymer crystallization.[104–107]

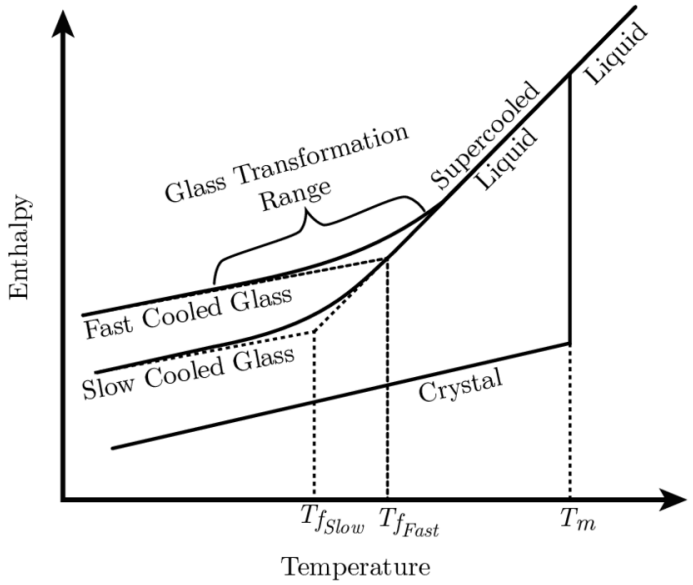

Figure 1-9 Schematic representation of the decrease in enthalpy/volume of an ideal one-component glass-forming liquid upon cooling.[109]

To ascertain the glass transition temperature using DSC, one must first understand the concepts of glass and the glass transition. As proposed by Zanotto et al., "Glass is a nonequilibrium, non-crystalline state of matter that appears solid on a short timescale but continuously relaxes towards the liquid state"[108] The behavior of glass transition is typically delineated in terms of enthalpy (or volume) as a function of temperature, as illustrated in **Figure 1-9**. In the context of glass-forming liquids, when the temperature drops below the melting point, entering the supercooled region, rapid cooling can prevent crystallization, yielding a supercooled liquid (SCL). With continued cooling, the relaxation time of the SCL increases exponentially, ultimately leading to the system becoming kinetically frozen as the relaxation time surpasses the laboratory (observation) timescale. At this point, atoms lack sufficient time for rearrangement to reach a metastable equilibrium state, resulting in a kinetic arrest of structural reconfiguration. Consequently, the enthalpy deviates from the SCL trajectory and instead follows the path of the configurationally frozen system. This transition occurs progressively, culminating in the creation of a nonequilibrium material known as glass.[109] During a

DSC scan, the change in the slope of the enthalpy-temperature curve (heat capacity), results in a characteristic signal, often appearing as a peak reminiscent of a step, at the glass transition temperature.

1.6.4 Thermogravimetric Analysis

Thermogravimetric analysis (TGA) stands as a potent thermal analytical technique designed to precisely quantify the weight loss experienced by a sample as it undergoes programmed heating within a controlled environmental setting.[110] It serves as a tool for the comprehensive examination of various aspects of materials, including their thermal stability, decomposition kinetics, compositional attributes, and other temperature-dependent processes, such as adsorption and desorption. The fundamental configuration of a TGA apparatus is outlined in **Figure 1-10**.

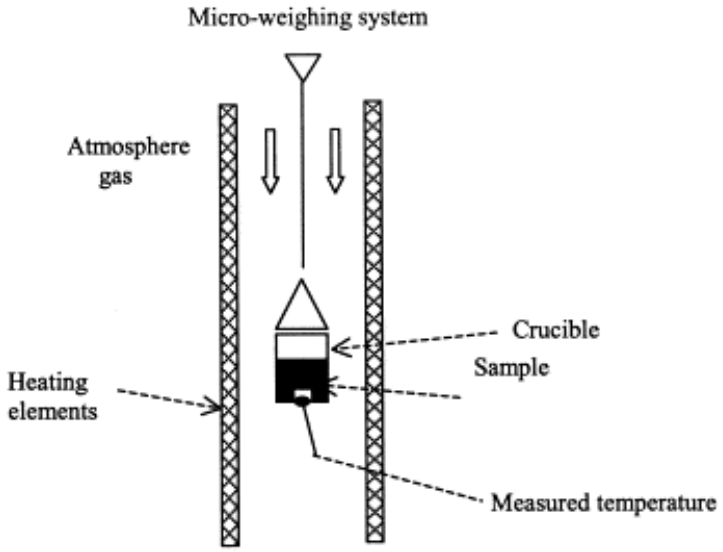

Figure 1-10 Principle of the TGA apparatus.[111]

Temperature measurement takes place at the crucible bottom to minimize temperature discrepancies between the thermocouple and the sample during dynamic tests.[111] The gaseous environment enveloping the sample is subject to variation, allowing for the utilization of various options, including dry air, inert gases such as nitrogen and argon, as well as gas mixtures like O_2/CO_2.[110–112]

Depending on the experimental design and sample properties, different atmosphere gases typically yield varying weight loss behaviors. For instance, Li et al. utilized TGA to investigate the combustion of pulverized coal in nitrogen and O_2/CO_2 environments, revealing differences in coal pyrolysis rates and resulting reaction products between the two atmospheres.[112] Additional factors, such as heating rate, can significantly impact the decomposition or reaction process, causing it to either delay or occur more rapidly, contingent upon the reaction kinetics.[112,113]

Moreover, the integration of TGA with other analytical instruments such as FTIR, DIS, DSC, and gas chromatography mass spectrometry (GC–MS) provides a powerful approach for comprehensively characterizing the thermal (pyrolysis) properties of samples, as well as elucidating details about their gaseous decomposition products and other relevant properties.[112–115] For example, Kreuer et al. concurrently conducted TGA and ionic conductivity measurements by placing two identical samples side by side on the balance pan and the conductivity sample holder, both in the same atmosphere environment.[110] Seo et al.[113] undertook the real-time monitoring of the gaseous composition generated during the TGA-driven pyrolysis of a coal sample. This process enabled the identification of specific hydrocarbon species by directing the evolved gases into a real-time gas analyzer and a micro-gas chromatography system.[113]

1.6.5 X-ray diffraction

X-ray diffraction (XRD) analysis serves as a valuable technique for elucidating the long-range order, or structural characteristics, of crystalline materials, as well as the short-range order in non-crystalline and semi-crystalline materials.[116] When a monochromatic X-ray beam impinges on the surface of a material, the atoms within the material interact with the X-ray radiation, resulting in various phenomena, including transmission, refraction, scattering, and absorption.[117] Diffraction occurs when the radiation is scattered by a periodic array of atoms, leading to constructive or destructive

interference at specific angles.[118] The sample diffracts the X-ray radiation at angles that adhere to Bragg's Law: $n\lambda=2d\sin\theta$, where n represents an integer, λ is the X-ray wavelength, *d* denotes the interplanar spacing responsible for the diffraction, and θ represents the incident angle of the x-rays.[117] It's crucial to mention that the diffraction criteria necessitate the incident radiation's wavelength, λ, to be shorter than the distance between the scattering sites, and that the scattering should occur in a coherent manner. Given that atomic spacings fall within the order of lattice constants (ranging from 0.2 nm to 0.4 nm), only X-rays and high-energy electrons possess wavelengths within this range.[116]

The application of XRD is diverse, and for the scope of this discussion, we will focus on its use in determining crystallinity in polymer materials. Polymers typically exhibit a semi-crystalline nature, wherein the XRD pattern displays a broad band in the glassy region and relatively sharp peaks in the crystalline region. The degree of crystallinity is determined using the equation:

$$\chi_c = \frac{A_c}{A_c + A_a}$$

Where χ_c represents the degree of crystallinity, A_c signifies the area under the crystalline peaks, and A_a represents the area under the amorphous peaks. However, it's essential to acknowledge that this method is less sensitive when dealing with samples of low crystallinity, and the results may diverge from those obtained through other measurement techniques.[119,120] For instance, a comparative study conducted by Doumeng et al. to measure the crystallinity of polyetheretherketone (PEEK) using DSC, XRD, and Raman spectroscopy revealed that XRD often underestimates the degree of crystallinity due to the challenge of isolating the crystalline part hidden by the halo originating from the amorphous phase.[121]

1.7 References

1. Rohan, R. et al. Functionalized polystyrene based single ion conducting gel polymer electrolyte for lithium batteries. *Solid State Ionics The 7th International Conference on Materials for Advanced Technologies (ICMAT 2013) Symposium A: Advanced Energy Storage Systems: Lithium ion batteries and beyond* **268**, 294-299 (2014).

2. Rohan, R. et al. A high performance polysiloxane-based single ion conducting polymeric electrolyte membrane for application in lithium ion batteries. *J. Mater. Chem. A* **3**, 20267-20276 (2015).

3. Tarascon, J.-M. & Armand, M. Issues and challenges facing rechargeable lithium batteries. *Nature* **414**, 359-367 (2001).

4. Arbizzani, C., Gabrielli, G. & Mastragostino, M. Thermal stability and flammability of electrolytes for lithium-ion batteries. *Journal of Power Sources* **196**, 4801-4805 (2011).

5. Chung, G. J., Han, J. & Song, S.-W. Fire-Preventing LiPF6 and Ethylene Carbonate-Based Organic Liquid Electrolyte System for Safer and Outperforming Lithium-Ion Batteries. *ACS Appl. Mater. Interfaces* **12**, 42868-42879 (2020).

6. Guan, Z., Zhang, Z., Du, B. & Peng, Z. A Non-Flammable Zwitterionic Ionic Liquid/Ethylene Carbonate Mixed Electrolyte for Lithium-Ion Battery with Enhanced Safety. *Materials* **14**, (2021).

7. Lalia, B. S., Yoshimoto, N., Egashira, M. & Morita, M. A mixture of triethylphosphate and ethylene carbonate as a safe additive for ionic liquid-based electrolytes of lithium ion batteries. *Journal of Power Sources* **195**, 7426-7431 (2010).

8. Sogawa, M. et al. Solvation-controlled lithium-ion complexes in a nonflammable solvent containing ethylene carbonate: structural and electrochemical aspects. *Phys. Chem. Chem. Phys.* **20**, 6480-6486 (2018).

9. Salem, N. & Abu-Lebdeh, Y. Non-Flammable Electrolyte Mixtures of Ringed Ammonium-Based Ionic Liquids and Ethylene Carbonate for High Voltage Li-Ion Batteries. *Journal of The Electrochemical Society* **161**, A1593 (2014).

10. Liang, H. et al. Nonflammable LiTFSI-Ethylene Carbonate/1,2-Dimethoxyethane Electrolyte for High-Safety Li-ion Batteries. *Journal of The Electrochemical Society* **167**, 090520 (2020).

11. Keller, M., Varzi, A. & Passerini, S. Hybrid electrolytes for lithium metal batteries. *Journal of Power Sources* **392**, 206-225 (2018).

12. Liu, J. et al. Non-solvating, side-chain polymer electrolytes as lithium single-ion conductors: synthesis and ion transport characterization. *Polym. Chem.* **11**, 461-471 (2020).

13. Liu, K., Zhang, R., Sun, J., Wu, M. & Zhao, T. Polyoxyethylene (PEO)$_{PEO–Perovskite}$PEO Composite Electrolyte for All-Solid-State Lithium Metal Batteries. *ACS Appl. Mater. Interfaces* **11**, 46930-46937 (2019).

14. Phan, T. N. T., Issa, S. & Gigmes, D. Poly(ethylene oxide)-based block copolymer electrolytes for lithium metal batteries. *Polym. Int.* **68**, 7-13 (2019).

15. Shen, X. et al. Semi-Interpenetrating Network-Structured Single-Ion Conduction Polymer Electrolyte for Lithium-Ion Batteries. *ChemElectroChem* **6**, 4483-4490 (2019).

16. Yu, Q. et al. Constructing Effective Interfaces for Li1.5Al0.5Ge1.5(PO4)3 Pellets To Achieve Room-Temperature Hybrid Solid-State Lithium Metal Batteries. *ACS Appl. Mater. Interfaces* **11**, 9911-9918 (2019).

17. Doyle, R. P. et al. Poly(ethylenimine)-Based Polymer Blends as Single-Ion Lithium Conductors. *Macromolecules* **47**, 3401-3408 (2014).

18. Lin, K.-J. & Maranas, J. K. Does decreasing ion–ion association improve cation mobility in single ion conductors? *Phys. Chem. Chem. Phys.* **15**, 16143-16151 (2013).

19. Song, J. Y., Wang, Y. Y. & Wan, C. C. Review of gel-type polymer electrolytes for lithium-ion batteries. *Journal of Power Sources* **77**, 183-197 (1999).

20. Wang, Z. et al. Porous poly(vinylidene fluoride) supported three-dimensional poly(ethylene glycol) thin solid polymer electrolyte for flexible high temperature all-solid-state lithium metal batteries. *Chemical Engineering Journal* **435**, 135106 (2022).

21. Wei, Z. et al. Superior lithium ion conduction of polymer electrolyte with comb-like structure via solvent-free copolymerization for bipolar all-solid-state lithium battery. *J. Mater. Chem. A* **6**, 13438-13447 (2018).

22. Appetecchi, G. B., Dautzenberg, G. & Scrosati, B. A New Class of Advanced Polymer Electrolytes and Their Relevance in Plastic-like, Rechargeable Lithium Batteries. *Journal of The Electrochemical Society* **143**, 6-12 (1996).

23. Chu, P. P., Reddy, M. J. & Kao, H. M. Novel composite polymer electrolyte comprising mesoporous structured SiO2 and PEO/Li. *Solid State Ionics* **156**, 141-153 (2003).

24. Scrosati, B., Croce, F. & Persi, L. Impedance Spectroscopy Study of PEO-Based Nanocomposite Polymer Electrolytes. *Journal of The Electrochemical Society* **147**, 1718 (2000).

25. Wieczorek, W., Florjanczyk, Z. & Stevens, J. R. Composite polyether based solid electrolytes. *Electrochimica Acta International symposium on polymer electrolytes* **40**, 2251-2258 (1995).

26. Bonilla, M. R. et al. Unveiling Interfacial Li-Ion Dynamics in Li7La3Zr2O12/PEO(LiTFSI) Composite Polymer-Ceramic Solid Electrolytes for All-Solid-State Lithium Batteries. *ACS Appl. Mater. Interfaces* **13**, 30653-30667 (2021).

27. Liu, W. et al. Ionic Conductivity Enhancement of Polymer Electrolytes with Ceramic Nanowire Fillers. *Nano Lett.* **15**, 2740-2745 (2015).

28. Duluard, S. et al. Dense on Porous Solid LATP Electrolyte System: Preparation and Conductivity Measurement. *J. Am. Ceram. Soc.* **100**, 141-149 (2017).

29. Giarola, M. et al. Structure and Vibrational Dynamics of NASICON-Type LiTi2(PO4)3. *J. Phys. Chem. C* **121**, 3697-3706 (2017).

30. Li, Z. et al. Ionic Conduction in Composite Polymer Electrolytes: Case of PEO:Ga-LLZO Composites. *ACS Appl. Mater. Interfaces* **11**, 784-791 (2019).

31. Guo, Q. et al. 20μm-Thick $Li_{6.4}La_3Zr_{1.4}Ta_{0.6}O_{12}$-Based Flexible Solid Electrolytes for All-Solid-State Lithium Batteries. *Energy Material Advances* **2022**, 9753506 (2022).

32. Villaluenga, I. et al. Cation only conduction in new polymer–SiO2 nanohybrids: Na+ electrolytes. *J. Mater. Chem. A* **1**, 8348-8352 (2013).

33. Pender, J. P. et al. Electrode Degradation in Lithium-Ion Batteries. *ACS Nano* **14**, 1243-1295 (2020).

34. Wang, F. et al. Does Polarization Increase Lead to Capacity Fade. *Journal of The Electrochemical Society* **167**, 090549 (2020).

35. Wang, W., Yi, E., Fici, A. J., Laine, R. M. & Kieffer, J. Lithium Ion Conducting Poly(ethylene oxide)-Based Solid Electrolytes Containing Active or Passive Ceramic Nanoparticles. *J. Phys. Chem. C* **121**, 2563-2573 (2017).

36. Guo, Q. et al. Poly(ethylene glycol) brush on Li6.4La3Zr1.4Ta0.6O12 towards intimate interfacial compatibility in composite polymer electrolyte for flexible all-solid-state lithium metal batteries. *Journal of Power Sources* **498**, 229934 (2021).

37. Chen, S. et al. In-situ preparation of poly(ethylene oxide)/Li3PS4 hybrid polymer electrolyte with good nanofiller distribution for rechargeable solid-state lithium batteries. *Journal of Power Sources* **387**, 72-80 (2018).

38. Bouchet, R. et al. Single-ion BAB triblock copolymers as highly efficient electrolytes for lithium-metal batteries. *Nature Materials* **12**, 452-457 (2013).

39. Dai, H. & Zawodzinski, T. A. The dependence of lithium transference numbers on temperature, salt concentration and anion type in poly (vinylidene fluoride)–hexafluoropropylene copolymer-based gel electrolytes1Presented at the Electrochemical Society Symposium: Processes in Polymers and Polymer|Metal Interfaces, Montreal, 4–9 May 1997.1. *Journal of Electroanalytical Chemistry* **459**, 111-119 (1998).

40. Shah, D. B. et al. Effect of Anion Size on Conductivity and Transference Number of Perfluoroether Electrolytes with Lithium Salts. *Journal of The Electrochemical Society* **164**, A3511 (2017).

41. Zhang, X.-W., Wang, C., Appleby, A. J. & Little, F. E. Characteristics of lithium-ion-conducting composite polymer-glass secondary cell electrolytes. *Journal of Power Sources* **112**, 209-215 (2002).

42. Diederichsen, K. M., McShane, E. J. & McCloskey, B. D. Promising Routes to a High Li+ Transference Number Electrolyte for Lithium Ion Batteries. *ACS Energy Lett.* **2**, 2563-2575 (2017).

43. Kobayashi, N., Uchiyama, M. & Tsuchida, E. Poly[lithium methacrylate-co-oligo(oxyethylene)methacrylate] as a solid electrolyte with high ionic conductivity. *Solid State Ionics* **17**, 307-311 (1985).

44. Dou, S., Zhang, S., Klein, R. J., Runt, J. & Colby, R. H. Synthesis and Characterization of Poly(Ethylene Glycol)-Based Single-Ion Conductors. *Chem. Mater.* **18**, 4288-4295 (2006).

45. Hoffmann, J. F., Pulst, M. & Kressler, J. Enhanced ion conductivity of poly(ethylene oxide)-based single ion conductors with lithium 1,2,3-triazolate end groups. *Journal of Applied Polymer Science* **136**, 46949 (2019).

46. Matsumi, N., Sugai, K. & Ohno, H. Ion Conductive Characteristics of Alkylborane Type and Boric Ester Type Polymer Electrolytes Derived from Mesitylborane. *Macromolecules* **36**, 2321-2326 (2003).

47. Allcock, H. R., Welna, D. T. & Maher, A. E. Single ion conductors—polyphosphazenes with sulfonimide functional groups. *Solid State Ionics* **177**, 741-747 (2006).

48. Manuel Stephan, A. & Nahm, K. S. Review on composite polymer electrolytes for lithium batteries. *Polymer* **47**, 5952-5964 (2006).

49. Wang, C., Zhang, X.-W. & Appleby, A. J. Solvent-Free Composite PEO-Ceramic Fiber/Mat Electrolytes for Lithium Secondary Cells. *Journal of The Electrochemical Society* **152**, A205 (2005).

50. Croce, F., Appetecchi, G. B., Persi, L. & Scrosati, B. Nanocomposite polymer electrolytes for lithium batteries. *Nature* **394**, 456-458 (1998).

51. Zhang, H., Zhang, X., Shiue, E. & Fedkiw, P. S. Single-ion conductors for lithium batteries via silica surface modification. *Journal of Power Sources* **177**, 561-565 (2008).

52. Zhao, H. et al. Plasticized Polymer Composite Single-Ion Conductors for Lithium Batteries. *ACS Appl. Mater. Interfaces* **7**, 19494-19499 (2015).

53. Rafael, V.-B. Ch. 1 (IntechOpen, Rijeka, 2020).

54. Schaefer, J. L., Moganty, S. S. & Archer, L. A. Nanoscale Organic Hybrid Electrolytes. *Adv. Mater.* **22**, 3677-3680 (2010).

55. Kim, Y. et al. High Ion Conducting Nanohybrid Solid Polymer Electrolytes via Single-Ion Conducting Mesoporous Organosilica in Poly(ethylene oxide). *Chem. Mater.* **29**, 4401-4410 (2017).

56. Oh, H. et al. Poly(arylene ether)-Based Single-Ion Conductors for Lithium-Ion Batteries. *Chem. Mater.* **28**, 188-196 (2016).

57. Petronico, A. et al. Solid–Liquid Lithium Electrolyte Nanocomposites Derived from Porous Molecular Cages. *Journal of the American Chemical Society* **140**, 7504-7509 (2018).

58. Rohan, R. et al. Functionalized meso/macro-porous single ion polymeric electrolyte for applications in lithium ion batteries. *J. Mater. Chem. A* **2**, 2960-2967 (2014).

59. Zhu, Y. et al. A Composite Gel Polymer Electrolyte with High Performance Based on Poly(Vinylidene Fluoride) and Polyborate for Lithium Ion Batteries. *Adv. Energy Mater.* **4**, 1300647 (2014).

60. Jung, Y.-C. et al. Ceramic separators based on Li+-conducting inorganic electrolyte for high-performance lithium-ion batteries with enhanced safety. *Journal of Power Sources* **293**, 675-683 (2015).

61. Keller, M. et al. Electrochemical performance of a solvent-free hybrid ceramic-polymer electrolyte based on Li7La3Zr2O12 in P(EO)15LiTFSI. *Journal of Power Sources* **353**, 287-297 (2017).

62. Choi, J.-H., Lee, C.-H., Yu, J.-H., Doh, C.-H. & Lee, S.-M. Enhancement of ionic conductivity of composite membranes for all-solid-state lithium rechargeable batteries incorporating tetragonal Li7La3Zr2O12 into a polyethylene oxide matrix. *Journal of Power Sources* **274**, 458-463 (2015).

63. Bae, J. et al. A 3D Nanostructured Hydrogel-Framework-Derived High-Performance Composite Polymer Lithium-Ion Electrolyte. *Angew. Chem.* **130**, 2118-2122 (2018).

64. Brinker, C. J. & Scherer, G. W. (eds Brinker, C. J. & Scherer, G. W.) 96-233 (Academic Press, San Diego, 1990).

65. Nairn, K. M., Best, A. S., Newman, P. J., MacFarlane, D. R. & Forsyth, M. Ceramic-polymer interface in composite electrolytes of lithium aluminium titanium phosphate and polyetherurethane polymer electrolyte. *Solid State Ionics* **121**, 115-119 (1999).

66. Plcharski, J. & Weiczorek, W. PEO based composite solid electrolyte containing nasicon. *Solid State Ionics* **28-30**, 979-982 (1988).

67. Chen, L. et al. PEO/garnet composite electrolytes for solid-state lithium batteries: From "ceramic-in-polymer" to "polymer-in-ceramic". *Nano Energy* **46**, 176-184 (2018).

68. Nairn, K., Forsyth, M., Every, H., Greville, M. & MacFarlane, D. R. Polymer-ceramic ion-conducting composites. *Proceedings of the 10th International Conference on Solid State Ionics* **86-88**, 589-593 (1996).

69. Sheng, L. et al. In-situ polymerized separator enables propylene carbonate electrolyte compatible with high-performance lithium batteries. *Journal of Power Sources* **551**, 232172 (2022).

70. Wan, J., Zhang, J., Yu, J. & Zhang, J. Cellulose Aerogel Membranes with a Tunable Nanoporous Network as a Matrix of Gel Polymer Electrolytes for Safer Lithium-Ion Batteries. *ACS Appl. Mater. Interfaces* **9**, 24591-24599 (2017).

71. Ye, Y.-S., Rick, J. & Hwang, B.-J. Ionic liquid polymer electrolytes. *J. Mater. Chem. A* **1**, 2719-2743 (2013).

72. Balo, L., Shalu, Gupta, H., Kumar Singh, V. & Kumar Singh, R. Flexible gel polymer electrolyte based on ionic liquid EMIMTFSI for rechargeable battery application. *Electrochimica Acta* **230**, 123-131 (2017).

73. Efimova, A., Pfützner, L. & Schmidt, P. Thermal stability and decomposition mechanism of 1-ethyl-3-methylimidazolium halides. *Thermochimica Acta* **604**, 129-136 (2015).

74. Hofmann, A., Schulz, M. & Hanemann, T. Gel electrolytes based on ionic liquids for advanced lithium polymer batteries. *Electrochimica Acta* **89**, 823-831 (2013).

75. Yuan, C. et al. Preparation and characterization of a novel ionic conducting foam-type polymeric gel based on polymer PVdF-HFP and ionic liquid [EMIM][TFSI]. *Colloid and Polymer Science* **293**, 1945-1952 (2015).

76. Zhou, Q., Fitzgerald, K., Boyle, P. D. & Henderson, W. A. Phase Behavior and Crystalline Phases of Ionic Liquid-Lithium Salt Mixtures with 1-Alkyl-3-methylimidazolium Salts. *Chem. Mater.* **22**, 1203-1208 (2010).

77. Zhou, Q. et al. Phase Behavior of Ionic Liquid–LiX Mixtures: Pyrrolidinium Cations and TFSI– Anions – Linking Structure to Transport Properties. *Chem. Mater.* **23**, 4331-4337 (2011).

78. Venkateswara Rao, A. & Bhagat, S. D. Synthesis and physical properties of TEOS-based silica aerogels prepared by two step (acid–base) sol–gel process. *Solid State Sciences* **6**, 945-952 (2004).

79. Owens, G. J. et al. Sol–gel based materials for biomedical applications. *Progress in Materials Science* **77**, 1-79 (2016).

80. Bronstein, L. M. et al. Solid Polymer Single-Ion Conductors: Synthesis and Properties. *Chem. Mater.* **18**, 708-715 (2006).

81. Meyer, M. et al. Single-ion conductor nanocomposite organic–inorganic hybrid membranes for lithium batteries. *J. Mater. Chem. A* **2**, 12162-12165 (2014).

82. Choi, W., Shin, H.-C., Kim, J. M., Choi, J.-Y. & Yoon, W. Modeling and Applications of Electrochemical Impedance Spectroscopy (EIS) for Lithium-ion Batteries. *Journal of electrochemical science and technology* **11**, 1-13 (2020).

83. von Hauff, E. Impedance Spectroscopy for Emerging Photovoltaics. *J. Phys. Chem. C* **123**, 11329-11346 (2019).

84. Macdonald, J. R. Impedance spectroscopy. *Annals of Biomedical Engineering* **20**, 289-305 (1992).

85. Kochowski, S. & Nitsch, K. Description of the frequency behaviour of metal–SiO2–GaAs structure characteristics by electrical equivalent circuit with constant phase element. *Thin Solid Films* **415**, 133-137 (2002).

86. R., H. & J., S. Extending Randles's Battery Model to Predict Impedance, Charge–Voltage, and Runtime Characteristics. *IEEE Access* **8**, 85321-85328 (2020).

87. Ruiz, G. A. & Felice, C. J. Electrochemical-Fractal Model Versus Randles Model: A Discussion About Diffusion Process. *International Journal of Electrochemical Science* **10**, 8484-8496 (2015).

88. Andre, D. et al. Characterization of high-power lithium-ion batteries by electrochemical impedance spectroscopy. II: Modelling. *Selected papers presented at the 12th Ulm ElectroChemical Talks (UECT):2015 Technologies on Batteries and Fuel Cells* **196**, 5349-5356 (2011).

89. Gao, P., Zhang, C. & Wen, G. Equivalent circuit model analysis on electrochemical impedance spectroscopy of lithium metal batteries. *Journal of Power Sources* **294**, 67-74 (2015).

90. Cortés, M. et al. *Equivalent circuits of cylindrical lithium-ion batteries for different cases of generation sources* 2016).

91. Berthomieu, C. & Hienerwadel, R. Fourier transform infrared (FTIR) spectroscopy. *Photosynthesis Research* **101**, 157-170 (2009).

92. Chen, Y. et al. Applications of Micro-Fourier Transform Infrared Spectroscopy (FTIR) in the Geological Sciences—A Review. *International Journal of Molecular Sciences* **16**, 30223-30250 (2015).

93. Griffiths, P. R. Fourier transform infrared spectrometry. *Science* **222**, 297-302 (1983).

94. Qiu, K. et al. Comparison of ATR/transmittance FTIR combined with Beer's law and PLS to determine fipronil in matrine formulation. *Anal. Methods* **5**, 4790-4797 (2013).

95. Masson, J.-F., Pelletier, L. & Collins, P. Rapid FTIR method for quantification of styrene-butadiene type copolymers in bitumen. *J. Appl. Polym. Sci.* **79**, 1034-1041 (2001).

96. Kazarian, S. G. & Chan, K. L. A. ATR-FTIR spectroscopic imaging: recent advances and applications to biological systems. *Analyst* **138**, 1940-1951 (2013).

97. Iglesias, M. J., Jimenez, A., Laggoun-Defarge, F. & Suarez-Ruiz, I. FTIR Study of Pure Vitrains and Associated Coals. *Energy Fuels* **9**, 458-466 (1995).

98. Lis, G. P., Mastalerz, M., Schimmelmann, A., Lewan, M. D. & Stankiewicz, B. A. FTIR absorption indices for thermal maturity in comparison with vitrinite reflectance R0 in type-II kerogens from Devonian black shales. *Organic Geochemistry* **36**, 1533-1552 (2005).

99. Hind, A. R., Bhargava, S. K. & McKinnon, A. At the solid/liquid interface: FTIR/ATR — the tool of choice. *Advances in Colloid and Interface Science* **93**, 91-114 (2001).

100. Gill, P., Moghadam, T. T. & Ranjbar, B. Differential scanning calorimetry techniques: applications in biology and nanoscience. *J Biomol Tech* **21**, 167-193 (2010).

101. Haines, P. J., Reading, M. & Wilburn, F. W. Handbook of Thermal Analysis and Calorimetry Vol. 1. (1998).

102. Abd-Elghany, M. & Klapötke, T. M. A review on differential scanning calorimetry technique and its importance in the field of energetic materials. *Physical Sciences Reviews* **3**, (2018).

103. Danley, R. L. New heat flux DSC measurement technique. *Thermochimica acta* **395**, 201-208 (2002).

104. Freeman, E. S. & Carroll, B. The Application of Thermoanalytical Techniques to Reaction Kinetics: The Thermogravimetric Evaluation of the Kinetics of the Decomposition of Calcium Oxalate Monohydrate. *J. Phys. Chem.* **62**, 394-397 (1958).

105. Kissinger, H. E. Reaction Kinetics in Differential Thermal Analysis. *Anal. Chem.* **29**, 1702-1706 (1957).

106. Patil, D. G. & Brill, T. B. Thermal decomposition of energetic materials 53. Kinetics and mechanism of thermolysis of hexanitrohexazaisowurtzitane. *Combustion and Flame* **87**, 145-151 (1991).

107. Šesták, J. & Berggren, G. Study of the kinetics of the mechanism of solid-state reactions at increasing temperatures. *Thermochimica Acta* **3**, 1-12 (1971).

108. Zanotto, E. D. & Mauro, J. C. The glassy state of matter: Its definition and ultimate fate. *Journal of Non-Crystalline Solids* **471**, 490-495 (2017).

109. Zheng, Q. et al. Understanding Glass through Differential Scanning Calorimetry. *Chem. Rev.* **119**, 7848-7939 (2019).

110. Kreuer, K. D., Schönherr, E. & Maier, J. Proton and oxygen diffusion in BaCeO3 based compounds: A combined thermal gravimetric analysis and conductivity study. *Solid State Ionics* **70-71**, 278-284 (1994).

111. David, C., Salvador, S., Dirion, J. L. & Quintard, M. Determination of a reaction scheme for cardboard thermal degradation using thermal gravimetric analysis. *Journal of Analytical and Applied Pyrolysis* **67**, 307-323 (2003).

112. Li, Q., Zhao, C., Chen, X., Wu, W. & Li, Y. Comparison of pulverized coal combustion in air and in O2/CO2 mixtures by thermo-gravimetric analysis. *Pyrolysis 2008* **85**, 521-528 (2009).

113. Seo, D. K., Park, S. S., Kim, Y. T., Hwang, J. & Yu, T.-U. Study of coal pyrolysis by thermo-gravimetric analysis (TGA) and concentration measurements of the evolved species. *Journal of Analytical and Applied Pyrolysis* **92**, 209-216 (2011).

114. Yu, J. et al. Characterization of microplastics in environment by thermal gravimetric analysis coupled with Fourier transform infrared spectroscopy. *Marine Pollution Bulletin* **145**, 153-160 (2019).

115. Ayrault, C. et al. Differential thermal analysis, thermal gravimetric analysis, and solid phase micro-extraction gas chromatography analysis of water and fuel absorption in diesel soot. *Journal of Aerosol Science* **41**, 237-241 (2010).

116. Khan, H. et al. Experimental methods in chemical engineering: X-ray diffraction spectroscopy—XRD. *The Canadian Journal of Chemical Engineering* **98**, 1255-1266 (2020).

117. Bunaciu, A. A., Udriştioiu, E. G. & Aboul-Enein, H. Y. X-Ray Diffraction: Instrumentation and Applications. *Critical Reviews in Analytical Chemistry* **45**, 289-299 (2015).

118. Chauhan, A. & Chauhan, P. Powder XRD Technique and its Applications in Science and Technology. *Journal of analytical and bioanalytical techniques* **5**, 1-5 (2014).

119. Kljun, A. et al. Comparative Analysis of Crystallinity Changes in Cellulose I Polymers Using ATR-FTIR, X-ray Diffraction, and Carbohydrate-Binding Module Probes. *Biomacromolecules* **12**, 4121-4126 (2011).

120. Aggarwal, S., Sajwan, M. & Singh, R. Crystallinity of HDPE Pipes by DSC, XRD and FTIR Spectroscopy - A Forensic Comparison. *Indian Journal of Criminology and Criminalistics* **29**, 141-148 (2008).

121. Doumeng, M. et al. A comparative study of the crystallinity of polyetheretherketone by using density, DSC, XRD, and Raman spectroscopy techniques. *Polymer Testing* **93**, 106878 (2021).

CHAPTER II Contiguous High-Mobility Interphase Surrounding Nano- Precipitates in Polymer Matrix Solid Electrolyte

Original Publication Information

The work in this chapter was published in ACS Applied Materials & Interfaces as: Wang, G. & Kieffer, J. Contiguous High-Mobility Interphase Surrounding Nano-Precipitates in Polymer Matrix Solid Electrolyte. *ACS Appl. Mater. Interfaces* 2023, 15, 848 – 858.

2.1 Introduction

In our earlier work we found evidence that the benefits of incorporating active nanoparticles into a polymer matrix to form a composite solid electrolyte (CSE) extend beyond suppressing crystallization and/or offering possible Li^+ conduits. Studying the composite made with $Li_{1.3}Al_{0.3}Ti_{1.7}(PO_4)_3$ (LATP) nanoparticles in a poly(ethylene) oxide (PEO) matrix, we also found that high-mobility cation migration pathways develop along the interfacial region that develops around the particles, or interphase.[1–3] We observed that the ionic conductivity in this material rises sharply upon adding LATP nanoparticles, and already at relatively small volume fractions significantly exceeds the ionic conductivity of pure LATP as well as of pure PEO. Evidently, this behavior cannot be explained using rules of mixture for binary systems. To evaluate our results quantitatively, we therefore developed an analytical model assuming the presence of a third phase, corresponding to the interphase. Our tri-phase model not only allows us to discern the magnitude of the Li^+

conductivity within the interphase, but it also predicts the maximum conductivity in the LATP/PEO composite, provided that the nanoparticles are evenly distributed in space.[1] This latter condition is essential, because when the nanoparticles cluster or aggregate, the direct contact with one another overlaps with, and therefore eliminates potential highly conductive interphase volume. Hence, we pursue the concept of *in-situ* precipitation, which involves liquid phase mixing and thus, spatially random nucleation sites, while avoiding alteration of interfacial chemistries. We reformulated the sol-gel wet synthesis route for LATP and added dialysis purification steps,[4] to establish a novel processing method that generates well dispersed LATP nanoparticles in a PEO matrix, achieving a particle loading of up to 30 wt% and an ambient temperature ionic conductivity of 3.8×10^{-4} $S\cdot cm^{-1}$, which has never been reported for the LATP/PEO system. In this paper we provide a detailed description of our *in-situ* precipitation synthesis, report on the ionic conductivities measured in materials fabricated using this method, discuss the results in the context of our tri-phase analytical model, and convey new insights gained regarding design criteria for CSE materials.

2.2 Experimental Methods

2.2.1 In-situ precipitation of LATP/PEO composite

To prepare LATP/PEO composite electrolyte, 1.2715 ml titanium (IV) isopropoxide (97%, Aldrich) is added into 15 ml of deionized water, Titanium hydroxide precipitate formed immediately. The titanium hydroxide is filtered and washed with 20 ml of deionized water, then transferred into a 100 ml beaker. Nitric acid (30%) is added drop by drop to the precipitate until it fully dissolves and a clear solution of $TiO(NO_3)_2$ is formed. After that, 30 ml deionized water, 0.2241 g $LiNO_3$ (Reagent Plus, Aldrich) and 0.2813 g Al $(NO_3)_3\,9H_2O$ (99%, Aldrich) are added into the $TiO(NO_3)_2$ aqueous solution. Then, 2 g of 900k PEO are added to the solution and it takes 1.5 h for it to fully dissolve. Upon completion of the homogenization step, the beaker is immersed into an ice water

bath. Once the target temperature is reached, the prefabricated $NH_4H_2PO_4$ aqueous solution with 0.8627 g of $NH_4H_2PO_4$ is added into the beaker drop by drop. Under continuous stirring any precipitating LATP nanoparticles remain in suspension. The rest of the PEO is premixed with the prescribed amount of water is added to the slurry, while stirring for another 30 mins until a uniformly translucent slurry is formed. By adjusting the total amount of PEO added, particle loading from 0 to 30 wt%, in increments of 5 wt%, are obtained.

2.2.2 Purification

To remove NH_4^+ and NO_3^- from the slurry so obtained, it is purified by means of dialysis. 40 cm of cellulose dialysis tube (14000 cut-off molecular weight, Aldrich) is used. Before usage, the tube must be hydrated for 10 mins. After that, one side of the tube is sealed using a clip and filled with the slurry, leaving about 10 ml space above the liquid. The dialysis tube is then vertically submerged into 1 L of deionized water. Ice cubes are used to cool the system during dialysis. Water and ice are continuously stirred and refreshed about every 15 mins, while monitoring the pH of the medium, to accelerate the ion exchange process. Dialysis is stopped when the pH of the washing medium stabilizes at the level of pure deionized water. The dialysis usually takes 2-3 h to complete, depending on samples' chemical composition.

2.2.3 Solution casting and post treatment

The dialyzed slurry is transferred back into a 100 ml beaker, while still being cooled in the ice water bath. $LiClO_4$ salt is added to the slurry and dissolved. In the literature, the salt concentration is represented as the number of ethylene oxide (EO) repeat units per number of $LiClO_4$ molecules (EO/Li ratio). In these terms, the materials we examined exhibit EO/Li ratios of 10 and 20. The EO/Li ratio reflects the average spacing between cation sites. In addition, we created a series of samples containing no lithium salt, i.e., EO/Li = ∞. Finally, the slurry is post-homogenized for

1.5 h and then cast onto a Teflon plate. Water is allowed to evaporate slowly under ambient conditions for 48 h. The resulting LATP/PEO composite films are peeled off and further dried in a vacuum oven at 40°C for 48 h before property characterization. **Figure 2-1** illustrates the entire synthesis procedure.

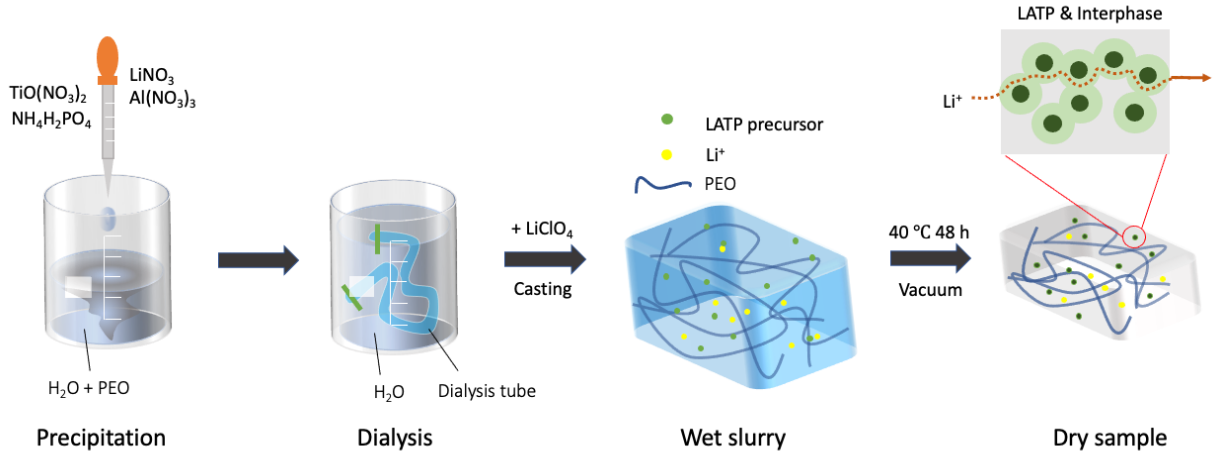

Figure 2-1 Schematic illustration of the synthesis procedure for LATP/PEO composite electrolytes.

2.2.4 Characterization techniques

The measurement of ionic conductivity was carried out using a Novocontrol broadband dielectric impedance spectrometer (DIS). To this end, samples were cut into circular discs with a 12.5 mm diameter. Samples were sandwiched between two polished stainless-steel discs, which served as blocking electrodes.[1] Measurements were made for temperatures ranging from 10°C to 70°C, and frequencies from 0.1 Hz to 10 MHz. The Li^+ conductivity is derived from the location of the intercepts with the abscissa in the Nyquist plot of the complex dielectric impedance (see **Appendix Figure A. 2** Nyquist plot for LATP/PEO composites with EO/Li = 20 and different particle loadings at 20°C). Differential scanning calorimetry (DSC) was performed using a TA2000 calorimeter. Samples were scanned from –60°C to 100°C with a heating rate of 10 K min^{-1} for two

cycles. Surface and cross section images of the nanocomposite were taken using the JEOL JSM-IT500HR scanning electron microscopy (SEM). XRD scans are obtained using the Rigaku Miniflex 600, with a scanning range of 10° to 50° and a step width of 0.01°. Fourier transform infrared (FTIR) spectroscopy was carried out using a Jasco FT/IR-4100 spectrometer in attenuated total reflectance mode. This allows us to characterize as cast samples of the polymer matrix composites and of pure polymer. We also measured spectra of sequestered LATP, which we obtained both via liquid feed flame spray pyrolysis (LF-FSP)[1] and by recovering in-situ precipitated nanoparticles from the composite by heating the latter to 230ºC, at which temperature PEO is eliminated via decomposition but LATP remains unaltered because the process occurred well below its T_g.

2.3 Results and Discussion

2.3.1 Confirmation of the tri-phase model

In earlier work we observed that in a LATP-PEO mixture the ionic conductivity surpasses that of either constituent,[1] suggesting that a third phase develops at the interface between the two components. This new interphase is the result of structural rearrangements within the polymer in the region adjacent to the nanoparticle surface and is characterized by higher ionic mobility. The region is estimated to have a thickness of the order of the nanoparticle radius, and thus provides a sizeable cross section for lithium cation passageways. Accordingly, we can attribute the volume fractions ϕ_N and ϕ_I to the nanoparticles and interfacial region, respectively. Defining, $\phi = \phi_N + \phi_I$, then the remaining volume fraction of unperturbed polymer matrix is $(1-\phi)$. Considering that the interphase forms a halo around the particles, ϕ_N and ϕ_I are linked, i.e.,

$$\phi_I = f\left(\phi_N, \delta\right)\phi_N = \left(\frac{k}{\varepsilon}\ln\left(1-\varepsilon\phi_N\right)+\left(1+\delta\right)^3-1\right)\phi_N, \qquad (2\text{–}1)$$

where δ is a model parameter that is optimized during data fitting, the value for k is determined by the boundary condition that $f = 0$ at $\phi_N = 1$, and $\varepsilon < 1$, is an arbitrarily chosen tolerance factor to prevent a singularity in the expression. A detailed derivation of Equation (2–1) is provided in Appendix A.

Each of these phases is characterized by a different Li^+ mobility. The overall ion transport across the composite is modeled by considering independent (parallel) as well as sequential (in series) pathways across the polymer and the interphase. While for the former conductivities are additive, the latter account for the fact that the volume fraction of the nanoparticles never exceeds the random percolation threshold, and they are always surrounded by an interfacial region. Hence, pathways involving LATP must include the consecutive crossing of at least two or all three phases. Accordingly, the ionic conductivity of the composite as a function of ϕ_N can be described using the equation

$$\sigma = \left(1-\phi\right)\sigma_P + \phi_I\sigma_I + \phi_N\left(\left(1-\phi\right)/\sigma_P + \phi_I/\sigma_I + \phi_N/\sigma_N\right)^{-1}, \qquad (2\text{–}2)$$

where σ_P, σ_I, and σ_N represent the ionic conductivities of the bulk polymer, the interphase and the nanoparticles respectively. Note that in Equation (2–2) ϕ_N is chosen by design, as controlled by the amount of LATP that precipitates in a sample. From this we calculate ϕ_I according to Equation (2–1), and the remaining volume fraction of unperturbed polymer is calculated as the maximum of ($1-\phi_N-\phi_I$) and zero. Accordingly, the function represented by Equation (2–2) exhibits a discontinuity when $\phi_N+\phi_I$ reaches unity, at which point ϕ_I is maximized, and beyond which the material turns into a two-phase system. The relative proportions of each phase are shown in **Figure 2-2**(a).

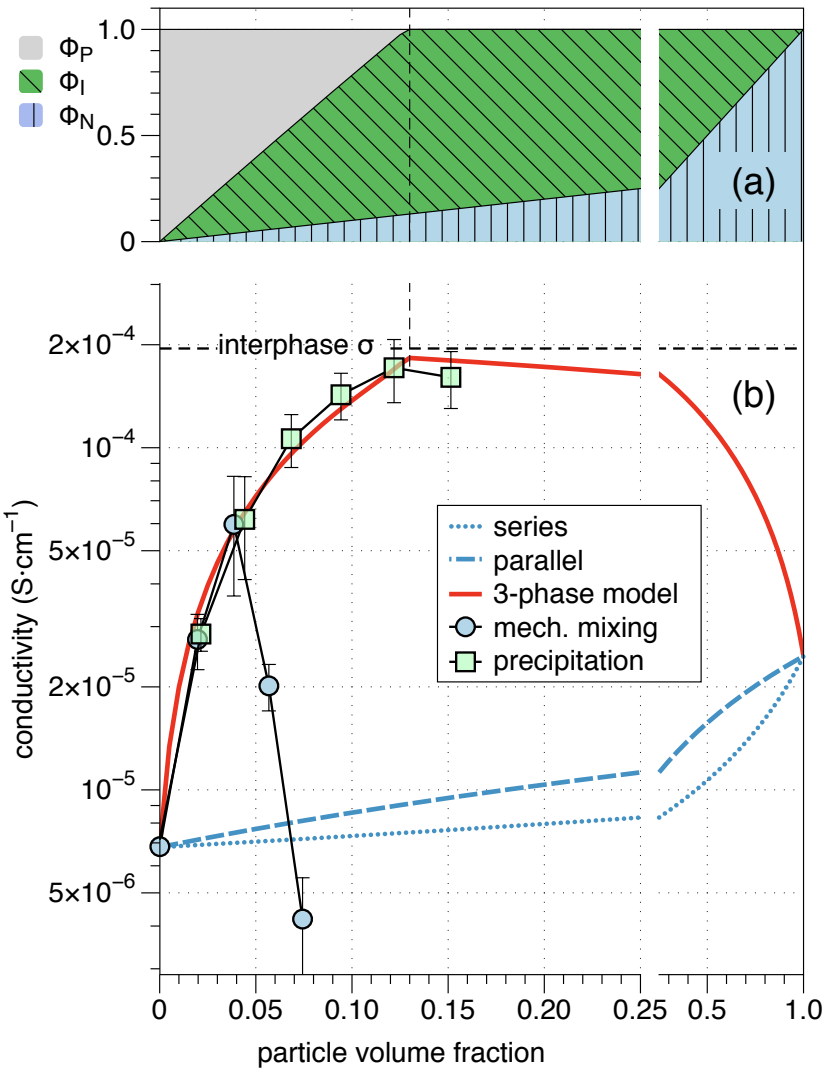

Figure 2-2 (a) estimated volume fractions of nanoparticles, interphase, and doped polymer; (b) Ionic conductivities as a function of LATP content in PEO-$LiClO_4$-LATP nanocomposite electrolyte with EO/Li=20 at room temperature. The upper and lower bounds of conductivity assuming a mixture of polymer and nanoparticles are shown as dashed and dotted lines. The sold red line represents the best fit of the tri-phase model (assuming the participation of an interphase as a third composite component) of the data obtained for the mechanical mixture, as reported in reference [18] (see text).

Through non-linear regression of ionic conductivity data of samples with varying particle loading using Equation (2–2), we optimize the values for σ_I and δ. The Li^+ ionic conductivity of amorphous LATP, σ_N, is known from the literature,[5] to be 2.46×10^{-5} S·cm^{-1}, and that of the of bulk polymer, σ_P, is 6.9×10^{-6} S·cm^{-1} and 1.4×10^{-5} S·cm^{-1}, for EO/Li ratios of 20 and 10, respectively, based on our

measurements. These values agree well with literature data.[5] As mentioned, this approach was inspired by data obtained in earlier work, which exhibits a maximum conductivity at relatively low nanoparticle loading, but clearly exceeded that of bulk polymer and the amorphous LATP. We interpreted the observed behavior to be indicative of the formation of a highly conducting interphase, but falling short of potential performance due to poor nanoparticle dispersion. We surmised that with sufficient spatial separation between particles, a larger fraction of interphase should develop, resulting in higher overall ionic conductivity. Proving this, and by inference, the validity of the tri-phase model is a first objective of the present work.

Thus, we begin by juxtaposing two conductivity data sets for EO/Li = 20 and at ambient temperature in **Figure 2-2**, comparing the results of mechanical mixing and precipitation processing. The circles in **Figure 2-2**(b) represent the data for samples fabricated by mechanical mixing of polymer and LATP nanoparticles, exhibiting an early maximum, as reported in reference[1], while the squares represent conductivities of samples generated by *in-situ* precipitation of the nanoparticles in the present investigation. The ascending trend in the conductivity *vs* particle loading clearly extends to much higher volume fractions, and nearly reaches the predicted maximum conductivity at 12.5 vol%. Indeed, the solid red line in **Figure 2-2**(b) represents the best fit of Equation (2–2) to the data for the mechanical mixture samples, as already reported in reference.[1] This comparison demonstrates how well the new data follows the trend predicted by tri-phase model, providing evidence of its applicability.

2.3.2 Analysis of Cation Mobility and Charge Carrier Density

For the samples prepared in this study, involving the precipitation of LATP nanoparticles, the ascending flank in the conductivity data extends to higher particle loading. Furthermore, comparing the conductivities for three series of samples with different $LiClO_4$ concentrations warrants analysis

at the cation mobility level. The results are shown in **Figure 2-3**. We focus on the data obtained for material in which LATP particles precipitated at 0°C, which includes three sets of room temperature conductivities for samples containing $LiClO_4$ at EO/Li ratios of 10, 20, and ∞ are plotted as a function of the particle loading. Accordingly, while for the first two, finite amounts of $LiClO_4$ are dissolved in the polymer, the latter material contains no lithium salt and solely depends on the LATP nanoparticles as the charge carrier source. Samples at EO/Li = 10 have the overall highest conductivity, due to large charge carrier concentration and free ion mobility.[1,6] The maximum ambient temperature ionic conductivity is 3.8×10^{-4} S·cm^{-1} for EO/Li = 10 and 1.71×10^{-4} S·cm^{-1} for EO/Li = 20, which is very close to the value we predicted in preceding work using a tri-phase model,[1] and high enough to have practical value.

Given the variations in charge carrier density, we must explicitly identify this variable in the expression given by Equation (2–2), to which end we substitute

$$\sigma_M = z q_e \rho_M \mu_M , \qquad (2–3)$$

where $z = +1$ for Li^+, q_e is the charge of an electron, ρ_M corresponds to the volumetric charge carrier concentration, and μ_M is the ionic mobility in response to an applied electric field, in accordance with Ohm's law. The subscript *M* refers to the medium in which the transport process takes place, and can appropriately be replaced with *P*, *I*, and *N*, indicating the polymer, the interphase, and the LATP nanoparticles, respectively. However, we assume that the lithium dissolved in the polymer can move freely between interphase and bulk polymer, i.e., $\rho_P \equiv \rho_I$, and continue to refer to this quantity as ρ_P. Combining Equation (2–1), (2–2), and (2–3) yields

$$\sigma = ze\left[\left(1-\phi\right)\rho_P\mu_P + f\left(\phi_N,\delta\right)\phi_N\rho_P\mu_I + \frac{\phi_N}{\frac{\left(1-\phi\right)}{\rho_P\mu_P} + \frac{f\left(\phi_N,\delta\right)\phi_N}{\rho_P\mu_I} + \frac{\phi_N}{\rho_N\mu_N}}\right]. \quad (2\text{–}4)$$

For the samples with finite EO/Li ratios there exist in principle two Li^+ sources, the salt and the LATP nanoparticles that we must formally account for. The amount of Li^+ introduced by salt is simply derived from the nominal $LiClO_4$ concentration. To estimate the contribution from nanoparticles is the reason why we examined the series of PEO/LATP composites with no added salt. As expected, for samples in this series with finite nanoparticle loading we observe a measurable ionic conductivity, which increases as a function of ϕ_N. It is therefore logical to attribute this to a finite amount of Li^+ that emanates from the nanoparticles into the polymer matrix, or else the conductivity magnitude would not effectively vanish at zero particle loading and we would more likely observe a rapid transition upon approaching the particle-particle percolation threshold as opposed to the gradual increase in conductivity evident in **Figure 2-3**.

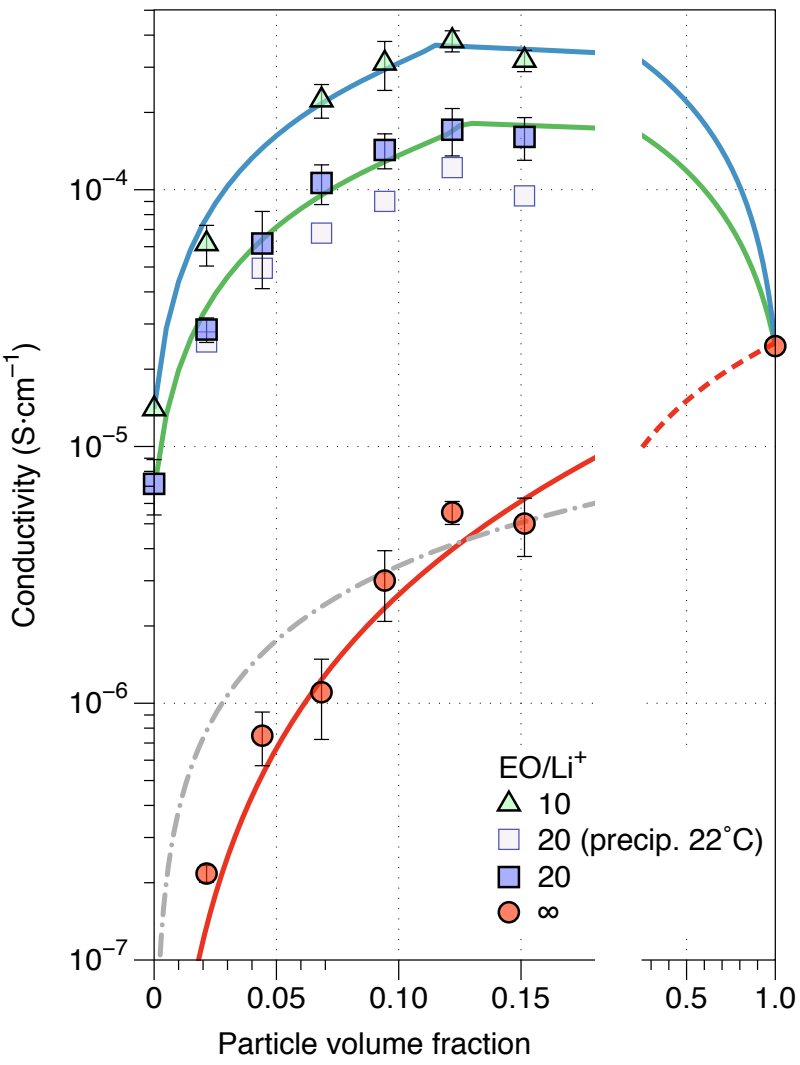

Figure 2-3 Measured Li^+ conductivities of conductivities in PEO-$LiClO_4$-LATP nanocomposite electrolytes containing different amounts of salt, as a function of LATP volume fraction. The solid lines represent the best fits of the data by the tri-phase model, assuming a space charge equilibrium of Li^+ originating from the nanoparticles at the interface with the polymer. The gray dash-dotted line represents the best fit by the model assuming a homogeneous distribution in the polymer of Li^+ originating from the nanoparticles. The dashed line towards high particle loading is added as a guide for the eye; assumptions made for the space charge layer become inaccurate at high particle loading. Note that the conductivity for the material containing neither salt nor nanoparticles is $2.62\times10^{-9} \pm 0.9\times10^{-9}$ S·cm^{-1}. It has been included in the data fits but is not shown in the figure to improve legibility of the vertical scale. Precipitation of LATP occurred at 0°C, except when otherwise noted in the legend.

Hence, we can describe the amount of lithium provided by the particles in terms of a simple solvation reaction, $Li^+(N) \underset{K}{\rightleftharpoons} Li^+(P)$, where the constant K defines the equilibrium concentrations according to the law of mass action, $K \simeq \rho_P^{(R)} / \rho_N^{(R)}$, assuming ideal solutions. The

superscript *R* indicates that this equilibrium is established at the interface between LATP and polymer (i.e., at the radius *R* of the nanoparticle). Neither the equilibrium constant nor the amount of charge released by the nanoparticles is known *a priori*. These quantities must be deduced from the measured conductivities since they depend on the charge densities in either phase as described by Equation (2–4), especially for samples containing no salt. We consider two scenarios: (i) a homogeneous charge distribution across the polymer and LATP, and (ii) a charge distribution governed by a space charge equilibrium at the interface between LATP and polymer. The first scenario is straightforward. The charge carrier density is assumed to be the same anywhere in the polymer phase and equal to that at the interface with LATP, which is determined by the above dissolution equilibrium. As derived in Appendix A, this charge carrier density depends on the nanoparticle volume fraction according to

$$\rho_P^{(f)} = \frac{\phi_N \rho_N^{(i)} + (1-\phi_N)\rho_P^{(i)}}{\phi_N / K + (1-\phi_N)}, \qquad (2\text{–}5)$$

where $\rho_P^{(i)}$ is the initial charge carrier density in polymer, before contribution from the LATP particles. The only unknown in this expression is the equilibrium constant, *K*, which is determined by fitting the measured conductivity data using Equation (2–4), after substituting $\rho_P \equiv \rho_P^{(f)}$ from Equation (2–5), and optimizing for *K*, μ_I, and δ. All other quantities are known from the literature or measurement. For the sample series containing no added salt, the best fit of the conductivity data using Equation (2–4) with this approach for ρ_P is shown in **Figure 2-3** as a dash-dotted gray line. However, this fit does not appear to properly capture the trend in the data. We therefore refined the approach, considering that dissolution of Li^+ from the nanoparticles results in charge separation and, because of the ensuing electric field, the equilibrium concentration is not spatially invariant. Instead, we must assume that this Li^+ remains strongly attracted to the nanoparticle surface, and rather forms

a diffuse space charge layer.[3] Furthermore, because of the large energetic cost of the charge imbalance created inside the LATP phase, the amount of lithium donated to the polymer is expected to be low at small particle loading. Within the scope of the present analysis, describing the charge carrier density as decaying exponentially with the distance *r* from the interface is a reasonable approximation, [7] i.e. for the polymer phase,

$$\rho_P(r) - \rho_P^{(i)} = \left(\rho_P^{(R)} - \rho_P^{(i)}\right) e^{-(r-R)/\lambda_P}, \tag{2–6}$$

where λ_P represents the decay length of the space charge and $\rho_P^{(R)}$ is the charge carrier concentration in the polymer at the interface with the nanoparticle of radius *R*. As before, we assume that the ratio of charge carrier densities on either side of the LATP/polymer interface is described by the equilibrium constant *K*. Given this constraint, we then evaluate the total amount of charge donated by the nanoparticles to the polymer phase and express it in terms of an average charge carrier density. As detailed in Appendix A, this yields

$$\rho_P = \frac{3\phi_N}{(1-\phi_N)}\left(\frac{\rho_N^{(i)}\alpha_N + \rho_P^{(i)}\alpha_P}{(\alpha_P + \alpha_N/K)} - \rho_P^{(i)}\right)\alpha_P + \rho_P^{(i)}, \tag{2–7}$$

where $\alpha_P = \left(\frac{\lambda_P}{R}\right)^3\left[\left(\frac{1}{\lambda_P/R}+1\right)^2+1\right]$ and $\alpha_N = \left(\frac{\lambda_N}{R}\right)^3\left[\left(\frac{1}{\lambda_N/R}-1\right)^2+1\right]$. λ_N is the decay length of the space charge in the nanoparticle. By selecting $\lambda/R \approx 0.03$ [8] and using the fact that the decay lengths scale like the dielectric permittivity of a material, which yields $\lambda_N/\lambda_P = \varepsilon_N/\varepsilon_P \sim 1.54$, as explained in Appendix A, the only remaining unknown in Equation (2–7) is again *K*. Substituting Equation (2–7) into Equation (2–4) and fitting the resulting expression to the measured conductivity data yields optimized values for *K*, μ_I, and δ. The conductivity data for samples that do not contain any salt, i.e., $\rho_P^{(i)} = 0$, essentially serve to determine *K*, which is then used to calculate an adjusted effective charge density

for samples with $LiClO_4$ dissolved in the polymer phase, i.e., $\rho_P^{(i)}$ = 0.83 nm^{-3} for EO/Li = 20 and 1.66 nm^{-3} for EO/Li = 10, which in either case is significantly less than the charge carrier density in LATP, i.e., $\rho_N^{(i)}$ = 5.96 nm^{-3}. Importantly, we find that the interphase mobility is essentially the same for the two series doped with salt, and independent of the salt concentration.

The data and best-fit curves are compared in **Figure 2-3** as solid lines. Accordingly, the conductivity data of the two sample series containing lithium salt are well described by our tri-phase model over the entire range of particle loading, including the cusp corresponding to the maximum possible Li^+ conductivity, beyond which the available interphase volume fraction decreases. The coefficient of determination (R^2) for these two fits is around 0.98. The rapid decline in conductivity, reported by several authors using conventional mechanical mixing to prepare their materials as due to particle agglomeration,[1,9,10] seems to be absent from our data, albeit only one data point was measured beyond the cusp. Nevertheless, it is safe to say that the *in-situ* precipitation processing significantly improves particle dispersion and, consequently, ionic conductivity. The quality of the fit of the data for the set of samples that contain no salt when assuming accrual of Li^+ near the LATP-PEO interface is significantly better than when assuming a homogeneous charge carrier distribution in the polymer. This reflects the fact that when forming a diffuse space charge layer surrounding the nanoparticles, the Li^+ cations are more effectively used for charge transport because they predominantly reside in the highly conductive interphase region. Here, a comparably lower charge density is required to achieve measurable ionic conductivity.

Indeed, the main reason for investigating the series of samples without salt is to determine the extent to which Li^+ is released from the LATP particles and contributes to cation transport in the polymer phase. This is embodied by the equilibrium constant K, which determines the surface charge density, $\rho_P^{(R)}$, and the assumed space charge decay length, λ_P. In combination, these

parameters determine the effective charge carrier density ρ_p. Our analysis yields $K = 0.23$, which brings about a charge density in the polymer of 0.019 lithium ions per nm^3 at $\phi_N = 0.125$ in the salt-free system. By comparison, in the system with EO/Li = 20 the Li^+ density increases by 0.008 nm^{-3} (~0.9%), while in the system with EO/Li = 10 it decreases by 0.0034 nm^{-3} (~0.2%), at the same particle loading. This suggests that in the latter system, the Li^+ concentration in PEO exceeds the solubilty relative to that in LATP, and some amount of lithium is transferred from polymer to nanoparticles. This finding is consistent with the observation that increasing amounts of $LiClO_4$ cause deterioration of the polymer's mechanical properties due to plasticization.[1] It is important to note that these results are indeed independent of the choice of λ_P and λ_N. Increasing the decay length results in a smaller optimized value for *K*, and *vice versa*, such that ρ_p remains unchanged. Ultimately, the charge carrier contribution to the polymer from the nanoparticles is nearly negligible when the matrix contains salt.

Table 2-1 Summary of lithium-ion transport properties

EO/Li Ratio	10	20	∞
Charge carrier density ρ_p (nm^{-3}) at $\phi_N = 0.125$	1.6526	0.8358	0.019
Interphase thickness δ/R	1.07	1.0	0.88
Interphase Li^+ mobility μ ($S\,cm^2 \cdot C^{-1}$)	$1.485 \cdot 10^{-6}$	$1.456 \cdot 10^{-6}$	$1.6 \cdot 10^{-6}$
Interphase Li^+ conductivity ($S \cdot cm^{-1}$)	$3.94 \cdot 10^{-4}$	$1.93 \cdot 10^{-4}$	$5.6 \cdot 10^{-6}$
Maximum measured composite conductivity ($S \cdot cm^{-1}$)	$3.80 \cdot 10^{-4}$	$1.713 \cdot 10^{-4}$	$5.53 \cdot 10^{-6}$ at $\phi_N = 0.125$

The salient quantities resulting from our analysis are summarized in **Table 2-1**. Accordingly, the highest measured composite conductivity at room temperature is 3.80×10^{-4} S·cm^{-1} for the system containing one Li^+ cation for every 10 EO units. This nearly reaches the theoretical limit of 3.94×10^{-4} S·cm^{-1}, which would be achieved if the material consisted entirely of polymer with the structure of the interphase. Our analysis attests to the highly effective dispersion of nanoparticles realized with our *in-situ* precipitation technique. The interpretation of our results is particularly validated by the fact that the cation mobility is independent of the cation concentration. Considering that the Li^+ mobility in PEO without LATP nanoparticles is $\mu_P = 5.2\times10^{-8}$ S cm^2·C^{-1}, by comparison, the Li^+ mobility in interphase is nearly 30 times higher. The relative constancy of the interphase thickness across systems with different salt concentrations suggests that the interphase formation is predominantly a configurational effect, and is not coextensive with an accumulation of charge carriers. Indeed, the estimated decay length of the space charge layer surrounding the nanoparticles is nearly two orders of magnitude smaller. However, based on our previous comparative study, some degree of chemical compatibility between nanoparticles and polymer matrix is prerequisite for the interphase formation.

In **Figure 2-3**, we also include one data set for composites with LATP precipitated at ambient temperature (22°C) and EO/Li = 20. The conductivities are consistently lower than for samples processed at 0°C. With an enhanced growth rate at the higher temperature one can expect larger particles to form. One explanation would be that the ratio of interphase thickness to particle radius decreases with increasing particle size, i.e., less interfacial region is created with larger particles. If that were the case, however, the cusp in the data would occur at a higher particle loading, which it does not. Moreover, micrograph did not reveal distinctly larger particles. Therefore, we believe that the ratio of interphase thickness to particle ratio remains approximately constant, which is consistent with the notion that electrochemical potential gradients on either side of the interface govern the

extent of the interphase, and that the change in conductivity with processing conditions is due to differences in the randomness of particle dispersion, i.e., residual agglomeration of particles is more prevalent at higher precipitation temperatures.

2.3.3 Thermal Activation of the Cation Transport Process

In **Figure 2-4** we examine the temperature dependence of the conductivity data for the series of samples with EO/Li = 20, by plotting it in the form of the natural logarithm of $\sigma \cdot T$ *vs.* the reciprocal of the thermal energy available to the system. Symbols represent the measured data, and the lines represent the best fits using models described in the following. Generally, the higher the particle loading, the higher the ionic conductivity. However, it is also apparent that this progression occurs in two separate groupings. The fit lines describing the data for samples with a particle loading of 4.42 vol.% or lower converge at a distinctly lower intercept with the ordinate than those for the group of samples with higher particle loadings. Furthermore, while the slope of the fit lines becomes less steep with increasing particle loading, especially at low temperatures, a marked readjustment of this trend is manifest between the two groups of samples. Between 4.42 and 6.84 vol.% particle loading the slope abruptly increases in magnitude, whereas towards higher loading the lessening of the slope magnitude resumes.

Based on the above analysis, the interphase region surrounding the LATP particles has a thickness commensurate with the radius of the particles, and hence the outer perimeter of this layer encompasses a volume roughly eight times larger than the particles themselves. Assuming a perfectly random placement of nanoparticles, at $\phi_N = 4.42$ the space occupied by the interphase and the nanoparticle amounts to one third of the total volume, which corresponds to the percolation threshold for the interphase.[11] Accordingly, above the percolation threshold Li^+ transport is instantly dominated by the conduction pathways through the interphase, in which it has a 30 times

higher mobility, i.e., about 93% of the ionic current goes through the interphase. Conversely, below the percolation threshold these transport pathways are blocked by the much less conductive pristine polymer phase. While this transition is not immediately obvious in the conductivity *vs.* particle volume fraction data, the changeover in transport mechanism is evident in the temperature dependence of the conductivity.

Fundamental insights into the cation transport process can be gained by determining the activation energy associated with a cation jump, as defined in the framework of transition state theory (TST). Accordingly, we can express the ionic conductivity as $\sigma = \left(k_B T\right)^{-1} \rho_P \left(zq_e\right)^2 \gamma d_0^2 \nu e^{-G_a/k_B T}$,[12] where γ is the geometry coefficient, e.g. 1/6 for an isotropic amorphous medium, d_0 is the jump distance of the cation, ν is the attempt frequency, and $G_a = E_a - T \cdot S_a$ is the Gibbs free energy of activation. Multiplying both sides of this expression with the temperature, separating enthaly and entropy, and taking the logarithm of each term then yields

$$\ln\left(\sigma T\right) = \ln\left(\rho_P \left(zq_e\right)^2 \gamma d_0^2 \nu k_B^{-1}\right) + S_a / k_B - \beta E_a = \ln \sigma_0 - \beta E_a \qquad (2\text{–}8)$$

where we abbreviated $\beta = \left(N_A k_B T\right)^{-1}$ and $\ln \sigma_0 = \ln\left(\rho_P \left(zq_e\right)^2 \gamma d_0^2 \nu k_B^{-1}\right) + S_a / k_B = P + S_a / k_B$. Data that follows this description is said to observe Arrhenius behavior, characterized by a uniquely defined activation energy.

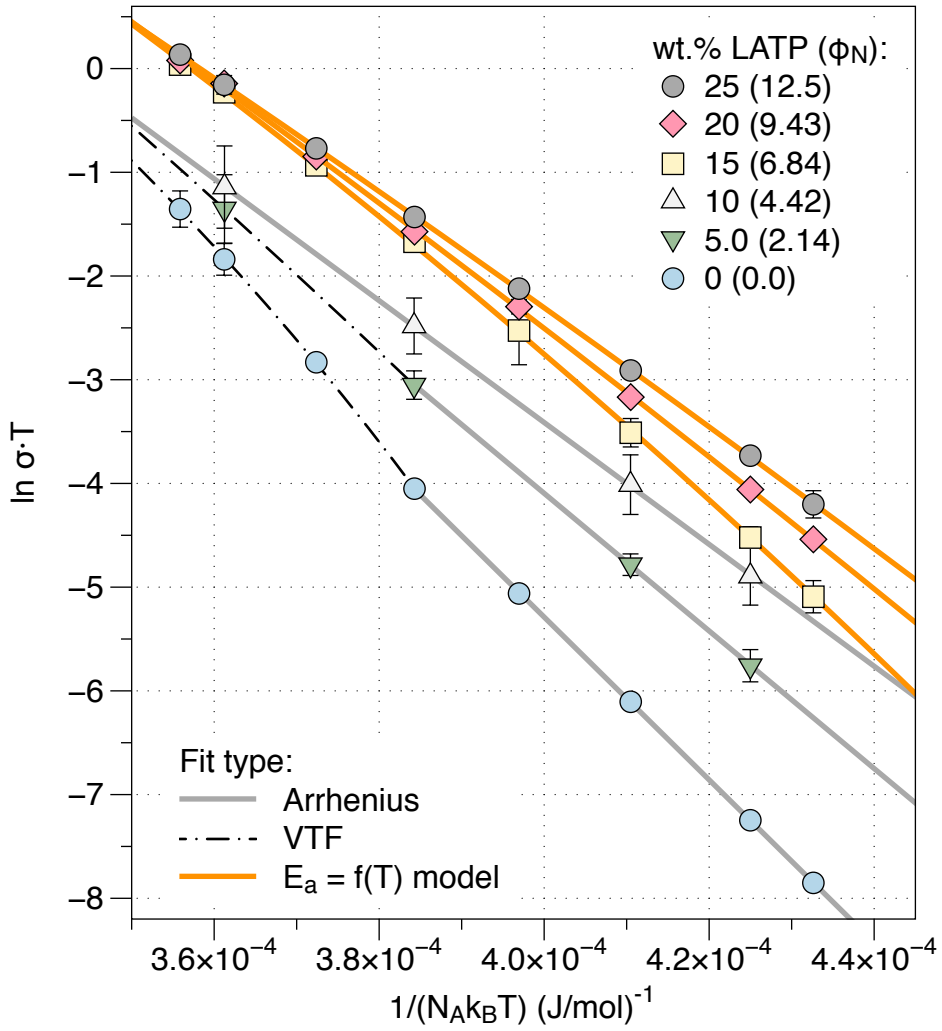

Figure 2-4 Dependence of the ionic conductivity on the reciprocal temperature for PEO-$LiClO_4$-LATP nanocomposite electrolytes containing different LATP volume fractions. Where not apparent, error bars are smaller than the symbol size.

However, close examination of the data in **Figure 2-4** reveals distinct curvature for some compositions or temperature ranges. Such curvature is ubiquitous in the ionic conductivity data of a variety of materials, and has prompted the widespread use of alternative models to describe the observed behavior, such as the Vogel-Tammann-Fulcher (VTF) equation,[1,10,13]

$$\sigma T = Ae^{-B/(T-T_0)} \Rightarrow \ln(\sigma T) = \ln A - \beta k_B B/(1-\beta N_A k_B T_0) \qquad (2\text{–}9)$$

While the VTF model fits the data very well, it deviates from the conventional statistical mechanical description of probability densities, by eliminating the quantity $N_A k_B T_0$ from the thermal energy available to the system for attaining a target energy level. Consequently, the quantity $k_B B$ in the above expression must not be understood as an activation energy in the sense stipulated by TST; it is inconsistent with the microscopic interpretations of measures such as heat capacity and elastic moduli. Moreover, the Vogel temperature T_0 does not reliably correlate with the glass transition temperature, T_g, nor the Kautzmann temperature,[13–15] and according to Diederichsen *et al* should be considered an empirical fitting parameter.[16] As such, the VTF parameters do not reveal the most reliable insight into the relationship between molecular structure and transport properties of an electrolyte.

Instead, we pursue a different approach where we account for the change in the free energy landscape as a consequence of the gradual changes in molecular packing density, atomic interaction topology, and the structural reconfigurations that occur in the temperature range between the melting temperature and T_g, in which the material transitions between a supercooled liquid and a glass. Accordingly, we fit our data using a model allowing for a correlative activation free energy (CAFE), expressed by

$$\ln(\sigma T) = P + S_0/k_B + \psi(\beta)(\Delta S_a/k_B - \beta \Delta E_a) - \beta E_0 . \qquad (2\text{–}10)$$

Here we describe the temperature dependence of the activation energy as $E_a(\beta) = \psi(\beta)(E_G - E_0) + E_0 = \psi(\beta)\Delta E_a + E_0$, where E_G and E_0 are the activation energies for cation migration in the glass and at $\beta = 0$, respectively, and similarly, for the expression for the activation entropy is $S_a(\beta) = \psi(\beta)\Delta S_a + S_0$. The changeover of these quantities between the values pertaining to the liquid and glass state are described by the so-called logistic function

$\psi(\beta) = \left(1 + C_0 e^{-\nu H(\beta - \beta_C)}\right)^{-1/\nu}$, which has a sigmoidal shape whose steepness, asymmetry, and location of the inflection point are controlled by the parameters H, ν, and β_C, respectively. C_0 is a constant that depends on the value of $\psi(\beta)$ at $\beta = \beta_C$. Details of this CAFE model are described in Appendix B. Our approach is not to be confused with the concept of a distribution of activation energies that has long been considered to describe the viscoelastic response of amorphous materials, [17] and more recently, for ionic conductivity.[18,19] A distribution of activation energies is postulated for disordered structures in which a range of transition states coexist for a given process. Whether this is the case or not, we cannot infer from our analysis. However, a distribution of activation energies alone is not able to describe the negative curvature in $\ln \sigma \cdot T$ *vs.* β dependency we consistently observe.

Using the measured conductivity data, we determine the best-fit values for H, ΔE_a, ΔS_a, E_0, and S_0. The value of $P = \ln\left(\rho_P \left(zq_e\right)^2 \gamma d_0^2 \nu k_B^{-1}\right) = -6.92$ is calculated based on estimates of its constituent quantities. The results are summarized in **Table 2-2** and **Figure 2-5**.

Table 2-2 Summary of quantities associated with the thermal activation of cation hopping in LATP/PEO composites with various filler content and EO/Li = 20

ϕ_N (%)	0.0	2.14	4.42	6.84	9.43	12.5
E_a (kJ/mol) Arrhenius	78.46*	66.34	58.75	67.25	60.68	56.31
$N_A k_B B$ (kJ/mol) VTF	13.79*	—	—	24.13	37.72	36.67
$E_a = E_0 + \Delta E_a$ (kJ/mol) CAFE model	62.3 … 83.5	—	—	65.0 … 72.8	60.0 … 63.5	55.5 … 58.3
S_0 (J/mol·K)	100.0	—	—	100.7	103.2	102.9
$S_a = S_0 + \Delta$ S_a (J/mol·K)	217.1 … 223.5	—	—	247.4 … 273.6	231.7 … 242.6	218.3 … 226.9

ΔH (kJ/mol)	5.68	—	—	2.02	1.08	0.98
T_C	261.6	—	—	206.8	207.6	206.1

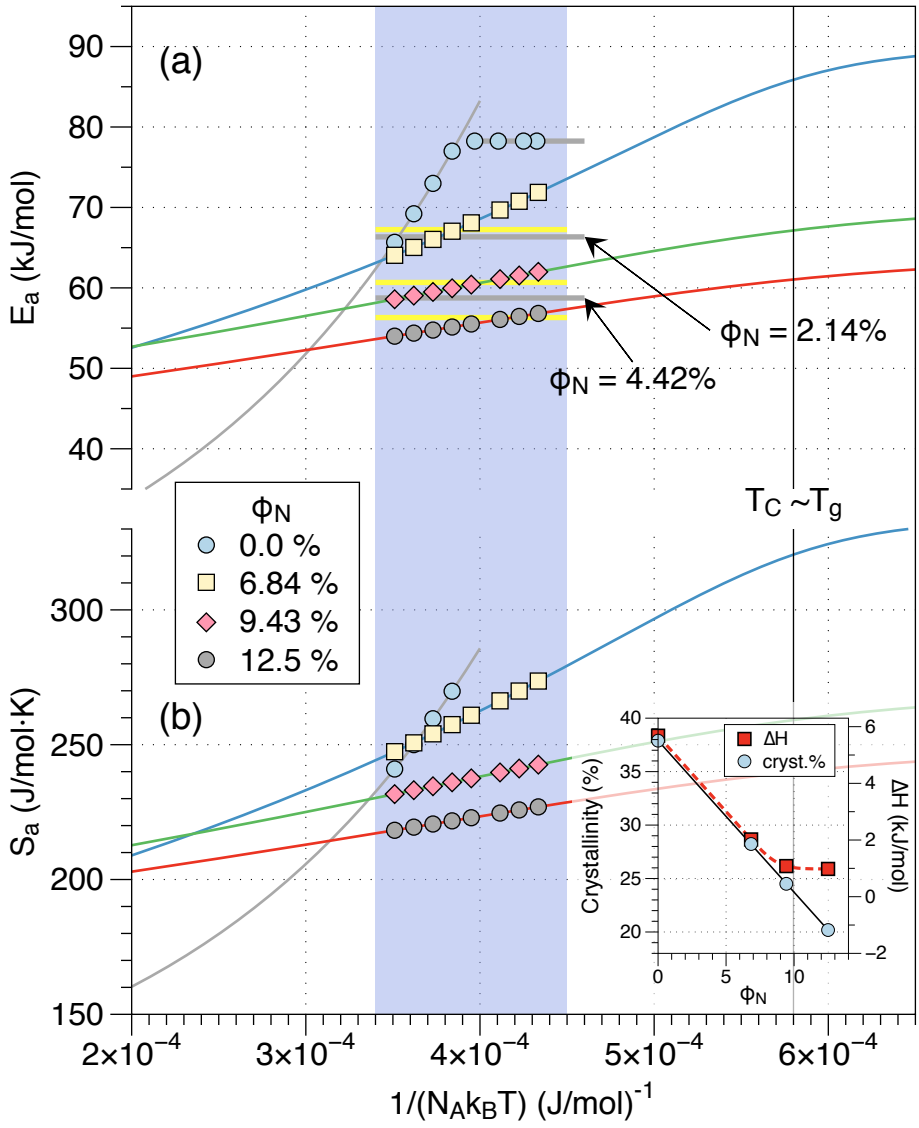

Figure 2-5 Activation enthalpies, E_a, and entropies S_a as a function of the reciprocal temperature, as determined using the CAFE model. The solid curved lines represent the best fit of the ionic conductivity data by the CAFE model, extrapolated beyond the measurement range (shaded blue); symbols identify locations where measurements were taken. The horizontal gray lines represent the activation energy where data exhibits Arrhenius behavior, while the horizontal yellow lines represent the activation energies resulting from the best fit of Equation (2–8), in cases where the temperature dependence of the conductivity deviates from Arrhenius behavior, i.e., materials with particle loading of 6.84 vol.% or higher. The inset shows a comparison between the degree of crystallinity and the transformation enthalpy that controls the steepness of the logistic function.

As mentioned above, the temperature dependence of the ionic conductivity differs depending on whether the system is below or above the interphase percolation threshold. In **Figure 2-5**, the activation energies and entropies are plotted as a function of the scaled reciprocal temperature. The solid curves represent the best fit of the ionic conductivity data using Equation (2–10), extended over a wide temperature range; symbols identify locations where measurements were taken. The horizontal gray lines represent the activation energy for data exhibiting Arrhenius behavior, i.e., the samples containing zero or small concentrations of LATP. Among these, the conductivity *vs.* β of the material without nanoparticles shows discernable curvature within the subset of the four highest-temperature data points (small β-values), which has been fitted using Equation (2–10) to yield temperature dependent activation energies and entropies. At lower temperatures (large β-values) the conductivity data very exactingly exhibits Arrhenius behavior. This changeover between two regimes with different temperature dependences of the ionic conductivity is highly reproducible for this nanoparticle-free system. As mentioned above, since adding nanoparticles to the polymer matrix suppresses the formation of crystalline domains,[20,21] we expect significant crystallization to occur in this system (**Appendix Figure A. 3**, **Appendix Figure A. 5**). Indeed, based on thermal analysis, we estimate that crystalline domains make up about 38% of the PEO (see inset of **Figure 2-5**). Hence, we interpret the varying slope of the conductivity *vs.* β, as a consequence of this crystallization. By this we do not mean that the fraction of crystalline domains, which effectively block the passage of cations, varies with temperature. Instead, the mechanical constraints imposed by their formation on remaining amorphous PEO causes structural modifications in the latter that are subject to relaxation at high temperatures, but are kinetically arrested at low temperatures. We conclude this because conductivity data is collected upon heating and the melting of crystals has a sharply defined thermal signature, unlike the gradual change we observe.

The variation in activation energy and entropy with β is most pronounced for the neat PEO, as reflected in the largest ΔH in the logistic function, and thus suggesting the most significant structural changes in terms of their impact on cation mobility. However, changes in the free energy of activation are only manifest above 35°C; below that, ionic conductivities exhibit Arrhenius behavior. Similarly, while in materials with small LATP nanoparticle loading Arrhenius behavior is prevalent, as soon as the interphase percolation threshold is crossed, non-Arrhenius behavior is abruptly manifest again. As shown in **Figure 2-5**, the temperature dependences of the activation energies and entropies are more moderate compared to that for neat PEO, but they persist across the entire temperature range. The higher the nanoparticle loading, the lower are both components of the activation free energy and the less it varies with temperature.

Essentially, for the group of materials with high particle loading the activation entropy converges to the same value at $\beta = 0$, which suggests that their structures possess a similar cohesive framework, but closer to the glass transition subtle structural differences develop both as a function of the nanoparticle loading and the temperature. Increasing the nanoparticle concentration causes overlap of influence from different nanoparticles on the polymer structure in any given location. This stabilizes the structure, making it less susceptible to temperature changes. Furthermore, it is possible that the temperature dependence of K, which controls the equilibrium chemical potential of Li^+, and thus affects the structure of the interphase, is reflected in the temperature dependence of the cation mobility. However, we expect this effect to be minor considering the small amount of Li^+ donated by the particles. As a benchmark, the horizontal yellow lines in **Figure 2-5** represent the activation energies resulting from the best fit of Equation (2–8) , in materials with particle loading of 6.84 vol.% or higher; they typically fall within the range of the temperature dependent activation energy.

These results are also included in **Table 2-2**, allowing one to compare the activation energies derived from fitting the data using the Arrhenius or CAFE models with the pseudo-activation energy the VTF model yields, i.e., $N_A k_B B$. While the former two are in good agreement with one another, the pseudo-activation energy deviates from those not only in terms of their magnitudes, but also based on their trend with composition. Indeed, while the activation energies obtained using the Arrhenius and CAFE steadily decrease as a function of the nanoparticle loading, those obtained using the VTF model do the opposite. This is misleading when using the VTF to seek a mechanistic interpretation of the data. Also remarkable is that the activation energy for the system with 4.42 vol.% LATP is lower than for that with 6.84 vol.% by 10%, and yet the room temperature conductivity for the latter is almost twice as high. This illustrates the importance of the activation entropy in defining the cation mobility.

2.4 Complementary Analyses

Thermal analysis does not reveal any specific information regarding the nature of the interphase. The polymer glass transition temperature is –29±1 ºC, regardless of the particle loading, and consequently, the volume fraction of interphase. The degree of polymer crystallinity decreases linearly with ϕ_N, as shown in the inset of **Figure 2-5**(b), which suggests ordered polymer domains are not a feature of the interphase. Conversely, infrared spectroscopy provides an initial qualitative insight into the differences between the neat PEO and interphase structures. **Figure 2-6**(a) shows the FTIR spectrum of a PEO-matrix composite containing 25 wt.% LATP nanoparticles generated via *in-situ* precipitation, but no lithium salt. Panels b and c show the spectra of LATP and pure PEO (thin black line), respectively. Accordingly, the spectra for LATP particles obtained from LF-FSP and in-situ precipitation overlap within experimental error, confirming that the two synthesis routes yield the same amorphous material. Both spectra show two broad bands, i.e., 600–800 cm^{-1} and

900–1300 cm^{-1}, associated to Ti-O and P-O stretching modes, respectively.[22] For PEO, peaks located at 2876 cm^{-1}, 1465 cm^{-1} and 1341 cm^{-1} are attributed to C-H stretching, scissoring and wagging modes, respectively. The 960 cm^{-1} and 841 cm^{-1} peaks are due to CH_2 rocking. C-O-C stretching is observed at 1145 cm^{-1}, 1095 cm^{-1}, and 1058 cm^{-1}.[1,23]

To obtain the IR spectrum corresponding of the interphase polymer we begin with the premise that, in a first approximation, the spectrum of the composite (I_c in **Figure 2-6**(a)) should be a linear combination of those for pure LATP (I_N) and PEO (I_p), i.e., $I_c = a \cdot I_N + (1-a)I_p$, where $a \leq 1$. The value of a is determined by comparing the IR absorbance of the composite and pure LATP at 650 cm^{-1}, since that of pure PEO at this frequency is close to zero. We found $a = 0.3$. Note that at 25 wt.%, according to our tri-phase analysis, essentially all of the polymer exhibits interphase character. Therefore, evaluating $(I_c - a \cdot I_N)/(1-a)$ does not yield the spectrum for neat PEO, but that for interphase polymer. This spectrum (I_i) is superimposed on that of neat PEO in **Figure 2-6**(c). Over wide spectral ranges, the two polymer spectra are closely similar, but significant differences are manifest in the ranges 1000–1200 cm^{-1} and 2800–3000 cm^{-1}, as shown on a magnified scale in **Figure 2-6**(d). In the first range we observe a softening (red-shift) and broadening of the C-O-C stretching modes, reflecting increased disorder in the regions of the polymer structure that establish the Li^+ cation sites, thus potentially providing more open passageways for cation migration. The shift towards lower frequencies may also be indicative of the lowering of the activation barrier for cation hopping. The intensification of the C-H stretching mode could be the result of a redistribution of thermal energy as a result of the increased disorder in the polymer backbone.

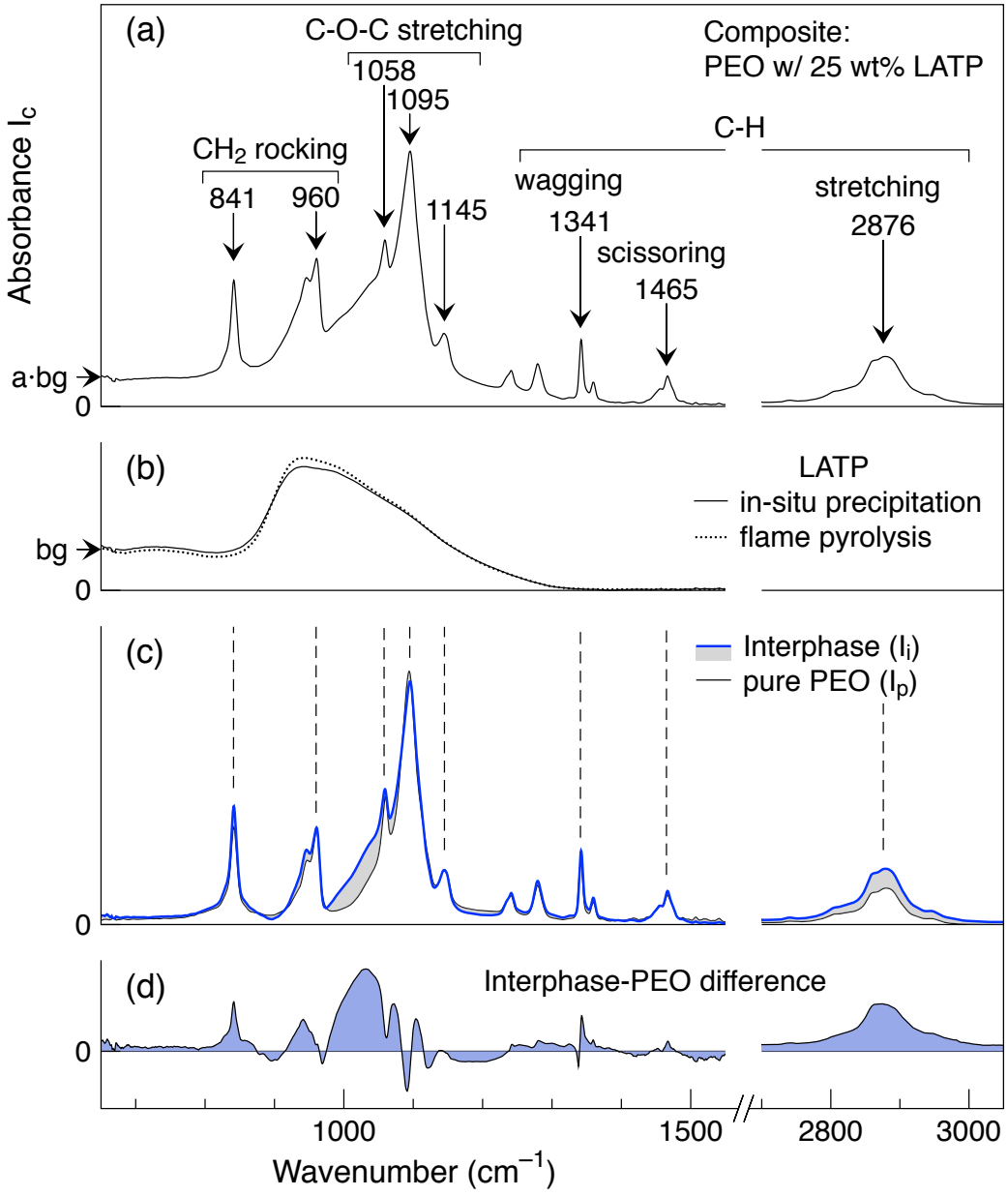

Figure 2-6 (a) FTIR spectrum of a PEO-matrix composite containing 25 wt.% LATP nanoparticles generated via *in-situ* precipitation, with mode assignments; (b) FTIR spectra of LATP generated via *in-situ* precipitation and flame spray pyrolysis, respectively; (c) FTIR spectra of bulk PEO and of PEO in the interfacial region, obtained by deconstructing the spectrum in (a) as a linear combination of the spectra for bulk PEO and LATP; (d) residuals obtained when subtracting I_p from I_i.

2.5 Conclusion

We have developed a novel and environmentally friendly water based *in-situ* precipitation processing method for fabricating LATP/PEO composite electrolyte. This method effectively eliminates particle agglomeration in composites with up to 30 wt%, taking full advantage of interphase region to increase ionic conductivity. The maximum ambient temperature ionic conductivity of 3.8×10^{-4} $S\cdot cm^{-1}$ is observed at 25 wt% LATP loading and EO/Li = 10, while the peak value calculated using our tri-phase model is 4.36×10^{-4} $S\cdot cm^{-1}$, thus validating this analytical approach. Relying exclusively on the LATP nanoparticles as the source for Li^+ reveals that the active filler contributes less than 2% of the mobile charge carriers. The temperature dependence of the conductivity allows one to distinguish two groups of behavior, one below and the other above the interphase percolation threshold. We use a newly developed formalism based on a correlative activation free energy (CAFE), to extract both the activation energy and entropy for cation migration from the measured data. Both activation energies and entropies decrease as a function of the LATP particle loading in both regimes, but an abrupt increase in these quantities occurs at the interphase percolation threshold. This leads to a narrow 'inversion' region just above the percolation threshold, where higher ionic conductivities are achieved despite an increase in activation energy, which is due to the simultaneous increase in activation entropy. With increasing particle loading, activation energies for materials with a percolating interphase region drop below those for materials below the percolation threshold. However, this finding underscores the importance of entropic contributions to the transport process. The interphase is characterized by a larger degree of disorder in the C-O-C groups of the polymer backbone and shallower potential wells at the lithium cation sites.

2.6 References

1. Wang, W., Yi, E., Fici, A. J., Laine, R. M. & Kieffer, J. Lithium Ion Conducting Poly(ethylene oxide)-Based Solid Electrolytes Containing Active or Passive Ceramic Nanoparticles. *J. Phys. Chem. C* **121**, 2563-2573 (2017).

2. Bonilla, M. R. et al. Unveiling Interfacial Li-Ion Dynamics in Li7La3Zr2O12/PEO(LiTFSI) Composite Polymer-Ceramic Solid Electrolytes for All-Solid-State Lithium Batteries. *ACS Appl. Mater. Interfaces* **13**, 30653-30667 (2021).

3. Li, Z. et al. Ionic Conduction in Composite Polymer Electrolytes: Case of PEO:Ga-LLZO Composites. *ACS Appl. Mater. Interfaces* **11**, 784-791 (2019).

4. Sample-Lord, K. & Shackelford, C. Dialysis Method to Control Exchangeable Sodium and Remove Excess Salts From Bentonite. *Geotech. Test. J.* **39**, 206-216 (2016).

5. Chen, H., Tao, H., Zhao, X. & Wu, Q. Fabrication and ionic conductivity of amorphous Li_Al_Ti_p_O thin film. *Journal of Non-crystalline Solids* **357**, 3267-3271 (2011).

6. Ahmed, H. T., Jalal, V. J., Tahir, D. A., Mohamad, A. H. & Abdullah, O. G. Effect of PEG as a plasticizer on the electrical and optical properties of polymer blend electrolyte MC-CH-LiBF4 based films. *Results in Physics* **15**, 102735 (2019).

7. Jiang, S. & Wagner, J. B. A theoretical model for composite electrolytes—I. Space charge layer as a cause for charge-carrier enhancement. *Journal of Physics and Chemistry of Solids* **56**, 1101-1111 (1995).

8. de Klerk, N. J., J. & Wagemaker, M. Space-Charge Layers in All-Solid-State Batteries; Important or Negligible. *ACS Appl. Energy Mater.* **1**, 5609-5618 (2018).

9. Lee, J. K., Lee, Y. J., Chae, W.-S. & Sung, Y. M. Enhanced ionic conductivity in PEO-LiClO4 hybrid electrolytes by structural modification. *Journal of Electroceramics* **17**, 941-944 (2006).

10. Liu, W. et al. Ionic Conductivity Enhancement of Polymer Electrolytes with Ceramic Nanowire Fillers. *Nano Lett.* **15**, 2740-2745 (2015).

11. Kieffer, J. & Wagner, J. B. Electrical Conductivity of Metal-Metal Oxide Composites. *Journal of The Electrochemical Society* **135**, 198 (1988).

12. Barsoukov, E. & Macdonald, J. R. *Impedance Spectroscopy: Theory, Experiment, and Applications* (Wiley, 2018).

13. Nookala, M., Kumar, B. & Rodrigues, S. Ionic conductivity and ambient temperature Li electrode reaction in composite polymer electrolytes containing nanosize alumina. *Journal of Power Sources* **111**, 165-172 (2002).

14. Ahmed, H. T. & Abdullah, O. G. Structural and ionic conductivity characterization of PEO:MC-NH4I proton-conducting polymer blend electrolytes based films. *Results in Physics* **16**, 102861 (2020).

15. Leo, C. J., Subba Rao, G. V. & Chowdari, B. V. R. Studies on plasticized PEO–lithium triflate–ceramic filler composite electrolyte system. *Solid State Ionics* **148**, 159-171 (2002).

16. Diederichsen, K. M., Buss, H. G. & McCloskey, B. D. The Compensation Effect in the Vogel–Tammann–Fulcher (VTF) Equation for Polymer-Based Electrolytes. *Macromolecules* **50**, 3831-3840 (2017).

17. Tweer, H., Simmons, J. H. & Macedo, P. B. Application of the Environmental Relaxation Model to the Temperature Dependence of the Viscosity. *The Journal of Chemical Physics* **54**, 1952-1959 (2003).

18. Bischoff, C., Schuller, K., Beckman, S. P. & Martin, S. W. Non-Arrhenius Ionic Conductivities in Glasses due to a Distribution of Activation Energies. *Phys. Rev. Lett.* **109**, 075901 (2012).

19. Dyre, J. C. Some remarks on ac conduction in disordered solids. *Journal of Non-Crystalline Solids* **135**, 219-226 (1991).

20. Chu, P. P., Reddy, M. J. & Kao, H. M. Novel composite polymer electrolyte comprising mesoporous structured SiO2 and PEO/Li. *Solid State Ionics* **156**, 141-153 (2003).

21. Masoud, E. M., El-Bellihi, A.-A., Bayoumy, W. A. & Mousa, M. A. Effect of LiAlO2 nanoparticle filler concentration on the electrical properties of PEO–LiClO4 composite. *Materials Research Bulletin* **48**, 1148-1154 (2013).

22. Kozawa, T. Combined wet milling and heat treatment in water vapor for producing amorphous to crystalline ultrafine Li1.3Al0.3Ti1.7(PO4)3 solid electrolyte particles. *RSC Adv.* **11**, 14796-14804 (2021).

23. Noor, S. A. M., Ahmad, A., Talib, I. A. & Rahman, M. Y. A. Morphology, chemical interaction, and conductivity of a PEO-ENR50 based on solid polymer electrolyte. *Ionics* **16**, 161-170 (2010).

CHAPTER III Sol-Gel Derived Bifunctionalized Nano-Porous Hybrid Silica-PEO Single-Ion Conducting Solid Electrolyte

3.1 Introduction

In the realm of lithium-ion batteries (LIBs), a significant shift toward solid-state electrolytes (SSEs) is underway to address the longstanding challenges associated with conventional liquid electrolytes. This transition is driven by a compelling array of advantages, including enhanced safety, superior stability, and the potential to mitigate the formation of hazardous lithium dendrites during charging. Liquid electrolytes, while effective, are prone to Li dendrite growth, leakage and pose inherent safety risks due to their flammability.[1–3] Furthermore, when the source of Li^+ is in the form of a salt, as is typically the case in liquid electrolytes, Li^+ and its counterion move to the opposite electrodes during charge and discharge of these batteries. Research conducted by Villaluenga et al. has illuminated a significant insight regarding dual-ion conducting electrolytes, wherein only approximately one-third of the conductivity can be attributed to Li^+.[4] This attribution is quantified by the cation transference number (t^+), defined as $t^+ = \sigma_{cation}/(\sigma_{cation}+\sigma_{anion})$, where σ_S represents the ionic conductivity of species *S*. In this context, only the cation partakes in electrochemical reactions at the battery's electrodes. Over time, the anion tends to accumulate at the anode while depleting at the cathode, a phenomenon that can lead to electrode degradation, capacity deterioration, and a reduction in the batteries' output voltage.[4–6] A diminished cation transference number can also contribute to

dendrite growth. During the constant current density electrodeposition of Li^+ onto the anode, exist a critical moment when the salt concentration near the electrode approaches zero. This happens as lithium ions are consumed by the anode at a rate surpassing the replenishment from diffusion flux, creating an instability. Within this instability, lateral fluctuations induce the formation of preferred transport channels that carry lithium toward the anode, initiating the growth of lithium dendrites. The pivotal moment in this sequence is defined by Sand's time, τ, i.e., the time when lithium dendrite starts growing, given by

$$\tau = \pi D\left(\frac{eC_0}{2Jt_a}\right)^2, \quad (3\text{-}1)$$

where D is the diffusion coefficient of metal ions, e is the electronic unit charge, C_0 is the molar ion concentration in the bulk electrolyte, J is the current density, and t_a is the transport number of anions which is equal to $(1- t^+)$.[7] Accordingly, Sand's time is inversely proportional to the square of the anion transport number. Consequently, small transport numbers, which corresponds to large cation transference numbers are more likely to extend Sand's time beyond the charging cycle duration, effectively suppressing dendrite growth.

Hence, in the pursuit of SSE development, diverse strategies aimed at limiting the mobility of the counterion, thereby establishing what is commonly referred to as a 'single-ion electrolyte,' are currently under exploration.[8–11] In a straightforward approach, single-ion character is sought by using binary lithium salts that involve low-mobility bulky anions. Dai *et al.* investigated the Li^+ transference numbers (t^+) of various lithium salts with different anions, including CF_3SO^{3-} (Tf), $N(CF_3SO_2)^{2-}$ (TFSI), $N(C_2F_5SO_2)^{2-}$ (BETI), and $C(CF_3SO_2)^{3-}$ (TFSM), within poly(vinylidene fluoride)–hexafluoropropylene copolymer. Their findings indicate that larger anions are associated with higher Li^+ transference numbers.[12] Another strategy is the copolymerization of the ion donor. Examples of polymerized ion donors include poly(trifluoromethane)sulfonimide lithium styrene

(LiPSTFSI), poly[(4-styrenesulfonyl)(trifluoromethanesulfonyl)imide], and poly(4-styrene sulfonyl (phenylsulfonyl)imide).[8,9,13–17] However, these material systems typically exhibit ambient temperature conductivities ranging from 10^{-7} to 10^{-5} S cm^{-1},[8,9] inadequate for the desired energy and power density, and low glass transition temperature (T_g) polymers tend to have limited thermal stability and mechanical rigidity.

Recently, silica-based hybrid materials have been increasingly researched. These materials are characterized by unique conjugates of organic and inorganic materials.[18] Early endeavors in this field include the work of Zhang et al., who covalently linked silica particles with 2-acrylamido-2-methyl-1-propanesulfonic acid (AMPS), resulting in a material exhibiting room temperature conductivity of 10^{-6} S cm^{-1}.[19] Schaefer et al.[20] introduced a hybrid SSE by covalently bonding oligo-polyethylene glycol (PEG) to silica particles and doping it with Lithium bis(trifluoromethanesulfonimide) (LiTFSI). This SSE displayed an ambient ionic conductivity of 10^{-4} S cm^{-1} and significantly higher modulus compared to the material without the attached polymer. Kim et al.[1] grafted 2-[(Trifluoromethanesulfonylimido)-N-4-sulfonylphenyl] ethyl (TFSISPE) anions onto silica particles. The functionalized hybrid particles were then blended with polyethylene oxide (PEO), achieving conductivities approaching 10^{-3} S cm^{-1} at 30ºC.

3.2 Experimental procedures

3.2.1 Materials design concept

For most of the hybrid SSEs described in the literature, the load bearing aspect of the material is also delegated to the low T_g -polymer the matrix. Since ionic mobility and mechanical stiffness are opposing attributes in a material, we pursue a different hybrid SSE design, which consist of an inorganic nano-porous backbone containing an organic phase that facilitates the cation transport. The rigid porous backbone provides continuous three-dimensional network with high elastic

modulus and load bearing capability, suppressing dendrite growth, and improving the thermal stability.[21] The organic filler occupying the network pores exhibits the segmental mobility needed for establishing fast ion conduction pathways. To resolve the aforementioned cell polarization issue, we also focus on improving the t^+. Our approach is to immobilize the cation donor by attaching it directly to the structural backbone. As the cation donor we selected 2-[(Trifluoromethanesulfonylimido)-N-4-sulfonylphenyl] ethyl (TFSISPE) because of its strong electron withdrawing group that can increase the degree of charge delocalization of anions, resulting in improvement of the dissociation of Li^+ and ionic conductivity.[22] Furthermore, we introduce an oligo PEG brush that is attached to the backbone to further stabilize the organic filler, which for the present study is 600 Mw polyethylene oxide (PEO), i.e., about 14 ethylene oxide (EO) units per chain.

To assess the effect that each of these design elements has on the properties pertinent to electrolyte performance, the respective constituents have been implemented separately and in various combinations. In the following we describe the fabrication and characterization of four series of specimens. All materials contain a silica backbone and TFSISPE cation donor that is covalently bonded to one another. By changing the relative proportions of these two ingredients we control the Li^+ concentration in the material. One series of samples consists of only these two constituents at various molar ratios. These materials are referred to as monofunctionalized. In a second series we fill the pores of the monofunctionalized silica network with short-chained PEO. The PEO is not bonded to the backbone. A third series consists of the silica backbone with both TFSISPE and oligo-PEG covalently grafted on it, which we refer to as bifunctionalized. Finally, in fourth series we fill the pores of the bifunctionalized backbone with short-chained PEO. For each of these series we examine up to three different silica-to-TFSISPE molar ratios. The exact compositions are determined using thermogravimetric analysis, and for a given silica-to-TFSISPE molar ratio, the

actual Li^+ concentration depends on what additional components are included in the material (see **Table 3-1** and **Table 3-2** below). In the following, we refer to the electrolyte materials we examined based their composition, using the abbreviations $SiO_2T_xOl_y[EO]_z$, where x, y, and z designate the molar ratios of TFSISPE-to-SiO_2, EO-to SiO_2 from oligo-PEG, and EO-to-SiO_2 from PEO, respectively. The square brackets around EO signify that the short-chain PEO filling the pores are not covalently bonded to the backbone. All materials contain SiO_2 and TFSISPE, but Oligo-PEG and PEO are only mentioned if they are part of the specimens.

3.2.2 Materials synthesis

The grafting of organic components onto the inorganic backbone can be done either as a one-pot or two-step procedure.[4,19] While mixing precursors at the beginning of the one-pot approach relies on fortuitous self-assembly of the desired structure, two-step process allows for better control of structural evolution by separating backbone formation and surface functionalization.[13,15,23] The disadvantage of the one-pot approach is that the introduction of the organic phase precursor may disturb the network formation of the backbone, resulting in insufficient structural integrity. Conversely, the two-step method limits the concentration of grafting sites, as it requires diffusion of relatively large organic moieties across a porous network, which is possibly self-limited due to reaction at the pore mouths and, consequently, blocking flow into the pore.[19]

Our approach is devised to avoid these impasses through a phased combining of precursors that is carefully coordinated with the reactivities of different constituents. The backbone of the porous network is made of silica and is produced via sol-gel route using tetraethyl-orthosilicate (TEOS). The silanol groups on the pore surface provide ample reaction sites for functionalization.[24–26] Seamless integration of the ion donor is achieved by using the TFSISPE anion, which is configured with a trimethoxysilane group that reacts with the backbone silanol groups through a condensation

reaction.[1,4] To achieve the desired pore structure, the TEOS precursor must be pre-hydrolyzed and partially condensed before TFSISPE is introduced. Adding the latter too soon will stunt the formation of a three-dimensional silica network; adding it too late prevents the ion donor from permeating the pore structure evenly. Thus, the two solutions are prepared separately in a carefully phased manner so that progress along their respective reaction paths is properly synchronized. Since the oligo-PEG relies on similar grafting chemistry as TFSISPE, for those materials that contain it, oligo-PEG is introduced at the same time as TFSISPE. Finally, filler PEO (M_w = 600) is infused into the pores through fluid exchange.

Preparation of pre-hydrolyzed and lightly gelled silica backbone precursor — The preparation of the partially gelled silica backbone precursor involves mixing 29.6 ml of Tetraethyl orthosilicate (TEOS, 99%, Aldrich) with 10.1 ml of deionized water within a 100 ml beaker. A catalyst, 1.8 ml of 1M HCl, is then introduced into the mixture. The system is sealed and stirred continuously for 3 hours, allowing for complete hydrolysis of TEOS. Subsequently, the system is continuously stirred for an additional 4 hours at 65 °C, facilitating the condensation reaction.

Synthesis and pre-hydrolysis of the triethylammonium 2-[(trifluoromethanesulfonylimido)-N-4-sulfonylphenyl]ethyl-trimethoxysilane — 1 g of Trifluoromethanesulfonamide (95%, Aldrich) and 4.66 ml triethylamine (99.5%, Aldrich) are combined with 28 ml of dichloromethane (99.8%, Aldrich and vigorously stirred until dissolution is complete. Subsequently, 4.28 g of 4-[2-(trimethoxysilyl)-ethyl] benzene-1-sulfonyl chloride (50 wt% solution in dichloromethane, Aldrich) is added to the solution, followed by a 24-hour stirring period at 40°C. This yields a dark, orange-colored wax-like substance, which is further purified by vacuum drying at 85°C for 2 hours, effectively removing excessive triethylamine and residual solvents.[4]

Phased grafting of the anion group and oligo-PEG — For the grafting of these species, 0.4 g of 2-[Methoxy(polyethyleneoxy)$_{6\text{-}9}$propyl] trimethoxysilane (oligo-PEG) and 3.0 g of TFSISPE ion donor are mixed with 0.55 ml water and 1.4 ml ethanol. The mixture is heated to 45°C for 2.5 h for prehydrolyzation. Subsequently, this pre-hydrolyzed mixture is combined with different amounts of the partially gelled backbone precursor to achieve different Li^+ concentrations in the final product. The specific amount added, which ranges between 5 and 21 ml, serves to control the cation donor, and thus, the Li^+ concentration in the electrolyte. The resulting mixture is maintained at 65°C for 30 minutes, while continuously stirred. Following this, the viscous solution is cast into a plastic container, where gelation occurs. After gelation, the gel is aged in an oven at 50°C for 24 hours, resulting in a transparent, orange-colored functionalized silica backbone. To ensure purity, the backbone is thoroughly washed with deionized water and ethanol to remove any excessive trifluoromethanesulfonamide, triethylamine, unattached TFSISPE or oligo-PEG, and unreacted TEOS.

Ion exchange and polymer penetration — An ion exchange solution is prepared by dissolving 0.1 g Lithium hydroxide (LiOH, 98%, Aldrich) in 100 ml of deionized water. The ion exchange process is initiated by immersing the aged backbone in this LiOH solution for 1 hour, during which the triethylammonium cation is displaced by Li^+ ions. Following this, the backbone undergoes further purification involving rinsing with deionized water and ethanol for a total duration of 2 hours to eliminate any residual LiOH. Subsequently, the backbone is immersed in 50 ml of molten filler PEO (Molecular weight = 600, Aldrich) at 45°C for 12 hours. The final product is then subjected to vacuum drying at 50°C for 24 hours.

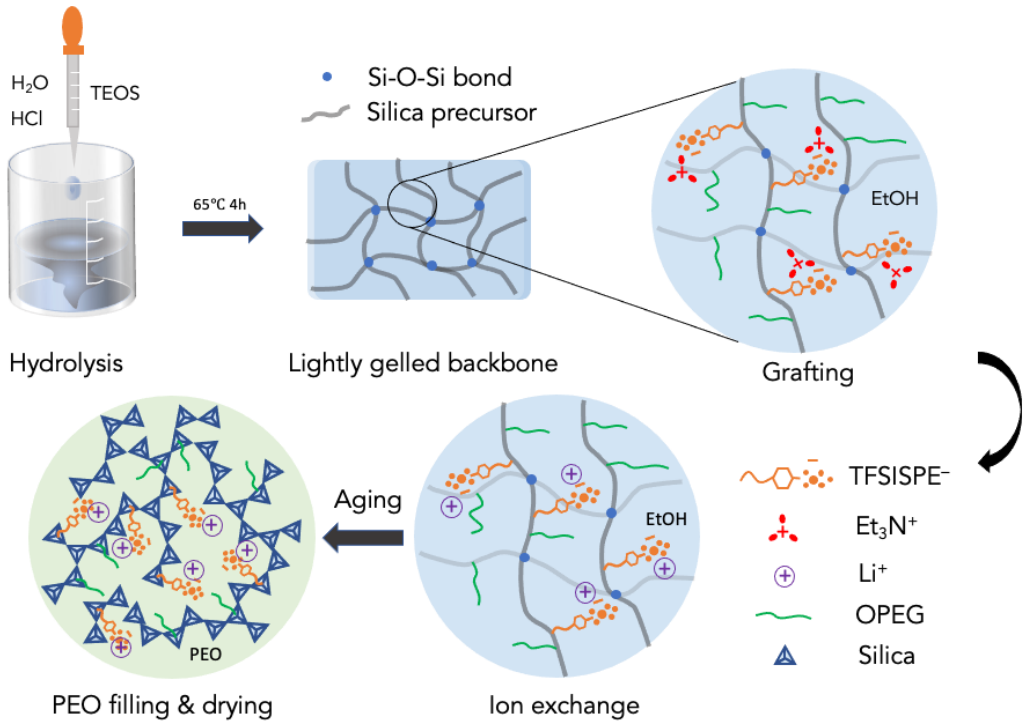

Figure 3-1 Schematic illustrating the synthesis procedure for hybrid silica-PEO electrolytes.

3.2.3 Characterization techniques

The ionic conductivity measurements are measured using a Novocontrol broadband dielectric impedance spectrometer (DIS). Two polished stainless-steel discs serve as blocking electrodes, between which the sample is sandwiched.[27] Measurements cover a temperature range from 5°C to 70°C, and a frequency range from 0.1 Hz to 10 MHz. Infrared spectra were captured utilizing a Jasco FT/IR-4100 spectrometer within the 600-4000 cm^{-1} frequency range. The surface and cross section morphologies of the composite electrolyte are determined via scanning electron microscopy (SEM) using the Tescan NIRA3 instrument. To this end, samples are sputter coated with platinum at 5×10^{-2} mbar and 25°C for 2 min. prior to the SEM analysis. Differential scanning calorimetry (DSC) is determined using the TA Instruments Discovery DSC, by performing temperature scans from –60°C to 200°C at a heating rate of 10 $K \cdot min^{-1}$ for two cycles. Glass transition temperatures (T_g) are identified at the midpoint of characteristic steps. Thermogravimetric analysis (TGA) is

performed using the TA Instruments Discovery TGA, scanning samples from 50°C to 700°C at a heating rate of 7 $K \cdot min^{-1}$, while under an N_2 atmosphere. The lithium-ion transference number are determined by employing the Bruce-Vincent method,[28] which combines DC polarization and AC impedance measurements. Additional details of these procedures that may be relevant to the interpretation of the results are provided in subsequent sections.

3.3 Results and discussion

Using the above characterization techniques we probe our materials for their chemical composition, pore structure, and thermal properties, which we employ to interpret trends observed in the measured ionic conductivities and to identify the most effective materials design criteria for enhancing Li^+ cation mobility and transference numbers, while maintaining mechanical and electrochemical stability of the electrolyte.

3.3.1 FTIR

In **Figure 3-2** we compare the FTIR spectra of the materials we synthesize with those of the various chemical constituents used for their synthesis, including neat silica gel, TFSISPE ion donor, Et_3NHCl, PEO (M_w = 600 g/mol), as well as the hybrid samples. This comparison allows us to identify the structural entities that prevail in the final product and to what extent their vibrational behavior has changed upon incorporation into the hybrid configuration. We first discuss the spectra of the neat constituents. The spectrum for the silica gel (**Figure 3-2**(a)) exhibits a broad absorption band in the range of 3200–3500 cm^{-1}, which is attributed to O-H stretching vibrations. Additional features include the asymmetric Si-O stretching vibration at 1000-1100 cm^{-1}, peaks at 960 cm^{-1} corresponding to Si-OH and SiO-H stretching motion of terminal silanol, and symmetric Si-O stretching vibrations at 800 cm^{-1}.[29] Specifically, the Si-O-Si band observed in the FTIR spectrum of silica gel is much broader than that of quartz. The widening of this band can be attributed to the

large specific surface area of silica gels, because at the pore surface the Si-O-Si linkage likely incurs a greater number of defects that are terminated in –OH groups.[30]

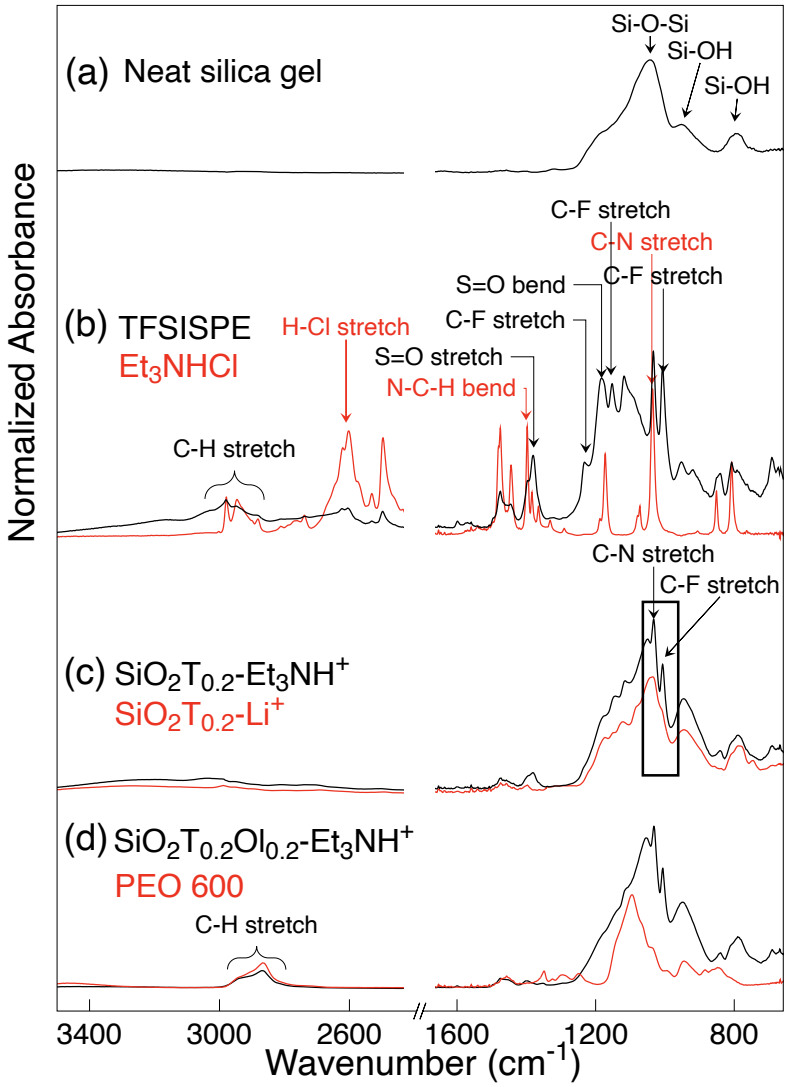

Figure 3-2 FTIR spectra of (a) neat silica gel; (b) TFSISPE ion donor and Et_3NHCl byproduct; (c) $SiO_2T_{0.2}$-Et_3NH^+ (before ion exchange) and $SiO_2T_{0.2}$-Li^+ (after ion exchange) monofunctionalized samples; and (d) $SiO_2T_{0.2}Ol_{0.2}$-Et_3NH^+ bifunctionalized sample. The spectrum of PEO (Mw = 600 g mol^{-1}) is superimposed in part (d) to demonstrate the C-H stretching vibration peaks of the ethylene oxide repeat unit.

In the spectrum of freshly synthesized TFSISPE ion donor, the stretching vibration associated with the O=S=O functional groups occurs at 1380 cm^{-1}, the O=S=O bending mode at 1181 cm^{-1}, the vibrations associated with C–F stretching at 1235 cm^{-1} and 1152 cm^{-1}, while C-H stretching

vibrations are manifest in the 2860-3050 cm^{-1} range. These vibrational modes, which are consistent with the findings reported by Rey et al., [31] clearly identify the molecular structure of TFSISPE. During the synthesis of the TFSISPE ion donor, Et_3NHCl is generated as byproduct. The FTIR spectrum of Et_3NHCl reveals distinctive features, such as the C-N stretching mode at 1035 cm^{-1}, the C-H stretching vibrations spanning the range of 2850-3000 cm^{-1}, and the N-C-H bending vibrations at 1400 cm^{-1}. Notably, the signature of N-H stretching vibration, which would manifest at around 3400 cm^{-1} for the primary amine and 3300 cm^{-1} for the secondary amine is absent, consistent with the chemical structure. The prominent broad band emerging at approximately 2600 cm^{-1} is due to the hydrochloride. As can be seen in **Figure 3-2**(b), several peaks in the spectrum of TFSISPE appear at the same spectral positions as in that of Et_3NHCl, notably between 2500 and 2700 $cm^{-1}$and between 1400 and 1500 cm^{-1}. This is due to the remanent Et_3NHCl byproduct in the as-synthesized ion donor; it is removed in subsequent washing steps.

Figure 3-2(c) shows the IR spectrum of the monofunctionalized sample denoted as $SiO_2T_{0.2}$-Et_3NH^+. In this material the TFSISPE group is covalently grafted to the silica backbone but, as the suffix 'Et_3NH^+' indicates, the cation type is still the pre-ion exchange triethylamine group. The spectrum of $SiO_2T_{0.2}$-Et_3NH^+ consists of an amalgamation of the spectra of the underlying TFSISPE and silica gel constituents, with the dominant features of the latter two clearly identifiable. A similar rationale applies to the $SiO_2T_{0.2}Ol_{0.2}$-Et_3NH^+ spectrum shown in **Figure 3-2**(d). The essential differences between $SiO_2T_{0.2}$ and $SiO_2T_{0.2}Ol_{0.2}$ are manifest in the 2800-3000 cm^{-1} range—a spectral region, primarily governed by the stretching vibrations of C-H groups within the Oligo PEG component. These C-H stretching vibration peaks are characteristic of the ethylene oxide repeat unit. To demonstrate, we superimposed the spectrum of PEO (M_w = 600 g/mol) in this figure.

The post-grafting of washing and ion exchange steps are intended to eliminate the residual Et_3NHCl byproduct and replace Et_3NH^+ with Li^+ ions. The effectiveness of these steps can be gauged by comparing the spectra of $SiO_2T_{0.2}$-Et_3NH^+ and $SiO_2T_{0.2}$-Li^+ shown in **Figure 3-2**(c). The latter represents the hybrid sample after washing and ion exchange, for which we point out the conspicuous absence of the robust C-N stretching peak characteristic of Et_3NH^+ at 1035 cm^{-1}. This confirms the successful removal of both Et_3NH^+ and Et_3NHCl. Furthermore, the C-F stretching band, located at 1005 cm^{-1} for the TFSISPE molecule is almost entirely suppressed in the $SiO_2T_{0.2}$-Li^+ spectrum. This suggests a decrease in the concentration of -CF_3 groups, which can be attributed to the removal of surplus trifluoromethanesulfonamide introduced during the ion donor synthesis.

3.3.2 TGA analysis

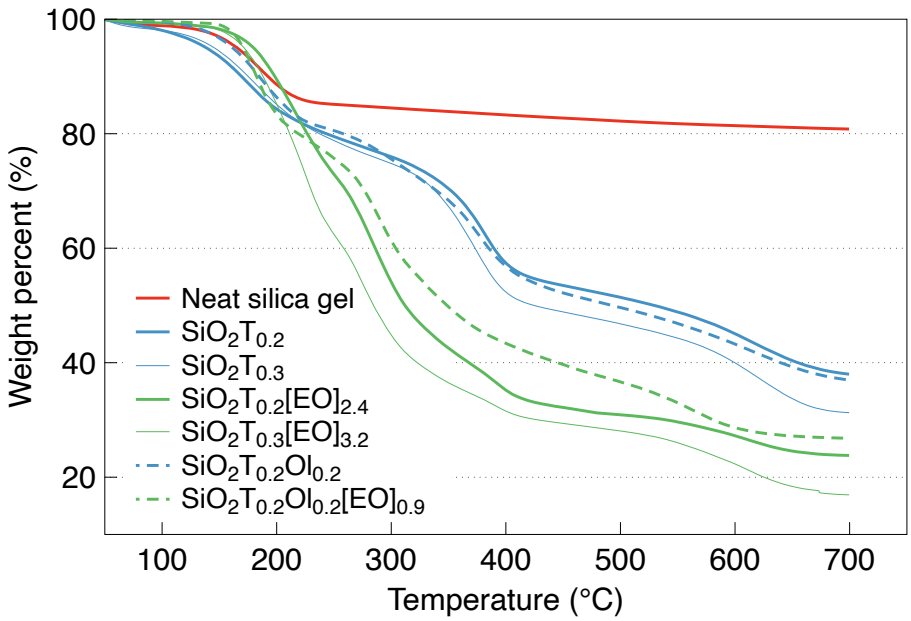

Figure 3-3 Thermogravimetric analysis an traces for neat silica gel, monofunctionalized and bifunctionalized samples, and composite electrolytes, showing the weight loss of these species as a function of temperature when heat at 7ºC·min^{-1}.

TGA data reported here correspond to samples that underwent post-grafting washing procedures to eliminate Et_3NHCl and trifluoromethanesulfonamide. Note that these samples were not yet

subjected to ion exchange. TGA results for silica gel, hybrid samples both with and without short-chain PEO filling the pores are illustrated in **Figure 3-3**. The primary objective of TGA analysis is to determine composition of the materials under investigation. In the case of silica gel, the initial reduction in weight by approximately 1 wt% observed in the TGA curve, corresponds to the removal of adsorbed moisture and chemisorbed water from the porous structure. Subsequently, a weight loss event occurs around 180°C is characteristic of acid-catalyzed gels. This phenomenon arises from the decomposition of the residual Si-OEt groups and liberate ethanol, as elucidated in previous studies.[29] The cumulative weight loss for silica gel, up to 700°C, amounts to approximately 19%. This substantial weight loss is in alignment with existing literature findings; it is emblematic of the porous nature of silica gel and the abundance of surface Si-OEt groups within its structure.[29] In the TGA profiles of the hybrid samples, namely $SiO_2T_{0.3}$, $SiO_2T_{0.2}$, and $SiO_2T_{0.2}Ol_{0.2}$, a distinctive weight loss commencing around 180°C is observed. This phenomenon can be attributed to the decomposition of Et_3NH^+ ions and the concurrent release of H^+ ions, a process accompanied by the liberation of Et_3N. Meanwhile, the primary TFSISPE anion undergoes a two-step decomposition. Initially, the tail TFSI structure degrades around 380°C, followed by the decomposition of the alkyl linker at approximately 550°C, as reported in prior studies.[32] For samples containing PEO (Molecular Weight = 600 g mol^{-1}), namely $SiO_2T_{0.3}[EO]_{3.2}$, $SiO_2T_{0.2}[EO]_{2.4}$, and $SiO_2T_{0.2}Ol_{0.2}[EO]_{0.9}$, the decomposition of the polymer also occurs in two distinct stages, spanning temperature ranges of 180°C – 250°C and 270°C – 450°C. The calculation of weight fractions for each component relies on the fact that the TGA weight loss observed at each step can be attributed to the weight loss of individual components within each temperature intervals. This allows the formulation of a system equation that can be systematically solved. The details pertaining to these calculations are available in the **Appendix D**, and the resulting weight fractions are provided in **Table 3-1**.

Table 3-1 Summary of the TGA derived components weight fractions result; ω_{13} , and ω_{14} are fitting parameters governing the ratio of mass loss of PEO in stage 1 and 2, and the ratio of mass loss of Oligo PEG in stage 1 and 2, respectively

	m_{Et}	m_T	m_P	m_{Ol}	m_{SiO2}	ω_{13}	ω_{14}
$SiO_2T_{0.3}$	10.88	58.34			30		
$SiO_2T_{0.3}[EO]_{3.2}$	5.63	37.28	40.32		17.05	0.6	
$SiO_2T_{0.2}$	13.64	49.07			37.5		
$SiO_2T_{0.2}[EO]_{2.4}$	8.18	29.55	39.84		22.57	0.28	
$SiO_2T_{0.1}$	10.83	35.64			53.09		
$SiO_2T_{0.1}[EO]_{1.9}$	6.04	24.03	41.33		29.32	0.892	
$SiO_2T_{0.2}Ol_{0.2}$	6.12	52.51		6.04	35.22		0.17
$SiO_2T_{0.2}Ol_{0.2}[EO]_{0.9}$	5.27	44.3	18.79	4.41	27.6	0.34	0.65
$SiO_2T_{0.1}Ol_{0.1}$	7.56	37.22		5.01	50.1		0.35
$SiO_2T_{0.1}Ol_{0.1}[EO]_{0.7}$	5.3	31.6	19.57	3.9	40.36	0.26	0.71

The symbols m_{SiO2}, m_{Et}, m_T, m_P, and m_{Ol} represent the mass losses of the constituents identified by the subscripts, where SiO_2, Et, T, P, Ol, stand for silica, ethanol, TFSISPE, PEO, Oligo PEG, respectively. The symbols ω_{13} , and ω_{14} are fitting parameters governing the ratio of mass loss of PEO in stage 1 and 2, and the ratio of mass loss of Oligo PEG in stage 1 and 2, respectively.

Our calculations reveal that in composite samples devoid of Oligo PEG, denoted as $SiO_2T_{0.3}[EO]_{3.2}$, $SiO_2T_{0.2}[EO]_{2.4}$, and $SiO_2T_{0.1}[EO]_{1.9}$, the PEO contents (m_P) remain consistently close, hovering around the 40 wt%. In contrast, a discernible reduction in m_P is apparent in the $SiO_2T_{0.2}Ol_{0.2}[EO]_{0.9}$ and $SiO_2T_{0.1}Ol_{0.1}[EO]_{0.7}$ samples. This effect is likely attributed to structural modifications within the pore network induced by grafting of Oligo PEO. Furthermore, according to our TGA results, composite samples exhibit minimal weight loss at temperature below 110°C. This observation underscores the heightened thermal stability of our system in comparison to conventional liquid and gel-type electrolytes, which is promising for practical applications of our material.[14,15,17,23,33]

While the TGA results provide weight fractions for each component within the composite samples, in view of assessing cation mobilities it is useful to convert these quantities into molar

concentrations or number densities expressed in units of molecules per cubic nanometer (molecules/nm³). The conversion process is straightforward, except that adhering to the convention of choosing the molecular weight of PEO as the mass of the entire chain would project the role of the polymer onto length scales that are not relevant to the elementary atomic transport process. In our conversion, we therefore choose the molecular weight of PEO as that of the ethylene oxide repeat unit (EO) rather than its total molecular weight. A comprehensive description of the conversion process can be found in the **Appendix C**. The result of the conversion is listed in **Table 3-2**.

Table 3-2 Summary of the number densities (molecules/nm³) of components in hybrid materials

	ρ (kg/m3)	EtOH	TFSISPE	EO	Oligo PEG	SiO_2
$SiO_2T_{0.3}[EO]_{3.2}$	1433.7	2.69	0.77	7.89		2.45
$SiO_2T_{0.2}[EO]_{2.4}$	1462.2	4.0	0.62	7.96		3.31
$SiO_2T_{0.1}[EO]_{1.9}$	1467	2.94	0.51	8.24		4.29
$SiO_2T0.2Ol_{0.2}[EO]_{0.9}$	1577.2	2.77	1.01	4.04	0.95	4.35
$SiO_2T_{0.1}Ol_{0.1}[EO]_{0.7}$	1604.9	2.83	0.73	4.27	0.85	6.46

3.3.3 SEM

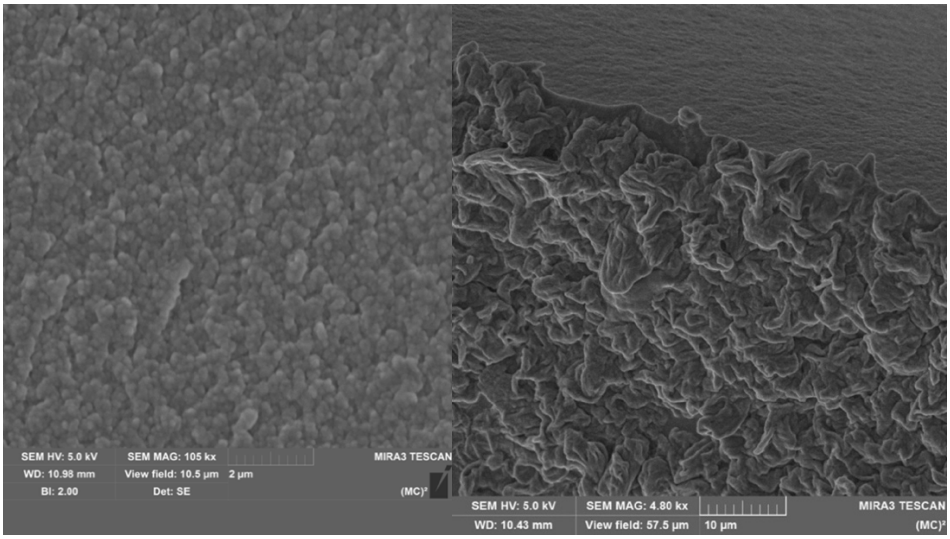

Figure 3-4 SEM images of intersection and surface morphology for hybrid material $SiO_2T_{0.2}Ol_{0.2}[EO]_{0.9}$.

The morphology of the hybrid electrolytes is analyzed by using scanning electron microscopy (SEM). **Figure 3-4** shows the cross-sectional view and surface characteristics of the $SiO_2T_{0.2}Ol_{0.2}[EO]_{0.9}$ material. The cleaving of the specimens occurs during the sputter coating process as a result of plasma-induced cracking of the material. This cross-section clearly reveals a three-dimensional network structure composed of nodular entities that coalesced together, indicative of an uninterrupted sequence of particle seeding, growth, and aggregation during the gelation process.[29,34,35] Individual nodules measure between 100 and 300 nm in diameter. The resolution constraints prevent the identification of internal structures within the nodules, so we cannot confirm whether they comprise smaller clusters. The interstitial channels and pores between the nanoparticles measure approximately 100 nm across, while smaller pores remain indiscernible. These intervening spaces are filled with filler PEO and grafted organic materials, without any observable hollow pores. Notably, the SEM image, acquired under high vacuum, show no signs of component vaporization, serving as direct evidence for the higher vacuum stability of our materials compared to conventional organic liquid electrolytes. On the sample surface, a flake-stacking structure is apparent. Note that the plasma employed for coating causes some surface damage, leading to peeling and the formation of irregularities resembling fish scales. As a result, the surface morphology image may be less representative of the true surface features.

3.3.4 DSC

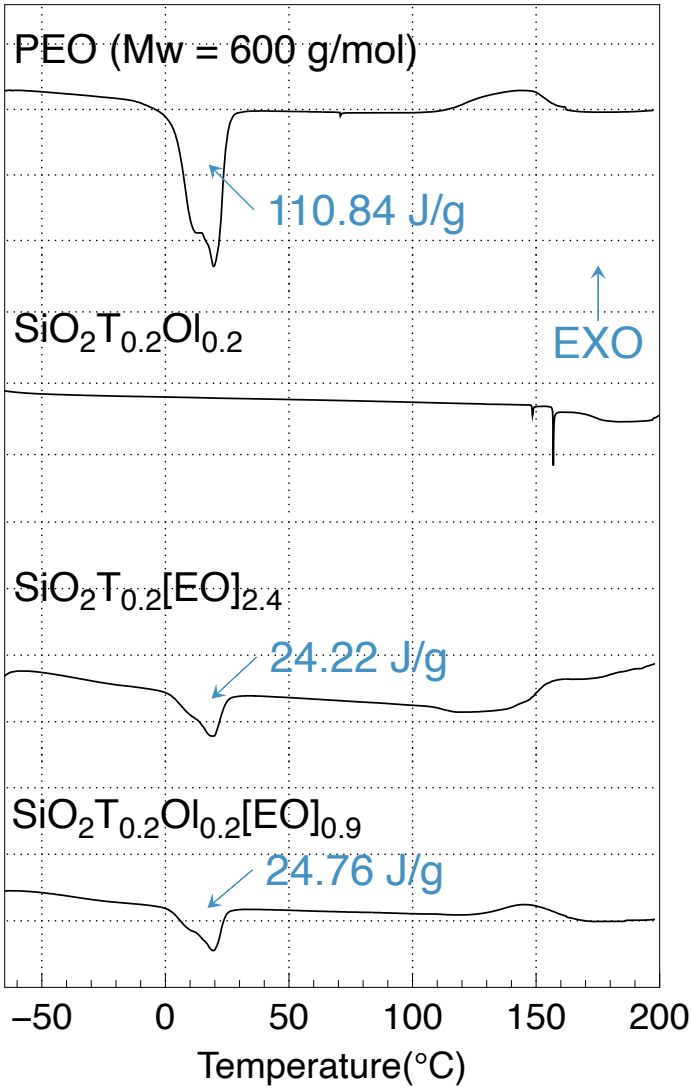

Figure 3-5 DSC thermograms of selected functionalized hybrid backbones $SiO_2T_{0.2}Ol_{0.2}$ with unfilled pores and hybrids with PEO occupying the pores $SiO_2T_{0.2}[EO]_{2.4}$ and $SiO_2T_{0.2}Ol_{0.2}[EO]_{0.9}$.

The DSC traces, illustrated in **Figure 3-5**, furnish insights into the thermal attributes of the materials under scrutiny. We compare traces for PEO (Mw = 600 g mol^{-1}), functionalized hybrid backbones $SiO_2T_{0.2}Ol_{0.2}$ with unfilled pores and hybrids with PEO occupying the pores $SiO_2T_{0.2}[EO]_{2.4}$ and $SiO_2T_{0.2}Ol_{0.2}[EO]_{0.9}$. Significantly, for the $SiO_2T_{0.2}Ol_{0.2}$ hybrid material, no glass transition temperature, T_g, for either the silica phase or the grafted organic constituents could be discerned

within the temperature range probed. Indeed, T_g for silica is expected at elevated temperature beyond the capability of the DSC instrument we used, while the grafted oligomer and TFSISPE do not form an adequate contiguous phase. This is consistent with the findings by Vrandečić et al., report the elusiveness of T_g for oligo PEG.[36] However, our DSC trace of $SiO_2T_{0.2}Ol_{0.2}$ reveals a sequence of sharply defined endothermal peaks in the temperature range of 150-200 °C. These sharp peaks are highly reproducible, persistent through consecutive scans, albeit with a gradual waning in intensity. The presence of these sharp peaks indicates rapid events, while their gradual reduction in intensity during successive scans suggests an only partially irreversible process. A similar observation of a broad band in the range of 160-200 °C has previously been documented by Rubio et al. for silica gel samples subjected to extended drying periods. [37] In this matter, the TGA analysis of $SiO_2T_{0.2}Ol_{0.2}$ provides complementary information in that it reveals a weight loss initiation at around 100°C, attributed to the commencement of decomposition reaction involving Si-OEt groups. These reactions result in the release of ethanol as a byproduct, consistent with established literature findings.[29] We therefore surmise that the sharp peaks and broad band observed in the DSC of $SiO_2T_{0.2}Ol_{0.2}$ can be linked to the removal of ethanol originating from these decomposition reactions.[37] The repeated appearance of these features during successive scans can be attributed to the recombination of ethanol with highly strained Si-O-Si surface groups. The decrease in peak intensities likely results from a diminishing population of such surface Si-O-Si groups due gradual relaxation of the silica network.

In the PEO trace, the endothermal peak observed around 20°C corresponds to the melting of crystalline domains. Interestingly, this melting peak is split into two adjoining peaks, which may be attributed to different levels of confinement of PEO in silica network pores, which exhibits a wide pore size distribution, causing crystallites to melt at distinct temperatures depending of the size of

the pore they are confined to. The broad exothermal peak centered around 145°C indicates some form of degradation within the PEO.

Melting peaks attributable to PEO are also present in the traces of $SiO_2T_{0.2}[EO]_{2.4}$ and $SiO_2T_{0.2}Ol_{0.2}[EO]_{0.9}$, with melting enthalpies of 24.2 J g^{-1} and 24.76 J g^{-1}, respectively. Taking the PEO weight fraction in these composite samples into consideration, the calculated melting enthalpies for the PEO phase in $SiO_2T_{0.2}[EO]_{2.4}$ and $SiO_2T_{0.2}Ol_{0.2}[EO]_{0.9}$ are 60.74 J g^{-1} and 106.72 J g^{-1}, respectively, which are both lower than the value of 110.84 J g^{-1} for the pure filler PEO. Since these enthalpies are normalized with respect to the sample weight, we interpret these differences in melting enthalpy as reflecting the different degrees of crystallinity. Accordingly, the immediate understanding this observation conveys is that the presence of the backbone suppresses the crystallization of PEO. Furthermore, contrary to conventional wisdom, even with a relatively low weight fraction, grafted oligo PEG appears to interact with PEO in a manner that promotes crystallinity. This is particularly intriguing given that $SiO_2T_{0.2}Ol_{0.2}[EO]_{0.9}$, which contains oligo PEG, has smaller pore sizes compared to $SiO_2T_{0.3}[EO]_{3.2}$. Smaller pores are more inclined to impede polymer chain organization, thereby restraining the formation of crystalline structures. Furthermore, the sharp peaks observed in $SiO_2T_{0.2}Ol_{0.2}$ are absent in both $SiO_2T_{0.2}[EO]_{2.4}$ and $SiO_2T_{0.2}Ol_{0.2}[EO]_{0.9}$. The observed disparity may be ascribed to the phenomenon wherein ethanol, resulting from decomposition reactions, forms hydrogen bonds with the oxygen atoms in the PEO chain. Therefore, the heat released during the formation of these hydrogen bonds partially compensates for the energy required for decomposition. Such compensation cause the observed peaks to be not as well defined. Regarding the exothermal band in materials containing PEO, we note that the band in $SiO_2T_{0.2}Ol_{0.2}[EO]_{0.9}$ resembles that of pure PEO, albeit the onset temperature is shifted from 110°C to around 130°C. However, in $SiO_2T_{0.2}[EO]_{2.4}$ the curve starts to deviate negatively from the baseline at 110°C (endothermal), which might due to the start of decomposition of constituents, and

reverts to exothermal as the temperature rises. The small endothermal feature in this trace suggests that the oligo PEG-grafted ($SiO_2T_{0.2}Ol_{0.2}[EO]_{0.9}$) exhibits superior thermal stability compared to the one without oligo PEG ($SiO_2T_{0.2}[EO]_{2.4}$). This improvement may be attributed to smaller pore sizes in the backbone of oligo PEG-grafted sample. Nevertheless, whether oligo PEG itself contributes to stabilizing the PEO phase remains an open question.

3.3.5 DIS

The determination of Li^+ ionic conductivity is derived from the following equation,

$$\sigma = L / (R_b \cdot S), \tag{3-2}$$

where σ represents the ionic conductivity, S denotes the cross-sectional area of the sample, L represents the sample thickness, and R_b is the d.c. Ohmic resistance of the sample. R_b is conveniently determined from a Cole-Cole plot of the measured complex impedance, where the imaginary component is drawn vs. the real component of the impedance. The dielectric response of most solid electrolytes can be modeled using a two-element equivalent circuit connected in series, one of which consisting of a capacitance and an Ohmic resistance in parallel and the other on corresponding to the Warburg resistance.[16,38] The Cole-Cole plot for such an equivalent circuit exhibits a semicircular arc for the high-frequency response and a low-frequency tail that reflecting the balance between charge polarization and diffusive dissipation in the material (Warburg resistance). The quantity R_b is determined as the intersection of the semicircle that fits the high frequency with the real component axis of the Cole-Cole plot.[16,39]

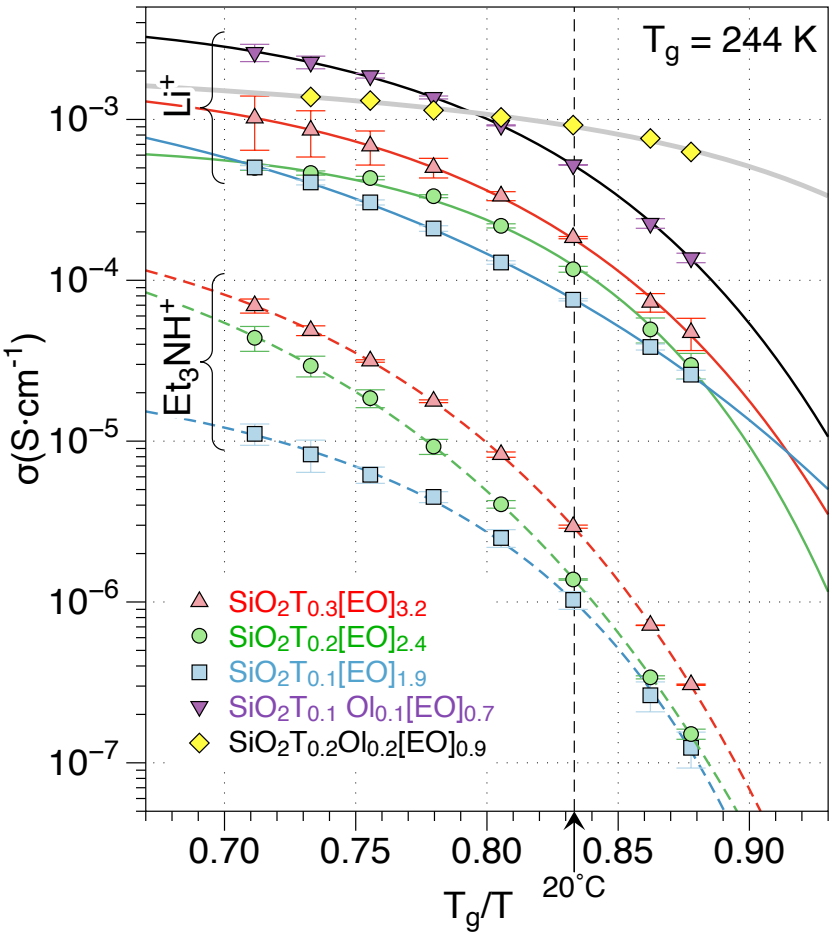

Figure 3-6 Temperature dependance ionic conductivities for hybrid materials with different ion types (Li^+ or Et_3NH^+) and ion donor concentration, with or without Oligo-PEG grafting.

Figure 3-6 provides a summary of the temperature dependence of ionic conductivity. We compare results for materials with three different cation donor grafting densities, and consequently cation concentrations, before and after exchanging the Et_3NH^+ group with Li^+ cations. The figure also includes data for systems with grafted oligo-PEG for comparison. Notably, samples with the same ion concentration but differing in ion type, bundle into two different groups identified by a curly bracket and labeled as Et_3NH^+ and Li^+, respectively. Their respective ionic conductivities differ by roughly two orders of magnitude. This comparison between Li^+ and the bulkier trimethylammonium cation (Et_3NH^+) demonstrates the effect that cation size has on the cation

mobility. The molecular masses of Li^+ and Et_3NH^+ differ by approximately one order of magnitude, based on which one could estimate the attempt frequency for cation hopping of Li^+ to surpass that of Et_3NH^+ by a factor of 3.2. However, the measure conductivities in the systems containing Li^+ exceed those of the those containing Et_3NH^+ by a factor of 20 to 200, depending on concentration and temperature. Hence, the mass difference between charge carriers accounts only for a minor fraction of the conductivity increase. Accordingly, the more significant contribution is due to steric hinderance and the associated activation barrier heights.

The activation free energy for cation transport is a measure that reflects the energy landscape of the system, which in turn is representative of the molecular configuration and interactions between constituents. It is therefore an important attribute in view of elucidating elementary transport mechanisms. As evident from the data shown in **Figure 3-6**, ln σT *vs.* T^{-1} does not exhibit Arrhenius behavior, and the empirical formalisms commonly employed to capture the curvature in the data do not yield the activation enthalpies or entropies as fitting parameters. Here we employ a new approach we developed based on transition state theory (TST), which accounts for the non-Arrhenius behavior in the temperature dependence of conductivity that is characteristic for many glass forming materials above the glass transition temperature. As the supercooled liquid traverses the glass transition regime, structural rearrangements that involve gradual shifts in molecular packing density and reconfiguration of atomic interaction topology are accompanied by changes in the free energy landscape. Changes in the activation enthalpy and entropy for atomic transport processes are consequentially manifest. A detailed discussion of the rationale behind our correlative activation free energy (CAFE) model can be found in our earlier publication.[40] We begin with the basic formalism for ionic conductivity expressed in the context of TST,[41]

$$\sigma = \frac{\rho_{Li^+}\left(zq_e\right)^2}{k_B T}\gamma d_0^2 \Gamma_0 e^{S_a(T)/k_B} e^{-E_a(T)/k_B T}, \quad (3\text{-}3)$$

where ρ_{Li^+} is the volumetric number density of cations, z is its valence, q_e is electronic unit charge, k_B is the Boltzmann factor, γ is the geometry factor, which is equal to one over twice the dimensionality of the underlying space, d_0 is the cation jump distance and Γ_0 is the attempt frequency. E_a and S_a are the activation enthalpy and entropy, respectively. The main difference compared to the basic formulation of this expression is that E_a and S_a are assumed to be temperature dependent. Specifically, expressing these quantities as a function of the reciprocal temperature normalized with respect to T_g, i.e., $\chi = T_g/T$, $E_a(\chi) = \psi(\chi)(E_G - E_0) + E_0 = \psi(\chi)\Delta E_a + E_0$, where E_G and E_0 represent activation enthalpies for cation migration in the material at T_g and at infinite temperature, respectively. Similarly, $S_a(\chi)$ takes a similar form $S_a(\chi) = \psi(\chi)\Delta S_a + S_0$. Here, $\psi(\chi)$ is the generalized logistic function $\psi(\chi) = \left(1 + C_0 e^{\nu\beta_g H(1-\chi)}\right)^{-1/\nu}$, which is adopted to capture the change in free energy landscape during the transition behavior between liquid and glass states. It exhibits a skewed sigmoidal shape, governed by parameters H, ν, and $\beta_g = \left(N_A\, k_B\, T_g\right)^{-1}$, controlling the steepness, asymmetry, and inflection point of the curve, respectively. C_0 is a constant determined by the value of $\psi(\chi)$ at $\chi = 1$. Substituting, multiplying both sides with the temperature, and taking the logarithm yields

$$\ln(\sigma T) = P + S_0/k_B + \psi(\chi)(\Delta S_a/k_B - \chi\Delta E_a) - \chi E_0, \quad (3\text{-}4)$$

where we grouped temperature independent terms from the pre-factor as $P = \ln\left(\rho_{Li^+}\left(zq_e\right)^2 \gamma d_0^2 \Gamma_0 k_B^{-1}\right)$.

Note that our analysis is distinct from the notion that the relaxation of disordered structures is governed by a distribution of activation energies to account for the fact that multiple relaxation mechanisms coexist. This concept results in a linear combination of Boltzmann factors, one for

each relaxation mechanism, which cannot describe the negative curvature observed for $\ln(\sigma T)$ vs. $1/T$ data. However, our analysis can be adapted to account for such an activation energy distribution, if necessary.

The lines in **Figure 3-6** represent the best fits of the data using the CAFE model. The dashed and solid lines identify systems with Et_3NH^+ and Li^+ as the cation, respectively. The data fitting was carried out using an interior point method with the non-linear constraints $H\Delta S_a/k_B^2T_g - \Delta E_a/k_BT_g - E_0/k_BT_g e^{H/k_B} < 0$ and $H\Delta S_a/k_B^2T_g - 2\Delta E_a/k_BT_g < 0$, which are imposed so that the slope and curvature of function expressed by Equation (3-3) are negative for all values $0 \leq \chi \leq 1$. Positive values would imply extrema and inflection points, which would be physically unrealistic. From the data fitting we can extract the values for the $P+S_0/k_B$, ΔS_a, E_0, ΔE_a, and H. Note that the first of these parameters consists of two terms, P and S_0/k_B. The relative contribution of either term cannot be determined based on the measure conductivity data alone. However, the values of z, q_e, γ, and k_B are known, and that of ρ_{Li^+} is determined using thermogravimetric analysis (see **Table 3-3**). This leaves d_0 and Γ_0 as unknown quantities making up P. The jump distance can be readily assessed for crystalline materials, where cation sites are defined witin a periodic lattice structure. It is less obvious for amorphous materials. However, based on our molecular dynamics simulations of comparable systems, we understand that cation transport in amorphous structures also occurs via a hopping mechanism and typical jump distances are of the order of interatomic spacings or slightly below[42]. Hence we estimate d_0 between 1 and 2 Å. The attempt frequency is often gauged using the relationship $\Gamma_0 \simeq k_B\theta_D/h$, where θ_D is the Debeye frequency and h is Planck's constant. For short-chain linear polymers, $\theta_D \simeq 50$ K,[43] $\Gamma_0 \simeq 10^{12}$ Hz. This approach, however, is rather arbitrary; there is no physics-based argument as to whether this particular frequency, which is one of many that are accessible to the system, is indeed the decisive one from a hopping mechanistic perspective.

Furthermore, if we were to assume $\Gamma_0 = 10^{12}$ Hz, then the balance between P and S_0/k_B would result in a negative activation entropy in some cases. Considering that the construct of extrapolating $\ln(\sigma T)$ vs. $1/T$ to infinite temperature to determine $P+S_0/k_B$ is based on the assumption that the material preserves its condensed liquid phase character, characterized by a finite density, a negative activation entropy is not expected by any common practice method for evaluating this quantity. To illustrate, consider an instantaneous snapshot of the structure of a high-temperature liquid, and allow it to expand until the potential energy landscape is essentially flat in between atoms, which is when the activation entropy would drop to zero. The density of such a configuration would be that of a rarified gas, which is contrary to the assumption of TST, even at infinite temperature. In our analysis, we do not constrain the value of the fitting parameter $P+S_0/k_B$, but in deconstructing this quantity we require that $S_0 \geq 0$ and report the quantity $d_0^2\Gamma_0$ in **Table 3-3**.

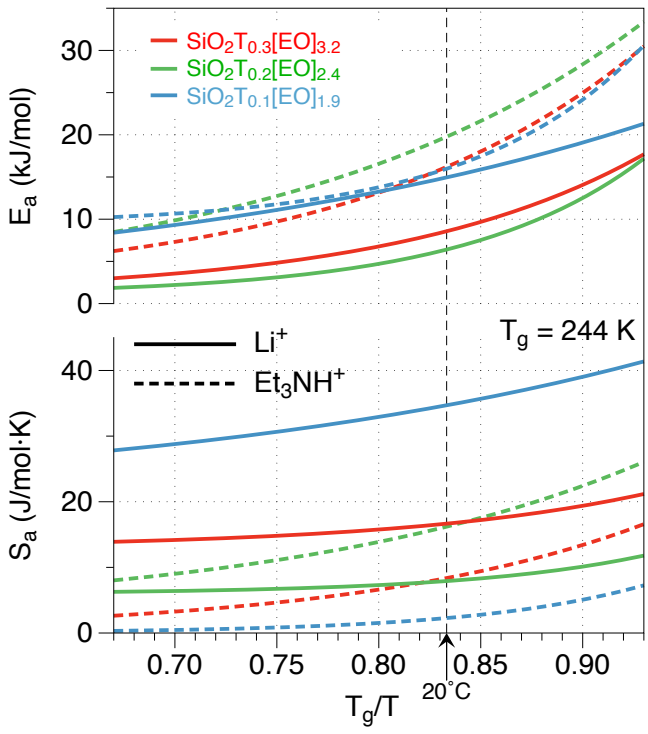

Figure 3-7 (a) Activation entropies, S_a, and (b) activation enthalpies E_a as a function of the reciprocal temperature, as determined using the CAFE model. The solid and dotted curves correspond to samples with Li^+ or Et_3NH^+ as charge carriers.

Based on this premise, we are now able to compute the activation enthalpies and entropies as a function of the normalized reciprocal temperature, shown in **Figure 3-7**. Different ion donor concentrations are distinguished by color, while solid and dashed curves represent samples with Li^+ or Et_3NH^+ as charge carriers, respectively. Generally, systems containing Et_3NH^+ exhibit higher activation enthalpies and lower activation entropies compared to those containing Li^+, which is to be expected based on the difference in cation size and structural complexity. The former also show a more pronounced relative increase in these quantities with decreasing temperature, indicating more substantial structural changes throughout the glass transition regime exerting a commensurate influence on cation mobility. While the relative magnitudes of both activation enthalpies and entropies between different compositions within each group are preserved over the temperature range explored by our measurements, i.e., solid or dashed lines do not cross one another, the magnitudes do not change monotonically as a function of the cation concentration. The highest activation enthalpies and entropies are observed in the system with the lowest cation concentration, whereas the lowest activation enthalpies and entropies are found for the system with intermediate cation concentration. We point out that high activation enthalpies are typically accompanied by high activation entropies, which have opposing effects on the cation mobility. The two measures must therefore be considered concurrently to correctly assess the effects of structural or compositional changes on ionic conductivity.

Table 3-3 Summary of calculated Li^+ mobilities in hybrid materials with different constituents

Composition	Ion donor number density (nm^{-3})	conductivity (S cm^{-1}) at 20 °C	Li^+ mobility (S cm^2 C^{-1})	Li^+ $d_0^2\Gamma_0$ (cm^2 s^{-1})
$SiO_2T_{0.3}[EO]_{3.2}$	0.77	1.842×10^{-4}	1.493×10^{-6}	4.73×10^{-6}
$SiO_2T_{0.2}[EO]_{2.4}$	0.62	1.172×10^{-4}	1.180×10^{-6}	2.05×10^{-6}

$SiO_2T_{0.1}[EO]_{1.9}$	0.51	7.570×10^{-5}	9.265×10^{-7}	1.12×10^{-5}
$SiO_2T_{0.2}Ol_{0.2}[EO]_{0.9}$	1.01	9.222×10^{-4}	5.700×10^{-6}	1.74×10^{-5}
$SiO_2T_{0.1}Ol_{0.1}[EO]_{0.7}$	0.73	5.220×10^{-4}	4.464×10^{-6}	1.16×10^{-5}
$SiO_2T_{0.1}[EO_{200}]_{0.2}/[EO_{600}]_{1.7}$	0.51	2.15×10^{-4}	2.631×10^{-6}	1.95×10^{-3}

For the remainder of the discussion, we focus on systems with Li^+ as the charger carrier species. According to Equation (3-3), the ionic conductivity is expected to increase linearly with the Li^+ concentration, assuming the material structure and all other factors remain constant. As can be gleaned from **Table 3-3** and as shown in **Figure 3-8**, this is closely the case for materials without oligo-PEG. The data for materials with oligo-PEG, for which we have only have two viable data points, do not align with the former, but besides the upward jog, still show a similar positive slope. Notably, among the materials without grafted oligo-PEG, $SiO_2T_{0.3}[EO]_{3.2}$-Li^+ achieves the highest ionic conductivity at 20 °C, reaching 1.8×10^{-4} S cm^{-1}. The addition of grafted oligo PEG to the system clearly enhances ionic conductivity beyond what could be achieved by increasing the charge carrier concentration. For example, we find a sevenfold increase in Li^+ conductivity for $SiO_2T_{0.1}Ol_{0.1}[EO]_{0.7}$ compared to $SiO_2T_{0.1}[EO]_{1.9}$. The highest ionic conductivity at 20°C is attained by $SiO_2T_{0.2}Ol_{0.2}[EO]_{0.9}$, which has a higher Li^+ concentration and a conductivity approaching 10^{-3} S cm^{-1}. Evidently, the introduction of oligo-PEG causes some fundamental structural changes. First, we note that the increase in Li^+ concentration is achieved at the expense of the short-chain PEO content. For a given TFSISPE-to SiO_2 ratio, the PEO content decreases roughly by a factor of 2.7. This suggests some degree of collapse of the pores in the silica backbone and compromise of its mechanical rigidity due to the incorporation of the additional tri-silane groups that serve as grafting sites for the oligo-PEG. An excessive number of tri-saline groups results in cracking of samples at

elevated temperatures during the DIS measurement. Indeed, materials with functional groups-to–Si ratios larger than 0.4 (sum of subscripts for T_x and Ol_y) are not stable. The measured quantities for these systems are not reliable and therefore not reported here.

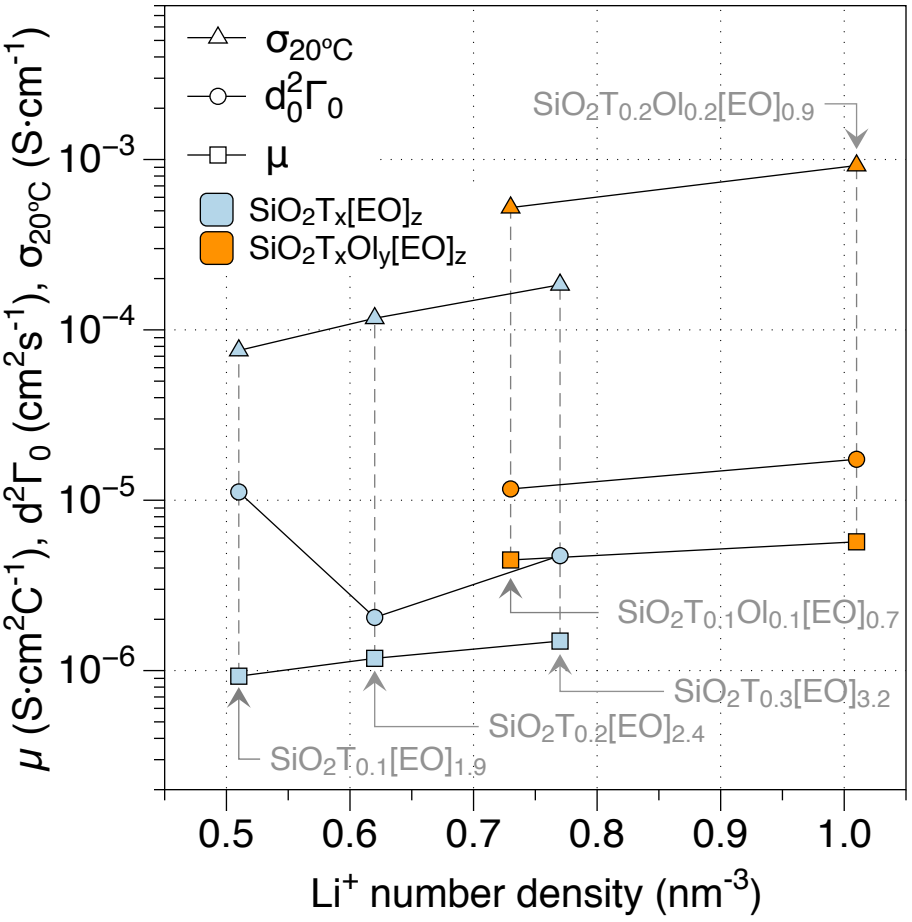

Figure 3-8 Comparison of 20 °C conductivities, charge carrier mobilities, and the values of parameter $d_0^2\Gamma_0$ between materials featuring different ion donor concentration, with or without oligo-PEG grafting.

To decouple the transport properties from the charge carrier concentration in different materials and to clarify the influence of structure on the cation hopping mechanism, it is advised to discern between conductivity and cation mobility, which are related according to

$$\sigma = z\, q_e\, \rho_{Li^+}\, \mu \qquad (5)$$

where z=1 for Li^+, q_e and ρ_{Li^+} have been defined earlier, and μ is the ionic mobility, which is defined as the average cation migration velocity normalized with respect to the applied electric field. The calculated Li^+ carrier mobilities for the materials systems under investigation are compiled in the **Table 3-3**.

Accordingly, Li^+ mobilities fall within the range of $9.3 \cdot 10^{-7}$ to $5.7 \cdot 10^{-6}$ S cm^2 C^{-1}. As a reference, the Li^+ mobility in bulk PEO (Mw = 900k g mol^{-1}) is 5.2×10^{-8} S cm^2 C^{-1}.[40] The Li^+ mobility in our hybrid materials systems is between 18 and 110 times greater. We attribute this mobility increase primarily to structural changes in the filler polymer due to the confinement to small pores and the proximity of the rigid silica backbone. Drawing from our previous studies on ionic conductivity within PEO-matrix composites containing active nanoparticles, we have established that the interfacial region exhibits significantly higher ion mobility than the bulk matrix, achieving levels of up to 1.4×10^{-6} S cm^2 C^{-1}.[27,40] While the cation mobility in the polymer matrix composites is independent of the lithium salt concentration, for the hybrid materials studied here we observe that mobility tends to increase with the ion donor concentration. However, we do not believe that there is a direct causal relationship between Li^+ cation mobility and the volumetric concentration thereof. Considering that for every Li^+ present in the material there exists a terminal donor group that is anchored in the silica backbone. Hence, with increasing Li^+ concentration the network connectivity decreases, which in turn affects the backbone topology, pore structure, flexibility, tortuosity, constrictivity. It is this network modification, a term we adopt from the description of inorganic glass structures to mean 'converting two connected units into disconnected (terminal) units,' that likely defines the Li^+ cation mobility.

Such network modification is even more pronounced in systems that have oligo-PEG grafted to the backbone. Various reasons can be given for the remarkable boost in Li^+ mobility due to the

insertion of oligo-PEG, and very likely a combination of these apply. For one, the increased network modification creates a more compliant backbone, which promotes a higher fill factor of the pores by polymer, especially since the pore walls are already partially coated with short EO segments, providing for greater compatibility between silica and polymer phases. This argument is supported by the consistently higher mass densities of the materials containing oligo-PEG compared to those that do not (**Table 3-2**). Part of the reason for this is the larger fraction of silica backbone in the systems containing oligo-PEG. However, when applying a simple role of mixture to estimate the porosity in these materials based on the molar fractions of their constituents determined by TGA, we arrive at about 5% for materials without oligo-PEG and less than 1% for materials with oligo-PEG. The elimination of nano-porosity (or increased fill factor), results in better contact between backbone and polymer, which potentially results in the development of increased amounts of the highly conductive interfacial area between the pore surface and filler. Even if the interfacial region did not exhibit the benefits of the interphase that develops between a polymer matrix and $Li_{1.3}Al_{0.3}Ti_{1.7}(PO_4)_3$ (LATP) nanoparticles,[27,40] as we found in our previous study, by simply removing voids from the structure, we increase the conduction cross-section, leading to higher conductivity. As already mentioned, the introduction of oligo-PEG reduces the total amount of polymer compared to silica backbone, which leads to an increase in the number of Li^+ donor sites per unit volume. This not only leads to a higher conductivity proportional to the Li^+ concentration, but also a higher cation mobility, a measure that is independent of said concentration.

To further substantiate whether the observed effect is predominantly due to an increased fill factor or the development of a chemically more compatible interface between organic and inorganic components, we prepared a material where the oligo PEG is not grafted to the backbone, but instead a mixture of polymers with different chain lengths is used to fill the pores. The mixture contains our regular PEO (Mw = 600 $g \cdot mol^{-1}$), as well as PEG (Mw = 200 $g \cdot mol^{-1}$), i.e., similar to

the oligo-PEG. The PEO:PEG mixing ratio is set to approximate that in $SiO_2T_{0.1}Ol_{0.1}[EO]_{0.7}$ and the total amount of EO groups relative to SiO_2 units matches that of $SiO_2T_{0.1}[EO]_{1.9}$. All three materials have the same ratio of Li^+-to-SiO_2.

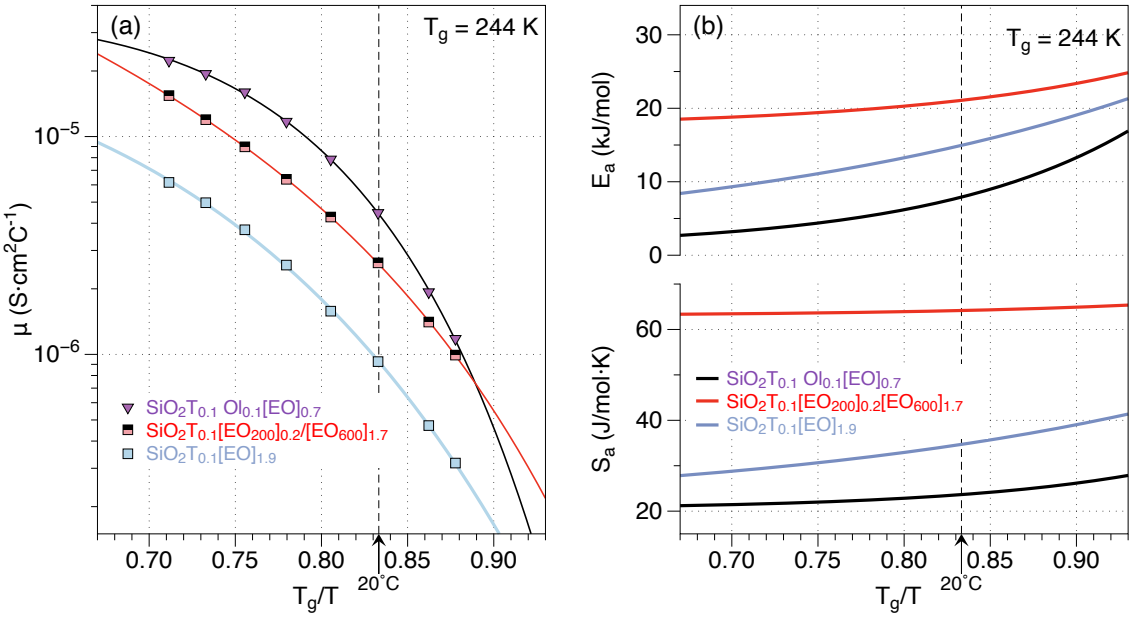

Figure 3-9 (a) Ionic mobilities for hybrid materials with PEO (M_w = 600 g mol^{-1}) filler and mixed molecular weight filler as a function of the normalized reciprocal temperature. The Oligo-PEG grafted material $SiO_2T_{0.1}Ol_{0.1}[EO]_{0.7}$ is plotted as reference. (b) Activation enthalpies and entropies as a function of the normalized reciprocal temperature.

As shown in **Figure 3-9**(a), the mobility for this mixed-length polymer material, referred to as $SiO_2T_{0.1}[EO_{200}]_{0.2}/[EO_{600}]_{1.7}$, is 2.85 times higher than that of $SiO_2T_{0.1}[EO]_{1.9}$ at room temperature, whereas for $SiO_2T_{0.1}Ol_{0.1}[EO]_{0.7}$ it is 4.8 times higher. We attribute this 'partial' improvement to the fact that the shorter polymer segments can easily insert themselves into smaller pores and better conform to the irregular surface of the pore walls. However, the benefits of grafted oligo PEG go beyond increasing the fill factor. PEG with one end covalently bonded to the backbone surface can also serve as a coupling agent, resulting in the reduction in osmotic drag. Covalent grafting also improves affinity between the inorganic backbone and the polymer. This is supported by our DSC data, which shows that the $SiO_2T_{0.2}Ol_{0.2}[EO]_{0.9}$ material exhibits better thermal stability than both the

$SiO_2T_{0.2}[EO]_{2.4}$ and pure PEO. We attribute this not only to smaller pore volume in $SiO_2T_{0.2}Ol_{0.2}[EO]_{0.9}$ but also to enhanced phase compatibility. In our earlier work, we already ascertained that chemical compatibility between mechanically disparate phases, such as the existence of a chemical element common to both phases, is a key requisite for the development of a highly conducting interfacial region.[40] The formation of covalent bonds between organic and inorganic constituents may have a similar influence.

The activation enthalpies and entropies of the three systems under scrutiny for this comparison are plotted vs. the normalized reciprocal temperature in **Figure 3-9**(b). The blue curves represent the data for $SiO_2T_{0.1}[EO]_{1.9}$, which are bracketed by the activation enthalpies and entropies for the $SiO_2T_{0.1}Ol_{0.1}[EO]_{0.7}$ system on the lower side and those for the $SiO_2T_{0.1}[EO_{200}]_{0.2}/[EO_{600}]_{1.7}$ system on the higher side. In particular, the activation entropy for the latter system is remarkably high and solely responsible for the increased Li^+ mobility over that in the system with only 600 Mw PEO. Accordingly, the mixing of polymer with different lengths creates local configurations with flattened saddle point potential energy contours, while the energy difference between ground and activated states remains relatively high. Such a scenario can be envisioned when the embedding structure is disrupted to offer unobstructed passage for the cation jump or when the structure is capable of significant deformation synchronous with the cation jump. Evidently, in mixture of different-length polymer, there is a higher concentration of end groups, which establish both disruption in the structure and higher segmental mobility. Both these features contribute to the aforementioned structural characteristics. We also point out the values of the factor $d_0^2\Gamma_0$, which for the $SiO_2T_{0.1}[EO_{200}]_{0.2}/[EO_{600}]_{1.7}$ system is two orders of magnitude higher than for the other two materials in this comparison, suggesting both a higher attempt frequency and jump distance in the mixed-polymer system.

Finally, the degree of deviation from Arrhenius behavior in the mobility (or conductivity) data, also referred to as 'fragility,'[42] is strongest for the system with oligo-PEG and weakest for the system with no oligo-PEG and only one type of polymer filler. This fragility is measured by the *H* parameter in our CAFÉ model. *H* represents the difference in the ground-state potential energy of the system in the high temperature liquid state and at T_g. The values for *H* we determined using our analysis are 7.8 kJ/mol for $SiO_2T_{0.1}[EO]_{1.9}$, 14.8 kJ/mol for $SiO_2T_{0.1}[EO_{200}]_{0.2}/[EO_{600}]_{1.7}$, and 17.5 kJ/mol for $SiO_2T_{0.1}Ol_{0.1}[EO]_{0.7}$. Accordingly, ionic mobilities scale with fragility. Overall, it appears as though the increased density of defects in the structure, i.e., polymer end groups is the predominant factor for ionic mobility, but if such structural disruption conforms with the geometry of the rigid silica backbone, this provides an advantage that nearly doubles the mobility.

3.3.6 Transference number

The lithium transference number is determined at 20°C using a methodology that combines DC voltage and AC impedance measurements, as detailed by Evans et al.[28] For these measurements, a symmetric Li metal/ electrolyte/Li metal cell is assembled within an argon-filled glove box, with an atmosphere containing less than 0.4 ppm of water vapor. After stabilizing the cell by short-circuiting for 4h, a constant voltage of 35 mV is applied for 1000 s, and both the initial and steady-state AC impedance are gauged before and after this polarization step. Notably, the sample size employed is 0.712 cm^2. The transference number is subsequently computed using the following formula:

$$t_{Li}^{+} = \frac{I^{\infty}(\Delta V - I^{0}R_i^{0})}{I^{0}(\Delta V - I^{\infty}R_i^{\infty})},$$

where ΔV denotes the applied constant potential across the symmetric cell, R_i is the interfacial resistance, and *I* is the current. The superscripts 0 and ∞ correspond to the initial and steady state quantities.[28,43,44]

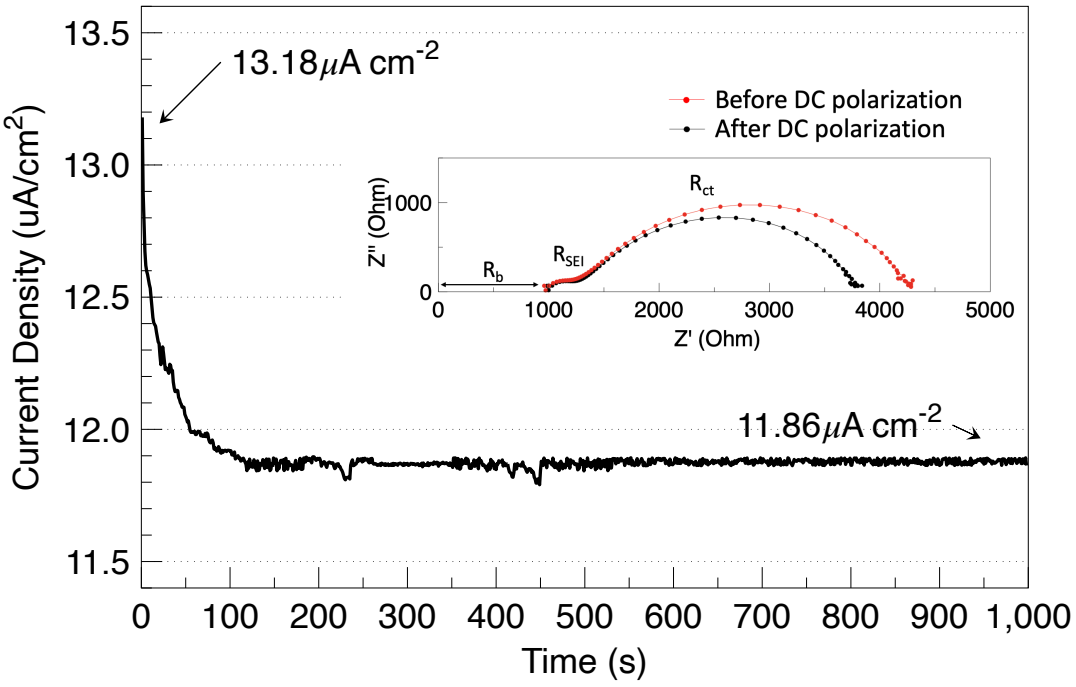

Figure 3-10 Alterations in the DC current density over time measured from $SiO_2T_{0.2}[EO]_{2.4}$-Li^+ samples subjected to 1000s of DC polarization. The insert depicts the Nyquist plot of AC impedance from the sample before and after the DC polarization.

The results of DC polarization and AC impedance are shown in **Figure 3-10**. The R_b represents the bulk resistance of the cell, encompassing resistance contributed by the electrolytes and current collector.[43–45] The semicircle observed in the high-frequency region pertains to the resistance attributed to the solid electrolyte interface layers (R_{SEI}), while the semicircle in the middle frequency range relates to the charge transfer resistance (R_{ct}) at the electrode/electrolyte interface.[38] The significance of accounting for interfacial resistance lies in the fact that the decline in current from initial value to the steady-state value is attributed to two distinct processes. Firstly, there is the formation of passivating layers at the electrode and electrolyte interfaces. Secondly, a concentration gradient is established in the electrolyte, restricting the movement of anions. [28] The AC impedance measurement does reveal an elevated interfacial resistance, evident in the increased diameter of the double semicircle after DC polarization.

Table 3-4 Result summary of the transference number measurement for $SiO_2T_{0.2}[EO]_{2.4}$-Li^+

	I (μA)	R_I (Ω)	t^+
Initial value	9.88	2599	0.91
Steady state value	8.44	3109	

The obtained transference number for this system is ~ 0.91, which confirms the single ion conducting nature.

3.4 Conclusion

The hybrid design, featuring an inorganic nanoporous silica backbone coupled with an organic phase effectively addresses the challenge of balancing ionic mobility and mechanical stiffness. With the functionalization with TFSISPE ion donor, as evidenced by a near unity transference number, the material exhibits single-ion-conducting behavior. We have developed an approach based on transition state theory (TST) for activation free energy analysis, specifically tailored for non-Arrhenius behavior in the temperature dependence of conductivity.

Charge carrier mobility calculation of the hybrid material indicates a significant increase (between 18 and 110 times) compared to bulk PEO (Mw = 900kg mol^{-1}), primarily attributed to structural changes in the filler polymer induced by confinement to small pores and proximity to the rigid silica backbone. Variation in Li^+ mobility among samples with different ion donor concentrations is linked to varying degrees of backbone network modification. Comparative analysis between samples with different ion types, Et_3NH^+ and Li^+, reveals a substantial difference in their ionic mobilities, primarily attributed to steric hindrance and the associated activation barrier heights for the bulkier Et_3NH^+. Systems containing Et_3NH^+ exhibit higher activation enthalpies and lower activation entropies, aligning with expectations based on cation size and structural complexity.

The introduction of oligo-PEG grafting results in a substantial boost in Li^+ mobility, attributed in part to the induced network modification by grafting, leading to a higher fill factor. Similarly, the mobility of the material filled with mixed PEO chain lengths is 2.85 times higher than in systems filled with only 600 M_w PEO. This partial improvement is linked to the shorter polymer segments easily inserting themselves into smaller pores and conforming better to the irregular surface of the pore walls. However, the benefits of grafted oligo-PEG extend beyond increasing the fill factor. The covalent bonding of PEG to the backbone surface serves as a coupling agent, reducing osmotic drag and enhancing the affinity between the inorganic backbone and the polymer. Uniquely, activation free energy analysis for the mixed chain length sample highlights remarkably high activation entropy, primarily responsible for the increased Li^+ mobility compared to the system with only 600 Mw PEO. Aligning with the fact that a higher concentration of end groups exists in a mixture of different-length polymer, which establish both disruption in the structure and higher segmental mobility. Essentially, the higher $d_0^2\Gamma_0$ factor value in the mixed-chain system, compared to the oligo-PEG grafted system, suggest a higher attempt frequency and jump distance in the mixed-polymer system.

3.5 References

1. Kim, Y. et al. High Ion Conducting Nanohybrid Solid Polymer Electrolytes via Single-Ion Conducting Mesoporous Organosilica in Poly(ethylene oxide). Chem. Mater. 29, 4401-4410 (2017).
2. Masias, A., Marcicki, J. & Paxton, W. A. Opportunities and Challenges of Lithium Ion Batteries in Automotive Applications. ACS Energy Lett. 6, 621-630 (2021).
3. Wu, X. et al. Safety Issues in Lithium Ion Batteries: Materials and Cell Design. Frontiers in Energy Research 7, (2019).

4. Villaluenga, I. et al. Cation only conduction in new polymer–SiO2 nanohybrids: Na+ electrolytes. J. Mater. Chem. A 1, 8348-8352 (2013).

5. Pender, J. P. et al. Electrode Degradation in Lithium-Ion Batteries. ACS Nano 14, 1243-1295 (2020).

6. Wang, F. et al. Does Polarization Increase Lead to Capacity Fade. Journal of The Electrochemical Society 167, 090549 (2020).

7. Yan, Y. et al. Modulating Sand's time by ion-transport-enhancement toward dendrite-free lithium metal anode. Nano Research 15, 3150-3160 (2022).

8. Bouchet, R. et al. Single-ion BAB triblock copolymers as highly efficient electrolytes for lithium-metal batteries. Nature Materials 12, 452-457 (2013).

9. Feng, S. et al. Single lithium-ion conducting polymer electrolytes based on poly[(4-styrenesulfonyl)(trifluoromethanesulfonyl)imide] anions. Electrochimica Acta 93, 254-263 (2013).

10. Doyle, R. P. et al. Poly(ethylenimine)-Based Polymer Blends as Single-Ion Lithium Conductors. Macromolecules 47, 3401-3408 (2014).

11. Mazor, H., Golodnitsky, D., Peled, E., Wieczorek, W. & Scrosati, B. A search for a single-ion-conducting polymer electrolyte: Combined effect of anion trap and inorganic filler. Journal of Power Sources. Selected Papers Presented at the 3rd INTERNATIONAL CONFERENCE ON POLYMER BATTERIES FUEL CELLS(PBFC 2007) on the occasion of Professor Bruno Scrosati's70th birthday 178, 736-743 (2008).

12. Dai, H. & Zawodzinski, T. A. The dependence of lithium transference numbers on temperature, salt concentration and anion type in poly (vinylidene fluoride)–hexafluoropropylene copolymer-based gel electrolytes1Presented at the Electrochemical Society Symposium: Processes in Polymers and Polymer|Metal Interfaces, Montreal, 4–9 May 1997.1. Journal of Electroanalytical Chemistry 459, 111-119 (1998).

13. Rohan, R. et al. Functionalized meso/macro-porous single ion polymeric electrolyte for applications in lithium ion batteries. J. Mater. Chem. A 2, 2960-2967 (2014).

14. Rohan, R. et al. Functionalized polystyrene based single ion conducting gel polymer electrolyte for lithium batteries. Solid State Ionics. The 7th International Conference on Materials for Advanced Technologies (ICMAT 2013) Symposium A: Advanced Energy Storage Systems: Lithium ion batteries and beyond 268, 294-299 (2014).

15. Rohan, R. et al. A high performance polysiloxane-based single ion conducting polymeric electrolyte membrane for application in lithium ion batteries. J. Mater. Chem. A 3, 20267-20276 (2015).

16. Wan, Z. et al. Low Resistance–Integrated All-Solid-State Battery Achieved by Li7La3Zr2O12 Nanowire Upgrading Polyethylene Oxide (PEO) Composite Electrolyte and PEO Cathode Binder. Adv. Funct. Mater. 29, 1805301 (2019).

17. Zhu, Y. et al. A Composite Gel Polymer Electrolyte with High Performance Based on Poly(Vinylidene Fluoride) and Polyborate for Lithium Ion Batteries. Adv. Energy Mater. 4, 1300647 (2014).

18. Rafael, V.-B. Ch. 1 (IntechOpen, Rijeka, 2020).

19. Zhang, H., Zhang, X., Shiue, E. & Fedkiw, P. S. Single-ion conductors for lithium batteries via silica surface modification. Journal of Power Sources 177, 561-565 (2008).

20. Schaefer, J. L., Moganty, S. S. & Archer, L. A. Nanoscale Organic Hybrid Electrolytes. Adv. Mater. 22, 3677-3680 (2010).

21. Sakuda, A., Hayashi, A. & Tatsumisago, M. Sulfide Solid Electrolyte with Favorable Mechanical Property for All-Solid-State Lithium Battery. Scientific Reports 3, 2261 (2013).

22. Benrabah, D., Sylla, S., Alloin, F., Sanchez, J.-Y. & Armand, M. Perfluorosulfonate-polyether based single ion conductors. Electrochimica Acta 40, 2259-2264 (1995).

23. Oh, H. et al. Poly(arylene ether)-Based Single-Ion Conductors for Lithium-Ion Batteries. Chem. Mater. 28, 188-196 (2016).

24. Bernards, T. N. M., MJ, V. B. & Jansen, J. A. J. The Effect of HF in a Two-Step Sol-Gel Process of TEOS. Journal of Sol-Gel Science and Technology 13, 749-752 (1998).

25. Ng, L. V. & McCormick, A. V. Acidic Sol−Gel Polymerization of TEOS: Effect of Solution Composition on Cyclization and Bimolecular Condensation Rates. J. Phys. Chem. 100, 12517-12531 (1996).

26. Wen, J. & Mark, J. E. Sol–Gel Preparation of Composites of Poly(dimethylsiloxane) with SiO2 and SiO2/TiO2, and Their Mechanical Properties. Polymer Journal 27, 492-502 (1995).

27. Wang, W., Yi, E., Fici, A. J., Laine, R. M. & Kieffer, J. Lithium Ion Conducting Poly(ethylene oxide)-Based Solid Electrolytes Containing Active or Passive Ceramic Nanoparticles. J. Phys. Chem. C 121, 2563-2573 (2017).

28. Evans, J., Vincent, C. A. & Bruce, P. G. Electrochemical measurement of transference numbers in polymer electrolytes. Polymer 28, 2324-2328 (1987).

29. Brinker, C. J. & Scherer, G. W. (eds Brinker, C. J. & Scherer, G. W.) 514-615 (Academic Press, San Diego, 1990).

30. Ellerbrock, R., Stein, M. & Schaller, J. Comparing amorphous silica, short-range-ordered silicates and silicic acid species by FTIR. Scientific Reports 12, 11708 (2022).

31. Rey, I., Lassègues, J. C., Grondin, J. & Servant, L. Infrared and Raman study of the PEO-LiTFSI polymer electrolyte. Electrochimica Acta 43, 1505-1510 (1998).

32. Tseng, Y.-C. et al. Polymer electrolytes based on Poly(VdF-co-HFP)/ionic liquid/carbonate membranes for high-performance lithium-ion batteries. Polymer 173, 110-118 (2019).

33. Khan, K., Tu, Z., Zhao, Q., Zhao, C. & Archer, L. A. Synthesis and Properties of Poly-Ether/Ethylene Carbonate Electrolytes with High Oxidative Stability. Chem. Mater. 31, 8466-8472 (2019).

34. Brinker, C. J. & Scherer, G. W. (eds Brinker, C. J. & Scherer, G. W.) 96-233 (Academic Press, San Diego, 1990).

35. Brinker, C. J. & Scherer, G. W. (eds Brinker, C. J. & Scherer, G. W.) 302-355 (Academic Press, San Diego, 1990).

36. Vrandečić, N. S., Erceg, M., Jakić, M. & Klarić, I. Kinetic analysis of thermal degradation of poly(ethylene glycol) and poly(ethylene oxide)s of different molecular weight. Thermochimica Acta 498, 71-80 (2010).

37. Rubio, F., Rubio, J. & Oteo, J. L. A DSC study of the drying process of TEOS derived wet silica gels. Thermochimica Acta 307, 51-56 (1997).

38. Choi, W., Shin, H.-C., Kim, J. M., Choi, J.-Y. & Yoon, W. Modeling and Applications of Electrochemical Impedance Spectroscopy (EIS) for Lithium-ion Batteries. Journal of electrochemical science and technology 11, 1-13 (2020).

39. Liu, W. et al. Ionic Conductivity Enhancement of Polymer Electrolytes with Ceramic Nanowire Fillers. Nano Lett. 15, 2740-2745 (2015).

40. Wang, G. & Kieffer, J. Contiguous High-Mobility Interphase Surrounding Nano-Precipitates in Polymer Matrix Solid Electrolyte. ACS Appl. Mater. Interfaces 15, 848-858 (2023).

41. Macdonald, J. R. & Johnson, W. B. 1-20 2018).

42. Beg, C. & Kieffer, J. Fragility and the rate of change of the energy landscape topography. Journal of Non-Crystalline Solids: X 14, 100101 (2022).

43. Borca, C. N. et al. Influence of dynamical scattering in crystalline poly(vinylidene fluoride-trifluoroethylene) copolymers. Appl. Phys. Lett. 74, 347-349 (1999).

44. Shigenobu, K., Dokko, K., Watanabe, M. & Ueno, K. Solvent effects on Li ion transference number and dynamic ion correlations in glyme- and sulfolane-based molten Li salt solvates. Phys. Chem. Chem. Phys. 22, 15214-15221 (2020).

45. Chintapalli, M. et al. Relationship between Conductivity, Ion Diffusion, and Transference Number in Perfluoropolyether Electrolytes. Macromolecules 49, 3508-3515 (2016).

46. Yu, Z. et al. A Dynamic, Electrolyte-Blocking, and Single-Ion-Conductive Network for Stable Lithium-Metal Anodes. Joule 3, 2761-2776 (2019).

CHAPTER IV Cation Donor Functionalized Silica-Based Organo-Gel as Single-Ion Conducting Hybrid Electrolyte for Lithium-Ion Batteries

4.1 Introduction

Electrolytes are essential to the performance and the operational safety of Lithium-ion batteries.[1] The development of solid electrolytes that exhibit high ionic conductivity, good thermal and electrochemical stability, and appreciable mechanical rigidity, so they can serve as a thin load bearing separator, is an ongoing quest .[2] Unfortunately, high mobility and mechanical stiffness are opposing attributes for most monolithic materials, and a composite design strategy is indicated. A promising construct in this regard are hybrid electrolytes consisting of a porous but rigid backbone material, with its pores infused with an agile material, such as a low-glass transition temperature polymer. The inherently high modulus network structure of this rigid backbone can effectively mitigate dendrite growth and augment the overall thermal stability of the electrolytic system.[3] Various materials, including covalent organic frameworks (COFs), porous organic cages, and silica gel have been extensively explored as potential candidates for such backbone materials in hybrid electrolyte development.[4–7] These frameworks possess nano-sized pores that provide effective confinement for the conducting fillers, but still allow for continuous passage for small elemental cations.[1,4,8–11]

In principle, only the ion involved the redox reaction in the battery would need to shuttle between the electrodes. In fact, the migration of other ions in the electrolyte can be detrimental by causing issues such as concentration polarization, dendrite proliferation, and inherent safety concerns.[12–15] The lithium cation transference number identifies the relative proportions of the electric current across the electrolyte due to Li^+ and the total current. It is defined as $t_{Li^+} = I_{Li^+}/(I_{Li^+} + I_{A^-})$, where I_{Li^+} and I_{A^-} are the current carried by Li^+ and counter anion respectively.[16] Accordingly, the ideal electrolyte would possess a t_{Li^+} value approaching unity, a goal that has been pursued using various materials design approaches and has led to the designation of single ion conductors (SICs) in the literature, to reflect the occurrence where nearly all current across the electrolyte is carried by the lithium cation.[12–15] For comparison, reported transference number measurements for conventional salt-based electrolytes, i.e., containing compounds such as $LiClO_4$ that dissociate when dissolved in organic carbonate solvents, typically exhibit a t_{Li^+}-range of 0.3 to 0.55, depending on solvent composition and salt concentration.[17] This range implies a general balance, if not dominance by the counter anion in the overall charge transport.

In our preceding research, we demonstrated close to SIC behavior in silica gel-based hybrid materials containing short-chain polyethylene oxide (PEO) filler. Our unique materials design comprises a porous silica backbone modified with two covalent types of functionalization that each play a role in enhancing lithium cation mobility and transference number. One functionalization is the 2–[(Trifluoromethanesulfonylimido)–N–4–sulfonylphenyl]ethyl (TFSISPE) anion group, which effectively anchors the cation donor to the backbone, and the other is oligo-PEG, which enhances the chemical compatibility between silica and the PEO filler and, by acting as a molecular brush, reduces the osmotic drag during lithium shuttling. The resulting material exhibits that a transference number of 0.91 and an ionic conductivity of 5.2×10^{-4} $S\cdot cm^{-1}$ at 20°C. While these findings constitute significant progress compared to polymer matrix composites, the vast majority of PEO-

based electrolytes, particularly those that can be classified as SIC, have yet to attain the desired level of ionic conductivity exceeding 10^{-3} S·cm^{-1} at room temperature.[8,13,15]

Within this context, ethylene carbonate (EC) and propylene carbonate (PC) emerge as commonly favored organic liquid fillers, primarily due to their elevated ionic dissociation potential and facile ion migration attributes. Because of the crystalline nature of EC (melting point of 36.2 °C), it is usually mixed with PC to form a room temperature solution.[17] Research also indicates that the EC and PC mixture (EC/PC) is chemically more stable in contact with Li metal when compared with PC alone, due to a more stable solid electrolyte interphase (SEI) that is formed by EC.[18] According to relevant research, the room temperature ionic conductivity for carbonate electrolytes and their derivatives reach 10^{-3} S·cm^{-1}.[1,9,10,12]

In present work, we have successively implement a range of strategies with the goal of improving the performance and deepening our understanding of the conducting mechanism of the silica-based hybrid electrolyte. First, we systematically explore the wetting behavior of EC/PC mixtures as a filler substance to pinpoint the optimal weight ratio of EC to PC in terms of the resulting ionic conductivity. Second, we control of the pore volume and pore size distribution in the silica-based backbone by alternating the water to TEOS ratio during backbone synthesis. This gives us insights into how alterations in pore volume affect both the conductivity and thermal stability of the electrolyte. Third, we examine the role of oligo-PEG functional groups grafted to the silica backbone on electrolyte performance. Finally, we evaluate the benefits of additionally doping the system with $LiClO_4$ salt to increase carrier concentrations.

4.2 Experimental procedures

4.2.1 Materials design concept

For most hybrid electrolytes discussed in the literature, the polymer serves both as the material's load-bearing component and to provide high-mobility conduction pathways. In light of the inherent inconsistency between ionic mobility and mechanical stiffness in a material, we pursue an alternative design for hybrid electrolytes consisting an inorganic nano-porous backbone housing an organic phase that facilitates cation transport. The backbone establishes a continuous three-dimensional network that has a high elastic modulus and therefore can mechanically support the electrolyte structure, suppress dendrite growth from the anode, and enhance thermal stability.[3] To address cell polarization concerns, we prioritize improving the cation transference number. To this end we immobilize the cation donor by covalently attaching it to the backbone. We have selected 2-[(Trifluoromethanesulfonylimido)-N-4-sulfonylphenyl] ethyl (TFSISPE) as the cation donor due to its robust electron-withdrawing tendency, which enhances the charge delocalization of anions and thereby improves Li^+ dissociation and ionic conductivity.[19] Additionally, we incorporate an oligo polyethylene glycol (Oligo-PEG) brush, also covalently attached to the backbone to provide further stabilization for the organic filler. In this study, the organic filler is a mixture of ethylene carbonate and propylene carbonate (EC/PC).

To evaluate the impact of each design element on properties relevant to electrolyte performance, we implemented these constituents individually and in various combinations, requiring the fabrication and characterization of four distinct series of specimens. All materials feature a silica backbone to which TFSISPE cation donor groups are covalently bonded. The Li^+ concentration in the material is controlled by adjusting the relative proportions of these two components. The first series comprises monofunctionalized materials, consisting of only the silica backbone and TFSISPE at

various molar ratios, but no organic filler phase. In the second series, we fill the pores of the monofunctionalized silica network with EC/PC. The third series involves the silica backbone with both TFSISPE and oligo-PEG covalently grafted to it, termed bi-functionalized backbone, and no filler. Lastly, the fourth series incorporates EC/PC filling the pores of the bi-functionalized backbone. The exact compositions are determined using thermogravimetric analysis, and the actual Li^+ concentration depends on the various components included in the material. We identify the electrolyte materials based on their composition, using the abbreviations $SiO_2T_xOl_y[EC/PC]_z$, where x, y, and z denote the molar ratios of TFSISPE-to-SiO_2, EO-to-SiO_2 from oligo-PEG, and EC/PC-to-SiO_2, respectively. While, Si, O, T, and Ol form covalently bonded compounds, the square brackets around EC/PC signify that the organic carbonate mixture is not covalently bonded to the backbone. Unless otherwise specified, the weight ratio of EC to PC in the EC/PC mixture is 4:1 (80wt% EC). Indeed, the EC/PC was only changed while establishing of the optimizal EC to PC ratio in terms of ion conductivity. For materials where Li^+ concentration are enhanced via $LiClO_4$ doping, the molar concentration of $LiClO_4$ added to the nomenclature. All materials contain SiO_2 and TFSISPE, while Oligo-PEG, EC/PC and $LiClO_4$ are specified only when they are added to the composition.

4.2.2 Materials synthesis

The incorporation of organic components into the inorganic backbone can be achieved through either a one-pot or a two-step procedure.[13,15] In the one-pot approach, the mixing of precursors at the beginning relies on the fortuitous self-assembly of the desired structure. In fact, it may lead to insufficient structural integrity as the introduction of the organic phase precursor could disturb the silica network formation. In contrast, the two-step process separates backbone formation from

surface functionalization, allowing for better control of structural evolution, but it may limit the concentration of grafting sites.[13]

To overcome these challenges we purposely phase the combination of precursors, each having undergone different durations of incubation depending on their respective reaction rates. The backbone of the porous network is composed of silica, produced via the sol-gel route using tetraethyl orthosilicate (TEOS). Silanol groups on the pore surface provide reaction sites for functionalization. Seamless integration of the ion donor is achieved using the TFSISPE anion configured with a trimethoxysilane group that reacts with the backbone silanol groups through a condensation reaction.[8,15] To achieve the desired pore structure, the TEOS precursor is pre-hydrolyzed and partially condensed before introducing TFSISPE. Careful synchronization of the phased preparation ensures proper progress along their respective reaction paths. Since oligo-PEG relies on similar grafting chemistry as TFSISPE, it is introduced simultaneously in materials that contain it. Finally, EC/PC is infused into the pores through fluid exchange.

Preparation of pre-hydrolyzed and lightly gelled silica backbone precursor — A 50 ml beaker is employed to combine 10.00 g of Tetraethyl orthosilicate (TEOS, 99%, Aldrich) and 0.48 ml of 1M HCl. Additionally, various quantities of deionized water is introduced into the mixture, so as to achieve the desired water to TEOS ratio (R_w) for the envisaged variation in pore size. We examined materials obtained for R_w values of 3, 5, and 15. The resulting mixture is homogenized for 3 hours at room temperature, ensuring complete hydrolysis of TEOS. Subsequently, the system is continuously stirred for an additional 4 hours at 65°C, facilitating the occurrence of the condensation reaction.

Synthesis and pre-hydrolysis of the triethylammonium 2-[(trifluoromethanesulfonylimido)-N-4-sulfonylphenyl]ethyl-trimethoxysilane — Into a 50 ml three-neck flask, 1.00g of

Trifluoromethanesulfonamide (95%, Aldrich) and 4.66 ml of triethylamine (99.5%, Aldrich) are introduced. Following this, 28.00 ml of dichloromethane (99.8%, Aldrich) is added as the solvent, and the system is stirred until complete dissolution is achieved. Subsequently, 4.28g of 4–[2–(trimethoxysilyl)–ethyl] benzene–1–sulfonyl chloride (50 wt% solution in dichloromethane, Aldrich) is added, leading to a slight yellow tint in the solution. The resulting mixture is stirred at 40°C overnight. The solvent and excess triethylamine is then eliminated via distillation, yielding a dark orange-colored wax product.[15] This final product is subjected to further purification by placing it in a vacuum oven under 1kPa at 85°C for 2 hours, facilitating the removal of residual volatiles.

Grafting of ion donor and oligo PEO — for materials containing grafted oligo-PEG, 0.40 g of 2–[Methoxy(polyethyleneoxy)$_{6\text{-}9}$propyl] trimethoxysilane (oligo-PEG) and 3.00 g of TFSISPE ion donor are combined with 0.55 ml of water and 1.40 ml of ethanol. This mixture is subjected to prehydrolyzation by keeping it at 45°C for 2.5 hours. Subsequently, precise quantities of lightly gelled backbone precursor, prehydrolyzed ion donor, and oligo-PEG are mixed together. The amounts of the backbone precursor are 9.20 ml, 10.40 ml and 16.40 ml for R_w ratios equal to 3, 5, 15 samples respectively. This mixture is homogenized at 65°C for approximately 30 minutes until achieving a viscous consistency. The resulting gel is cast into a plastic container, sealed, and allowed to stand for another 30 minutes, leading to gel solidification. The container is then placed an oven at a set temperature of 50°C for the gel to age. After 24 hours of aging, a transparent, yellow-colored functionalized backbone is obtained. The backbone is freed of residual reactants by rinsing it with a combination of deionized water and ethanol.

Ion exchange and organic solvent infusion — The functionalized backbone is immersed in a 0.04 M aqueous solution of Lithium hydroxide (LiOH, 98%, Aldrich) for a duration of 1 hour. The solution is replaced every 15 minutes during this period. Subsequently, the backbone undergoes

thorough rinsing using a generous quantity of deionized water and ethanol to effectively eliminate residual LiOH. Then, the backbone undergoes a filler penetration process. This involves immersing the backbone in 25.00 ml of EC and PC liquid mixture at 45°C under 1k Pa vacuum for 2 hours. This step is repeated three times with fresh EC/PC mixture to ensure thorough solvent exchange. Subsequently, the sample is vacuum-dried at 45°C for 12 hours to complete the removal of residual ethanol and water.

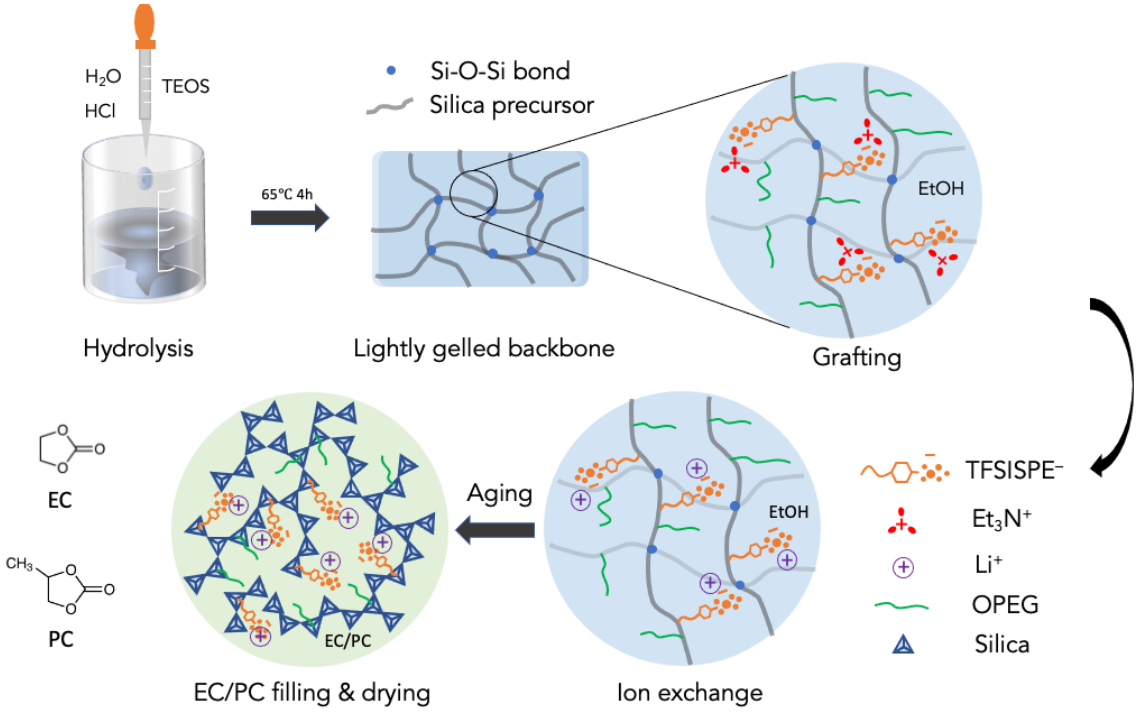

Figure 4-1 Schematic illustrating the synthesis procedure for hybrid silica backbone and gel-type electrolytes.

4.2.3 Characterization techniques

Thermal gravimetric analysis (TGA) is conducted using the TA Instruments DISCOVERY TGA. The samples are subjected to a nitrogen (N_2) atmosphere (flow rate: 60 cm^3 min^{-1}) and scanned within a temperature range from 50°C to 700°C at a heating rate of 7 K min^{-1}. Differential scanning calorimetry (DSC) is performed using the TA Instruments DISCOVERY DSC, employing a heating

rate of 10 K min^{-1} for scans spanning from –60°C to 200°C. The pore volume, pore diameter, specific surface area of the backbone are determined using the Micromeritics ASAP 2000 porosimetry analyzer. To this end the hydrogel prepared as described above, including bi-functionalization with TFSISPE and oligo-PEG is supercritically dried. This first involves replacement of the ethanol-water solvent acetone at ambient pressure and subsequently the acetone is preplaced with carbon dioxide under pressure, before the gel is undergoes supercritical drying at 304 K and 7.38 MPa. Once the supercritical condition is attained, the system's temperature is gradually raised to 313 K over a period of 6 hours while maintaining a constant pressure. This is achieved by slowly releasing gas. The resulting aerogel is gently crushed before measurement. For the determination of ionic conductivity, a Novocontrol broadband dielectric impedance spectrometer (DIS) is utilized. The electrolyte is positioned between two highly polished stainless steel current collectors. The measurements are conducted across a temperature range from 5°C to 70°C under a controlled nitrogen (N_2) atmosphere, while frequencies range from 0.1 Hz to 10 MHz. Before the impedance measurement, the system is heated to 70°C to optimize the contact between the electrolyte and the current collectors.[20] The cross-section morphologies of the composite electrolyte are determined via scanning electron microscopy (SEM) using the Tescan NIRA3 instrument. Samples are sputter coated with Platinum under 5×10^{-2} mbar at 25°C for 2 mins prior to the SEM analysis. The measurement of lithium-ion transference numbers (t_{Li^+}) involves a combination of DC polarization and AC impedance techniques.[21] In an argon-filled glove box with water vapor levels below 0.4 ppm, a symmetric cell comprising Li metal/electrolyte/Li metal is assembled. A constant 15 mV DC voltage is applied to the cell for approximately 1000 seconds, enabling the determination of initial and steady-state resistance before and after the DC polarization.

4.3 Result and discussion

In the following we elaborate on the use of IR spectroscopy to monitor the success of chemical synthesis, as well as information regarding the chemical composition and pore structure revealed by the combination of TGA, porosimetry, and SEM techniques. We use these insights to interpret the measured ionic conductivity and mobility data in view of identifying optimal materials design criteria.

4.3.1 FTIR

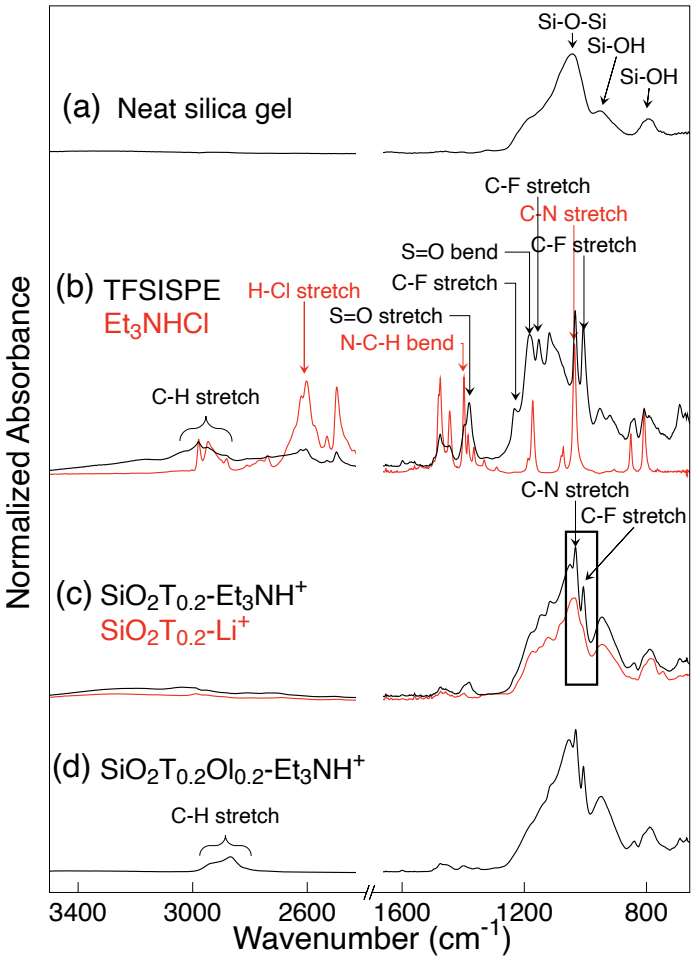

Figure 4-2 FTIR spectra of (a) neat silica gel, (b) TFSISPE ion donor and Et_3NHCl byproduct, (c) monofunctionalized samples before and after ion exchange ($SiO_2T_{0.2}$-Et3NH$^+$ and $SiO_2T_{0.2}$-Li^+, respectively) and (d) bifunctionalized material $SiO_2T_{0.2}Ol_{0.2}$-Et_3NH^+.

Figure 4-2 shows the FTIR spectra, juxtaposing the synthesized materials with various chemical constituents involved in their creation for comparison. The reference spectra include pure silica gel, TFSISPE ion donor, and Et_3NHCl. This comparison helps identify prevailing structural elements and changes in their vibrational characteristics upon integration into the hybrid configuration. The spectrum of neat silica gel (**Figure 4-2**(a)) shows absorption bands characteristic for stretching vibrations of O-H groups at 3200–3500 cm^{-1} (broad band), asymmetric Si-O^- stretching vibration at 1000–1100 cm^{-1}, Si-OH and SiO-H stretching of terminal silanol groups at 960 cm^{-1}, and symmetric Si-O stretching at 800 cm^{-1}.[22] Specifically, the Si-O-Si band in silica gel appears broader compared to that of quartz due to the material's larger specific surface area. This broadening is attributed to an increased number of Si-O-Si groups located at the pore surface, leading to an abundance of defects terminated in -OH groups.[23] The absence of the absorption band at 1600-1650 cm^{-1} is expected, confirming the removal of molecular coordinated water from the SiO_2 structure during drying.[23]

In the spectrum of the TFSISPE ion donor, the stretching vibration of O=S=O group is evident at 1380 cm^{-1}, along with the O=S=O bending mode at 1181 cm^{-1}. The C-F stretching vibrations occur at 1235 cm^{-1} and 1152 cm^{-1}, while C-H stretching vibrations are observed in the 2860–3050 cm^{-1} range. These vibrational modes are characteristic of the molecular structure of TFSISPE.[24] During the synthesis of the TFSISPE ion donor, Et_3NHCl is generated as byproduct. In the spectrum of Et_3NHCl, the C-N stretching mode is observed at 1035 cm^{-1}, the C-H stretching vibrations at 2850–3000 cm^{-1}, and N-C-H bending vibrations at 1400 cm^{-1}. While the signature of N-H stretching vibrations, which would occur at around 3400 cm^{-1} is absent, distinct and broad band corresponding to HCl at approximately 2600 cm^{-1} is observed, consistent with the chemical structure. The presence of overlapping peaks between the spectra of TFSISPE and Et_3NHCl becomes evident in **Figure 4-2**(b), which can be attributed to the retention of the byproduct within the ion donor. This byproduct is subsequently eliminated through repeated washing and the ion exchange.

The monofunctionalized material, labelled as $SiO_2T_{0.2}$-Et_3NH^+, is shown in **Figure 4-2**(c), where "Et_3NH^+" refers to the cation type. Note that this sample had not been subject to the solvent washing and ion exchange protocols in order to verify the efficacy of the grafting process through the presence spectral feature of Et_3NHCl. Accordingly, the spectrum of $SiO_2T_{0.2}$-Et_3NH^+ should be a superposition of the TFSISPE and the silica gel spectra. A similar argument can be made for the spectrum of the bi-functionalized $SiO_2T_{0.2}Ol_{0.2}$-Et_3NH^+ shown in **Figure 4-2**(d), with the most pronounced divergence found within the 2800–3000 cm^{-1}, a range dominated by the stretching vibration of C-H within the Oligo-PEG component.

The post-synthesis washing and ion exchange serve to eradicate of residual Et_3NHCl byproduct and substitute Li^+ for Et_3NH^+. To gauge the effectiveness of these steps, we compare the spectrum of $SiO_2T_{0.2}$-Et_3NH^+ with that of $SiO_2T_{0.2}$-Li^+ shown in **Figure 4-2**(c), the latter being the hybrid sample after washing and ion exchange. Indeed, the absence of the robust C-N stretching peak at 1035 cm^{-1}, characteristic of Et_3NH^+, confirms the successful removal of both Et_3NH^+ and residual Et_3NHCl byproduct. Similarly, the C-F stretching band at 1005 cm^{-1} is reduced to a faint shoulder in the $SiO_2T_{0.2}$-Li^+ spectrum as a result of the removal of surplus trifluoromethanesulfonamide that was introduced during the ion donor synthesis.

4.3.2 TGA

Thermogravimetric analysis is carried out on sample that underwent post-grafting washing procedures to eliminate Et_3NHCl and trifluoromethanesulfonamide, but the cation exchange did not yet take place. The primary goal of TGA is to determine the composition of the materials under investigation, but at the same time it reveals information regarding the materials thermal stability of the materials components.

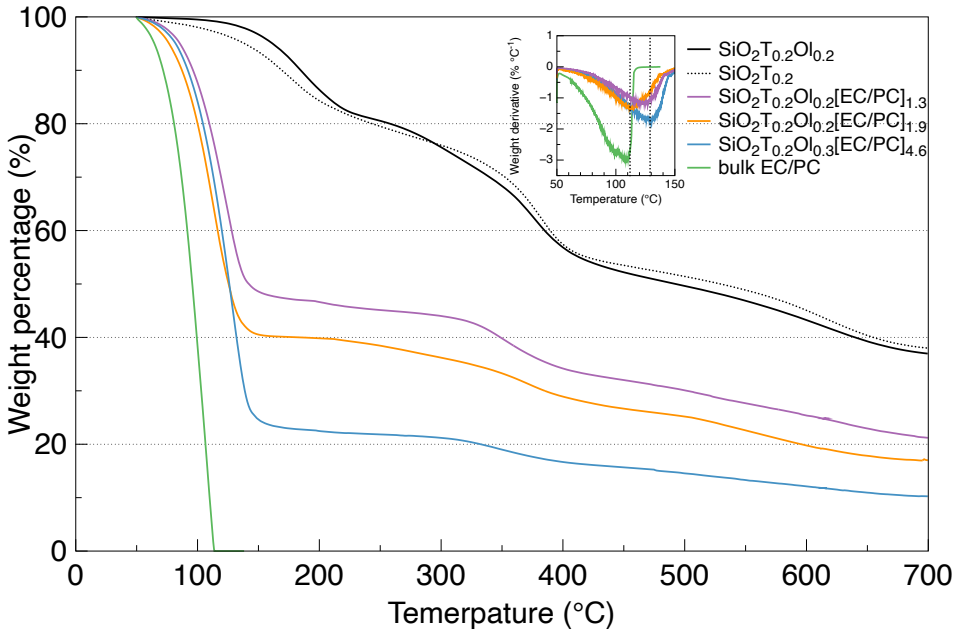

Figure 4-3 TGA diagram of EC/PC mixture with 80wt% of EC, monofunctionalized and bifunctionalized backbone samples, and hybrid electrolytes. The inserted diagram on the upper right side illustrates the derivative of the weight loss curves for hybrid samples, with the dotted lines marked their peak positions.

In **Figure 4-3** we compare TGA profiles for the EC/PC liquid containing 80 wt.% EC, materials consisting of mono- and bi-functionalized backbones samples, denoted as $SiO_2T_{0.2}$ and $SiO_2T_{0.2}Ol_{0.2}$, respectively, as well as bi-functionalized materials whose pored exhibit three different size distributions and are filled with the 80/20 EC/PC mixture. As can be seen, the weight loss curves for $SiO_2T_{0.2}$ and $SiO_2T_{0.2}Ol_{0.2}$ follow a similar temperature dependence, with the onset of weight loss occurring around 180°C. The initial drop can be ascribed to the decomposition of Et_3NH^+ ions, releasing of H^+ ions and Et_3N. The primary TFSISPE ion donor undergoes a two-step decomposition process, starting with the degradation of the tail TFSI structure around 380°C, followed by the decomposition of the alkyl linker at approximately 550°C, consistent with the findings of prior studies.[25] Note that for the bi-functionalized backbone, $SiO_2T_{0.2}Ol_{0.2}$, the weight loss between 50,C and 290°C is delayed compared to that for the monofunctionalized $SiO_2T_{0.2}$, indicating improved thermal stability as a result of the introduction of oligo-PEG, at least at low

temperatures. Given that each oligo-PEG molecule anchored on the silica backbone requires one branch of a silane group to become terminal, the insertion of oligo-PEG changes the network connectivity. This likely results in a partial network collapse that obstructs the release of Et_3N. At temperatures exceeding 290°C, the distinctions between these two materials become less apparent, with $SiO_2T_{0.2}$ exhibiting a slightly better stability.

For the hybrid electrolyte, e.g., $SiO_2T_{0.2}Ol_{0.2}[EC/PC]_{1.9}$, the weight loss in the temperature range between 50 and 140°C can be attributed to the removal of the EC/PC phase, in addition to the decomposition of Et_3NH^+.[9,12] Above 150°C, with all liquid carbonate removed, the weight loss curve for the hybrid electrolytes follows a similar trend to that of the functionalized backbone by itself. By comparison, bulk EC/PC exhibits a steeper weight loss, revealing that the confinement in the backbone pores delays the degradation of EC/PC by about 20ºC.

To further improve the thermal stability of our hybrid materials, we explore the effect of pore size on filler volatility by varying the water-to-TEOS ratio (R_w ratio) during synthesis of the backbone. The resulting hybrid materials, denoted as $SiO_2T_{0.2}Ol_{0.2}[EC/PC]_{1.3}$, $SiO_2T_{0.2}Ol_{0.2}[EC/PC]_{1.9}$, and $SiO_2T_{0.2}Ol_{0.3}[EC/PC]_{4.6}$, all consist of a similar bi-functionalized backbone and are fabricated with R_w ratios of 3, 5, and 15, respectively. As indicated by the nomenclature, the higher the R_w ratio, the greater the EC/PC molar content, i.e. the larger the pore volume. The inset in **Figure 4-3** shows the weight loss rates for these three materials. The peak location, reflecting the temperature of maximum EC/PC expulsion rate, serves to quantify the filler volatility. Accordingly, the material with the lowest pore volume, $SiO_2T_{0.2}Ol_{0.2}[EC/PC]_{1.3}$, exhibits the highest thermal stability and vice versa. This trend is further analyzed in the next section with knowledge of pore size distribution derived from nitrogen adsorption-desorption measurements of the supercritically dried backbone.

The calculation of component weight fractions involves fitting the TGA curves to determine the heights of sample weight drops at the various stages. This analysis yields a system of linear equations with the unknowns being the masses of each materials constituent. Because some steps account for the loss of more than a single constituent, the system of equations is typically underdetermined and the best solution must be sought, assuming that the relative amount of silica to the remaining components of the backbone remains unchanged, whether the pore is filled or not. A comprehensive description of this analysis procedure is provided in the **Appendix D**. The resulting weight fractions are listed in **Table 4-1**, as m_S, m_{Et}, m_T, m_E and m_O, where *S*, *Et*, *T*, *E*, *O*, stand for silica, ethanol, TFSISPE, EC/PC, and Oligo-PEG respectively. ω_{14} is a fitting parameter representing the ratio of mass loss of oligo-PEG in stage 1 and 2.

Table 4-1 Summary of the TGA derived components weight fractions; $\omega 14$ is a fitting parameter governing the ratio of mass loss of Oligo-PEG in stage 1 and 2, respectively.

	m_{Et}	m_T	m_E	m_O	m_S	ω_{14}
$SiO_2T_{0.2}$	13.64	49.07	–	–	37.50	–
$SiO_2T_{0.2}[EC/PC]_{3.4}$	4.00	14.94	66.70	–	12.95	–
$SiO_2T_{0.2}Ol_{0.2}$	6.12	52.51	–	6.04	35.22	0.17
$SiO_2T_{0.2}Ol_{0.2}[EC/PC]_{1.3}$	3.79	31.30	40.04	3.67	21.20	0.77
$SiO_2T_{0.2}Ol_{0.2}[EC/PC]_{1.9}$	3.45	27.77	48.35	2.28	17.20	0.74
$SiO_2T_{0.2}Ol_{0.3}[EC/PC]_{4.6}$	1.57	14.49	70.43	1.94	10.21	0.73

The above results confirm that the EC/PC weight fractions in hybrid electrolytes increase gradually with the R_w ratio, increasing from 40.04 wt% to 70.43 wt%, indicative of a corresponding increase in pore volume. Additionally, we observe that EC/PC content, m_E, is significantly smaller when the backbone is functionalized with oligo-PEG ($SiO_2T_{0.2}Ol_{0.2}[EC/PC]_{1.9}$) compared to when it is not ($SiO_2T_{0.2}[EC/PC]_{3.4}$), consistent with our findings for systems with different filler materials and confirming the partial collapse of network pores associated with oligo-PEG.

The TGA results yield weight fractions for each component within the hybrid materials, which can straightforwardly be converted to molar concentrations or number densities in units of molecules/nm³, which are used to derive cation mobilities from the measure ionic conductivities and transference numbers.

Table 4-2 Summary of component number densities (molecules nm^{-3}) in hybrid electrolytes

	ρ (kg/m3)	EtOH	TFSISPE	EC	PC	oligo-PEG	SiO_2
$SiO_2T_{0.2}[EC/PC]_{3.4}$	1435.0	0.76	0.31	5.32	1.15	–	1.89
$SiO_2T_{0.2}Ol_{0.2}[EC/PC]_{1.3}$	1552.6	0.77	0.70	3.40	0.73	0.78	3.31
$SiO_2T_{0.2}Ol_{0.2}[EC/PC]_{1.9}$	1521.6	0.69	0.62	4.07	0.88	0.48	2.65
$SiO_2T_{0.2}Ol_{0.3}[EC/PC]_{4.6}$	1416.0	0.29	0.30	5.54	1.19	0.38	1.47

4.3.3 Nitrogen adsorption-desorption analysis

To further evaluate the impact of R_w ratios on pore volume, size, surface area, and assess the accuracy of TGA pore volume results, we conduct Nitrogen adsorption-desorption analysis on the oligo-PEG grafted bifunctionalized backbone $SiO_2T_{0.2}Ol_{0.2}$ with R_w ratios of 3, 5, and 15. Aerogel samples of the backbone are required for the measurement. Supercritical drying with carbon dioxide is performed to avoid pore shrinkage, though shrinkage of 10% to 20% is still observed during the process. It's important to note that the measured pore volume fraction from nitrogen adsorption-desorption is expected to be different from that obtained from TGA analysis since the sample types used in these measurements are not the same. However, by accounting for the shrinkage during supercritical drying, it is possible to calculate the initial pore volume of the wet gel, thus enable the cross-verification of volume fraction data.

It's pertinent to acknowledge that, due to the inherent characteristics of the Brunauer-Emmett-Teller (BET) isotherm, its suitability for assessing micropores (defined as pores with diameters below 2nm)

and macropores (with diameters exceeding 50nm) is limited. Consequently, the surface area associated with micropores is evaluated employing the Dubinin-Astakhov adsorption isotherm. Moreover, it is crucial to underscore that BET surface area measurement yields an averaged value, offering a broader perspective on porosity rather than specific insights into individual pore sizes. For a more detailed pore size distribution analysis, we utilize the Barrett-Joyner-Halenda (BJH) method. The outcomes of these analyses are succinctly summarized in the provided **Table 4-3**.

Table 4-3 Summary of nitrogen adsorption-desorption results of BET surface area, BJH pore volume and BET average pore diameter.

Sample name	BET Surface Area ($m^2 \cdot g^{-1}$)	BJH Desorption Pore Volume ($cm^3 \cdot g^{-1}$)	BET Average Pore Diameter (nm)
$SiO_2T_{0.2}Ol_{0.2}$_R_w 3_aerogel	257.61	0.9086	14.28
$SiO_2T_{0.2}Ol_{0.2}$_R_w 5_aerogel	296.94	1.2110	16.53
$SiO_2T_{0.2}Ol_{0.2}$_R_w 15_aerogel	286.65	1.3062	18.41

The measured surface areas of the aerogel consistently exceed 250 $m^2 \cdot g^{-1}$, indicative of their highly porous nature. It is notable that as the R_w ratio increases, there is a discernible rise in the average pore diameter. Moreover, the pore volume also exhibits an increase corresponding to the R_w ratio, aligning with the TGA results.

As mentioned earlier, supercritical drying of the wet backbone induces pore shrinkage. Similarly, the solvent exchange conducted on the wet backbone with EC/PC before TGA measurements also leads to shrinkage. To cross-verify the pore volume results, we calculate the initial wet backbone pore volume fraction from the data obtained through TGA and nitrogen adsorption-desorption measurements, taking into account the respective shrinkage data for both processes.

Starting from the Nitrogen adsorption-desorption, we first calculate the pore volume fraction ν of the aerogel by multiplying the measured aerogel pore volume V ($cm^3\ g^{-1}$) by the aerogel density ρ (g cm^{-3}). Subsequently, we consider three extreme scenarios during the supercritical drying process: First, the pore wall does not shrink but the pore dose; Second, the pore wall and pores experience the same degree of shrinkage; Third, the wall shrinks, but the pore does not. The third scenario appears unlikely. For the first case, the pore volume fraction of the wet backbone can be calculated using the formula:

$$\nu'_{wet}(N) = \frac{\nu/(1-\alpha)}{1-\nu+\nu/(1-\alpha)}$$

Where $\nu'_{wet}(N)$ represents the wet gel pore volume fraction before supercritical drying in the first case, and α denotes the degree of shrinkage.

In the second case, the pore volume fraction of the wet gel equals to that of the aerogel :

$$\nu''_{wet}(N) = \nu$$

Where $\nu''_{wet}(N)$ is the wet gel pore volume fraction for the second case.

The conversion of the wet gel pore volume fraction using TGA data follows a similar procedure to the one described above and are named as $\nu'_{wet}(TGA)$ and $\nu''_{wet}(TGA)$, for case one and two, respectively. The results are summarized in the **Table 4-4**.

Table 4-4 Summary of calculation for wet gel pore volume fraction at different R_w ratios using TGA and nitrogen adsorption-desorption measurements.

Backbone R_w ratio	**3**	**5**	**15**
Aerogel density ρ ($g \cdot cm^{-3}$)	0.59	0.55	0.55
BJH Pore Volume V ($cm^3 \cdot g^{-1}$)	0.909	1.211	1.306
Aerogel pore volume fraction ν	0.536	0.666	0.718
Shrinkage during supercritical drying α	0.15	0.19	0.35

$\nu'_{wet}(N)$	0.576	0.711	0.797
$\nu''_{wet}(N)$	0.536	0.666	0.718
Shrinkage during solvent exchange β	0.26	0.31	0.33
$\nu'_{wet}(TGA)$	0.557	0.660	0.836
$\nu''_{wet}(TGA)$	0.482	0.570	0.773

The results presented above clearly demonstrate that the upper bound (ν'_{wet}) and lower bound (ν''_{wet}) values, as determined by both the TGA and nitrogen adsorption-desorption methods, significantly overlap. This convergence strongly suggests that both methods provide accurate measurements within a reasonable margin of error. Interestingly, the shrinkage values exhibit an increase with the R_w ratio, possibly attributable to a decrease in the thickness of the backbone walls, leading to lower wall strength as the ratio increases. Furthermore, in general, shrinkage values are lower for the super critically dried samples, with the exception of the R_w = 15 material. This can be attributed to the fact that the capillary force during supercritical drying is typically lower than that experienced during the EC/PC solvent exchange.

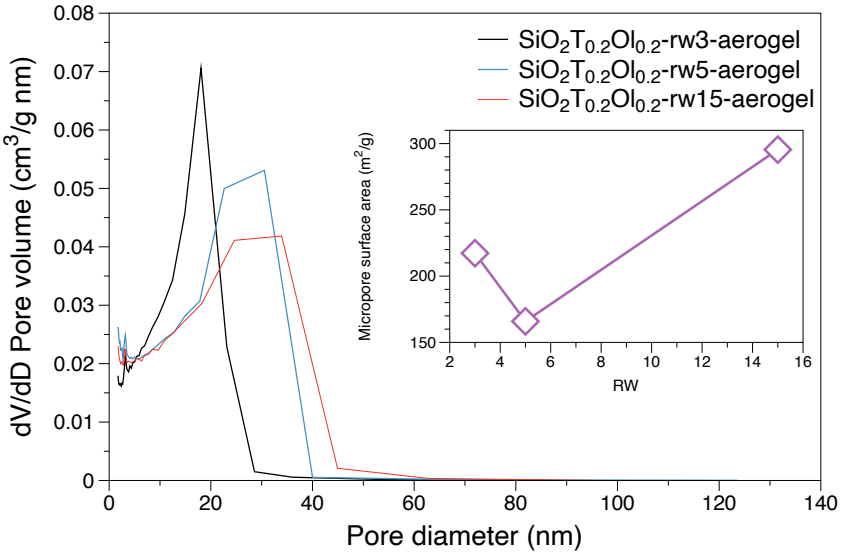

Figure 4-4 BJH desorption pore size distribution and Dubinin-Astakhov micropore surface area for aerogel samples derived from wet backbone gel with different R_w ratios.

The BJH desorption pore size distribution is presented in **Figure 4-4**. The distribution peak shifts towards larger pore diameters as the R_w ratio increases, consistent with the BET average pore diameter data present in **Table 4-3**. Interestingly, we observe that the distributions of pore diameter for R_w 5 and R_w 15 aerogel appear similar. This similarity can be attributed to the greater shrinkage experienced during the supercritical drying of the R_w 15 samples.

As shown in the inserted diagram, the micropore surface area, determined by the Dubinin-Astakhov adsorption isotherm, registers the lowest value for the R_w 5 sample, approximately 160 $m^2\ g^{-1}$. Despite this, the micropore surface area appears relatively large compared to the mesopore surface area measured by the BET isotherm. Hence, one cannot underestimate the impact of micropores on material properties. Micropores, providing the most effective nano-confinement, likely contribute to the R_w 5 material's relatively lower thermal stability during the TGA measurement.

4.3.4 SEM

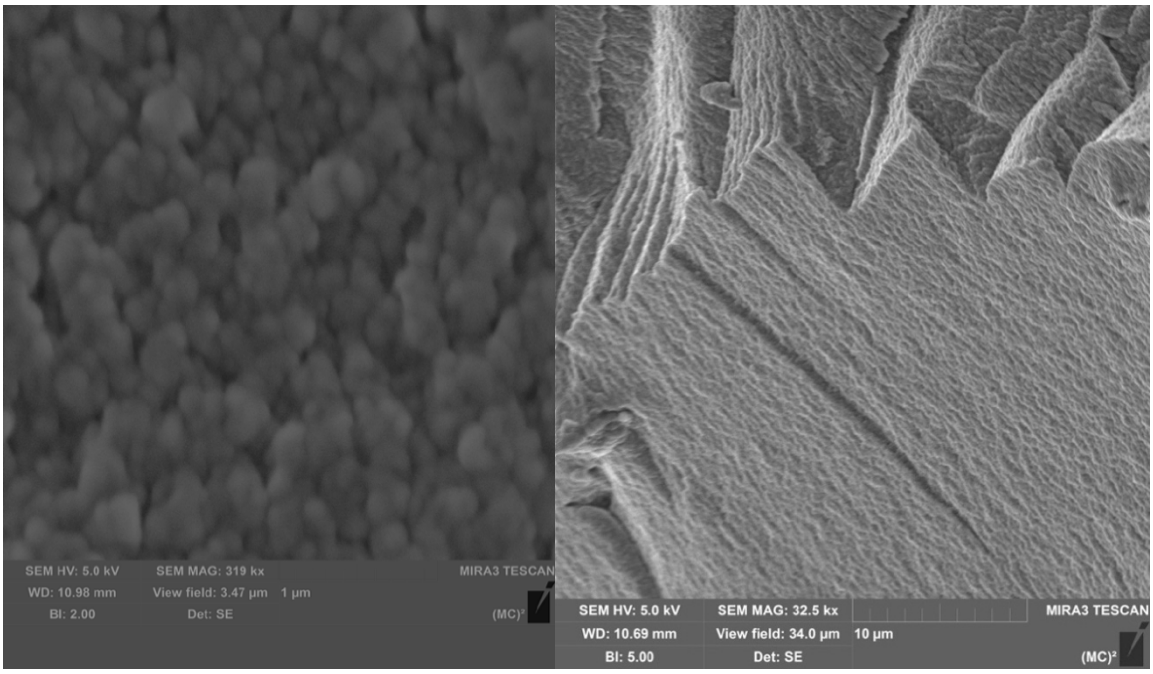

Figure 4-5 SEM cross section images for $SiO_2T_{0.2}OI_{0.2}[EC/PC]_{1.9}$ material

Figure 4-5 displays the SEM image of the intersection of the $SiO_2T_{0.2}Ol_{0.2}[EC/PC]_{1.9}$ material. In order to accommodate the electrical insulation nature of the composite electrolyte, a preliminary step involves sputter coating the sample with a thin layer of Platinum (Pt). This coating enhances surface conductivity, mitigating potential image blurring during SEM analysis. Upon close examination, it becomes evident that the backbone structure comprises an intricate assembly of nanosized particles, and the particles are roughly spherical in shape. This observation aligns with the dynamic processes of particle formation, growth, and agglomeration that occur during the sol-gel synthesis. The individual particle sizes exhibit variability, falling within the range of 100 to 300 nanometers, punctuated by nanosized inter-particle pores. The intricate inner structures of these particles remain beyond the resolution limits of our microscopy. Interestingly, some of the pores appear vacant, a phenomenon attributed to the high vacuum conditions within the SEM chamber, causing the contained EC/PC solvent to vaporize. This underscores that, despite the constraints of nano-confinement, the organic liquid filler retains a degree of volatility. In contrast, our former PEO-filled system demonstrates greater stability under high vacuum conditions, although it exhibits notably lower ionic conductivity compared to the current system.

4.3.5 DSC

The DSC traces, presented in **Figure 4-6** provide insights into the thermal behavior of the materials under investigation, including the bulk EC/PC mixture, the bifunctionalized backbone $SiO_2T_{0.2}Ol_{0.2}$, and the hybrid electrolyte $SiO_2T_{0.2}Ol_{0.2}[EC/PC]_{1.9}$. For the backbone material $SiO_2T_{0.2}Ol_{0.2}$, significantly, we do not observe any discernible glass transition temperature (T_g) for either the silica phase or the grafted organic constituents. This absence of a T_g form silica can be attributed to its significantly elevated T_g, which exceeds the measurement capability of our DSC apparatus. While the grafted oligomer and TFSISPE do not form an adequate contiguous phase, consistent with

previous research by Vrandečić et al., reported that low molecular weight PEG is typically undetectable in terms of T_g.[26]

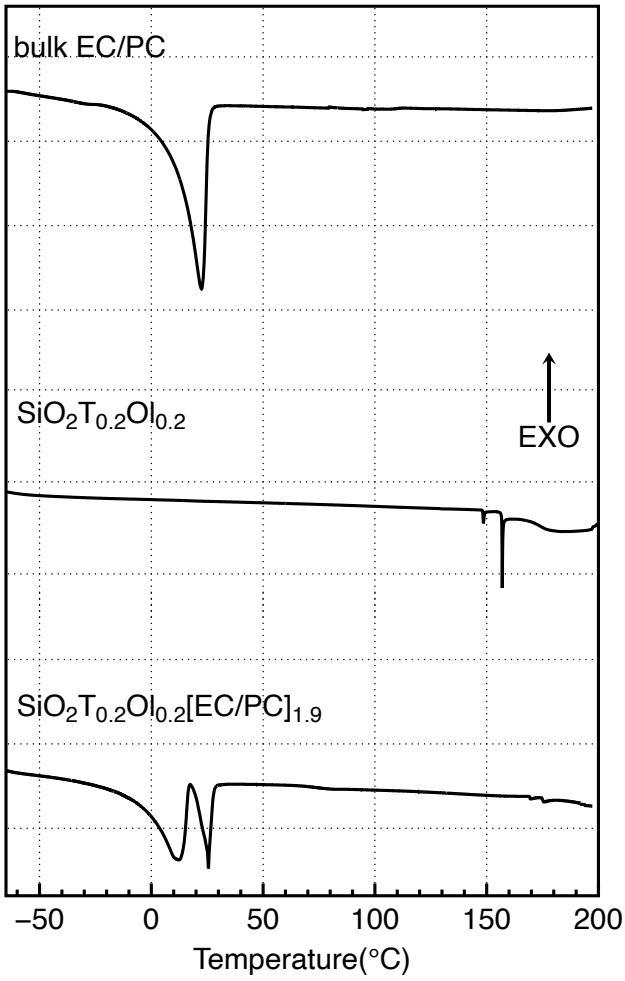

Figure 4-6 DSC heating traces for bulk EC/PC mixture, $SiO_2T_{0.2}Ol_{0.2}$ backbone and the $SiO_2T_{0.2}Ol_{0.2}[EC/PC]_{1.9}$ hybrid electrolyte.

Interestingly, our examination of $SiO_2T_{0.2}Ol_{0.2}$ does reveal several sharp endothermal peaks and a broad band in the range of 150 – 200°C. These sharp peaks exhibit reproducibility, persisting through the second and third scans, albeit with diminishing intensity. The presence of sharp peaks suggests rapid events, while the diminishment of these peaks across consecutive scans implies a partially irreversible process. A similar observation has been documented in prior research by Rubio et al.[27] From former TGA discussion, the backbone sample indicates a weight loss initiation at

approximately 100°C, partially attributed to decomposition and condensation reactions of residual Si-O-Et group, yielding ethanol as a byproduct.[22] We posit that the endothermal peaks and broad band are a consequence of the release of ethanol stemming from these decomposition reactions.[27] The reappearance of these features during subsequent scans can be attributed to the recombination of ethanol with highly strained Si-O-Si surface groups; with peak attenuation likely stemming from a reduction in the number of such strained Si-O-Si surface groups due to gradual relaxation of the silica network.

In the trace of bulk EC/PC mixture. A melting peak is evident at approximately 22.5°C during heating scan, while the cooling scan demonstrates a sharp crystallization peak at around –21°C. Of particular note is the unusual, highly crossed shape of the crystallization peak. Multiple parallel experiments, varying the cooling rate, consistently reproduce this unique peak shape. This behavior arises from the solvent undergoing rapid, near homogenized crystallization within a narrow temperature range. The concentrated heat release during crystallization can surpass the heat dissipation capacity of the equipment, leading to an increase in the crucible's internal temperature and thus the crossed appearance of the curve. While the crystallization temperature is reliable, caution must be exercised when interpreting the enthalpy due to these equipment limitations.

In the heating scan of the $SiO_2T_{0.2}Ol_{0.2}[EC/PC]_{1.9}$ hybrid electrolyte, the presence of the EC/PC phase manifests its melting behavior. However, rather than a singular peak, the curve exhibits two distinct peaks at 12.5°C and 25°C. This bifurcation can be attributed to variations in backbone nanopore sizes, as evidenced by the nitrogen adsorption-desorption measurements. Smaller pores, subjected to more pronounced confinement effects, may induce structural variations in the crystal, resulting in the formation of crystals with different melting temperatures. During the cooling scan, an EC/PC crystallization peak emerges at approximately –16°C, indicating lower undercooling than observed in the bulk mixture. This phenomenon might be attributed to the high surface area of

nanopores, providing nucleation sites that facilitate heterogeneous crystallization at a lower undercooling. Furthermore, the crystallization peak in $SiO_2T_{0.2}Ol_{0.2}[EC/PC]_{1.9}$ exhibits a less pronounced cross shape, suggesting a slower and more heterogeneous crystallization process compared to bulk EC/PC, consistent with the aforementioned hypothesis.

4.3.6 Transference number

The Li^+ transference number (t_{Li^+}) is determined using a combination of DC polarization and AC impedance methods within a Lithium symmetric cell, maintained at 20°C.[21] For this measurement, a DC voltage of 15 mV was applied for a duration of 1000 seconds. The sample sizes utilized were 0.71 cm^2 for $SiO_2T_{0.2}Ol_{0.2}[EC/PC]_{1.9}$ and 0.64 cm^2 for $SiO_2T_{0.2}Ol_{0.2}[EC/PC]_{1.9}$_0.5M samples. The "0.5M" in the later sample signifies the concentration of the introduced $LiClO_4$ salt. It is evident that this specific material is not anticipated to function as a single-ion conductor, given the inclusion of a binary salt. It's important to mention that in our prior research, a higher DC voltage of 35 mV was employed because of the elevated bulk resistance of the PEO filled system.

The transference number is calculated using:

$$t_{Li}^{+} = \frac{I^{\infty}(\Delta V - I^0 R_I^0)}{I^0(\Delta V - I^{\infty} R_I^{\infty})}$$

Where ΔV is the applied constant potential across the symmetric cell, R_I is the resistance of the interphase, I is the current and 0 and ∞ correspond to the initial and steady state.[21,28,29] Incorporating R_I into the transference number calculation is straightforward, as achieving a steady-state current following DC polarization involves both the development of a concentration gradient and the formation of a passivating layer at the electrode and electrolyte interface.[21]

The Nyquist plots for AC impedance of the two samples before and after DC polarization are presented in **Figure 4-7**, where the initial and steady states are distinguished by black and red colors,

respectively. In the high-frequency region, the presence of a semicircle, while not apparent, indicates the resistance through the solid electrolyte interface layers (R_{SEI}). The semicircle at a middle frequency represents the charge transfer resistance at the electrode/electrolyte interface (R_I).[30] Both samples exhibit an increase in R_I after DC polarization, this aligns with the theory of the formation of a passivating interfacial layer. The intercept of Nyquist curves at the Z' axis in the high-frequency region corresponds to the combination resistance (R_b), which encompasses the ionic resistance of the electrolyte and the contact resistance at the electrode/electrolyte interface.[28,29,31] R_b has significantly decreased in comparison to the former PEO-filled system, primarily due to the substantially lower bulk ionic resistivity.

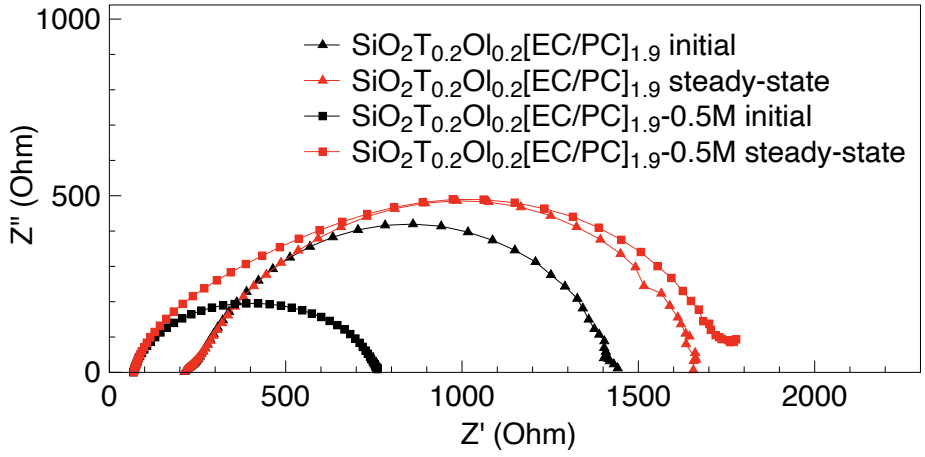

Figure 4-7 Nyquist plot of initial and steady-state AC impedance for single ion material $SiO_2T_{0.2}Ol_{0.2}[EC/PC]_{1.9}$ and $LiClO_4$ added material $SiO_2T_{0.2}Ol_{0.2}[EC/PC]_{1.9}$_0.5M. Both materials exhibit an increase in R_I after DC polarization.

The **Figure 4-8** displays the initial and steady-state DC current. As anticipated, the single-ion material $SiO_2T_{0.2}Ol_{0.2}[EC/PC]_{1.9}$, shows significantly less current drop compared to the material with added $LiClO_4$.

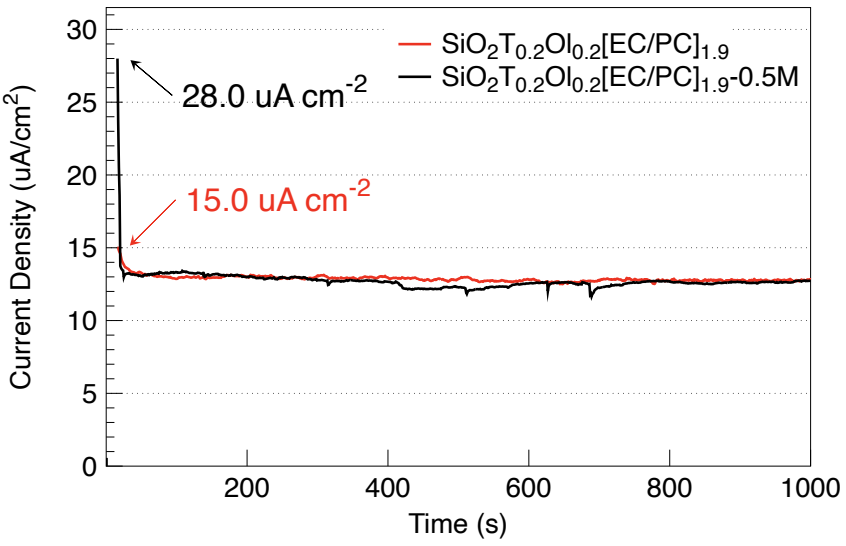

Figure 4-8 Initial and steady-state DC current density for single ion material $SiO_2T_{0.2}Ol_{0.2}[EC/PC]_{1.9}$ and $LiClO_4$ added material $SiO_2T_{0.2}Ol_{0.2}[EC/PC]_{1.9}$_0.5M. Labels demonstrate the initial current densities of both materials.

The resulting transference number for $SiO_2T_{0.2}Ol_{0.2}[EC/PC]_{1.9}$ is determined to be 0.90, which is slightly lower than what was observed in the former PEO-filled system. This difference could be attributed to the distinct nature of the ion-conducting phase in the current system and the potential measurement error.

Table 4-5 Summary of the transference number measurement parameters, the current I is calculated by multiplying the measured current density and the sample area.

	I (μA)	R_I (Ω)
$SiO_2T_{0.2}Ol_{0.2}[EC/PC]_{1.9}$ initial	10.650	1197
$SiO_2T_{0.2}Ol_{0.2}[EC/PC]_{1.9}$ steady state	8.946	1441
$SiO_2T_{0.2}Ol_{0.2}[EC/PC]_{1.9}$_0.5M initial	17.920	693
$SiO_2T_{0.2}Ol_{0.2}[EC/PC]_{1.9}$_0.5M steady state	7.808	1686

Nevertheless, this result provides confidence in the single ion-conducting characteristics of our sample. Furthermore, the measured t_{Li^+} for the sample containing 0.5M $LiClO_4$, reaches a value of

0.61. This figure is still superior to that of traditional organic liquid electrolytes using similar binary salt.[17]

4.3.7 DIS

The determination of ionic conductivity is based on the equation below:

$$\sigma = L / (R_b \cdot S)$$

Where S represents the cross-sectional area of the sample, L corresponds to the sample thickness, and R_b signifies the point of intersection between the semicircle located at high frequency and the x-axis on the AC impedance Nyquist plot.[20,32,33]

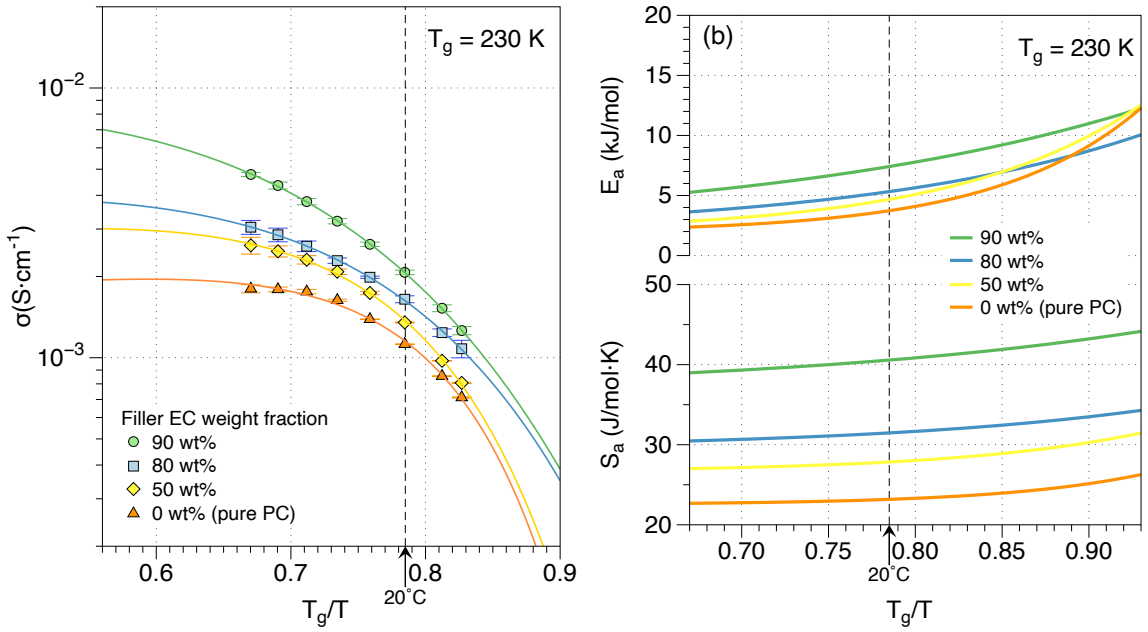

Figure 4-9 (a)Temperature dependence ionic conductivities for $SiO_2T_{0.2}Ol_{0.2}[EC/PC]_{1.9}$ hybrid electrolytes filled with EC/PC mixture with varying EC weight fractions. (b) Activation enthalpies E_a, and Activation entropies, S_a, as a function of the reciprocal temperature, as determined using the CAFE model.

Figure 4-9(a) provides a comprehensive overview of the temperature-dependent ionic conductivities for $SiO_2T_{0.2}Ol_{0.2}[EC/PC]_{1.9}$ hybrid electrolytes filled with an EC/PC mixture featuring different EC weight fractions, where 0wt% EC represents pure PC. The previously developed PEO

system exhibits typical ambient temperature ionic conductivity ranging around 10^{-4} S·cm^{-1}. In contrast, the EC/PC materials demonstrate a notable enhancement, approximately an order of magnitude higher conductivity, typically in the range of 10^{-3} S·cm^{-1}. The plot also reveals a consistent upward trend in ionic conductivity with increasing EC weight fraction. Of particular interest is the observation that the temperature-dependent conductivities for EC/PC-filled samples with different EC concentrations do not converge at elevated temperatures, as indicated by the fitting of the data points. This divergence suggests varying degrees of improvement in ion mobility due to increased thermal energy, indicating potential differences in underlying conducting mechanisms. This finding aligns with a study by Tobishima et al, which reported that the increase in the ionic dissociation degree of Li^+, the decrease in solvent viscosity, and the reduction in Li^+ radius are the main reasons for the conductivity enhancement with higher EC content, showcasing distinct mechanisms at play.[17] Despite the conductivity boost with increased EC content, it's crucial to consider the stability of EC/PC mixtures, particularly at high EC concentrations. Due to its crystalline nature, EC has a tendency to precipitate out from the mixture if it exceeds 90wt%. Precipitation can have detrimental effects on the electrolyte, leading to EC dendrites that may penetrate and weaken the silica backbone, obstructing the continuous ion migration pathway. Therefore, all subsequent results are based on the use of 80wt% EC, a composition thoroughly tested and confirmed to remain uniform across and above the temperature range of the DIS measurements (5°C – 70°C).

The activation free energy for cation transport is a measure that reflects the energy landscape of the system, which in turn is representative of the molecular configuration and interactions between constituents. It is therefore an important attribute in view of elucidating elementary transport mechanisms. As evident from the data shown in **Figure 4-9**(a), ln σT *vs.* T^{-1} does not exhibit Arrhenius behavior, and the empirical formalisms commonly employed to capture the curvature in

the data do not yield the activation enthalpies or entropies as fitting parameters. Here we employ a new approach we developed based on transition state theory (TST), which accounts for the non-Arrhenius behavior in the temperature dependence of conductivity that is characteristic for many glass forming materials above the glass transition temperature. As the supercooled liquid traverses the glass transition regime, structural rearrangements that involve gradual shifts in molecular packing density and reconfiguration of atomic interaction topology are accompanied by changes in the free energy landscape. Changes in the activation enthalpy and entropy for atomic transport processes are consequentially manifest. A detailed discussion of the rationale behind our correlative activation free energy (CAFE) model can be found in our earlier publication.[40] We begin with the basic formalism for ionic conductivity expressed in the context of TST,[41]

$$\sigma = \frac{\rho_{Li^+}\left(zq_e\right)^2}{k_B T}\gamma d_0^2 \Gamma_0 e^{S_a(T)/k_B} e^{-E_a(T)/k_B T}, \quad (1)$$

where ρ_{Li^+} is the volumetric number density of cations, z is its valence, q_e is electronic unit charge, k_B is the Boltzmann factor, γ is the geometry factor, which is equal to one over twice the dimensionality of the underlying space, d_0 is the cation jump distance and Γ_0 is the attempt frequency. E_a and S_a are the activation enthalpy and entropy, respectively. The main difference compared to the basic formulation of this expression is that E_a and S_a are assumed to be temperature dependent. Specifically, expressing these quantities as a function of the reciprocal temperature normalized with respect to T_g, i.e., $\chi = T_g/T$, $E_a(\chi) = \psi(\chi)(E_G - E_0) + E_0 = \psi(\chi)\Delta E_a + E_0$, where E_G and E_0 represent activation enthalpies for cation migration in the material at T_g and at infinite temperature, respectively. Similarly, $S_a(\chi)$ takes a similar form $S_a(\chi) = \psi(\chi)\Delta S_a + S_0$. Here, $\psi(\chi)$ is the generalized logistic function $\psi(\chi) = \left(1 + C_0 e^{\nu\beta_g H(1-\chi)}\right)^{-1/\nu}$, which is adopted to capture the change in free energy landscape during the transition behavior between liquid and glass states. It exhibits a

skewed sigmoidal shape, governed by parameters H, ν, and $\beta_g = \left(N_A\, k_B\, \mathrm{T}_g\right)^{-1}$, controlling the steepness, asymmetry, and inflection point of the curve, respectively. C_0 is a constant determined by the value of $\psi(\chi)$ at $\chi = 1$. Substituting, multiplying both sides with the temperature, and taking the logarithm yields

$$\ln(\sigma \mathrm{T}) = P + S_0/\mathrm{k}_B + \psi(\chi)(\Delta S_a/\mathrm{k}_B - \chi \Delta E_a) - \chi E_0, \quad (2)$$

where we grouped temperature independent terms from the pre-factor as $P = \ln\left(\rho_{\mathrm{Li}^+}\left(\tilde{z}q_e\right)^2 \gamma d_0^2 \Gamma_0 k_B^{-1}\right)$.

The lines depicted in **Figure 4-9**(b) illustrate the Activation enthalpies E_a, and entropies, S_a, as a function of the reciprocal temperature, determined using the CAFE model. Distinct EC weight fractions in the EC/PC mixture are differentiated by color. In general, systems with higher EC weight fractions exhibit elevated activation enthalpies and activation entropies, as anticipated due to the increased tendency to form crystalline domains, resulting in higher energy barriers for ion hopping. Systems with lower EC contents demonstrate a more noticeable relative increase in E_a with decreasing temperature. This observation suggests more substantial structural changes throughout the glass transition regime, exerting a commensurate influence on cation mobility. It is noteworthy that high activation enthalpies are typically accompanied by high activation entropies, as also observed in **Figure 4-9**(b), and these factors have opposing effects on cation mobility.

In our pursuit of enhancing ionic conductivity, we systematically explore three primary approaches. Firstly, building upon our prior work, where grafting oligo-PEG led to nearly a tenfold increase in sample conductivity by inducing network modification and improving compatibility between silica and organic phase, we apply the same concept here. Secondly, we introduce $LiClO_4$ as a direct means of intensifying charge carrier concentration. Thirdly, based on the TGA and nitrogen adsorption-desorption results indicating changes in pore volume with varying R_w ratios, we examine how these changes affect conductivity.

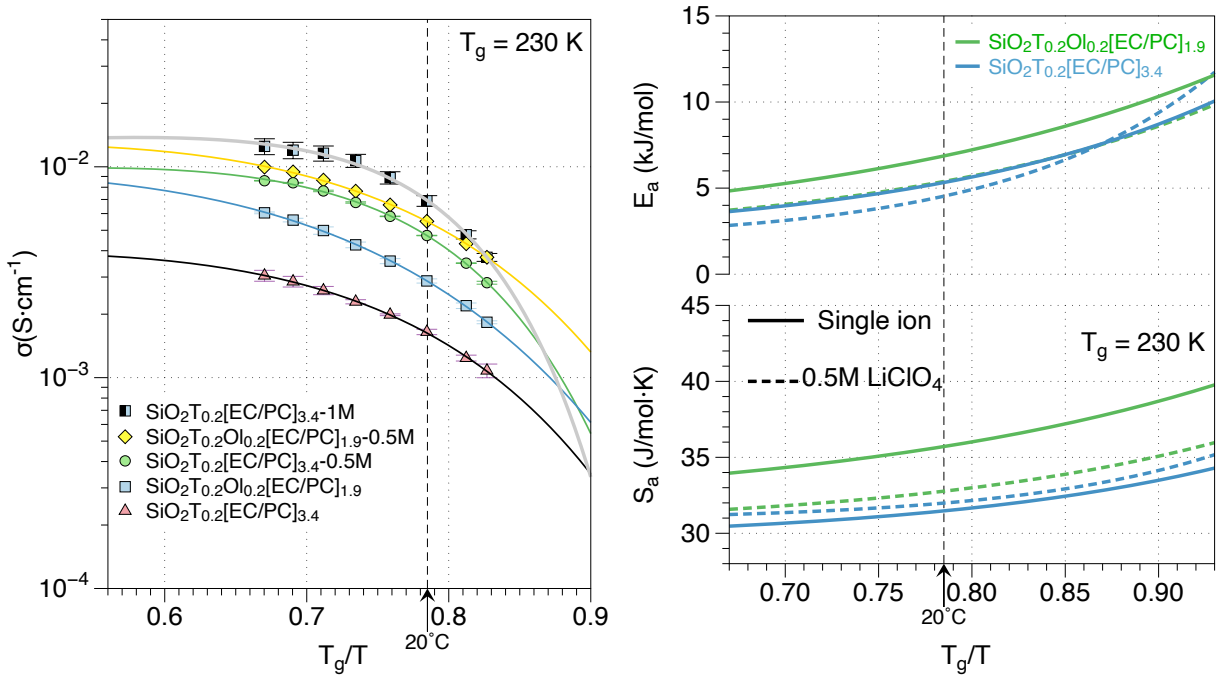

Figure 4-10 (a) Temperature dependent ionic conductivity comparation by applying strategies of oligo-PEG grafting, and adding different concentrations of $LiClO_4$ binary salt. (b) Activation entropies and enthalpies calculated by CAFÉ model for systems with or without oligo-PEG and $LiClO_4$. The solid line and dotted line distinguish the single ion materials and the $LiClO_4$ materials, respectively.

The results of implementing the first and second strategies are illustrated in **Figure 4-10**(a). In the current system, sole grafting of oligo-PEG leads to an approximately twofold increase in ion conductivity, which can be indicated by comparing $SiO_2T_{0.2}[EC/PC]_{3.4}$ with $SiO_2T_{0.2}Ol_{0.2}[EC/PC]_{1.9}$ materials. The improvement in ionic conductivity, although significant, does not reach the levels attained in the previous PEO-filled system, which demonstrated roughly an order of magnitude higher conductivity. Moreover, our experiments confirm that the addition of $LiClO_4$ is a highly effective method for enhancing conductivity. With a simple incorporation of a 0.5M concentration of lithium salt, the sample designated as $SiO_2T_{0.2}[EC/PC]_{3.4}$-0.5M achieves a room temperature conductivity of 4.72×10^{-3} S·cm^{-1}. Further elevating the salt concentration to 1 M results in an increase to 6.90×10^{-3} S·cm^{-1}. While effective, adding binary salt can lead to an increased concentration of mobile anions, specifically ClO^-, potentially causing a reduction in the transference

number. However, by combining oligo-PEG grafting with the addition of a modest concentration of binary salt (0.5 M), we still achieved a room temperature conductivity of 5.51×10^{-3} S·cm^{-1}, and an acceptable transference number of 0.61. In **Figure 4-10**(b), the activation energy vs. the normalized reciprocal temperature is illustrated. Generally, the activation enthalpies and entropies for oligo-PEG grafted materials are higher compared to materials without it. This is in contrast to the findings in the former PEO system, where we observed that oligo-PEG significantly reduced the activation enthalpy due to network modification and better coupling between the polymer and inorganic phases. While the former effect still exists in the EC/PC system and will be further discussed in the mobility analysis, the latter relies on the structural similarity between the oligo-PEG and the filler, which is not the case in the current system. Instead, the oligo-PEG might block the hopping of Li^+ due to steric hindrance, explaining the increase in activation energy in the grafted materials. The addition of $LiClO_4$, however, appears to reduce activation energy, and the curves show a more pronounced relative increase in E_a with decreasing temperature compared to single-ion materials (represented by solid lines). This might be due to the decrease in the number of solvent molecules surrounding the Li^+ due to higher ion concentration, which could reduce the size of the ion-solvent cluster sizes and improve transportation.

In **Figure 4-11**(a), the results of varying the R_w ratio are presented, with all materials in this plot having undergone oligo-PEG grafting. The $SiO_2T_{0.2}Ol_{0.3}[EC/PC]_{4.6}$ material, possessing the largest pore volume and the lowest ion donor concentration, shows the lowest conductivity, while the $SiO_2T_{0.2}Ol_{0.2}[EC/PC]_{1.3}$ sample exhibits the opposite trend. The **Figure 4-11**(b) shows calculated activation energies for above materials. In particular, the $SiO_2T_{0.2}Ol_{0.2}[EC/PC]_{1.9}$, shows the lowest activation enthalpy and entropy, despite having modest conductivity and pore volume. Recalling from the nitrogen adsorption-desorption, the modest pore volume materials show the lowest

micropore surface area. Combining this fact with the activation energy analysis, we posit that micropores have an undeniable effect that can hinder ion activation due to stronger confinement.

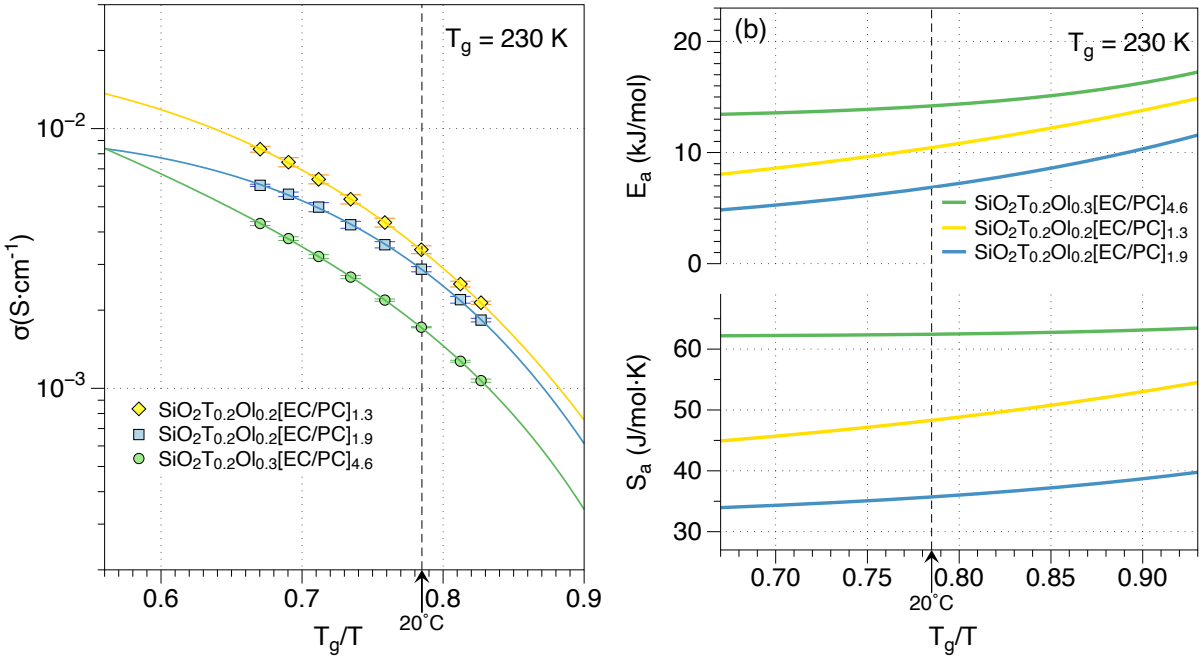

Figure 4-11 (a)Temperature dependent ionic conductivities of hybrid electrolytes fabricated using backbones with different pore volumes by alternating R_w ratio. (b)CAFÉ calculated activation energies for materials with different pore volumes.

Given the variations in charge carrier concentration of different materials and in order to clearly discern the influence of structure and cation hopping mechanism on the ionic conductivity, it is advised to discern between conductivity and mobility, which are related according to:

$$\sigma = z\, q_e\, \rho_{Li^+}\, \mu$$

Where $z = 1$ for Li^+, q_e represents the charge of an electron, which is 1.602×10^{-19} C , ρ_{Li^+} corresponds to the volumetric charge carrier concentration, and μ denotes the ionic mobility in response to an applied electric field, in accordance with Ohm's law. In contrast to ionic conductivity, carrier mobility offers a more intrinsic insight, closely linked to the material's inherent properties. This intrinsic aspect allows us to delve deeper into the conduction mechanism. By

leveraging the measured Li^+ transference number (t_{Li}^+), we can readily calculate the conductivity contributed by Li^+ by multiplying the measured total conductivity with t_{Li}^+. Given limited available data from the t_{Li}^+ measurements, we make the reasonable assumption that samples without added lithium salt (single ion samples) possess the same t_{Li}^+ value of 0.9. The corresponding results are presented in the **Table 4-6** below.

Table 4-6 Summary of the Li^+ mobility for hybrid electrolytes with varying pore volume, with or without added binary lithium salt and oligo-PEG

Designation	Li^+ number density (nm^{-3})	Conductivity ($S \cdot cm^{-1}$)	Li^+ conductivity ($S \cdot cm^{-1}$)	Li^+ mobility ($S\ cm^2 \cdot C^{-1}$)
$SiO_2T_{0.2}[EC/PC]_{3.4}$	0.31	$1.648 \cdot 10^{-3}$	$1.483 \cdot 10^{-3}$	$2.986 \cdot 10^{-5}$
$SiO_2T_{0.2}Ol_{0.2}[EC/PC]_{1.3}$	0.70	$3.419 \cdot 10^{-3}$	$3.077 \cdot 10^{-3}$	$2.744 \cdot 10^{-5}$
$SiO_2T_{0.2}Ol_{0.2}[EC/PC]_{1.9}$	0.62	$2.875 \cdot 10^{-3}$	$2.588 \cdot 10^{-3}$	$2.606 \cdot 10^{-5}$
$SiO_2T_{0.2}Ol_{0.3}[EC/PC]_{4.6}$	0.30	$1.719 \cdot 10^{-3}$	$1.547 \cdot 10^{-3}$	$3.219 \cdot 10^{-5}$
$SiO_2T_{0.2}Ol_{0.2}[EC/PC]_{1.9}$-0.5M	0.92	$5.514 \cdot 10^{-3}$	$3.364 \cdot 10^{-3}$	$2.282 \cdot 10^{-5}$

As shown in **Table 4-6**, the calculated Li^+ mobilities in the oligo-PEG grafted materials, i.e. $SiO_2T_{0.2}Ol_{0.2}[EC/PC]_{1.3}$, $SiO_2T_{0.2}Ol_{0.2}[EC/PC]_{1.9}$, and $SiO_2T_{0.2}Ol_{0.3}[EC/PC]_{4.6}$ do not show improvement when compared to that of the non oligo-PEG grafted $SiO_2T_{0.2}[EC/PC]_{3.4}$ material. As already mentioned in above analysis, this phenomenon contrasts with the former PEO-filled system, where the structural similarity between PEO and oligo-PEG significantly enhanced Li^+ mobility by improving fill factor and enhancing phase compatibility. In the EC/PC system, this mechanism does not come into play, which is reasonable given the apparent lack of structural similarity between EC/PC and oligo-PEG. However, the grafting of oligo-PEG still affect pore structure, as indicated

by the TGA. The introduction of oligo-PEG reduces the total amount of organic phase compared to the silica backbone, leading to an increase in the number of Li^+ donor sites per unit volume and, consequently, higher conductivity proportional to the Li^+ concentration. Furthermore, while carrier mobility is generally considered independent of carrier concentration, the argument above is not supported by comparing mobility data between $SiO_2T_{0.2}Ol_{0.2}[EC/PC]_{1.9}$ and $SiO_2T_{0.2}Ol_{0.2}[EC/PC]_{1.9}$-0.5M. These two samples only differ in carrier concentration, with the higher concentration sample exhibiting lower mobility. This phenomenon can be explained by the interaction between charge carriers at high concentration, where the conducting pathways become crowded, leading to a decrease in transportation efficiency.

Finally, the comparison of Li^+ mobility among oligo-PEG grafted samples with different pore volumes reveals an intriguing phenomenon. Although value of mobility does not vary too much, it appears that a minimum mobility exists somewhere between $SiO_2T_{0.2}Ol_{0.3}[EC/PC]_{4.6}$ and $SiO_2T_{0.2}Ol_{0.2}[EC/PC]_{1.3}$, as $SiO_2T_{0.2}Ol_{0.2}[EC/PC]_{1.9}$ demonstrating the lowest mobility. However, this observation must be tempered by the limitation of data points. Recall the activation enthalpy is the lowest for $SiO_2T_{0.2}Ol_{0.2}[EC/PC]_{1.9}$, these observations introduce a compelling puzzle. Conventionally, a lower activation free energy would suggest that ions surmount energy barriers more effortlessly, potentially resulting in higher mobility. However, the interplay between activation energy and mobility is intricate. Mobility hinges not solely on activation energy but also on an array of material-specific factors, encompassing structural attributes such as pore dimensions and morphology.

4.4 Conclusion

This study introduces an organic-inorganic hybrid electrolyte with a nanoporous silica backbone housing an EC/PC mixture, employing a correlative activation free energy analysis based on

transition state theory (TST) for a comprehensive understanding of the conducting mechanism. Verified through transference number measurements, the functionalization with TFSISPE ion donor ensures single-ion conducting behavior. Nitrogen adsorption-desorption measurements validate controlled pore structure manipulation by varying the R_w ratios. Cross-validation between nitrogen adsorption-desorption and TGA affirms the accuracy of both methods in measuring pore volume.

Conductivity variations with EC weight fraction in the EC/PC mixture demonstrate an increasing trend with EC concentration, cautioning against precipitation risks at 90 wt% EC. The hybrid material exhibits a noteworthy 10^{-3} S·cm^{-1} ionic conductivity, representing a tenfold improvement over the former PEO-filled system. Cation mobility calculations identify the $SiO_2T_{0.2}Ol_{0.3}[EC/PC]_{4.6}$ material, featuring oligo-PEG grafting and the largest pore volume, with the highest mobility at $3.219 \cdot 10^{-5}$ S cm^2·C^{-1}. However, oligo-PEG grafting minimally affects mobility improvement. CAFE analysis consistently indicates higher activation enthalpies and entropies for oligo-PEG grafted materials compared to those without, in contrast to the former PEO-filled system. This deviation may be attributed to the absence of structural similarity between oligo-PEG and EC/PC, rendering the coupling effect nonfunctional. Moreover, oligo-PEG may impede Li^+ hopping due to steric hindrance, elucidating the increase in activation energy in grafted materials. The addition of $LiClO_4$ effectively enhances conductivity by increasing carrier concentration and reduces activation energy, potentially due to decreased solvent molecules around Li^+ and subsequent improvements in ion-solvent cluster sizes for enhanced transportation.

4.5 References

1. Rohan, R. et al. A high performance polysiloxane-based single ion conducting polymeric electrolyte membrane for application in lithium ion batteries. J. Mater. Chem. A 3, 20267-20276 (2015).

2. Tarascon, J.-M. & Armand, M. Issues and challenges facing rechargeable lithium batteries. Nature 414, 359-367 (2001).

3. Sakuda, A., Hayashi, A. & Tatsumisago, M. Sulfide Solid Electrolyte with Favorable Mechanical Property for All-Solid-State Lithium Battery. Scientific Reports 3, 2261 (2013).

4. Petronico, A. et al. Solid–Liquid Lithium Electrolyte Nanocomposites Derived from Porous Molecular Cages. J. Am. Chem. Soc. 140, 7504-7509 (2018).

5. Wiers, B. M., Foo, M.-L., Balsara, N. P. & Long, J. R. A Solid Lithium Electrolyte via Addition of Lithium Isopropoxide to a Metal–Organic Framework with Open Metal Sites. J. Am. Chem. Soc. 133, 14522-14525 (2011).

6. Brinker, C. J. & Scherer, G. W. (eds Brinker, C. J. & Scherer, G. W.) 96-233 (Academic Press, San Diego, 1990).

7. Brinker, C. J. & Scherer, G. W. (eds Brinker, C. J. & Scherer, G. W.) 302-355 (Academic Press, San Diego, 1990).

8. Kim, Y. et al. High Ion Conducting Nanohybrid Solid Polymer Electrolytes via Single-Ion Conducting Mesoporous Organosilica in Poly(ethylene oxide). Chem. Mater. 29, 4401-4410 (2017).

9. Oh, H. et al. Poly(arylene ether)-Based Single-Ion Conductors for Lithium-Ion Batteries. Chem. Mater. 28, 188-196 (2016).

10. Rohan, R. et al. Functionalized meso/macro-porous single ion polymeric electrolyte for applications in lithium ion batteries. J. Mater. Chem. A 2, 2960-2967 (2014).

11. Zhu, Y. et al. A Composite Gel Polymer Electrolyte with High Performance Based on Poly(Vinylidene Fluoride) and Polyborate for Lithium Ion Batteries. Adv. Energy Mater. 4, 1300647 (2014).

12. Rohan, R. et al. Functionalized polystyrene based single ion conducting gel polymer electrolyte for lithium batteries. The 7th International Conference on Materials for Advanced Technologies (ICMAT 2013) Symposium A: Advanced Energy Storage Systems: Lithium ion batteries and beyond 268, 294-299 (2014).

13. Zhang, H., Zhang, X., Shiue, E. & Fedkiw, P. S. Single-ion conductors for lithium batteries via silica surface modification. Journal of Power Sources 177, 561-565 (2008).

14. Tian, L.-Y., Huang, X.-B. & Tang, X.-Z. Single-ionic gel polymer electrolyte based on polyvinylidene fluoride and fluorine-containing ionomer. European Polymer Journal 40, 735-742 (2004).

15. Villaluenga, I. et al. Cation only conduction in new polymer–SiO2 nanohybrids: Na+ electrolytes. J. Mater. Chem. A 1, 8348-8352 (2013).

16. Dewing, B. L., Bible, N. G., Ellison, C. J. & Mahanthappa, M. K. Electrochemically Stable, High Transference Number Lithium Bis(malonato)borate Polymer Solution Electrolytes. Chem. Mater. 32, 3794-3804 (2020).

17. Tobishima, S.-I. & Yamaji, A. Ethylene carbonate—propylene carbonate mixed electrolytes for lithium batteries. Electrochimica Acta 29, 267-271 (1984).

18. Katayama, N., Kawamura, T., Baba, Y. & Yamaki, J.-i. Thermal stability of propylene carbonate and ethylene carbonate–propylene carbonate-based electrolytes for use in Li cells. Journal of Power Sources 109, 321-326 (2002).

19. Benrabah, D., Sylla, S., Alloin, F., Sanchez, J.-Y. & Armand, M. Perfluorosulfonate-polyether based single ion conductors. Electrochimica Acta 40, 2259-2264 (1995).

20. Wang, W., Yi, E., Fici, A. J., Laine, R. M. & Kieffer, J. Lithium Ion Conducting Poly(ethylene oxide)-Based Solid Electrolytes Containing Active or Passive Ceramic Nanoparticles. J. Phys. Chem. C 121, 2563-2573 (2017).

21. Evans, J., Vincent, C. A. & Bruce, P. G. Electrochemical measurement of transference numbers in polymer electrolytes. Polymer 28, 2324-2328 (1987).

22. Brinker, C. J. & Scherer, G. W. (eds Brinker, C. J. & Scherer, G. W.) 514-615 (Academic Press, San Diego, 1990).

23. Ellerbrock, R., Stein, M. & Schaller, J. Comparing amorphous silica, short-range-ordered silicates and silicic acid species by FTIR. Scientific Reports 12, 11708 (2022).

24. Rey, I. et al. Spectroscopic and Theoretical Study of (CF3SO2)2N- (TFSI-) and (CF3SO2)2NH (HTFSI). J. Phys. Chem. A 102, 3249-3258 (1998).

25. Tseng, Y.-C. et al. Polymer electrolytes based on Poly(VdF-co-HFP)/ionic liquid/carbonate membranes for high-performance lithium-ion batteries. Polymer 173, 110-118 (2019).

26. Vrandečić, N. S., Erceg, M., Jakić, M. & Klarić, I. Kinetic analysis of thermal degradation of poly(ethylene glycol) and poly(ethylene oxide)s of different molecular weight. Thermochimica Acta 498, 71-80 (2010).

27. Rubio, F., Rubio, J. & Oteo, J. L. A DSC study of the drying process of TEOS derived wet silica gels. Thermochimica Acta 307, 51-56 (1997).

28. Shigenobu, K., Dokko, K., Watanabe, M. & Ueno, K. Solvent effects on Li ion transference number and dynamic ion correlations in glyme- and sulfolane-based molten Li salt solvates. Phys. Chem. Chem. Phys. 22, 15214-15221 (2020).

29. Chintapalli, M. et al. Relationship between Conductivity, Ion Diffusion, and Transference Number in Perfluoropolyether Electrolytes. Macromolecules 49, 3508-3515 (2016).

30. Choi, W., Shin, H.-C., Kim, J. M., Choi, J.-Y. & Yoon, W. Modeling and Applications of Electrochemical Impedance Spectroscopy (EIS) for Lithium-ion Batteries. Journal of electrochemical science and technology 11, 1-13 (2020).

31. Yu, Z. et al. A Dynamic, Electrolyte-Blocking, and Single-Ion-Conductive Network for Stable Lithium-Metal Anodes. Joule 3, 2761-2776 (2019).

32. Liu, W. et al. Ionic Conductivity Enhancement of Polymer Electrolytes with Ceramic Nanowire Fillers. Nano Lett. 15, 2740-2745 (2015).

33. Wan, Z. et al. Low Resistance–Integrated All-Solid-State Battery Achieved by Li7La3Zr2O12 Nanowire Upgrading Polyethylene Oxide (PEO) Composite Electrolyte and PEO Cathode Binder. Adv. Funct. Mater. 29, 1805301 (2019).

34. Wang, G. & Kieffer, J. Contiguous High-Mobility Interphase Surrounding Nano-Precipitates in Polymer Matrix Solid Electrolyte. ACS Appl. Mater. Interfaces 15, 848-858 (2023).

CHAPTER V Functionalized Porous Silica-Ionic Liquid Hybrid Electrolyte

5.1 Introduction

The role of electrolytes in the realm of lithium-ion batteries is undeniably pivotal. The increasing demand for applications necessitating rapid charge-discharge rates, the quest for high-performance electrolytes has gained vital significance. Such high-performance electrolytes must exhibit attributes including elevated ionic conductivity, robust thermal stability, and substantial mechanical integrity.[1–3] The presently used carbonate liquid electrolytes, including propylene carbonate (PC) and ethylene carbonate (EC) and their mixtures, fall short of meeting these requirements. Numerous efforts are underway to replace carbonate liquid electrolytes with both solid-state systems and gel-type systems based on polymers, ceramics, glasses, as well as combinations of these in the form of composites or hybrids.[4] Among these, a specific hybrid design consisting of an inorganic compound or thermoset polymer that forms a nano-porous rigid backbone whose pores are filled with a low-glass transition temperature organic phase stands out, as it has the potential to simultaneously satisfy the demands for simultaneously high mechanical strength and ionic conductivity. This is noteworthy because traditionally, these two properties oppose one another. The backbone material, characterized by a high modulus network structure, serves in a load-bearing capacity. It can also mitigate dendrite growth and enhance the overall chemical and thermal stability of the electrolytic system.[4] The pursuit of such backbone materials has led to extensive exploration of various substances,

encompassing inorganics like porous ceramic networks and silica-based gels, as well as organics like cross-linked polymers and high-stiffness linear polymers.[2,5–13] Among these, silica gel emerges as an exemplary choice due to its high specific surface area, high porosity, high rigidity, ease of synthesis, and functionalization. These properties have been demonstrated by previous research efforts.[14]

However, the backbone alone cannot function as an electrolyte without its pores being filled by additional materials, which typically serve as conduits for ion transport. The choices for fillers include liquids such as carbonates, low molecular weight polymers, and ionic liquids.[4] For solid fillers, high molecular weight polymers like poly(ethylene oxide) (PEO), polyvinylidene fluoride (PVDF), or copolymers containing polar groups are common choices.[4,11–13,15–17] The methods for introducing fillers into the pores can include vacuum-assisted impregnation, hot-pressing, or in-situ polymerization, depending on the filler and backbone properties and fabrication methods.[4,11,16] Polymer fillers, whether with high or low molecular weight, often exhibit high viscosity at room temperature due to chain entanglement and intermolecular attractions. Consequently, the resulting hybrid electrolytes typically have conductivities ranging from 10^{-7} to 10^{-4} $S \cdot cm^{-1}$, which is several orders of magnitude lower than the practical usage threshold of 10^{-3} $S \cdot cm^{-1}$.[12,16,18,19] On the other hand, carbonate fillers like EC or PC, while exhibiting a conductivity of 10^{-3} $S \cdot cm^{-1}$, can present potential safety concerns due to their volatility under elevated temperatures (i.e. >70°C), even when confined in a nano porous matrix.[20,21] In this context, ionic liquids (ILs) present a promising alternative to polymer and carbonate fillers. ILs are a class of organic salts that remain in a liquid state at or near room temperature. They comprise large organic cations and various anions, with common IL cations including imidazolium, pyridinium, alkylammonium, alkyl phosphonium, pyrrolidinium, guanidinium, and alkyl pyrrolidinium. IL anions can be chosen from a wide array of inorganic anions, including halides (Cl^-, Br^-, I^-), polyatomic inorganics (PF_6^-, BF_4^-), or organic anions such as NO_3^-, $TFSI^-$, and Tf^-.[22] ILs are known for their unique properties, including high

thermal stability, non-flammability, and high ionic conductivity.[23–28] Moreover, ILs often possess a wide electrochemical window, enabling them to operate over a broad range of voltages without undesirable side reactions. These characteristics are especially advantageous for high-energy-density batteries.[23]

5.2 Materials design rationale

In this study, we investigate a novel hybrid electrolyte design based on a functionalized porous silica backbone incorporating 1-Ethyl-3-methylimidazolium bis(trifluoromethylsulfonyl)imide (EMIM TFSI) ionic liquid for use in lithium-ion batteries. The silica backbone is derived from the sol-gel route using tetraethyl-orthosilicate (TEOS). Note that EMIM TFSI is a hydrophobic and water-immiscible IL. Thus, its compatibility with silica gel is expected to be poor due to the abundant Si-OH surface groups on the pore wall.[29,30] To address this issue, the pore surface of the backbone is grafted with 2-[(Trifluoromethanesulfonylimido)-N-4-sulfonylphenyl] ethyl (TFSISPE) groups. The structural similarities between TFSISPE and $TFSI^-$ in the IL allow the former to act as a coupling agent, facilitating the contact between the pore surface and the IL, potentially forming a highly conductive interface. Furthermore, TFSISPE exhibits good Li^+ donating capability, as the bulky imide groups have weak binding with Li^+.[5] With the influence of the backbone's structure on ion conduction process in mind, we control pore sizes by altering the water to TEOS ratio (R_w ratio) during the backbone sol-gel synthesis. The chemical composition of the hybrid electrolyte system is elucidated using vibrational spectroscopy (FT-IR). Additionally, electrolyte component weight fractions, thermal stability, and phase transformations are evaluated through thermal analysis using thermogravimetric analysis (TGA) and differential scanning calorimetry (DSC). The Li^+ transference number, t_{Li^+}, is measured using a combination of DC polarization and AC impedance methods. The electrical response of the polymer is examined through broadband dielectric

impedance spectroscopy (DIS) over a temperature range of 5°C – 70°C. With the conductivity and Li^+ concentration data in hand, charge carrier mobility is calculated and assessed relative to the R_w ratio. We report on our findings for two series of materials, one where all Li^+ ions are introduced via the TFSISPE donor group that is grafted to the silica backbone. The ionic liquid consists of only EMIM TFSI. For the second series, we add Lithium bis(trifluoromethane)sulfonimide (LiTFSI) to the EMIM TFSI pore fluid in various concentrations as a direct means of enhancing Li^+ concentrations. In both series, we vary the pore size distribution and study the resulting ionic transport properties.

5.3 Experimental procedures

5.3.1 Preparation of silica backbone precursor

A 50 ml beaker is used to combine 10.00 g (10.64 ml at 20 °C) of Tetraethyl orthosilicate (TEOS, 99%, Aldrich) with 0.48 ml of 1M HCl. Deionized water is then carefully added in varying quantities, depending on the desired water to TEOS ratio, also known as the R_w ratio, for each sample. Specifically, for R_w ratios of 3, 4, 5, 7 and 15, corresponding water volumes of 2.11 ml, 2.97 ml, 3.84 ml, 5.57 ml and 12.48 ml are employed. The resulting mixture undergoes a thorough homogenization process for 3 hours at room temperature to ensure complete TEOS hydrolysis. Subsequently, the system is continuously stirred for an additional 4 hours at 65°C to promote the condensation reaction.

5.3.2 Synthesis and prehydorlysis of the triethylammonium 2-[(trifluoromethanesulfonylimido)-N-4-sulfonylphenyl]ethyl-trimethoxysilane

In a 50 ml three-neck flask, 1.00 g of Trifluoromethanesulfonamide (95%, Aldrich) is combined with 4.66 ml of triethylamine (99.5%, Aldrich). To serve as a solvent, 28.00 ml of dichloromethane

(99.8%, Aldrich) is added and stirred until complete dissolution is achieved. Next, 4.28 g of 4-[2-(trimethoxysilyl)-ethyl] benzene-1-sulfonyl chloride (50wt% solution in dichloromethane, Aldrich) is introduced, causing a slight yellow tint in the solution. The resulting mixture undergoes stirring and heating at 40°C overnight. Subsequently, distillation is employed to remove the solvent and excess triethylamine, yielding a dark, orange-colored wax product.[31] This final product is further purified through vacuum oven treatment under 1 kPa (10 torr) conditions at 85°C for 2 hours, ensuring the removal of residual volatiles.

5.3.3 Grafting of ion donor and oligo PEO to the silica backbone

0.40 g of 2-[Methoxy(polyethyleneoxy)$_{6\text{-}9}$propyl] trimethoxysilane (oligo-PEG) and 3.00 g of TFSISPE ion donor are mixed with 0.55 ml of water and 1.40 ml of ethanol. This mixture undergoes prehydrolyzation by heating it to 45°C and maintaining this temperature for 2.5 hours. Following prehydrolyzation, a precise quantity of lightly gelled backbone precursor based on R_w ratio is introduced to the prehydrolyzed ion donor and oligo PEG. The amounts of the backbone precursor are 9.20 ml, 9.75 ml, 10.40 ml, 11.64 ml, and 16.40 ml for R_w ratios equal to 3, 5, and 15 samples, respectively. This mixture is homogenized at 65°C for approximately 30 minutes until it reaches a viscous consistency. The resulting gel is then cast into a plastic container, sealed, and allowed to stand for another 30 minutes, leading to gel solidification. To further enhance the mechanical integrity of the gel, the container is placed in an oven at a set temperature of 50°C, initiating an aging process. After 24 hours of aging, the result is a transparent, yellow-colored functionalized backbone. Purification of the backbone is carried out through a series of washing treatments with deionized water and ethanol.

5.3.4 Ion exchange and EMIMTFSI ionic liquid infiltration

The functionalized backbone is immersed in a 0.04 M aqueous solution of lithium hydroxide (98%, Aldrich) for 1 hour. The solution is replaced every 15 minutes during this period. Subsequently, the backbone undergoes thorough rinsing using a substantial amount of water and ethanol to effectively eliminate any lithium hydroxide residues. The next step involves the infiltration by the ionic liquid, which is achieved by first submerging the backbone in a 20.00 ml solution of EMIM TFSI at room temperature for 2 hours. Afterward, the old liquid is replaced with fresh EMIM TFSI, and the system is subjected to vacuum for an additional 2 hours, with this process repeated twice to guarantee thorough liquid exchange. The final step consists of drying the resulting composites under vacuum conditions at 50°C over a 24-hour period. In a separate series of experiments, aiming at further enhancing ionic conductivity, extra LiTFSI salt is added to the IL at various EMIM TFSI-to-LiTFSI weight ratios, including 10:1, 10:2, 10:3, 10:4, and 10:5. The LiTFSI and ionic liquid are pre-mixed and subjected to ultrasonication for 20 minutes to ensure complete dissolution. The subsequent backbone infiltration by the mixture follows the same procedure as previously described.

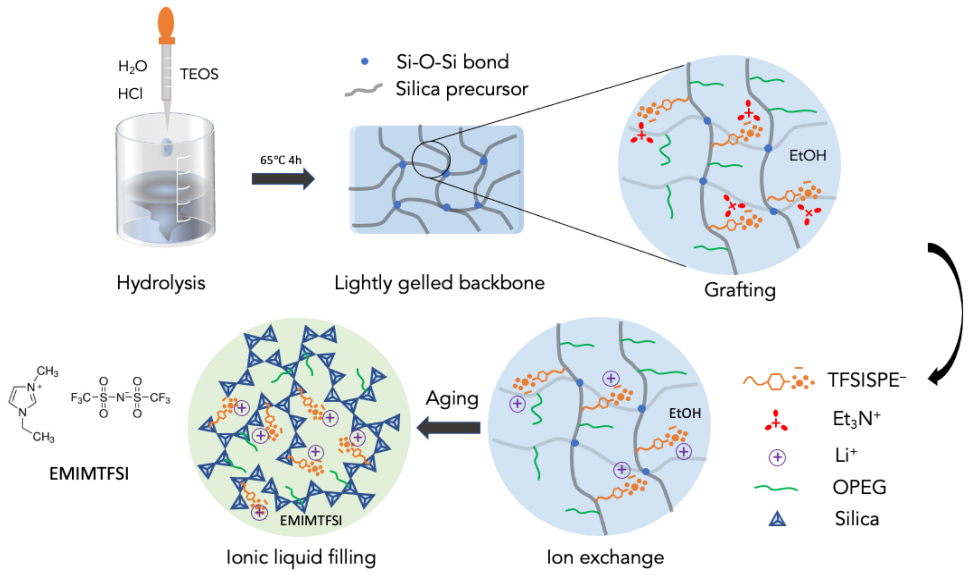

Figure 5-1 Illustration of the Synthesis Procedure for the Functionalized Backbone.

5.3.5 Characterization techniques

Thermogravimetric analysis (TGA) is conducted using the TA Instruments DISCOVERY TGA, with samples contained in a nitrogen (N_2) atmosphere (flow rate: 60 cm^3 min^{-1}) and scanned across a temperature range of 50°C – 700°C at a heating rate of 7 K min^{-1}. Differential scanning calorimetry (DSC) is performed using the TA Instruments DISCOVERY DSC, employing heating and cooling rates of 10 K min^{-1} for scans spanning from –60°C to 200°C. The Micromeritics ASAP 2000 analyzer is utilized to determine the pore volume, pore diameter, and specific surface area of the backbone. To prepare the aerogel, a solvent replacement process with acetone is employed to exchange ethanol from the pore structure of the backbone. Subsequently, the backbone undergoes supercritical carbon dioxide drying, resulting in an aerogel that is gently crushed before measurement. Fourier-transform infrared spectroscopy is recorded using a Jasco FT/IR-4100 spectrometer covering the frequency range of 600-4000 cm^{-1}. Ionic conductivity measurements are carried out using a Novocontrol broadband dielectric impedance spectrometer (DIS). Two meticulously polished stainless-steel plates are used as lithium-ion blocking current collectors, between which the electrolyte sample is sandwiched. The measurements are conducted across a temperature spectrum ranging from 5°C – 70°C under a controlled nitrogen (N_2) atmosphere, with frequencies ranging from 0.1 Hz to 10 MHz. To optimize the contact between the electrolyte and current collectors, the system is preheated to 70°C before impedance measurements. The cross-section morphologies of the composite electrolyte are determined via scanning electron microscopy (SEM) using the Tescan NIRA3 instrument. Prior to SEM analysis, samples are sputter-coated with Platinum under vacuum of 5×10^{-2} mbar at 25°C for 2 minutes. Lithium-ion transference numbers (t_{Li^+}) are determined using a combination of DC polarization and AC impedance techniques. Within an argon-filled glove box, maintaining water vapor levels below 0.40 ppm, a symmetric cell is meticulously assembled, comprising Li metal/electrolyte/Li metal. Subsequently, a consistent 15

mV DC voltage is applied to the cell for an approximate duration of 1000 seconds. During this period, both the initial and steady-state current density were recorded. AC impedance measurements were conducted both before and after the DC polarization to determine the interphase resistance.

5.4 Result and discussion

5.4.1 Fourier transform infrared (FTIR) spectroscopy

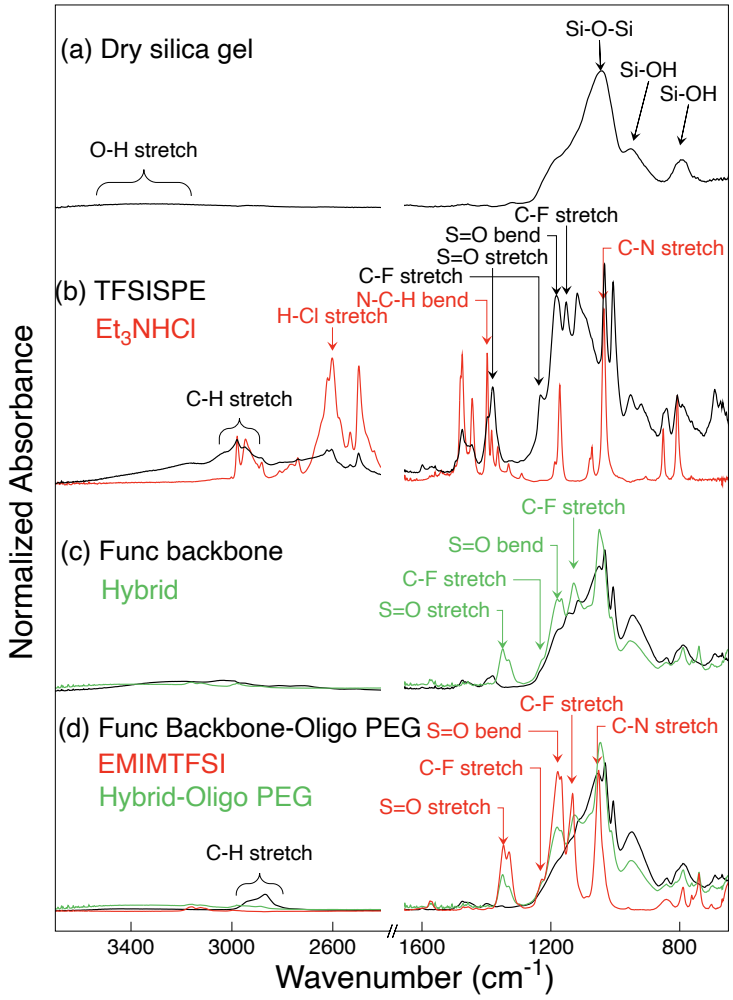

Figure 5-2 FTIR spectra of (a) dry silica gel, (b) freshly synthesized TFSISPE ion donor and Et_3NHCl byproduct, (c) functionalized backbone and hybrid composite electrolyte, and (d) bifunctionalized backbone with grafted oligo-PEG, EMIM TFSI ionic liquid and the resulting hybrid composite electrolyte. The O-H stretching band in (a) is flattened out due to the rigorous drying process before measurement.

In **Figure 5-2** we compare the FTIR spectra of the materials under investigation with those of their principal constituents, including dry silica gel, TFSISPE ion donor, Et_3NHCl, functionalized backbone and the hybird electrolytes. The spectrum of dry silica gel shows a weak absorption bands characteristic for stretching vibrations of O-H groups at 3200–3500 cm^{-1} (broad band), asymmetric Si-O^- stretching vibration at 1000–1100 cm^{-1}, Si-OH and SiO-H stretching of terminal silanol groups at 960 cm^{-1}, and symmetric Si-O stretching at 800 cm^{-1} (**Figure 5-2**(a)).[30] Notably, the asymmetric Si-O^- stretching band in silica gel is broader compared than that of quartz due to the material's larger specific surface area. This broadening is attributed to an increased number of Si-O-Si groups located at the pore surface, as explained by Ellerbrock et al.[32] An intriguing observation is the absence of the absorption band at 1600–1650 cm^{-1}, which is due to the removal of molecular coordinated water within the SiO_2 structure during the drying process, as discussed by the same authors.[32] In the spectrum of the TFSISPE ion donor (**Figure 5-2**(b)), the stretching vibrations of O=S=O groups are evident at 1380 cm^{-1}, as are the O=S=O bending modes at 1181 cm^{-1}. The presence of C-F stretching vibrations occur at 1235 cm^{-1} and 1152 cm^{-1}, while C-H stretching vibrations are observed in the 2860–3050 cm^{-1} range. These vibrational modes are consistent with the molecular structure of TFSISPE and are in agreement with the findings reported by Rey et al.[33]

During the synthesis of the TFSISPE ion donor, a significant amount of Et_3NHCl develops as a byproduct. In the FTIR spectrum of Et_3NHCl, discernible peaks are observed for C-N stretching at 1035 cm^{-1}, C-H stretching vibrations at 2850–3000 cm^{-1}, and N-C-H bending vibrations at 1400 cm^{-1}. Notably, the peaks attributed to N-H, which would manifest at around 3400 cm^{-1} for primary amine and 3300 cm^{-1} for secondary amine is absent. The broad and prominent band at approximately 2600 cm^{-1} is attributed to H-Cl stretching. This band prevails in the spectrum for TFSISPE revealing the retention of the Et_3NHCl byproduct within the ion donor. This byproduct is subsequently eliminated through washing and ion exchange steps post-grafting, as is evidenced by

the absence of the H-Cl stretching mode and peaks in the vicinity of 2600 cm^{-1} in the spectra for the hybrid materials (**Figure 5-2**(c) and (d)).

Although the EMIMTFSI ionic liquid shares the $TFSI^-$ structure with TFSISPE, distinct differences in peak positions are observed due to the changed chemical environment, as shown in **Figure 5-2**(d). The O=S=O stretching vibrations occur at 1350 cm^{-1}, with O=S=O bending observed at 1179 cm^{-1}. Similar to TFSISPE, C-F stretching vibrations are seen at 1230 cm^{-1} and 1131 cm^{-1}. Furthermore, the characteristic C-N stretching peak at 1052 cm^{-1}, unique to $EMIM^+$, is evidence for the presence of the $EMIM^+$ ion.[26]

Since backbone functionalization is done by grafting the ion donor to the silica precursor. The spectrum of the single-functionalized backbone in **Figure 5-2**(c) accurately represents both the TFSISPE and silica gel components. In **Figure 5-2**(d), the backbone that double-functionalized with ion donor and Oligo PEG displays a broad peak in the 2800–3000 cm^{-1} range, indicating the stretching vibration of C-H within the Oligo PEG, confirming successful grafting of the secondary component. The spectra for composite electrolytes are shown in **Figure 5-2**(c) and (d). Compared to backbone materials, the C-N stretching peak originating from the Et_3NHCl byproduct at 1035 cm^{-1} is smoothed out in the composite electrolyte spectrum, confirming the effectiveness of the washing step post-grafting.

5.4.2 Thermogravimetric analysis (TGA)

TGA is conducted to determine the thermal stability of the ionic liquid as a function of the size of the pores in the silica backbone, as well as to measure the relative amounts of the various materials constituents. TGA traces for the EMIM TFSI ionic liquid and for composite materials are shown in **Figure 5-3**. For clarity, traces for a select set of R_w ratios are shown. A composite electrolyte filled

with a mixture of 80 wt% EC/20 wt% PC is included in the graph to serve as a benchmark for thermal stability comparison.

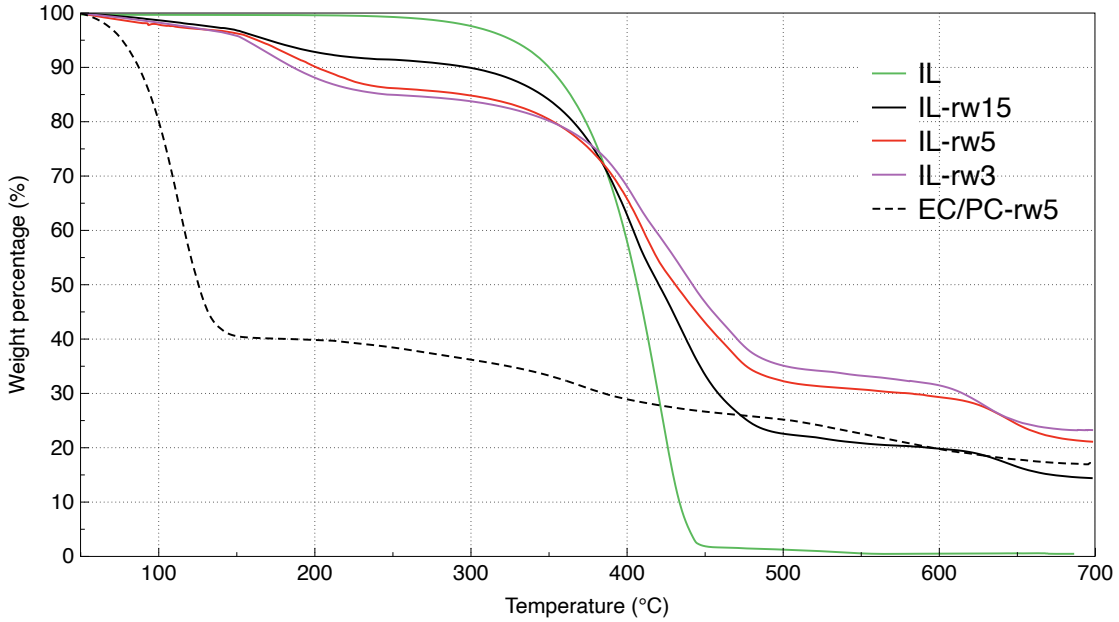

Figure 5-3 TGA plots of EMIMTFSI ionic liquid and ionic liquid filled hybrid composite electrolytes with different R_w ratios. The EC/PC filled hybrid composite electrolyte is depicted in dotted line as a reference.

The TGA curve for EMIM TFSI shows less than 1 wt% weight loss below 200°C. This slight weight loss can be attributed to volatile impurities initially present in the chemical reagent. Above 250°C, the ionic liquid exhibits a pronounced weight drop that continues to approximately 450°C, at which point it lost over 90 % of its weight. Based on TGA data we obtained in the context of TFSISPE grafted to a similar silica backbone as in the present study, but surrounded by short-chain polyethylene oxide, we found that the $TFSI^-$ group typically decomposes at around 380°C. Assuming that the somewhat different chemical environment does not drastically alter the thermal stability of the $TFSI^-$ group, we conclude that the weight loss of EMIM TFSI around 250°C can mostly be attributed to the gradual degradation of the $EMIM^+$ structure, consistent with other reports.[24]

The TGA traces for composite electrolytes filled with the ionic liquid exhibit weight loss between 50°C and 250°C, which can be primarily attributed to grafted functional moieties generated during the synthesis of the backbone. With an onset at 160°C, the initial step involves decomposition reaction of Si-O-Et groups, leading to the release of volatile organics. At 160°C Et_3NH^+ begins to degrade, resulting in the separation of Et_3N and H^+. While Et_3N departs from the system, H^+ is released and acts to balance the negative charge of the ion donor. In a second step, spanning from 250°C to 560°C, both the decomposition of EMIM TFSI and the ion donor take place. The TFSISPE ion donor undergoes a two-step decomposition that begins with the degradation of the tail $TFSI^-$ structure around 380°C and is followed by the decomposition of the alkyl linker at approximately 550°C, consistent with studies by Tseng et al.[34]. The final step, ranging from 560°C to 700°C, is attributed solely to the backbone since the ionic liquid has completely decomposed by this temperature. The TGA curves of the ionic liquid-filled electrolytes with different pore sizes exhibit similar pronounced sigmoidal weight drops with closely stacked inflection points, but the step heights varies due to differences in component weight fractions. Despite the variation in pore size, the thermal stability does not appear to vary much among these materials. However, in comparison with the EC/PC-filled material, the thermal stability of the IL filled hybrids increase by nearly 300ºC. Consequently, the ionic liquid emerges as a viable alternative to traditional organic liquids in terms of thermal stability.

To better quantify the component weight fractions, rather than visually gauging the plateau levels and inflection points in the TGA traces, we used a methodology based on numerical regression. Given data that exhibits *n* discernable weight loss steps, we begin by fitting the measured weight loss curve using a linear combination of symmetric logistic functions,

$$L(T) = \sum_{j=1}^{n} \left(w_j e^{-H_j(T-\theta_j)} \left(1 + e^{-H_j(T-\theta_j)}\right)^{-1} \right), \tag{5-1}$$

where w_j is the height of the j^{th} weight loss step, H_j is the steepness of this step, and θ_j is the temperature at which the inflection point for this step is located, i.e., the temperature at which the weight loss is most rapid. For the materials at hand we use up to $n = 3$ terms in Equation (5-1). While the symmetric shape of the logistic function may not it may not perfectly reproducing the physical phenomenon underlying the weight loss process, we found that it delivers an acceptable degree of precision for the TGA analysis. If necessary, one can use the generalized form of the logistic function, which adds an additional fitting parameter.[ref.] As the outcomes of the curve fitting, we obtain unbiased step heights and decomposition temperatures as defined by the maximum weight loss rate. These heights are subsequently leveraged to establish a system equation designed to calculate the component weight fractions. Further details on the systematic equation formulation can be perused in the supplementary material. It is noteworthy that our system equations, in most instances, tend to be either over-determined or under-determined, necessitating an optimization solution. The optimization criterion hinges on the supposition that the composition of the backbone remains relatively stable during the filler impregnation process. Consequently, the relative amount of silica to the remaining backbone components remains consistent for both composite samples and their hybrid backbone. For the functionalized backbone in this study, this constant is precisely determined to be 35.22 wt%. The outcomes disclosing the component weight fractions are thoughtfully presented in **Table 5-1**, as m_S, m_{Et}, m_T, m_{IL} and m_O, where *S*, *Et*, *T*, *IL*, *O*, stand for silica, ethanol, TFSISPE ion donor, EMIMTFSI ionic liquid, and Oligo PEG respectively. ω_{14} stands for a fitting parameter governing the ratio of mass loss of Oligo PEG in stage 1 and 2.

Table 5-1 Summary of the TGA derived composite constitution in wt%

	IL_R_w 3	**IL_R_w 4**	**IL_R_w 5**	**IL_R_w 15**
m_{Et}	4.73	3.97	3.60	2.37
m_T	32.37	31.93	31.61	21.01
m_{IL}	34.82	37.65	39.15	59.86
m_O	4.35	4.02	3.51	2.52
m_S	23.14	22.32	21.00	14.24
ω_{14}	0.73	0.77	0.76	0.825

The weight fractions, in combination with the overall materials mass density and the molecular weights of the constituents, are converted into volumetric number densities (in molecules per nm^3), which hold significance for our subsequent discussions on charge carrier mobilities. The resulting component number densities are presented in **Table 5-2** and **Table 5-3**.

Table 5-2 Summary of component number densities (molecules nm^{-3}) in hybrid composites with varying R_w ratios

	IL_ R_w 3	**IL_ R_w 4**	**IL_ R_w 5**	**IL_ R_w 15**
ρ (kg/m^3)	1663.4	1659.0	1652.0	1605.3
EtOH	1.03	0.86	0.79	0.50
TFSISPE	0.78	0.77	0.76	0.49
IL	0.90	0.96	1.01	1.48
Oligo PEG	1.00	0.91	0.80	0.55
SiO_2	3.89	3.72	3.52	2.30

Table 5-3 Summary of component number densities (molecules nm^{-3}) in hybrid composites filled with mixture of EMIM TFSI ionic liquid and LiTFSI salt with varying R_w ratios and salt comcentrations.

	IL/LITFSI:10:1-R_w 3	**IL/LITFSI:10:1-R_w 4**	**IL/LITFSI:10:1-R_w 5**	**IL/LITFSI:10:1-R_w 15**	**IL/LITFSI:10:5-R_w 5**
ρ (kg/m^3)	1663.0	1659.0	1652.0	1605.0	1649.0
EtOH	1.03	0.86	0.79	0.50	0.78
TFSISPE	0.78	0.77	0.76	0.49	0.76
IL	0.81	0.88	0.92	1.35	0.67
LiTFSI	0.11	0.12	0.12	0.18	0.46
Oligo PEG	0.99	0.91	0.80	0.55	0.80
SiO_2	3.87	3.72	3.52	2.29	3.52

5.4.3 Differential Scanning Calorimetry

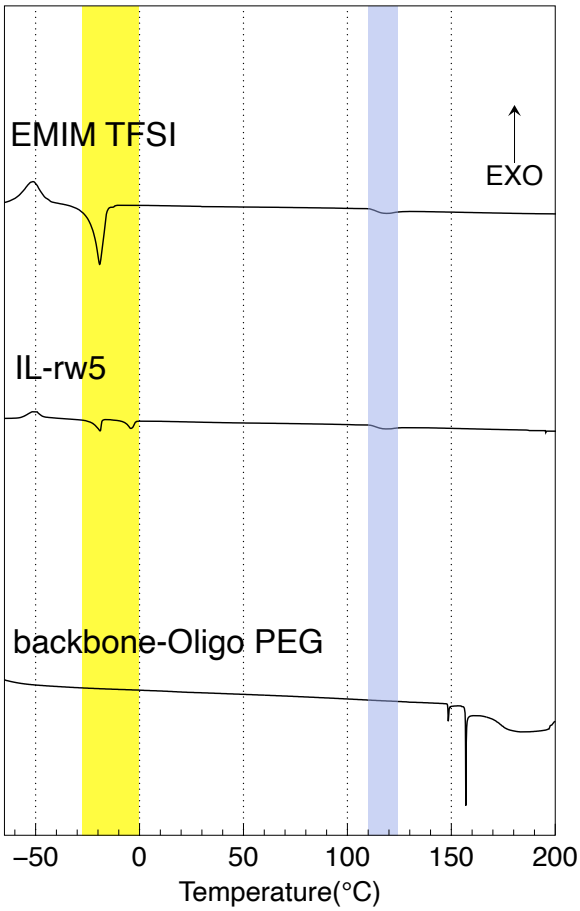

Figure 5-4 DSC spectra of EMIM TFSI ionic liquid, bifunctionalized backbone and composite electrolyte IL- R_w 5. The blue region illustrates the temperature range of an endothermal transition caused by dissociation of Li^+ and $TFSI^-$ clusters.

The DSC results are shown in **Figure 5-4**, encompassing the traces for the EMIM TFSI ionic liquid, the double-functionalized backbone, and the composite electrolyte consisting of the double functionalized backbone, prepared at a R_w ratio of 5, infused with ionic liquid. In the case of the functionalized backbone material by itself, no distinct glass transition temperature (T_g) is observed for either the silica or the grafted organics. The T_g for silica is expected to lie beyond the measurement range of our DSC apparatus. As to the grafted oligo PEG, previous research by Vrandečić *et al.* has established that T_g for low molecular weight PEG typically eludes detection.[35]

However, our DSC scan for the backbone does reveal several sharp endothermal peaks and a broad band within the 150–200°C range. The presence of these peaks is reproducible upon repeated scanning of the same sample, but their intensity diminishes with each subsequent scan, indicating an only partially reversible process. A comparable observation has been documented by Rubio et al.[36] From our TGA of the backbone material we understand that condensation and decomposition reactions involving Si-O-Et groups occur in the same temperature range, generating ethanol as a byproduct.[30] Notably, surface Si-O-Et groups, and to a lesser extent, Si-OH groups have the capacity to engage in hydrogen bonding with ethanol. We therefore surmise that the observed endothermal peaks and broad band in the backbone in the measured DSC scans result from the decomposition reaction and the dissociation of hydrogen-bonded ethanol.[36] The reappearance of these features in subsequent scans can likely be attributed to the recombination of ethanol with the remaining surface groups.

For the EMIM TFSI ionic liquid, characteristic crystallization and melting peaks are observed. The crystallization peak appeared at approximately –52°C, while the melting peak is evident around –20°C, consistent with prior research findings in the literature.[37,38] Several publications also report a weak exothermal peak near –43°C, corresponding to an enthalpy of 0.759 $J \cdot g^{-1}$. This peak is attributed to a solid-solid structural transition. In this transition, EMIM TFSI turns from monoclinic crystalline to an undefined structure, characterized by changes in the rotational motions of molecular groups.[37,39] However, in our results, this transition is overshadowed by the strong crystallization peak of the bulk ionic liquid. Additionally, due to the limited measurement temperature range of our DSC instrument, we do not detect any sign of a glass transition temperature for EMIM TFSI, which several investigators report to be located around –95°C.[38,40]

When embedded in the pores of the silica backbone, the crystallization behavior of the ionic liquid remains a single peak at –52°C, whereas melting occurs in multiple distinct stages. One of these

melting peaks occurs at the same temperature as that of bulk ionic liquid, around –20°C, while an additional peak appears at a higher temperature, approximately –5°C. Such melting behavior is also observed for the EC/PC-filled benchmark system, and can be explained by the variations in pore size causing differences in the crystallite morphologies of the filler and, consequently, disparate melting point. Moreover, the ionic liquid can possibly exist in more than one crystalline structure. Rotnicki *et al.* demonstrated the effect of confinement nanopores on the melting behavior of EMIM TFSI.[39] Their results also show DSC peak splitting for EMIM TFSI confined in a porous carbon matrix with average pore size of 3nm. X-ray diffraction and neutron diffraction measurements confirm that the crystal structure of EMIM TFSI confined to nanopores significantly differs from the structure of bulk EMIM TFSI due to interfacial interactions between the host material and the ionic liquid.[39] In our results, the peak at –20°C should correspond to melting of bulk-like crystals located in larger pores, while the peak at –5°C is due to the melting of ionic liquid contained in the smallest pores.

Both the ionic liquid and the hybrid material exhibit a weak endothermal peak between 110°C and 125°C. Such a peak is not observed in the scans for the backbone, confirming that it is associated with the ionic liquid. This peak is reproducible throughout multiple repeated scans of the same sample. The DSC traces for mixtures of EMIM TFSI and LiTFSI (marked as IL/LiTFSI) with different weight ratios, shown in **Figure 5-5**, possess similar peaks in the temperature range of 110°C to 125°C. However, the enthalpy associated with these peaks varies from 1.13 to 3.1 $J \cdot g^{-1}$ as the LiTFSI proportion in the mixture generally increases from 9 to 45 wt.%, except for an outlier with the IL/LiTFSI ratio of 10:2. Importantly, none of the IL/LiTFSI mixtures show crystallization or melting behaviors within the measurement temperature range, revealing the predominantly amorphous nature of the system. This aligns with previous research, where the authors determined that crystallization in similar mixtures required significant undercooling with weak

reproducibility.[27,28,41] While the mixture is largely amorphous, it does not imply the absence of microphases that exhibit localized ordered structures. Research conducted by Zhou et al. on a similar salt in ionic liquid system revealed that Li^+ can strongly coordinate with the $TFSI^-$ to form $[Li(TFSI)_2]^-$ ion pairs or even chain-like clusters, depending on the composition of the mixture.[27,28,42] This phenomenon was further confirmed by Raman spectra, even at temperature above 80°C. Hence, we submit that the endothermal transition we discovered here may result from the dissociation of these clusters, leading to a fully amorphous melt.

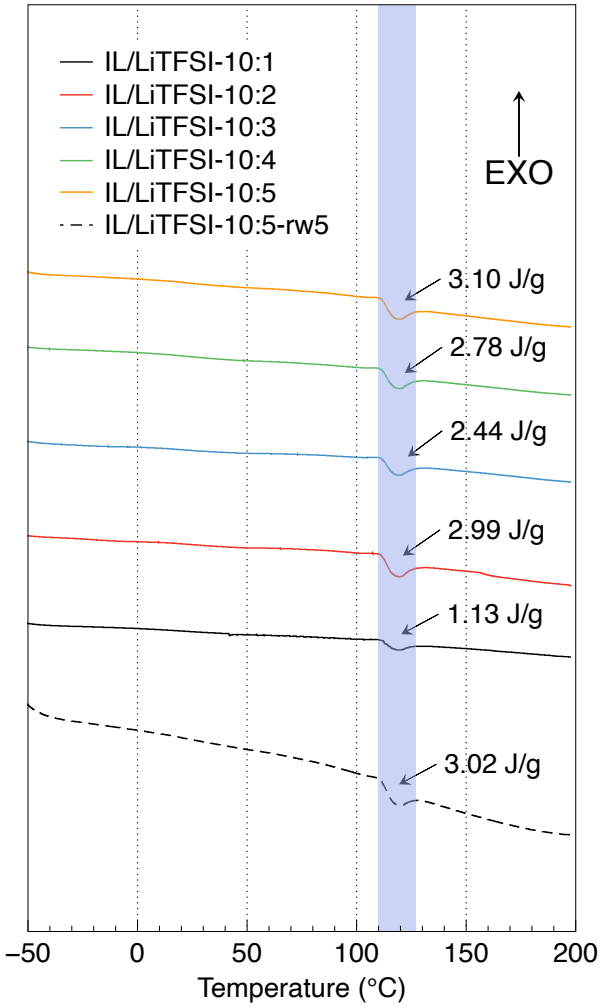

Figure 5-5 DSC spectra of EMIM TFSI and LiTFSI mixtures at different weight ratios and hybrid composite electrolyte filled with 10:5 mixture. The blue region indicates the temperature range of an endothermal transition attributed to the dissociation of Li^+ and $TFSI^-$ clusters.

In the DSC scan of the hybrid backbone filled with a IL/LiTFSI mixture at a 10:5 weight ratio, designated as IL/LiTFSI-10:5-R_w 5, the enthalpy of this transition is measured at 3.02 $J \cdot g^{-1}$, which is equivalent to 7.71 $J \cdot g^{-1}$ of the IL-LiTFSI liquid mixture, i.e., significantly higher than the bulk 10:5 mixture. This result may be explained by the backbone's functionalization with TFSISPE ion donors, which can serve as a source of Li^+. This additional influx of Li^+ could raise the formation of ion coordination clusters. Considering the presence of the same endothermal peak in pure EMIM TFSI, albeit weakest of all, it is conceivable that despite the steric hindrance imposed by $EMIM^+$ that shields its positive charge, it is still capable of forming ion pairs and chain-like clusters with $TFSI^-$.

5.4.4 Dielectric impedance spectroscopy (DIS)

Dielectric impedance spectroscopy is employed to investigate the ionic conductivity. The Nyquist plots obtained at 20°C for various composite samples with different R_w ratios are presented in **Figure 5-6**. These plots exhibit a depressed semicircle in the high-frequency region, which corresponds to the bulk resistance of the electrolytes, and a tilted spike, indicative of mass transportation processes. We find that the spikes for all R_w ratios, except for R_w of five, are not straight lines. They tend to have sigmoidal shapes with positive inflection, i.e., the curvature increases monotonically towards the low-frequency region. This observation leads us to hypothesize that the variations in pore structures, dictated by the differences in R_w ratios, influence the ion diffusion process, as also noted by previous studies.[43,44] Additionally, we consider the possibility that the middle-frequency portion of the spike is linked to the double-layer capacitance at the electrode-electrolyte interface. If this holds true, the unique shape of the spike further suggests a correlation between interfacial capacitance and pore structures.

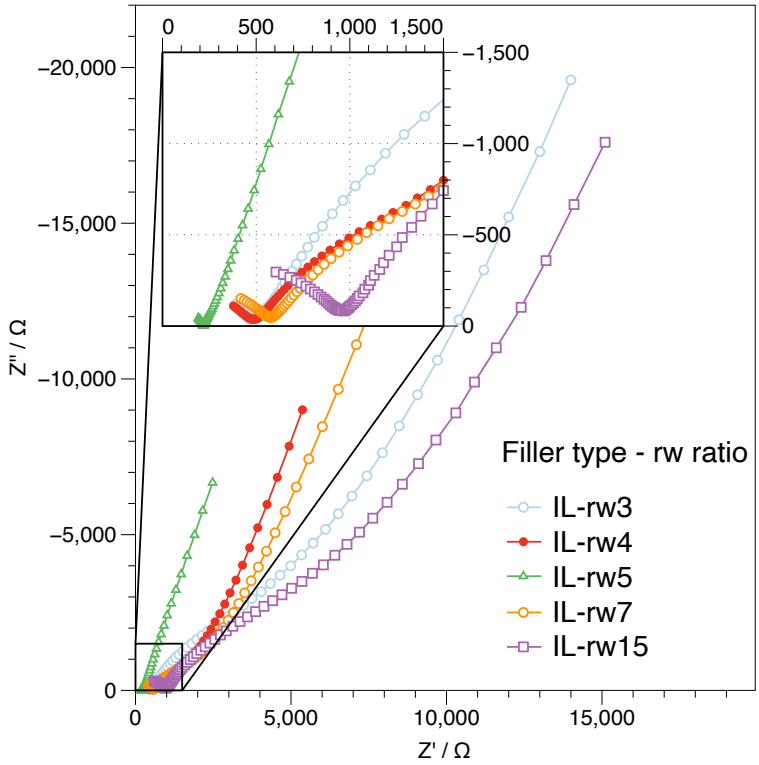

Figure 5-6 Nyquist plots for EMIM TFSI filled composite electrolytes with varying R_w ratios, measured at 20°C.

The ionic conductivity is determined from the Nyquist plot using

$$\sigma = L / (R_b \cdot S), \tag{5-3}$$

where, S denotes the cross-sectional area of the sample, L the sample thickness, and R_b the bulk resistance of the electrolytes obtained from the intersection of the semicircle at high frequency and the x-axis.[15,45,46]

In **Figure 5-7** we plot the ionic conductivity as a function of the scaled reciprocal temperature across various R_w ratios. This figure shows the findings for systems consisting of a silica backbone functionalized with TFSISPE Li^+ cation donors and pores filled with IL for various R_w ratios. The data for a material consisting of a silica backbone prepared at $R_w = 5$, filled with EC/PC, is included for comparison. Evidently, the ionic conductivity of the IL-filled system is comparable to that of the EC/PC system, but the IL exhibits significantly improved thermal stability to our TGA analysis.

The fact that the conductivity surpasses 10^{-3} S·cm^{-1} in all systems is encouraging in terms of their practical usability. Furthermore, by adjusting the pore size distribution during synthesis, as controlled by the R_w ratio, the ionic conductivity can be optimized. As shown in the inset plot, the conductivity at 20°C exhibits an apparent maximum of 3.75×10^{-3} S·cm^{-1} at $R_w = 5$. While trend in the data gives the conductivity for the $R_w = 5$ material the appearance of an outlier, we have confirmed the reproducibility of this data.[15,45,46]

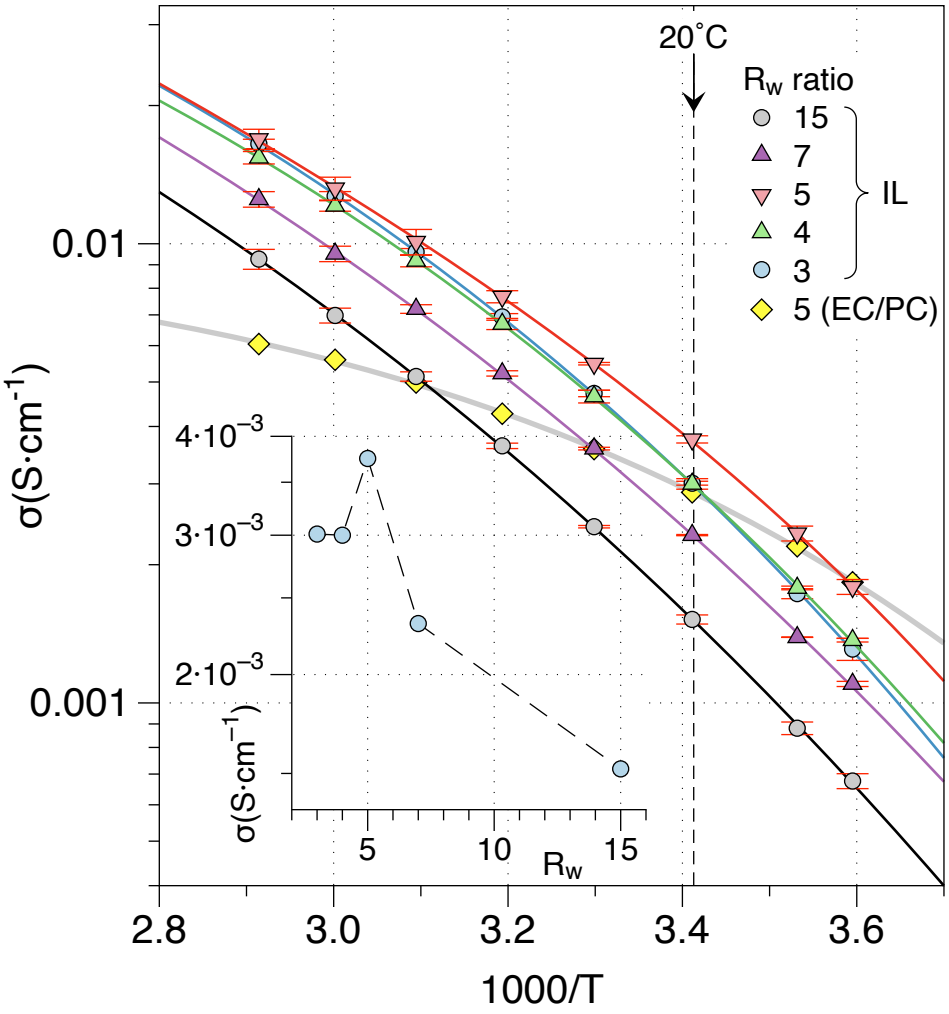

Figure 5-7 Temperature dependent ionic conductivities for ionic liquid filled samples with different R_w ratio, the EC/PC filled sample is showed as a reference group. Data are collected in the temperature range of 5 – 70°C. The inserted plot shows the 20°C conductivity versus the R_w ratio.

The lines in **Figure 5-7** represent best fits using our correlative activation free energy (CAFE) model, introduced in earlier publications.[47] This model applies to materials systems that undergo a transition from the liquid to a glassy state and accounts for the deviation from Arrhenius behavior of molecular transport phenomena. The structural rearrangements during this transition are associated with a correlative change in the free energy landscape. The activation free energy is a direct reflection of this change. Accordingly, the temperature dependence of the ionic conductivity is described by

$$\ln(\sigma T) = (P + S_0/k_B) + \psi(\chi)\Delta S_a/k_B - \chi\left(\beta_g E_0 + \psi(\chi)\beta_g \Delta E_a\right), \quad (5\text{-}4)$$

where $\chi = T_g/T$ and $P = \ln\left(\rho_{Li^+}(zq_e)^2 \gamma d_0^2 \Gamma_0 k_B^{-1}\right)$, with ρ_{Li^+} being the volumetric number density of the lithium cation, z is its valence, q_e is electronic unit charge, k_B is the Boltzmann factor, γ is the geometry factor, which is equal to one over twice the dimensionality of the underlying space, d_0 is the cation jump distance and Γ_0 is the attempt frequency. $\psi(\chi)$ is the generalized logistic function $\psi(\chi) = \left(1 + C_0 e^{\nu\beta_g H(1-\chi)}\right)^{-1/\nu}$, which is adopted to capture the change in free energy landscape during the transition behavior between liquid and glass states. It exhibits a skewed sigmoidal shape, governed by parameters H, ν, and $\beta_g = \left(N_A\, k_B\, T_g\right)^{-1}$, controlling the steepness, asymmetry, and inflection point of the curve, respectively. C_0 is a constant determined by the value of $\psi(\chi)$ at $\chi = 1$. ν is a hyper-parameter found to give best fits if chosen to be greater than 10. Along with H, S_0, ΔS_a, E_0 and ΔE_a are model parameters determined via non-linear regression data fitting that allow one to calculate the temperature dependent activation entropy and enthalpy according to

$$E_a(\chi) = E_0 + \psi(\chi)\Delta E, \text{ and} \quad (5\text{-}5)$$

$$S_a(\chi) = S_0 + \psi(\chi)\Delta S. \quad (5\text{-}6)$$

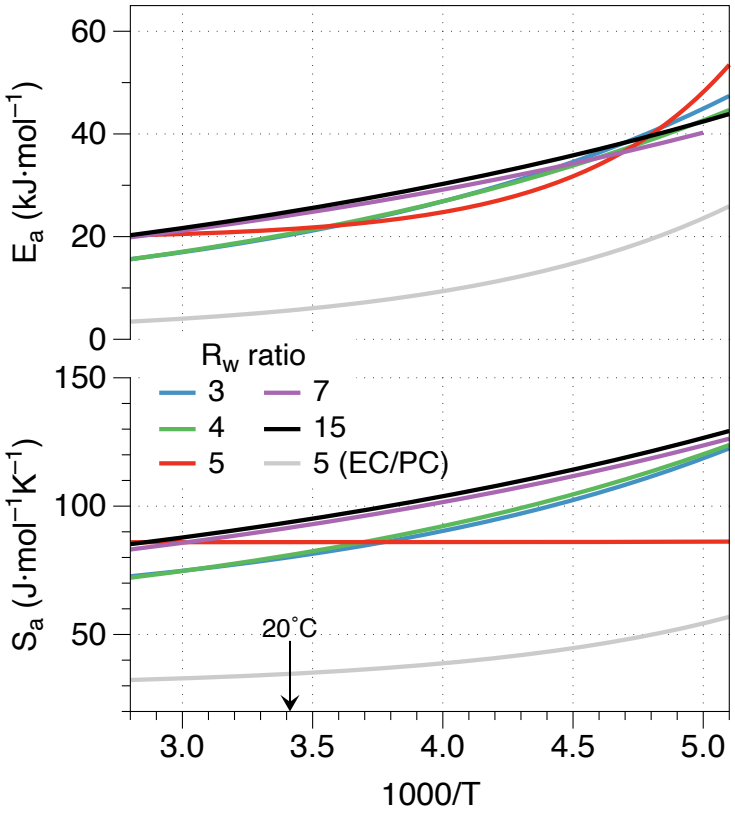

Figure 5-8 Activation enthalpies and entropies as a function of the scaled reciprocal temperature

The results of our analysis for silica the functionalized backbone and pores filled with IL are shown in **Figure 5-8**. The activation enthalpies increase with decreasing temperature, ranging between 20 and 55 kJ·mol^{-1}, while the entropies exhibit a similar temperature dependence and range between 70 and 130 J·mol^{-1}K^{-1}. These findings reveal that activation enthalpies and entropies are equally important in determining whether a cation jump occurs or not. Consider that at room temperature $E_a \sim 25$ kJ·mol^{-1} and $S_a = 90$ J·mol^{-1}K^{-1}, then a quick calculation yields the e^{S_a/k_B} and e^{-E_a/k_BT} nearly compensate. Hence, the cation migration rate is strongly determined by factors such as the jump distance and the attempt frequency, which depend on the materials structure and atomic interactions. The activation enthalpies and entropies closely follow the same trends for most R_w values, except for the system with $R_w = 5$, which is characterized with a stronger curvature in the

activation enthalpy *vs.* $1/T$, and a nearly flat activation entropy, again singling out this structure. In particular, strong curvature signifies large values for the parameter H, which can be understood as the difference in ground state energies between the high-temperature liquid and the glass state. For $R_w = 5$, $H = 14.2$ kJ·mol^{-1}, while those for the other R_w values range from 3 to 4.5 kJ·mol^{-1}. Accordingly, the $R_w = 5$ material undergoes more significant structural changes with varying temperature. The fact that the $R_w = 5$ structure corresponds to a cusp in H value, and conductivity for that matter, suggest that the related pore size distribution may coincide with a changeover between the liquid structures inside the pores, one bulk-like structure that exists in larger pores and another structure that is more constrained by the proximity of the walls in smaller pores.

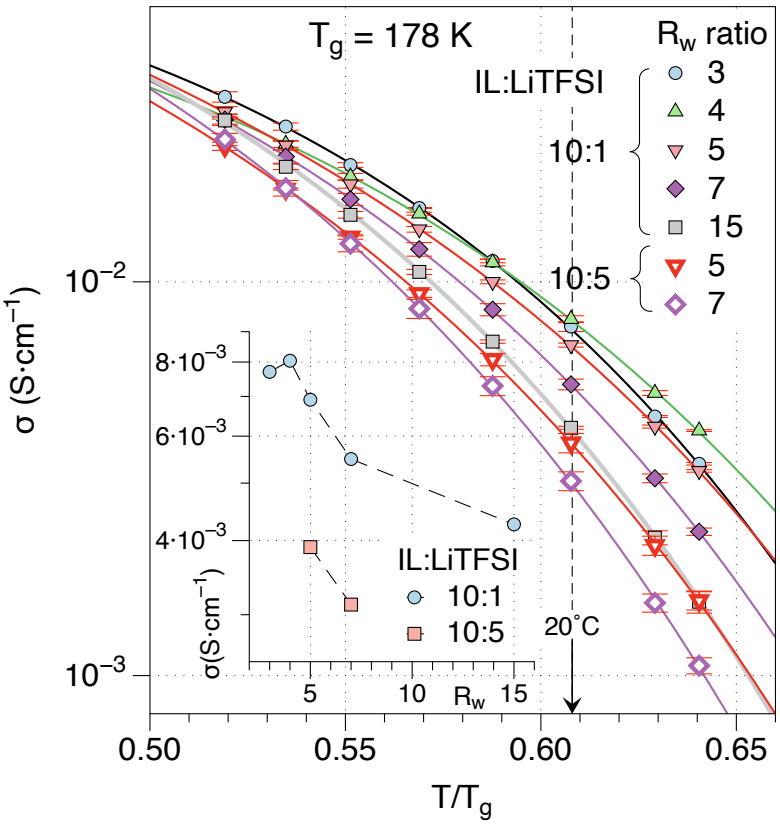

Figure 5-9 Ionic conductivity data as function of the reciprocal temperature normalized with respect to T_g for materials for which the EMIM TFSI ionic liquid is mixed with LiTFSI at two different concentrations, and for structure developed at various R_w ratios. Inset: ionic conductivities for IL/LiTFSI = 10:1 series as a function of the R_w ratio.

Figure 5-9 shows the ionic conductivity data as function of the reciprocal temperature normalized with respect to the glass transition temperature of the ionic liquid, which is 178 K, for systems that consist of the silica backbone functionalized with ion donating TFSISPE moieties, but contain a mixture of EMIM TFSI and LiTFSI at a weight ratio of 10:1 for all the R_w values, plus two systems (R_w = 5 and 7) with a EMIM TFSI-to-LiTFSI weight of 10:5. The doping with LiTFSI is done with objective to increase the ionic conductivity of the electrolyte. Indeed, the highest 20°C conductivity is achieved by the 10:1 sample with a R_w ratio of 4, reaching 8.04×10^{-3} S·cm^{-1}, twice as high as the non-doped sample. Surprisingly, the heavily (10:5) doped material only shows minimal improvement compared to the non-doped system and overall exhibits lower conductivity than the lightly (10:1) doped group. This finding aligns with reports from other authors, who observe a significant decrease in conductivity with increasing LiTFSI concentration in EMIM TFSI, particularly at IL/LiTFSI weight ratios exceeding 10:1.[28] The reason for this that is Li^+ complex formation, signs of which we detected in our DSC analysis. At light doping, the formation of individual $[Li(TFSI)_2]^-$ species has minimal impact on ionic mobility dynamics. In such compositions, most of the conductivity arises from uncoordinated ions. Conversely, further LiTFSI concentration increase leads to the formation of larger ionic aggregates (chains and networks) in which Li^+ cations act as links or cross-links between aggregated anions. This results in a substantial increase in system viscosity, and offsets the nominal benefit of higher Li^+ concentration for ionic conductivity.[27,28]

Given the non-monotonic influence of Li^+ concentration on the ionic conductivity, it serves to examine ion mobilities, which probes the transport mechanism in ways the effectively disconnect it from ion concentrations. To gain a deeper insight into the ion transport processes within samples featuring various pore sizes, it is imperative to explicitly determine the ionic conductivity. The conductivity σ is related to the mobility μ according to

$$t_{Li^+}\sigma = z\, q_e\, \rho_{Li^+}\, \mu \tag{5-7}$$

where ρ_{Li^+} is the volumetric number density of charge carriers, which we determined based on TGA, z their valence, and q_e the electronic unit charge.[43] The summary of the calculated Li^+ mobilities are provided in **Table 5-4**. Due to limited lithium cation transference number data, we assume that samples with different R_w ratios as well as for different IL:LiTFSI ratios have the same Li^+ transference number of 0.435 (see below), implying that Li^+ contributes similarly to the conductivity in at all systems studied. Considering that variations in pore sizes can differently influence the diffusivity of ions of different sizes, which could potentially lead to variations in t_{Li^+} values, our reported data should be considered as nominal quantities intended to calibrate the mobilities mainly with respect to the Li^+ concentrations derived from TGA. The accuracy of the calculated quantities should still be sufficient to reveal fundamental tendencies.

Table 5-4 Summary of the Lithium-ion mobility for ionic liquid filled composite electrolytes with varying R_w ratio and IL/LiTFSI ratio

IL/LiTFSI weight ratio	R_w ratio	Li^+ number density (nm^{-3})	Total Conductivity ($S \cdot cm^{-1}$)	Li^+ conductivity ($S \cdot cm^{-1}$)	Li^+ mobility ($S\ cm^2\ C^{-1}$)
∞	3	0.78	3.01×10^{-3}	1.31×10^{-3}	1.05×10^{-5}
∞	4	0.77	3.00×10^{-3}	1.31×10^{-3}	1.06×10^{-5}
∞	5	0.76	3.75×10^{-3}	1.63×10^{-3}	1.34×10^{-5}
∞	7	0.71	2.32×10^{-3}	1.01×10^{-3}	8.88×10^{-6}
∞	15	0.49	1.52×10^{-3}	6.61×10^{-3}	8.42×10^{-6}
10:1	3	0.89	7.70×10^{-3}	3.35×10^{-3}	2.35×10^{-5}
10:1	4	0.89	8.04×10^{-3}	3.50×10^{-3}	2.45×10^{-5}
10:1	5	0.88	6.91×10^{-3}	3.01×10^{-3}	2.14×10^{-5}

10:1	15	0.67	4.26×10^{-3}	1.85×10^{-3}	1.72×10^{-5}
10:5	5	1.22	3.90×10^{-3}	1.70×10^{-3}	8.70×10^{-6}

The calculated mobility data are plotted as a function of the normalized reciprocal temperature in **Figure 5-10**, and room-temperature values are compiled in **Table 5-4**. As shown in the inset of **Figure 5-10**, the trend of charge carrier mobility versus R_w ratio closely mirrors that of conductivity, with the $R_w = 4$ material achieving the highest Li^+ mobility of 2.45×10^{-5} S cm^2 C^{-1}. The negative influence of increasing LiTFSI concentration in the ionic liquid is more clearly manifest in the mobility data. In fact, for the system with the IL:LiTFSI ratio of 10:5, the mobility drops below that of the systems without any LiTFSI in the ionic liquid. These findings suggest that the pore size distribution has a strong and unexpected influence on the Li^+ transport properties. Intuitively, one might expect that larger pores would provide unobstructed passed for the carriers, our data show that smaller pores are beneficial to their mobility. We surmise that this is because of the structural changes induced in the IL due its interactions between the pore wall. Molecular dynamic research conducted by Beg *et al.* revealed that the highest mobility of a a solute in a network structure occurs when the system reaches the internal decohesion limit, i.e., the solute experiences tensile stress from all surrounding pore walls but there is not yet sufficient space for it to detach from one pore wall and attach to the opposite side of the pore.[48] Confined to a pore of just the right side, the IL could be extended in a similar way and offer easy passage to the charge carriers.

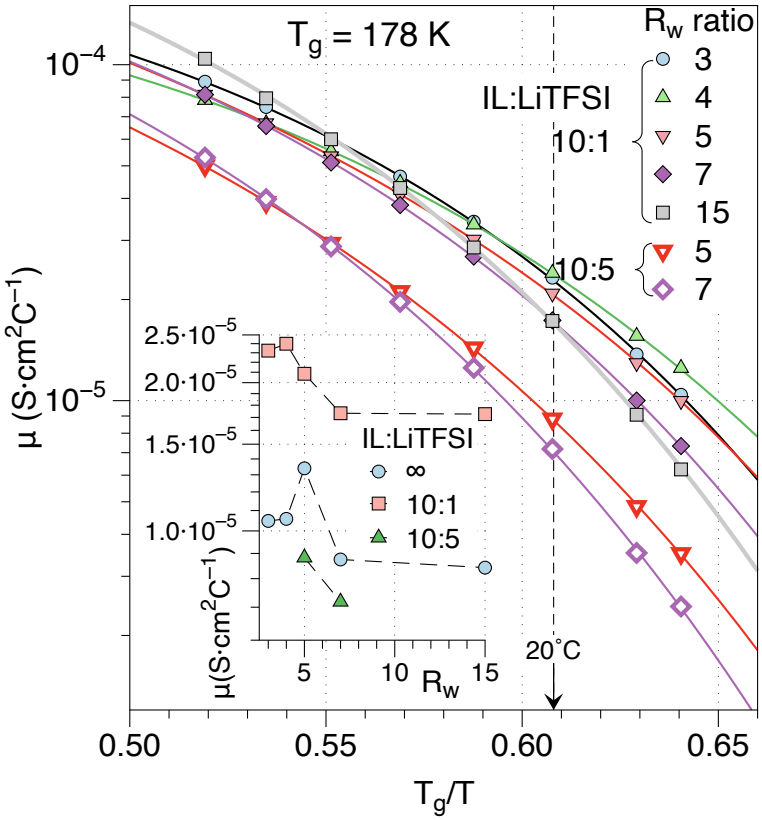

Figure 5-10 Calculated Li^+ mobilities as a function of the reciprocal temperature normalized with repect to the glass transition temperature for materials containing IL and LiTFSI at two different proportions and with backbones synthesized with various R_w ratios. Inset: room temperature Li^+ mobilities as a function of the R_w ratio for these materials; those for the the materials without LiTFSI are included for comparison.

Comparing the mobility of the ionic liquid-filled system with the previous systems filled with EC/PC or PEO, our data fall within the same order of magnitude as the EC/PC system and are approximately an order of magnitude higher than the PEO counterpart. This result suggests that the ionic liquid can effectively serve as a replacement for the EC/PC mixtures.

5.4.5 Transference number

In the material systems studied here, there are three mobile ionic species (Li^+, $EMIM^+$ and $TFSI^-$). We determine the Li^+ transference number (t_{Li^+}) using a combination of DC polarization and AC impedance measurements in a symmetric cell with non-blocking Lithium metal electrodes, as

outlined by Evans et al.[49] The specific composite chosen for the measurement possesses a R_w ratio of 5. It contains EMIM TFSI and the backbone is functionalized with ion-exchanged TFSISPE, but no additional LiTFSI is introduced. During the measurement, a fixed DC voltage of 27 mV is applied for a duration of 1100 seconds, and the sample area is 1.266 cm^2. The current is measured as a function of time for the duration needed to ascertain steady state (**Figure 5-11**).

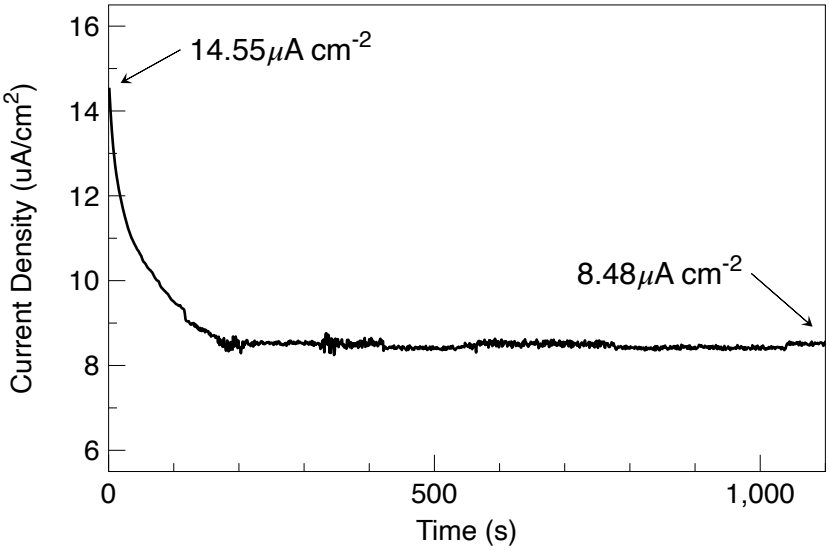

Figure 5-11 Current density as a function of time during DC polarization, with an applied voltage of 27 mV. The initial and steady state current density are marked.

The transference number is calculated using:

$$t_{Li}^{+} = \frac{I^{\infty}(\Delta V - I^{0}R_{I}^{0})}{I^{0}(\Delta V - I^{\infty}R_{I}^{\infty})}, \tag{5-8}$$

where ΔV is the applied constant potential across the symmetric cell, R_I are the resistance of the interphase, I is the current and superscripts 0 and ∞ indicate the initial and steady state values.[49–51]

Figure 5-12 shows the Nyquist plots of data obtained from the AC impedance measurements. The red and black curves represent the impedance of the symmetric cell before and after the DC polarization, respectively. The equivalent circuit used for the analysis is shown above the data. The

intercept with the real axis in the high-frequency range yields the resistance R_b of the electrolyte, electrodes, and the electrical contacts at the electrolyte/electrode interfaces.[52,53] The first partial semi-circle corresponds to the resistance stemming from the solid electrolyte interface layers, R_{SEI}, while the mid-frequency semi-circle is attributed to the charge transfer resistance at the electrode/electrolyte interfaces R_I.[44] Values of the latter resistance are used in Equation (5-8); depending on whether they are measured pre- or post-DC polarization they correspond to R_I^0 and R_I^∞, respectively.

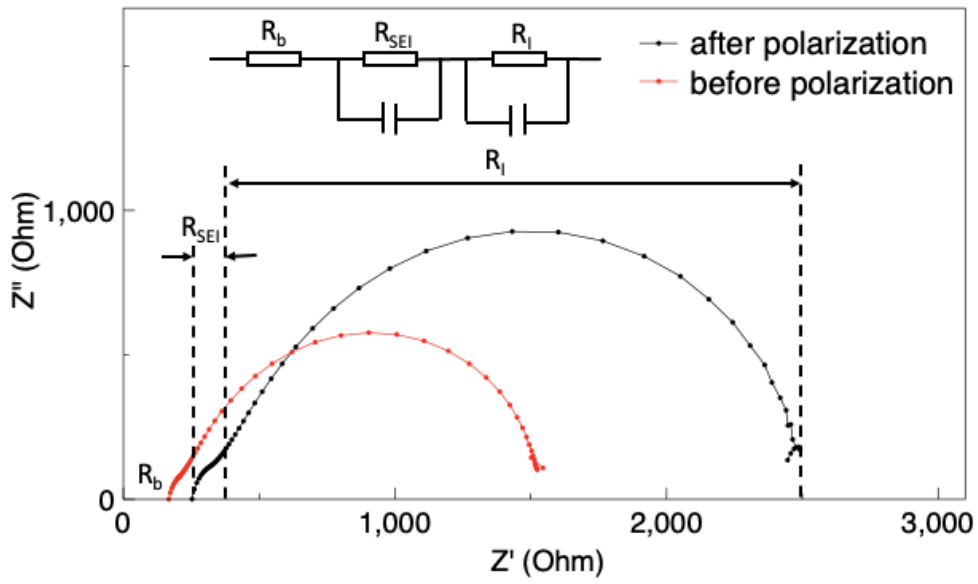

Figure 5-12 Nyquist plot of the composite electrolytes in a symmetric cell. The red and black lines represent the impedance spectrum before and after the polarization, respectively.

The measurement results are shown in the **Table 5-5** and the calculated Li^+ transference number $t_{Li^+} = 0.435$, which is lower than that for the PEO filled hybrid electrolyte we developed in Chapter II, but given the high overall ionic conductivity still holds significant relevance for practical applications, as highlighted by Balo et al.[25]

Table 5-5 Result of the transference number measurement for ionic liquid filled sample, with R_w ratio equals 5 and without LiTFSI doping

	I (μA)	R_I (Ω)	t^+
Initial state	18.417	1310	0.435
Steady state	10.740	2155	

For reference, the literature on the diffusivity of Li^+ in EMIM TFSI (with molar concentrations ranging from 0 to 0.2) at 300 K fall within the range of $1.0 – 1.5\times10^{-7}$ cm^2 s^{-1}. $EMIM^+$ and $TFSI^-$ ions also exhibit diffusivity within this range, as reported by Kubisiak *et al.*[42] Similarly, while generally corroborating these findings, Gouverneur *et al.* find the diffusivity of $EMIM^+$ to be marginally higher than that of $TFSI^-$.[54] The Li^+ transference numbers reported for salt in liquid EMIM TFSI fall in the range between 0 and 0.3; in fact, some authors even determine negative values and ascribe this to the formation of ion pairs.[42,55,56] Our results indicate that the motion of the relatively bulky ionic liquid may be impeded within the nanopores, resulting in a higher $t_{Li}{}^+$. This hindrance may be attributed to factors such as geometric constraints and non-bonding interactions with the pore walls.

5.5 Conclusion

A novel hybrid composite electrolyte, incorporating a functionalized silica backbone encapsulating EMIM TFSI ionic liquid, was developed, demonstrating superior ionic conductivity and thermal stability. Thermal analysis via TGA confirmed stability up to 290 °C. The R_w ratio significantly impacts the ionic conductivity. For system filled with pure EMIM TFSI, the maximum ionic conductivity of 3.75×10^{-3} $S\cdot cm^{-1}$ is found at R_w equals 5. Analysis of activation enthalpies and entropies unveil that R_w equals 5 system shows a stronger curvature in the activation enthalpy vs. 1/T and a nearly flat activation entropy. This suggests that the material undergoes more significant

structural changes with varying temperature. The observed phenomenon may be attributed to the related pore size distribution coinciding with a transition between liquid structures inside the pores. Larger pores exhibit a bulk-like structure, while smaller pores experience constraints imposed by the proximity of the walls. The lightly LiTFSI-doped system (10:1) shows a notable increase in ionic conductivity compared to the non-doped system, with the R_w equals 4 material reaching 8.04×10^{-3} $S\cdot cm^{-1}$, twice as high as the non-doped sample. However, the heavily (10:5) doped material shows only minimal improvement compared to the non-doped system and, surprisingly, exhibits lower conductivity than the lightly (10:1) doped group. DSC studies reveal the formation of coordination between Li^+ and $TFSI^-$, resulting in $[Li(TFSI)2]^-$ ion pairs and chain-like clusters. The concentration increase of LiTFSI leads to the formation of larger ionic aggregates, which can significantly increases system viscosity, offsetting the nominal benefit of higher Li^+ concentration for ionic conductivity. The calculated ion mobility reveals that the ionic liquid-filled system falls within the same order of magnitude as the EC/PC system and is approximately an order of magnitude higher than the PEO counterpart. Computational analysis between different R_w materials indicates that pore size distribution has a strong and unexpected influence on Li^+ transport properties, with smaller pore sizes actually improving ion mobility.

5.6 References

1. Rohan, R. et al. Functionalized polystyrene based single ion conducting gel polymer electrolyte for lithium batteries. The 7th International Conference on Materials for Advanced Technologies (ICMAT 2013) Symposium A: Advanced Energy Storage Systems: Lithium ion batteries and beyond 268, 294-299 (2014).
2. Rohan, R. et al. A high performance polysiloxane-based single ion conducting polymeric electrolyte membrane for application in lithium ion batteries.J. Mater. Chem. A 3, 20267-20276 (2015).
3. Tarascon, J.-M. & Armand, M. Issues and challenges facing rechargeable lithium batteries. Nature 414, 359-367 (2001).

4. Keller, M., Varzi, A. & Passerini, S. Hybrid electrolytes for lithium metal batteries. Journal of Power Sources 392, 206-225 (2018).

5. Kim, Y. et al. High Ion Conducting Nanohybrid Solid Polymer Electrolytes via Single-Ion Conducting Mesoporous Organosilica in Poly(ethylene oxide). Chem. Mater. 29, 4401-4410 (2017).

6. Oh, H. et al. Poly(arylene ether)-Based Single-Ion Conductors for Lithium-Ion Batteries. Chem. Mater. 28, 188-196 (2016).

7. Petronico, A. et al. Solid–Liquid Lithium Electrolyte Nanocomposites Derived from Porous Molecular Cages. Journal of the American Chemical Society 140, 7504-7509 (2018).

8. Rohan, R. et al. Functionalized meso/macro-porous single ion polymeric electrolyte for applications in lithium ion batteries. J. Mater. Chem. A 2, 2960-2967 (2014).

9. Zhu, Y. et al. A Composite Gel Polymer Electrolyte with High Performance Based on Poly(Vinylidene Fluoride) and Polyborate for Lithium Ion Batteries. Adv. Energy Mater. 4, 1300647 (2014).

10. Jung, Y.-C. et al. Ceramic separators based on Li+-conducting inorganic electrolyte for high-performance lithium-ion batteries with enhanced safety. Journal of Power Sources 293, 675-683 (2015).

11. Keller, M. et al. Electrochemical performance of a solvent-free hybrid ceramic-polymer electrolyte based on Li7La3Zr2O12 in P(EO)15LiTFSI. Journal of Power Sources 353, 287-297 (2017).

12. Choi, J.-H., Lee, C.-H., Yu, J.-H., Doh, C.-H. & Lee, S.-M. Enhancement of ionic conductivity of composite membranes for all-solid-state lithium rechargeable batteries incorporating tetragonal Li7La3Zr2O12 into a polyethylene oxide matrix. Journal of Power Sources 274, 458-463 (2015).

13. Bae, J. et al. A 3D Nanostructured Hydrogel-Framework-Derived High-Performance Composite Polymer Lithium-Ion Electrolyte. Angew. Chem. 130, 2118-2122 (2018).

14. Brinker, C. J. & Scherer, G. W. (eds Brinker, C. J. & Scherer, G. W.) 96-233 (Academic Press, San Diego, 1990).

15. Liu, W. et al. Ionic Conductivity Enhancement of Polymer Electrolytes with Ceramic Nanowire Fillers. Nano Lett. 15, 2740-2745 (2015).

16. Nairn, K. M., Best, A. S., Newman, P. J., MacFarlane, D. R. & Forsyth, M. Ceramic-polymer interface in composite electrolytes of lithium aluminium titanium phosphate and polyetherurethane polymer electrolyte. Solid State Ionics 121, 115-119 (1999).

17. Płcharski, J. & Weiczorek, W. PEO based composite solid electrolyte containing nasicon. Solid State Ionics 28-30, 979-982 (1988).

18. Chen, L. et al. PEO/garnet composite electrolytes for solid-state lithium batteries: From "ceramic-in-polymer" to "polymer-in-ceramic". Nano Energy 46, 176-184 (2018).

19. Nairn, K., Forsyth, M., Every, H., Greville, M. & MacFarlane, D. R. Polymer-ceramic ion-conducting composites. Proceedings of the 10th International Conference on Solid State Ionics 86-88, 589-593 (1996).

20. Sheng, L. et al. In-situ polymerized separator enables propylene carbonate electrolyte compatible with high-performance lithium batteries. Journal of Power Sources 551, 232172 (2022).

21. Wan, J., Zhang, J., Yu, J. & Zhang, J. Cellulose Aerogel Membranes with a Tunable Nanoporous Network as a Matrix of Gel Polymer Electrolytes for Safer Lithium-Ion Batteries.ACS Appl. Mater. Interfaces 9, 24591-24599 (2017).

22. Ye, Y.-S., Rick, J. & Hwang, B.-J. Ionic liquid polymer electrolytes. J. Mater. Chem. A 1, 2719-2743 (2013).

23. Hofmann, A., Schulz, M. & Hanemann, T. Gel electrolytes based on ionic liquids for advanced lithium polymer batteries. Electrochimica Acta 89, 823-831 (2013).

24. Efimova, A., Pfützner, L. & Schmidt, P. Thermal stability and decomposition mechanism of 1-ethyl-3-methylimidazolium halides. Thermochimica Acta 604, 129-136 (2015).

25. Balo, L., Shalu, Gupta, H., Kumar Singh, V. & Kumar Singh, R. Flexible gel polymer electrolyte based on ionic liquid EMIMTFSI for rechargeable battery application. Electrochimica Acta 230, 123-131 (2017).

26. Yuan, C. et al. Preparation and characterization of a novel ionic conducting foam-type polymeric gel based on polymer PVdF-HFP and ionic liquid [EMIM][TFSI]. Colloid and Polymer Science 293, 1945-1952 (2015).

27. Zhou, Q., Fitzgerald, K., Boyle, P. D. & Henderson, W. A. Phase Behavior and Crystalline Phases of Ionic Liquid-Lithium Salt Mixtures with 1-Alkyl-3-methylimidazolium Salts. Chem. Mater. 22, 1203-1208 (2010).

28. Zhou, Q. et al. Phase Behavior of Ionic Liquid–LiX Mixtures: Pyrrolidinium Cations and TFSI– Anions – Linking Structure to Transport Properties. Chem. Mater. 23, 4331-4337 (2011).

29. Lashkari, S., Chekini, M., Pal, R. & Pope, M. A. Aqueous, Mixed Micelles as a Means of Delivering the Hydrophobic Ionic Liquid EMIM TFSI to Graphene Oxide Surfaces. Langmuir 38, 531-540 (2022).

30. Brinker, C. J. & Scherer, G. W. (eds Brinker, C. J. & Scherer, G. W.) 514-615 (Academic Press, San Diego, 1990).

31. Villaluenga, I. et al. Cation only conduction in new polymer–SiO2 nanohybrids: Na+ electrolytes. J. Mater. Chem. A 1, 8348-8352 (2013).

32. Ellerbrock, R., Stein, M. & Schaller, J. Comparing amorphous silica, short-range-ordered silicates and silicic acid species by FTIR. Scientific Reports 12, 11708 (2022).

33. Rey, I. et al. Spectroscopic and Theoretical Study of (CF3SO2)2N- (TFSI-) and (CF3SO2)2NH (HTFSI). J. Phys. Chem. A 102, 3249-3258 (1998).

34. Tseng, Y.-C. et al. Polymer electrolytes based on Poly(VdF-co-HFP)/ionic liquid/carbonate membranes for high-performance lithium-ion batteries. Polymer 173, 110-118 (2019).

35. Vrandečić, N. S., Erceg, M., Jakić, M. & Klarić, I. Kinetic analysis of thermal degradation of poly(ethylene glycol) and poly(ethylene oxide)s of different molecular weight. Thermochimica Acta 498, 71-80 (2010).

36. Rubio, F., Rubio, J. & Oteo, J. L. A DSC study of the drying process of TEOS derived wet silica gels. Thermochimica Acta 307, 51-56 (1997).

37. Rotnicki, K. et al. Phase transitions, molecular dynamics and structural properties of 1-Ethyl-3-methylimidazolium bis(trifluoromethylsulfonyl)imide ionic liquid. Journal of Molecular Liquids 313, 113535 (2020).

38. Correia, D. M. et al. Ionic and conformational mobility in poly(vinylidene fluoride)/ionic liquid blends: Dielectric and electrical conductivity behavior. Polymer 143, 164-172 (2018).

39. Rotnicki, K. et al. The effect of pore size of the nanoporous activated carbon on the thermal behavior of confined 1–ethyl–3–methylimidazolium bis(trifluorosulfonyl)imide [EMIM TFSI]. Journal of Molecular Liquids 373, 121177 (2023).

40. Noda, A., Hayamizu, K. & Watanabe, M. Pulsed-Gradient Spin−Echo 1H and 19F NMR Ionic Diffusion Coefficient, Viscosity, and Ionic Conductivity of Non-Chloroaluminate Room-Temperature Ionic Liquids. J. Phys. Chem. B 105, 4603-4610 (2001).

41. Matsumoto, K., Hagiwara, R. & Tamada, O. Coordination environment around the lithium cation in solid Li2(EMIm)(N(SO2CF3)2)3 (EMIm=1-ethyl-3-methylimidazolium): Structural clue of ionic liquid electrolytes for lithium batteries. Solid State Sciences 8, 1103-1107 (2006).

42. Kubisiak, P., Wróbel, P. & Eilmes, A. Molecular Dynamics Investigation of Correlations in Ion Transport in MeTFSI/EMIM–TFSI (Me = Li, Na) Electrolytes. J. Phys. Chem. B 124, 413-421 (2020).

43. Arof, A. K., Amirudin, S., Yusof, S. & Noor, I. M. A method based on impedance spectroscopy to determine transport properties of polymer electrolytes. Physical chemistry chemical physics : PCCP 16, (2013).

44. Choi, W., Shin, H.-C., Kim, J. M., Choi, J.-Y. & Yoon, W. Modeling and Applications of Electrochemical Impedance Spectroscopy (EIS) for Lithium-ion Batteries. Journal of electrochemical science and technology 11, 1-13 (2020).

45. Wan, Z. et al. Low Resistance–Integrated All-Solid-State Battery Achieved by Li7La3Zr2O12 Nanowire Upgrading Polyethylene Oxide (PEO) Composite Electrolyte and PEO Cathode Binder. Adv. Funct. Mater. 29, 1805301 (2019).

46. Wang, W., Yi, E., Fici, A. J., Laine, R. M. & Kieffer, J. Lithium Ion Conducting Poly(ethylene oxide)-Based Solid Electrolytes Containing Active or Passive Ceramic Nanoparticles.J. Phys. Chem. C 121, 2563-2573 (2017).

47. Wang, G. & Kieffer, J. Contiguous High-Mobility Interphase Surrounding Nano-Precipitates in Polymer Matrix Solid Electrolyte. ACS Appl. Mater. Interfaces 15, 848-858 (2023).

48. Beg, C. & Kieffer, J. Anharmonicity and the emergence of diffusive behavior in a lattice-solute model solid-state electrolyte. Computational Materials Science 228, 112359 (2023).

49. Evans, J., Vincent, C. A. & Bruce, P. G. Electrochemical measurement of transference numbers in polymer electrolytes. Polymer 28, 2324-2328 (1987).

50. Chintapalli, M. et al. Relationship between Conductivity, Ion Diffusion, and Transference Number in Perfluoropolyether Electrolytes. Macromolecules 49, 3508-3515 (2016).

51. Shigenobu, K., Dokko, K., Watanabe, M. & Ueno, K. Solvent effects on Li ion transference number and dynamic ion correlations in glyme- and sulfolane-based molten Li salt solvates. Phys. Chem. Chem. Phys. 22, 15214-15221 (2020).

52. Tao, L. et al. High-efficiency and stable quasi-solid-state dye-sensitized solar cell based on low molecular mass organogelator electrolyte.J. Mater. Chem. A 3, 2344-2352 (2015).

53. Mei, B.-A., Munteshari, O., Lau, J., Dunn, B. & Pilon, L. Physical Interpretations of Nyquist Plots for EDLC Electrodes and Devices. J. Phys. Chem. C 122, 194-206 (2018).

54. Gouverneur, M., Kopp, J., van Wüllen, L. & Schönhoff, M. Direct determination of ionic transference numbers in ionic liquids by electrophoretic NMR. Phys. Chem. Chem. Phys. 17, 30680-30686 (2015).

55. Dong, D., Sälzer, F., Roling, B. & Bedrov, D. How efficient is Li+ ion transport in solvate ionic liquids under anion-blocking conditions in a battery. Phys. Chem. Chem. Phys. 20, 29174-29183 (2018).

56. Gouverneur, M., Schmidt, F. & Schönhoff, M. Negative effective Li transference numbers in Li salt/ionic liquid mixtures: does Li drift in the "Wrong" direction. Phys. Chem. Chem. Phys. 20, 7470-7478 (2018).

CHAPTER VI Conclusions and Future Directions

6.1 Conclusions

This research is dedicated to advancing materials development in the realm of solid-state and gel-type single-ion-conducting materials for battery electrolyte applications. The investigation encompasses two distinct material classes: PEO-based nanocomposites and silica-based inorganic-organic hybrid materials. The work detailed in this thesis has led to the identification of key parameters and design criteria specific to each material type. The major findings can be summarized as follows:

(1) PEO-based nanocomposite: Incorporating LATP nanoparticles via a novel in-situ precipitation processing method, effectively eliminated particle agglomeration even at high loadings (up to 30 wt%), leveraging the interphase region to enhance ionic conductivity. At an ambient temperature, a maximum ionic conductivity of 3.8×10^{-4} S·cm^{-1} is observed at 25 wt% LATP loading with an EO/Li ratio of 10. The tri-phase model predicts a peak value of 4.36×10^{-4} S·cm^{-1}, validating the analytical approach. Relying solely on LATP nanoparticles as the Li^+ source reveals their contribution to be less than 2% of the mobile charge carriers. The temperature dependence of conductivity distinguishes two behavior groups below and above the interphase percolation threshold. A novel formalism based on correlative activation free energy (CAFE) is employed to extract activation energy and entropy for cation migration. Both activation energies and entropies

decrease with LATP loading in both regimes, with an abrupt increase at the interphase percolation threshold, creating a narrow 'inversion' region where higher ionic conductivities are achieved despite an increase in activation energy, attributed to a simultaneous rise in activation entropy. The interphase is characterized by increased disorder in the C-O-C groups of the polymer backbone and shallower potential wells at lithium cation sites.

(2) Silica based organic-inorganic hybrid material filled by PEO: The hybrid design, integrating an inorganic nanoporous silica backbone with an organic phase, effectively addresses the challenge of balancing ionic mobility and mechanical stiffness. Functionalized with TFSISPE ion donor, the material exhibits single-ion-conducting behavior. We employ a transition state theory (TST) approach for activation free energy analysis, tailored for non-Arrhenius behavior in temperature-dependent conductivity. Charge carrier mobility calculations reveal a significant increase (between 18 and 110 times) compared to bulk PEO (Mw = 900 kg mol^{-1}), primarily attributed to structural changes in the filler polymer induced by confinement to small pores and proximity to the rigid silica backbone. Variation in Li^+ mobility with different ion donor concentrations correlates with varying degrees of backbone network modification. Comparative analysis between Et_3NH^+ and Li^+ systems underscore a substantial difference in their ionic mobilities, attributed to steric hindrance and associated activation barrier heights for bulkier Et_3NH^+. Systems containing Et_3NH^+ exhibit higher activation enthalpies and lower activation entropies, aligning with expectations based on cation size and structural complexity. The introduction of oligo-PEG grafting results in a substantial boost in Li^+ mobility, attributed in part to the induced network modification by grafting, leading to a higher fill factor. Similarly, the mobility of the material filled with mixed PEO chain lengths is 2.85 times higher than in systems filled with only 600 Mw PEO. This improvement is linked to the shorter polymer segments easily inserting themselves into smaller pores and conforming better to the irregular surface of the pore walls.

However, the benefits of grafted oligo-PEG extend beyond increasing the fill factor. The covalent bonding of PEG to the backbone surface serves as a coupling agent, reducing osmotic drag and enhancing the affinity between the inorganic backbone and the polymer. Uniquely, mixed chain length sample shows remarkably high activation entropy, primarily responsible for the increased Li^+ mobility compared to the system with only 600 Mw PEO. Aligning with the fact that a higher concentration of end groups exists in a mixture of different-length polymer, which establish both disruption in the structure and higher segmental mobility. Essentially, The higher $d_0^2\Gamma_0$ factor values in the mixed-chain system, compared to the oligo-PEG grafted system, suggest a higher attempt frequency and jump distance in the mixed-polymer system.

(3) Silica based organic-inorganic hybrid material filled by EC/PC: This study introduces an organic-inorganic hybrid electrolyte with a nanoporous silica backbone housing an EC/PC mixture, employing a correlative activation free energy analysis based on transition state theory (TST) for a comprehensive understanding of the conducting mechanism. Verified through transference number measurements, the functionalization with TFSISPE ion donor ensures single-ion conducting behavior. Nitrogen adsorption-desorption measurements validate controlled pore structure manipulation by varying the R_w ratios. Cross-validation between nitrogen adsorption-desorption and TGA affirms the accuracy of both methods in measuring pore volume.

Conductivity variations with EC weight fraction in the EC/PC mixture demonstrate an increasing trend with EC concentration, cautioning against precipitation risks at 90 wt% EC. The hybrid material exhibits a noteworthy 10^{-3} S·cm^{-1} ionic conductivity, representing a tenfold improvement over the former PEO-filled system. Cation mobility calculations identify the $SiO_2T_{0.2}Ol_{0.3}[EC/PC]_{4.6}$ material, featuring oligo-PEG grafting and the largest pore volume, with the highest mobility at $3.219 \cdot 10^{-5}$ S cm^2·C^{-1}. However, oligo-PEG grafting minimally affects mobility improvement.

CAFE analysis consistently indicates higher activation enthalpies and entropies for oligo-PEG grafted materials compared to those without, in contrast to the former PEO-filled system. This deviation may be attributed to the absence of structural similarity between oligo-PEG and EC/PC, rendering the coupling effect nonfunctional. Moreover, oligo-PEG may impede Li^+ hopping due to steric hindrance, elucidating the increase in activation energy in grafted materials. The addition of $LiClO_4$ effectively enhances conductivity by increasing carrier concentration and reduces activation energy, potentially due to decreased solvent molecules around Li^+ and subsequent improvements in ion-solvent cluster sizes for enhanced transportation.

(4) Silica based organic-inorganic hybrid material filled by EMIM TFSI ionic liquid: A novel hybrid composite electrolyte, incorporating a functionalized silica backbone encapsulating EMIM TFSI ionic liquid, was developed, demonstrating superior ionic conductivity and thermal stability. Thermal analysis via TGA confirmed stability up to 290 °C. The R_w ratio significantly impacts the ionic conductivity. For system filled with pure EMIM TFSI, the maximum ionic conductivity of 3.75×10^{-3} $S\cdot cm^{-1}$ is found at R_w equals 5. Analysis of activation enthalpies and entropies unveil that R_w equals 5 system shows a stronger curvature in the activation enthalpy vs. 1/T and a nearly flat activation entropy. This suggests that the material undergoes more significant structural changes with varying temperature. The observed phenomenon may be attributed to the related pore size distribution coinciding with a transition between liquid structures inside the pores. Larger pores exhibit a bulk-like structure, while smaller pores experience constraints imposed by the proximity of the walls. The lightly LiTFSI-doped system (10:1) shows a notable increase in ionic conductivity compared to the non-doped system, with the R_w equals 4 materials reaching 8.04×10^{-3} $S\cdot cm^{-1}$, twice as high as the non-doped sample. However, the heavily (10:5) doped material shows only minimal improvement compared to the non-doped system and, surprisingly, exhibits lower conductivity than the lightly (10:1) doped group. DSC studies reveal the formation of coordination between Li^+ and

$TFSI^-$, resulting in $[Li(TFSI)2]^-$ ion pairs and chain-like clusters. The concentration increase of LiTFSI leads to the formation of larger ionic aggregates, which can significantly increases system viscosity, offsetting the nominal benefit of higher Li^+ concentration for ionic conductivity. The calculated ion mobility reveals that the ionic liquid-filled system falls within the same order of magnitude as the EC/PC system and is approximately an order of magnitude higher than the PEO counterpart. Computational analysis between different R_w materials indicates that pore size distribution has a strong and unexpected influence on Li^+ transport properties, with smaller pore sizes improving ion mobility.

6.2 Future directions

Building on the insights into the interfacial ion-conducting mechanism gained from PEO-based nanocomposites, we have developed organic-inorganic hybrid electrolytes. These electrolytes incorporate a rigid silica backbone that can be functionalized to meet various requirements, including achieving single-ion conduction behavior, high ionic conductivity, and improved thermal stability. Here, we propose several potential directions for future exploration:

(1) Regarding PEO-based nanocomposites: Our findings demonstrate that interphase formation is primarily a configurational effect. This suggests that fast ion transport through the interphase is not exclusive to specific materials but may extend to other material systems. Exploring alternative polymer matrices, such as polyvinylidene fluoride (PVDF) or copolymers, as well as employing different filler materials, holds promise for achieving enhanced overall properties. However, the development of effective dispersion strategies is crucial for success in these endeavors. Additionally, measuring the transference number can provide valuable insights for a deeper understanding of interfacial conduction.

(2) For the hybrid system with EC/PC filler: The efficacy of oligo-PEG grafting in enhancing charge carrier mobility is evident in PEO-filled system, attributed to backbone network modification and the coupling of the organic phase with the inorganic backbone. However, this improvement relies heavily on the structural similarity between the grafted oligo-PEG and the filler PEO. Interestingly, oligo-PEG does not exhibit evidence of mobility improvement in EC/PC systems, underscoring the importance of structural compatibility. To further enhance ion mobility in the already conductive EC/PC system (above 10^{-3} S·cm^{-1}), exploring moieties with structural similarity to EC/PC is proposed.

The poor thermal stability of the EC/PC system, unaffected by varying pore structures, suggests alternative approaches, such as transitioning to polymerized EC. However, such changes may come at the cost of reduced conductivity. Blending EC/PC with polymers like PEO has shown no effect on improving thermal stability, as indicated by TGA data revealing no change in the onset vaporization temperature for the liquid carbonate with added PEO. This lack of improvement may stem from poor structural similarity between EC/PC and PEO. Therefore, blending EC/PC with polymerized EC is proposed as potential strategies for enhancing thermal stability, while minimized the potential negative effect on ionic conductivity.

(3) For the hybrid system with the IL filler: The primary challenge with the current system lies in its low transference number, approximately around 0.4, attributed to the salt nature of the ionic liquid. To address this, we introduced LiTFSI salt to increase the Li^+ concentration and reduce that of $EMIM^+$, aiming to theoretically raise the transference number. The effectiveness of this approach awaits confirmation through future transference number measurements. Exploring alternative solutions involves polymerizing the IL or grafting polymerized IL onto the backbone. However, these approaches pose challenges. Polymerization may increase viscosity, potentially decreasing ion mobility.

Additionally, the bulky size of the polymerized IL could lead to diffusion issues while filling pores, as indicated in Chapter III. Plasticizing the polymerized IL with IL could mitigate viscosity concerns but may result in a lower transference number due to mobile ions, presenting a trade-off that needs careful consideration.

(4) For the backbone itself: Present system relies on TFSISPE as the ion donor, which is associated with a high cost. Additionally, there are limitations to the grafting capability of the backbone, which could potentially restrict the Li^+ concentration. Future directions should involve exploring ion donors with different chemical structures that are easier to synthesize and more cost-effective. Polymerizing the ion donor could also be investigated as a strategy to increase the Li^+ concentration.

APPENDICES

APPENDIX A Supplementary Materials for Chapter II

Computing the interphase volume fraction

For simplicity a spherical particle shape is assumed. The volume fraction of the nanoparticles can then be expressed as

$$\phi_N = 4\pi\theta_N R^3/3, \tag{A1}$$

where $\theta_N = n/V_t$ is the particle number density. At low concentrations of nanoparticles, the combined volume fraction of nanoparticles and interphase can be reasonably approximated as

$$\phi = \phi_N + \phi_I = 4\pi\theta_N\left[\left(1+\delta\right)R\right]^3/3, \tag{A2}$$

where δ represents the thickness of the interfacial layer in units of *R*. For nanoparticles, δ can be of the same magnitude as *R*, or even larger. [1–3] Combining Equation (A1) and (A2) yields $\phi = \phi_N\left(1+\delta\right)^3$. However, as the particle concentration increases, this relationship gradually overestimates ϕ_I due to the overlap of the interfacial regions associated with neighboring nanoparticles. To correct for this overestimation, we replace $\phi = \phi_N\left(1+f\right)$, where the dependence

of *f* on the particle density is estimated following an approach similar to that proposed by Johnson et al.[4] Knowing that *f* must decrease as ϕ_N increases, the rate of decrease is inversely proportional to the volume fraction of polymer ($1-\phi_N$), into which the interphase can readily expand into, i.e.,

$$\frac{df}{d\phi_N} = -\frac{k}{1-\varepsilon\phi_N}, \tag{A3}$$

where the factor $\varepsilon < 1$ has been inserted to avoid the singularity at $\phi_N = 1$ and can be chosen arbitrarily close to, but not equal to one. Separation of variables and integration then yields

$$df = -\frac{k d\left(\varepsilon\phi_N\right)}{\varepsilon\left(1-\varepsilon\phi_N\right)} \Rightarrow f = \frac{k}{\varepsilon}\ln\left(1-\varepsilon\phi_N\right) + f_0 . \tag{A4}$$

At $\phi_N = 0$, $f = f_0 = \left(1+\delta_0\right)^3 - 1$, where δ_0 is the maximum interphase thickness, and at $f = 0 \Rightarrow k = -\varepsilon f_0 / \ln\left(1-\varepsilon\right)$. Hence, using this approach, only one parameter is undetermined, i.e., δ_0, the value of which is determined via data fitting.

Computing the amount of charge contributed by LATP nanoparticles under homogeneous charge carrier distribution assumption

Assuming a spherical particle shape, the charge carrier deficit of an LATP particle with radius *R* is

$$\Delta n_N = -\left(\rho_N^{(i)} - \rho_N^{(f)}\right)\frac{4}{3}\pi R^3, \tag{A5}$$

where the superscripts (*i*) and (*f*) refer to the initial and final charge carrier density, respectively.

Reformulating Equation (A1) as $\phi_N = \frac{4\pi R^3}{3V}$, where V is the volume of composite occupied by one particle on average, we get

$$\Delta n_N = -\left(\rho_N^{(i)} - \rho_N^{(f)}\right)\phi_N V . \tag{A6}$$

This quantity of charge carriers is transferred to the polymer phase, which occupies the volume $\left(1-\phi_N\right)V$ on average. Hence,

$$\Delta n_P = \left(\rho_P^{(i)} - \rho_P^{(f)}\right)\left(1-\phi_N\right)V , \tag{A7}$$

or

$$\left(\rho_N^{(i)} - \rho_N^{(f)}\right)\phi_N = \left(\rho_P^{(f)} - \rho_P^{(i)}\right)\left(1-\phi_N\right). \tag{A8}$$

From this follows that

$$\rho_P^{(f)} = \frac{\phi_N \rho_N^{(i)} + \left(1-\phi_N\right)\rho_P^{(i)}}{\phi_N / K + \left(1-\phi_N\right)}, \tag{A9}$$

where $K = \frac{a_{Li^+(P)}}{a_{Li^+(N)}} \simeq \frac{\rho_P^{(f)}}{\rho_N^{(f)}}$. When samples do not contain any salt, i.e., $\rho_p^{(i)} = 0$, and thus

$$\rho_P^{(f)} = \frac{\phi_N \rho_N^{(i)}}{\phi_N / K + \left(1-\phi_N\right)}. \tag{A10}$$

These charge carrier densities are assumed to be constant within each phase.

Computing the amount of charge contributed by LATP nanoparticles under the assumption of space charge layer at LATP/polymer interface

The space charge develops as a result of the chemically preferential dissolution of certain charged species from the LATP into the polymer phase and the electric field that arise between the dissociated charges. The chemical and electrostatic potential act oppositely on mobile charged

species, establishing a diffuse charge carrier distribution near the interface that in equilibrium can be described by an exponentially decaying function.[5] For the polymer phase we write

$$\rho_P(r) - \rho_P^{(i)} = \left(\rho_P^{(R)} - \rho_P^{(i)}\right) e^{-(r-R)/\lambda_P}, \tag{A11}$$

and for the LATP phase

$$\rho_N(r) - \rho_N^{(i)} = \left(\rho_N^{(R)} - \rho_N^{(i)}\right) e^{-(R-r)/\lambda_N}, \tag{A12}$$

where $\rho_P^{(i)}$ and $\rho_N^{(i)}$ are the initial charge carrier densities in polymer and LATP, respectively, while λ_P and λ_N represent the corresponding space charge decay lengths. At the interface the ratio of charge carrier densities is described by the dissolution eqilibrium constant, $K \simeq \rho_P^{(R)} / \rho_N^{(R)}$.

The number of charge carriers received by the polymer per nanoparticle is obtained by integrating the charge carrier density over space. For as long as particles remain well separated, and carrying out the integration using spherical coordinates,

$$\begin{aligned}
\Delta n_P &= 4\pi\left(\rho_P^{(R)} - \rho_P^{(i)}\right)\int_R^\infty r^2 e^{-(r-R)/\lambda_P}\, dr = 4\pi\left(\rho_P^{(R)} - \rho_P^{(i)}\right)\left[-\lambda_P r^2 e^{-(r-R)/\lambda_P}\Big|_R^\infty + 2\lambda_P \int_R^\infty r e^{-(r-R)/\lambda_P}\, dr\right] \\
&= 4\pi\left(\rho_P^{(R)} - \rho_P^{(i)}\right)\left[-\lambda_P r^2 e^{-(r-R)/\lambda_P}\Big|_R^\infty + 2\lambda_P\left\{-\lambda_P r e^{-(r-R)/\lambda_P}\Big|_R^\infty + \lambda_P \int_R^\infty r e^{-(r-R)/\lambda_P}\, dr\right\}\right] \\
&= 4\pi\left(\rho_P^{(R)} - \rho_P^{(i)}\right)\left[-\lambda_P r^2 e^{-(r-R)/\lambda_P}\Big|_R^\infty + 2\lambda_P\left\{-\lambda_P r e^{-(r-R)/\lambda_P}\Big|_R^\infty - \lambda_P^2 e^{-(r-R)/\lambda_P}\Big|_R^\infty\right\}\right]
\end{aligned}$$

$$\Delta n_P = 4\pi\left(\rho_P^{(R)} - \rho_P^{(i)}\right)\lambda_P\left[R^2 + 2\lambda_P R + 2\lambda_P^2\right] = 4\pi R^3\left(\rho_P^{(R)} - \rho_P^{(i)}\right)\left(\lambda_P/R\right)^3\left[\left(R/\lambda_P\right)^2 + 2\left(R/\lambda_P\right) + 2\right]. \tag{A13}$$

This amount of charge is equal and opposite that lost by the nanoparticle, which upon integration amounts to

$$\Delta n_N = 4\pi\left(\rho_N^{(R)} - \rho_N^{(i)}\right)\lambda_N\left[R^2 - 2\lambda_N R + 2\lambda_N^2\right] = 4\pi\left(\rho_N^{(R)} - \rho_N^{(i)}\right)R^3\left(\lambda_N/R\right)^3\left[\left(R/\lambda_N\right)^2 - 2\left(R/\lambda_N\right) + 2\right].$$

(A14)

Henceforth, we abbreviate $\alpha_P = \left(\frac{\lambda_P}{R}\right)^3 \left[\left(\frac{1}{\lambda_P/R}+1\right)^2+1\right]$ and $\alpha_N = \left(\frac{\lambda_N}{R}\right)^3 \left[\left(\frac{1}{\lambda_N/R}-1\right)^2+1\right]$, and

substituting in the above equations along with using $\phi_N = \frac{4\pi R^3}{3V}$, we obtain

$$\Delta n_N = 3V\phi_N \left(\rho_N^{(R)} - \rho_N^{(i)}\right)\alpha_N , \tag{A15}$$

and

$$\Delta n_P = 3V\phi_N \left(\rho_P^{(R)} - \rho_P^{(i)}\right)\alpha_P . \tag{A16}$$

The polymer occupies the volume $V - 4/3\pi R^3 = V\left(1-\phi_N\right) \Rightarrow 4/3\pi R^3 = V\left(1-\left(1-\phi_N\right)\right) = V\phi_N$ per particle, and hence this charge donated by one particle is placed in $\left(1-\phi_N\right)V$. With that the change in charge carrier density in the polymer phase is

$$\Delta\rho_P = \frac{\Delta n_P}{\left(1-\phi_N\right)V} = \frac{3\phi_N}{\left(1-\phi_N\right)}\left(\rho_P^{(R)} - \rho_P^{(i)}\right)\alpha_P , \tag{A17}$$

and the average charge carrier density in the polymer then is

$$\rho_P = \frac{3\phi_N}{\left(1-\phi_N\right)}\left(\rho_P^{(R)} - \rho_P^{(i)}\right)\alpha_P + \rho_P^{(i)} . \tag{A18}$$

Taking into account the charge balance between the LATP and polymer phases, we must have

$$\left(\rho_P^{(R)} - \rho_P^{(i)}\right)\alpha_P = \left(\rho_N^{(i)} - \rho_P^{(R)}/K\right)\alpha_N \Rightarrow \rho_P^{(R)}\left(\alpha_P + \alpha_N/K\right) = \rho_N^{(i)}\alpha_N + \rho_P^{(i)}\alpha_P , \tag{A19}$$

where we also used the fact that $\rho_N^{(R)} = \rho_P^{(R)}/K$ to eliminate one of the unknowns. Soving for $\rho_P^{(R)}$ we obtain

$$\rho_P^{(R)} = \frac{\rho_N^{(i)}\alpha_N + \rho_P^{(i)}\alpha_P}{\left(\alpha_P + \alpha_N/K\right)}. \tag{A20}$$

Substituting yields,

$$\rho_P = \frac{3\phi_N}{\left(1-\phi_N\right)}\left(\frac{\rho_N^{(i)}\alpha_N + \rho_P^{(i)}\alpha_P}{\left(\alpha_P + \alpha_N/K\right)} - \rho_P^{(i)}\right)\alpha_P + \rho_P^{(i)} \tag{A21}$$

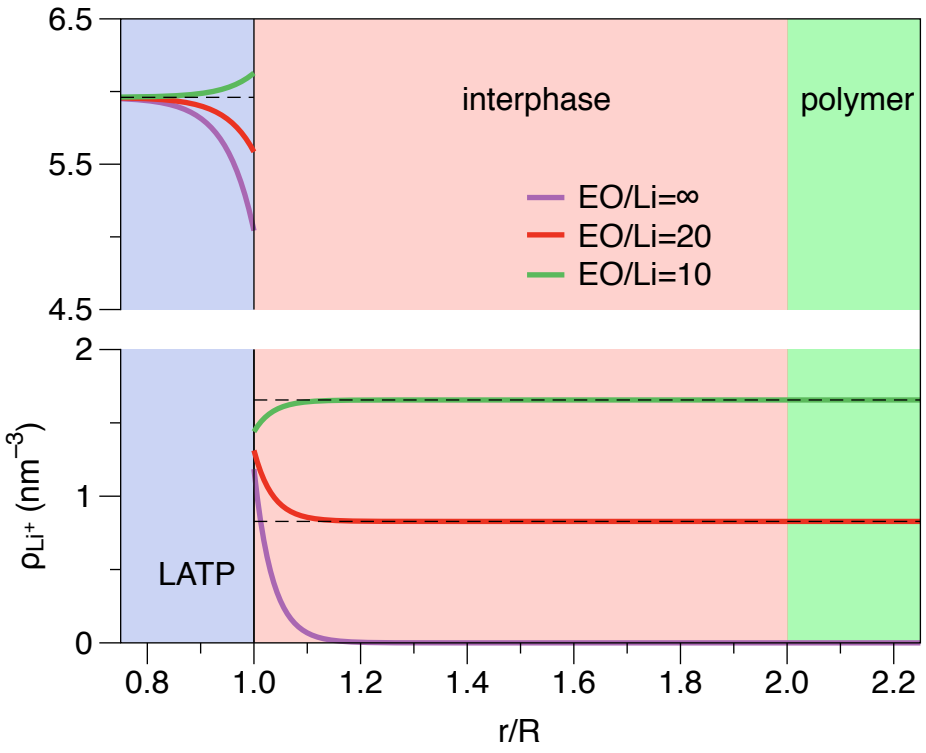

Appendix Figure A. 1 Li^+ ion number density near the LATP-polymer interface, as a function of the distance from the interface, assuming diffuse space charge layers described by an exponential decay. The dashed lines represent the initial Li+ ion number densities before cations are exchanged between phases.

Furthermore, for our analysis we use the fact that the decay length scales like the dielectric permittivity of a material, and hence, $\lambda_N/\lambda_P = \varepsilon_N/\varepsilon_P \sim 1.54$, which reduces the number of unknown parameters to two, i.e., λ_P, and K. Unfortunately, because these two quantities appear as a ratio in the above expression, attempting to optimize both their values simultaneously by fitting Equation (2–5) to the conductivity data renders the Jacobian calculated during the non-linear

regression ill-conditioned. Since our objective here is not to determine the exact shape of the charge carrier distribution at the interface is irrelevant, but to merely contrast the two scenarios of a homogenous charge distribution with that of a space charge layer localized near the LATP/polymer interface, we select a value for λ_P that is consistent with reports in the literature, e.g., $\lambda/R \approx 0.03$,[6] which leaves K as the only remaining fit parameter in the expression for ρ_P. The Li^+ ion number density spatial distributions estimated using this approach are shown in **Appendix Figure A. 1**.

Determination of the D.C. conductivity of the materials

The lithium-ion conductivity is derived from the location of the intercepts with the abscissa in the Nyquist plot of the complex dielectric impedance. **Appendix Figure A. 2** shows a typical Nyquist plot of the complex impedance at ambient temperature for LATP/PEO composite electrolyte with EO/Li = 20 and different amounts of LATP. The depressed semicircle describes the relationship between capacitance and resistance of an equivalent circuit with the two elements in parallel; the spike at low frequency is attributed to ion electro-diffusion.[7–9] The location on the abscissa where the imaginary component of the impedance vanishes corresponds to the resistance to charge transport across the specimen, R_b, which yields the conductivity according to $\sigma = L/(R_b \cdot S)$, where L is the thickness of the sample and S the cross-sectional area. With the particle loading increasing from 5 wt% to 25 wt%, the high frequency semicircle gradually decreases in size, indicates that the ionic conductivity increases.

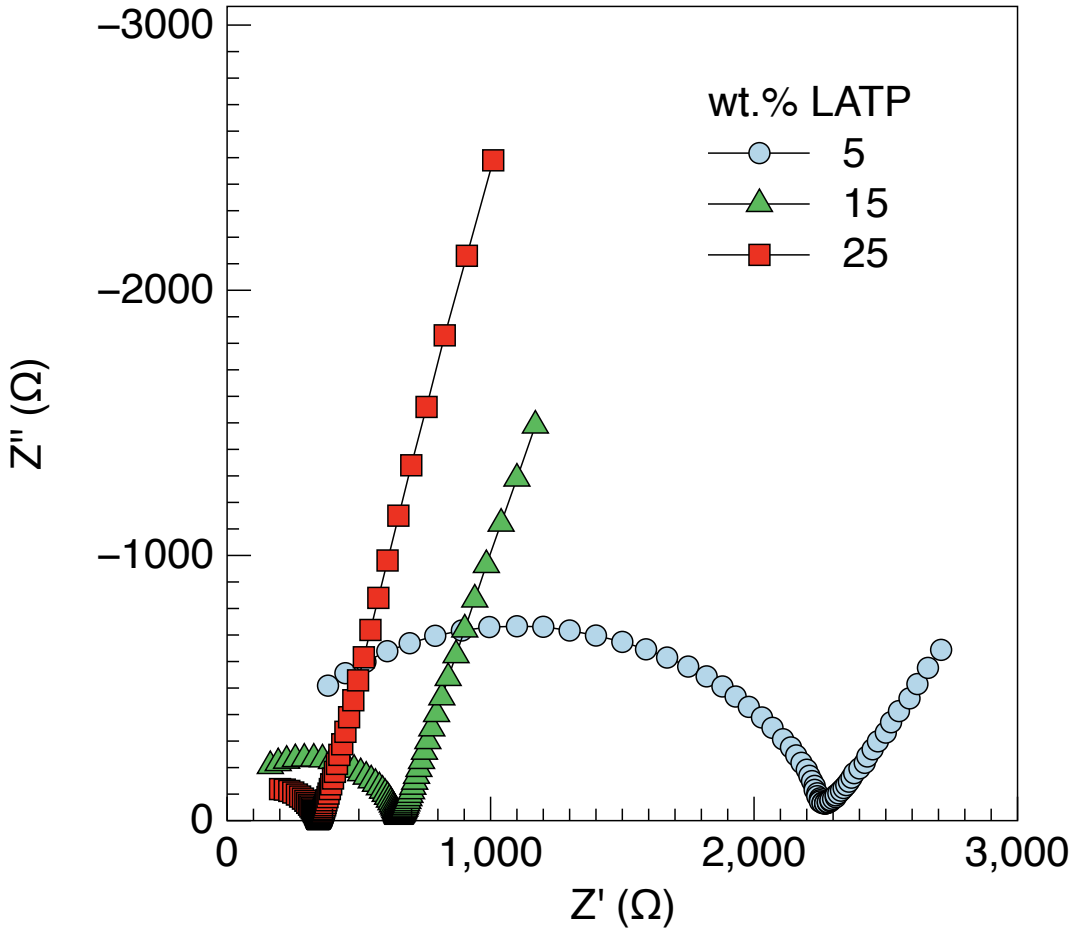

Appendix Figure A. 2 Nyquist plot for LATP/PEO composites with EO/Li = 20 and different particle loadings at 20°C

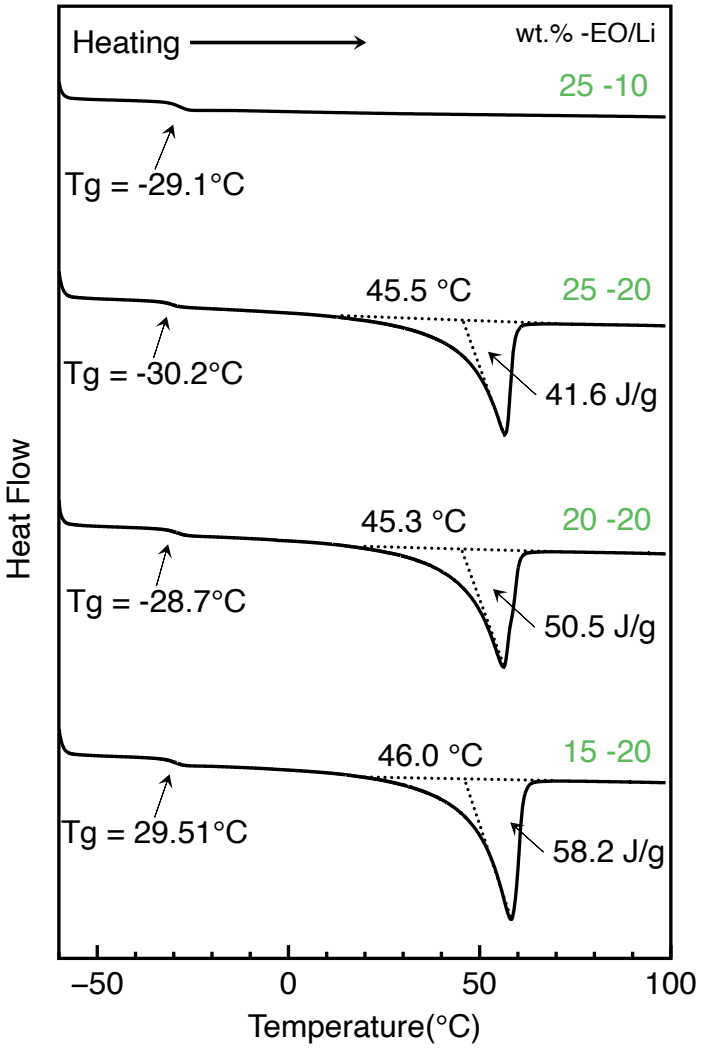

Appendix Figure A. 3 DSC thermograms of LATP/PEO composite with different particle loading and EO/Li.

Thermal properties are collected during the second scan of DSC measurement, the first scan aims to remove thermal history. Glass transition temperatures, T_g, are determined from the midpoint of the characteristic step in the experimental heat flow curve. T_g values range from –30°C to –28°C and do not vary significantly with particle loading and lithium salt concentration. The degree of crystallinity, χ_c, is calculated as $\chi_c = \Delta H_m/\Delta H_M^0$, where ΔH_m is the melting enthalpy of sample, and ΔH_M^0 is the melting enthalpy of pure 100% crystalline PEO (206 J g^{-1}).

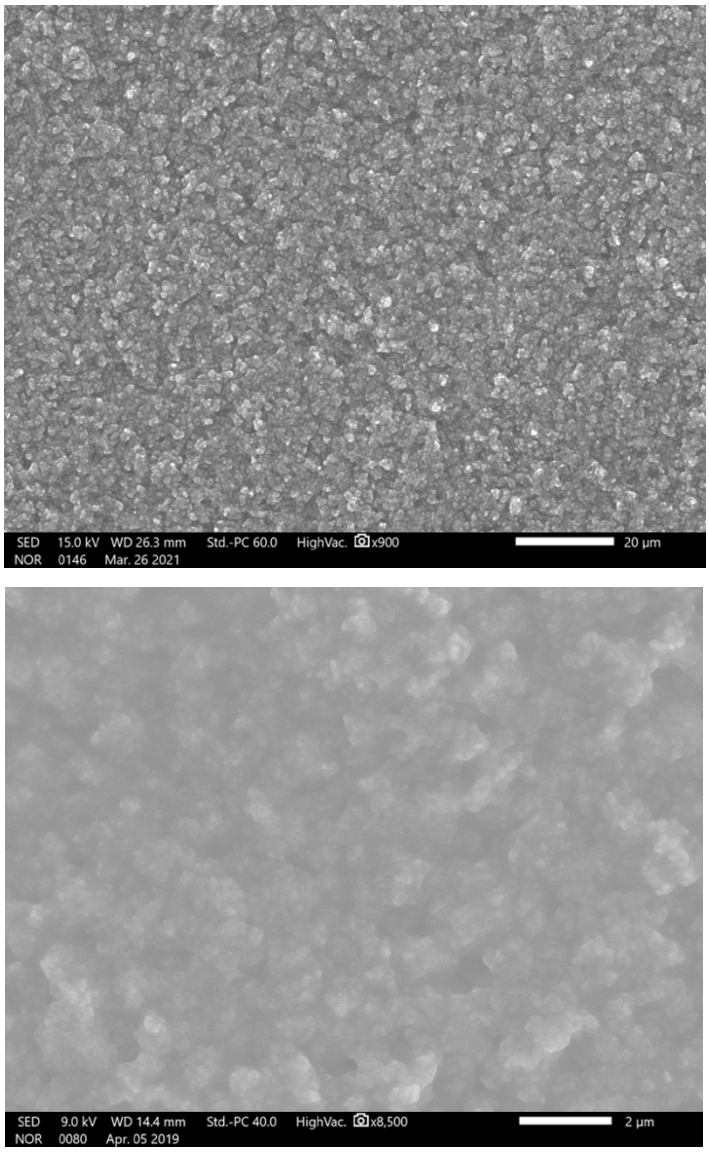

Appendix Figure A. 4 SEM images of LATP/PEO composite with 25 wt% LATP particles.

Particles are nanosized and evenly distributed in the matrix, no apparent agglomeration can be observed. The size of the particles is estimated to be 50–100 nm.

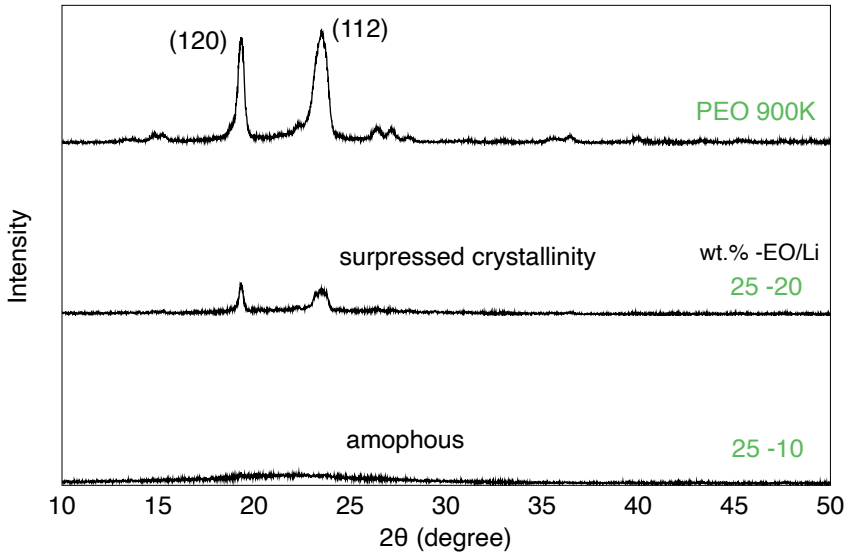

Appendix Figure A. 5 X-ray diffraction patterns of pure PEO 900K and composites with 25wt% LATP (EO/Li = 10 or 20).

Strong peaks at 19.3° and 23.4° are typical for pure PEO, indicating high degree of crystallinity. These peaks diminish in 25–20 sample, and eventually become a flat broad band in sample with higher lithium salt concentration. No peak for LATP was observed, indicating the amorphous nature of the in-situ precipitated particles.

APPENDIX B Correlative Activation Free Energy (CAFE)

A distribution of activation energies is postulated for disordered structures in which a range of transition states coexist for a given process, and it is sometimes given as the reason for deviation from Arrhenius behavior. However, this does not provide a satisfactory description in the present case, because low-activation energy processes begin to facilitate structural relaxation at low temperatures, whereas high-activation energy processes require increased amounts of thermal energy, which leads to a positively curved $\ln \sigma \cdot T$ *vs.* β dependency, instead of the negatively curved one we observe. Hence, in our analysis we account for a change in the activation free energy with temperature as a result of structural developments and a change in thermodynamic state.

In differential form, Equation (2–9) is $d\ln(\sigma T)/d\beta = -G_a - \beta\, dG_a/d\beta$, i.e., the leading term corresponds to the activation free energy. For systems exhibiting Arrhenius behavior only the leading term on right hand side prevails; $dG_a/d\beta = 0$ and G_a is a constant independent of temperature. Conversely, a non-zero derivative $dG_a/d\beta$ causes curvature in $\ln(\sigma T)$ *vs.* β, and evidently, reflects a change in G_a with β. Given the structural reconfiguration that occurs in the glass transition regime, the energy landscape topography changes, and hence, the difference between structural ground states and activated states inevitably evolves as well. While this evolution is abrupt in case of first order transitions, it is gradual in case of higher-order transitions. Since the activation

free energy represents a linear combination of state functions, its evolution between low-and high temperature values could assume an arbitrary form. Most likely, though, the changeover occurs gradually and monotonously. We therefore use Richard's generalized differential equation,[10] which was originally developed to describe growth phenomena, and is given by

$$\frac{dG_a(\beta)}{d\beta} = HG_a(\beta)\left(1-\left(G_a(\beta)/\Delta G_a\right)^{\nu}\right). \tag{B1}$$

This equation has the solution

$$G_a(\beta) = \Delta G_a\left(1+C_0 e^{-\nu H(\beta-\beta_C)}\right)^{-1/\nu} + C_1 = \Delta G_a \psi(\beta) + C_1, \tag{B2}$$

where $C_0 = \left(1/\psi(\beta_C)\right)^{\nu} - 1$ and $\psi(\beta_C)$ is the initial condition for the integration. H, ν, and β_C are adjustable parameters. For example, choosing $\nu = 1$ and $\psi(\beta_C) = 0.5$ yields the well-known probability density function for the two-level system, in which case H amounts to the energy difference between the two levels. With this, integrating Equation (B1) yields

$$\ln(\sigma T) = -\beta C_1 - \beta \Delta G_a \psi(\beta) + C_2 \tag{B3}$$

Upon separating the energy and entropy and determination of the integration constants we obtain

$$\ln(\sigma T) = P + S_0/k_B + \psi(\beta)\left(\Delta S_a/k_B - \beta \Delta E_a\right) - \beta E_0 \tag{2–10}$$

APPENDIX C Composition Conversion: Weight Fraction to Number Density

The methodology comprises three primary steps: initially, the conversion of weight fraction to molar fraction; subsequently, the conversion of molar fraction to molar concentration; and finally, the conversion of molar concentration to number density.

1. Converting Weight Fraction w_i to Molar Fraction x_i

Weight fraction (w_i) is the ratio of the mass of species i to the total mass of the system. The first step in the conversion process is to determine the molecular weight of species i (M_i) and the average molecular weight of the system (M).

$$M = \sum_i x_i M_i$$

Then we have

$$w_i = \frac{m}{\sum_j m_j} = \frac{n_i\ m_i}{\sum_j n_j M_J} = \frac{x_i M_i}{\sum_j x_j M_j} = x_i \frac{M_i}{M} \quad \text{(C1)}$$

Conversely, converting weight fraction into molar fractions requires one to invert the above equation,

$$x_i = w_i \frac{M}{M_i} \quad \text{(C2)}$$

When weight fractions are known, M can be calculated by

$$\frac{1}{M} = \frac{\sum_i x_i}{M} = \sum \frac{w_i}{M_i} \tag{C3}$$

Hance, by substituting equation (C3) into equation (C2),

$$x_i = \frac{w_i}{M_i \sum_j \frac{w_j}{M_j}} \tag{C4}$$

2. Converting Molar fraction x_i to Molar concentration c_i

Molar concentration is defined by $c_i = \frac{n_i}{V}$, where n_i is the number of mole of species i, and V is the volume of the system. This conversion involves determining the mass density of the system ρ, and is defined as $\rho = \frac{\sum_i m_i}{V}$, where m_i is the mass of species i. Since the Molar fraction x_i is known by applying the calculation in step 1, the molar concentration is determined by

$$c_i = \frac{n_i}{V} = \frac{n_i \sum_j n_j}{V \sum_j n_j} = \frac{x_i \sum_j n_j}{V} = \frac{x_i \rho \sum_j n_j}{\sum_j m_j} = \frac{x_i \rho \sum_j n_j}{\sum_j n_j M_j} = \frac{x_i \rho}{M} \tag{C5}$$

3. Converting Molar concentration c_i to number density N

Having obtained the molar concentration c_i, the next step is to convert it to number density N, which denotes the number of molecules per cubic nanometer (nm^3). The determination of molecular weight M_i in above expression can be arbitrary, as it is commonly defined to the mass of molecular units. For example, the molecular weight for PEO is defined as the molecular weight of the ethylene oxide unit (EO) instead of its total molecular weight. Each species i comprises a total of μ_i atoms, which is the sum of stoichiometric coefficients $\nu_{k(i)}$ of molecule i, where $k(i)$ represents the element k in molecule i. (e.g. for SiO_2, $\nu_{Si} = 1$, $\nu_O = 2$). The definition if the number density of element k is

$$N_k = \rho \sum_i \frac{w_i}{M_i} \nu_{k(i)} = \sum_i \nu_{k(i)} c_i \tag{C6}$$

The summation is performed over all compounds that contain element k. Therefore, a summation is required only when the species k is present in multiple molecular constituents. Using this information, we can calculate the overall number density of the system as follows:

$$N = \sum_k \sum_i \nu_{k(i)}\, c_i = \sum_i c_i \sum_k \nu_{k(i)} = \sum_i \mu_i c_i \quad \text{(C7)}$$

Take for example the $SiO_2T_{0.1}Ol_{0.1}[EO]_{0.7}$ hybrid material consisting of the grafted silica backbone and filler PEO (Mw = 600 g/mol), the composition and various quantities developed above are shown in **Appendix Table C.1**.

Appendix Table C.1 Conversion from weight fractions to molar fractions and number densities, use $SiO_2T_{0.1}Ol_{0.1}[EO]_{0.7}$ hybrid material as an example

Component	M (kg mol^{-1})	wt.-fraction	mol-fraction	c (mol m^{-3})	c (molecule nm^{-3})	ν_C	ν_H	ν_O	ν_{Si}	ν_S	ν_N	ν_F	$c_i \sum_i \nu_i$
EtOH	0.046	0.0530	0.0823	1831.74	1.1035	2	6	1					9.93
TFSISPE	0.417	0.3160	0.0543	1207.37	0.7273	15	24	4		2	2	3	36.37
PEO	0.044	0.1957	0.3184	7086.43	4.2689	2	4	1					29.88
OPEG	0.044	0.0390	0.0635	1412.22	0.8507	2	4	1					5.96
SiO_2	0.060	0.4036	0.4816	10717.39	6.4563			2	1				19.37
ρ(kg m^{-3})		$\sum \frac{w_i}{M_i}$	$\sum_i x_i M_i$			N_C	N_H	N_O	N_{Si}	N_S	N_N	N_F	
1604.9		13.9682	0.0721			23.36	44.56	22.04	6.46	1.45	1.45	2.18	101.50

APPENDIX D TGA Weight Fraction Calculation–PEO Filled System

Free variables: m_{SiO2} , m_{Et}, m_{T}, m_{P}, m_{Ol}, ω_{13} , and ω_{14} , where SiO_2, Et, T, P, Ol, ω_{13} , ω_{14} stand for silica, ethanol, TFSISPE, PEO (M_w = 600 g mol^{-1}), oligo-PEG, fitting parameter governing the ratio of mass loss of PEO in stage 1 and 2, and fitting parameter governing the ratio of mass loss of OPEG in stage 1 and 2.

Parameters from experimental result: m_{A}, m_{B}, m_{C} and m_{D}, where A, B, C and D represent the percent weight loss from 1st, 2nd, 3rd, and 4th steps of the TGA diagram.

Matrix establishment:

1) $\omega_{11} m_{Et} + \omega_{12} m_{T} + \omega_{13} m_{P} + \omega_{14} m_{Ol} = m_{A}$

2) $\omega_{21} m_{Et} + \omega_{22} m_{T} + \omega_{23} m_{P} + \omega_{24} m_{Ol} = m_{B}$

3) $\omega_{31} m_{Et} + \omega_{32} m_{T} = m_{C}$

4) $\omega_{45} m_{SiO2} = m_{D}$

5) $\omega_{12} m_{T} + \omega_{22} m_{T} + \omega_{32} m_{T} = m_{T}$, and $\omega_{12} : \omega_{22} : \omega_{32} = 119 : 212 : 130$

As a result, $\omega_{12} = 0.2581$, $\omega_{22} = 0.4599$, $\omega_{32} = 0.2820$

6) $\omega_{11} m_{Et} + \omega_{21} m_{Et} + \omega_{31} m_{Et} = m_{Et}$, and given that

$\omega_{11} : \omega_{21} : \omega_{31} = 15.5 : 2.3 : 1.38$ (for backbone materials)

$\omega_{11} : \omega_{21} : \omega_{31} = 14.87 : 2.65 : 1.66$ (for hybrid electrolytes)

As a result, $\omega_{11} = 0.8081$, $\omega_{21} = 0.1199$, $\omega_{31} = 0.0720$ (for backbone materials)

and $\omega_{11} = 0.7753$, $\omega_{21} = 0.1381$, $\omega_{31} = 0.0866$ (for hybrid electrolytes)

7) $\omega_{45} = 1$

8) $\omega_{13} m_P + \omega_{23} m_P = m_P$, and $\omega_{14} m_{Ol} + \omega_{24} m_{Ol} = m_{Ol}$

As a result, $\omega_{23} = 1 - \omega_{13}$, and $\omega_{24} = 1 - \omega_{14}$

Matrix for backbone materials:

$0.8081\, m_{Et} + 0.2581\, m_T + \omega_{14} m_{Ol} = m_A$

$0.1199\, m_{Et} + 0.4599\, m_T + (1 - \omega_{14}) m_{Ol} = m_B$

$0.0720\, m_{Et} + 0.2820\, m_T = m_C$

$m_{SiO2} = m_D$

The final matrix for composites:

$0.7753\, m_{Et} + 0.2581\, m_T + \omega_{13} m_P + \omega_{14} m_{Ol} = m_A$

$0.1381\, m_{Et} + 0.4599\, m_T + (1 - \omega_{13}) m_P + (1 - \omega_{14}) m_{Ol} = m_B$

$0.0866\, m_{Et} + 0.2820\, m_T = m_C$

$m_{SiO2} = m_D$

Other relationships:

The resolution of the aforementioned system of equations provides the numerical outcomes for each free variable, denoting the weight fraction of individual material components. Notably, these weight fractions represent a cumulative measure from various sources. To elaborate, for instance, the m_{SiO2} encompasses the combined weight fraction of SiO_2 originating from diverse contributors, such as the silica backbone, and the silane grafting group associated with the ion donor and oligo-PEG. A more detailed breakdown of the computed weight fractions could enhance comprehension regarding the composition of the material.

1) $m_{SiO2} = m_{SiO2\,(s)} + m_{SiO2\,(T)} + m_{SiO2\,(Ol)}$ (D1)

Where $m_{SiO2\,(s)}$, $m_{SiO2\,(T)}$, and $m_{SiO2\,(Ol)}$ refer to silica that originated from silica backbone, the ion donor, and oligo-PEG.

Gotten from the molecular structure, $m_{SiO2\,(T)} : m_{T} = 60 : 461$, and $m_{SiO2\,(Ol)} : m_{Ol} = 0.189 : 1$

So, $m_{SiO2\,(T)} = 0.1302\, m_{T}$ (D2)

$m_{SiO2\,(Ol)} = 0.1890\, m_{Ol}$ (D3)

Then, substitute (D2) and (D3) into (D1), yields

$m_{SiO2\,(s)} = m_{SiO2} - 0.1302\, m_{T} - 0.1890\, m_{Ol}$ (D4)

2) $m_{Et} = m_{Et(s)} + m_{Et(T)}$ (D5)

Where $m_{Et(s)}$ and $m_{Et(T)}$ represent ethanol originated from silica backbone and the ion donor, respectively. While the silane grafting group of the oligo-PEG does release ethanol during measurement, its weight fraction is relatively small. Consequently, the ethanol originating from this source is deemed negligible, and therefore, is not considered in the calculation.

Since $m_{Et(s)} : m_{SiO2\,(s)} = 19.18 : 80.82$ (determined from the TGA trace of the pure silica gel)

Then we get $m_{Et(s)} = 0.2373\ m_{SiO2\,(s)}$ (D6)

Then substitute (D4) into (D6) yields $m_{Et(s)} = 0.2373\ (m_{SiO2} - 0.1302\ m_{T} - 0.1890\ m_{Ol})$ (D7)

Finally, by substituting (D7) into (D5) yields

$$m_{Et(T)} = m_{Et} - m_{Et(s)} = m_{Et} - 0.2373\ m_{SiO2} + 0.0309\ m_{T} + 0.0448\ m_{Ol} \quad \text{(D8)}$$

References

1. Hamming, L. M., Qiao, R., Messersmith, P. B. & Brinson, L. C. Effects of dispersion and interfacial modification on the macroscale properties of TiO(2) polymer matrix nanocomposites. Compos Sci Technol 69, 1880-1886 (2009).

2. Ozmusul, M. S. & Picu, R. C. Elastic moduli of particulate composites with graded filler-matrix interfaces. Polymer Composites 23, 110-119 (2002).

3. Qiao, R., Deng, H., Putz, K. W. & Brinson, L. C. Effect of particle agglomeration and interphase on the glass transition temperature of polymer nanocomposites. Journal of Polymer Science Part B: Polymer Physics 49, 740-748 (2011).

4. Avrami, M. Kinetics of Phase Change. I General Theory. J. Chem. Phys. 7, 1103-1112 (2004).

5. Jiang, S. & Wagner, J. B. A theoretical model for composite electrolytes—I. Space charge layer as a cause for charge-carrier enhancement. Journal of Physics and Chemistry of Solids 56, 1101-1111 (1995).

6. de Klerk, N. J., J. & Wagemaker, M. Space-Charge Layers in All-Solid-State Batteries; Important or Negligible. ACS Appl. Energy Mater. 1, 5609-5618 (2018).

7. Mei, B.-A., Munteshari, O., Lau, J., Dunn, B. & Pilon, L. Physical Interpretations of Nyquist Plots for EDLC Electrodes and Devices. J. Phys. Chem. C 122, 194-206 (2018).

8. Nookala, M., Kumar, B. & Rodrigues, S. Ionic conductivity and ambient temperature Li electrode reaction in composite polymer electrolytes containing nanosize alumina. Journal of Power Sources 111, 165-172 (2002).

9. Sengwa, R. J. Effects of PEG plasticizer concentrations and film preparation methods on the structural, dielectric and electrical properties of PEo_PMMA blend based plasticized solid polymer electrolyte films. Indian Journal of Pure & Applied Physics 55, 7-18 (2017).

10. Richards, F. J. A Flexible Growth Function for Empirical Use. Journal of Experimental Botany 10, 290-301 (1959).